CFD Analysis of 3D Dynamic Stall

by

Agis Spentzos BEng

Thesis submitted to the Faculty of Engineering of

University of Glasgow

for the degree of Doctor of Philosophy

University of Glasgow

Aerospace Engineering

December 2005

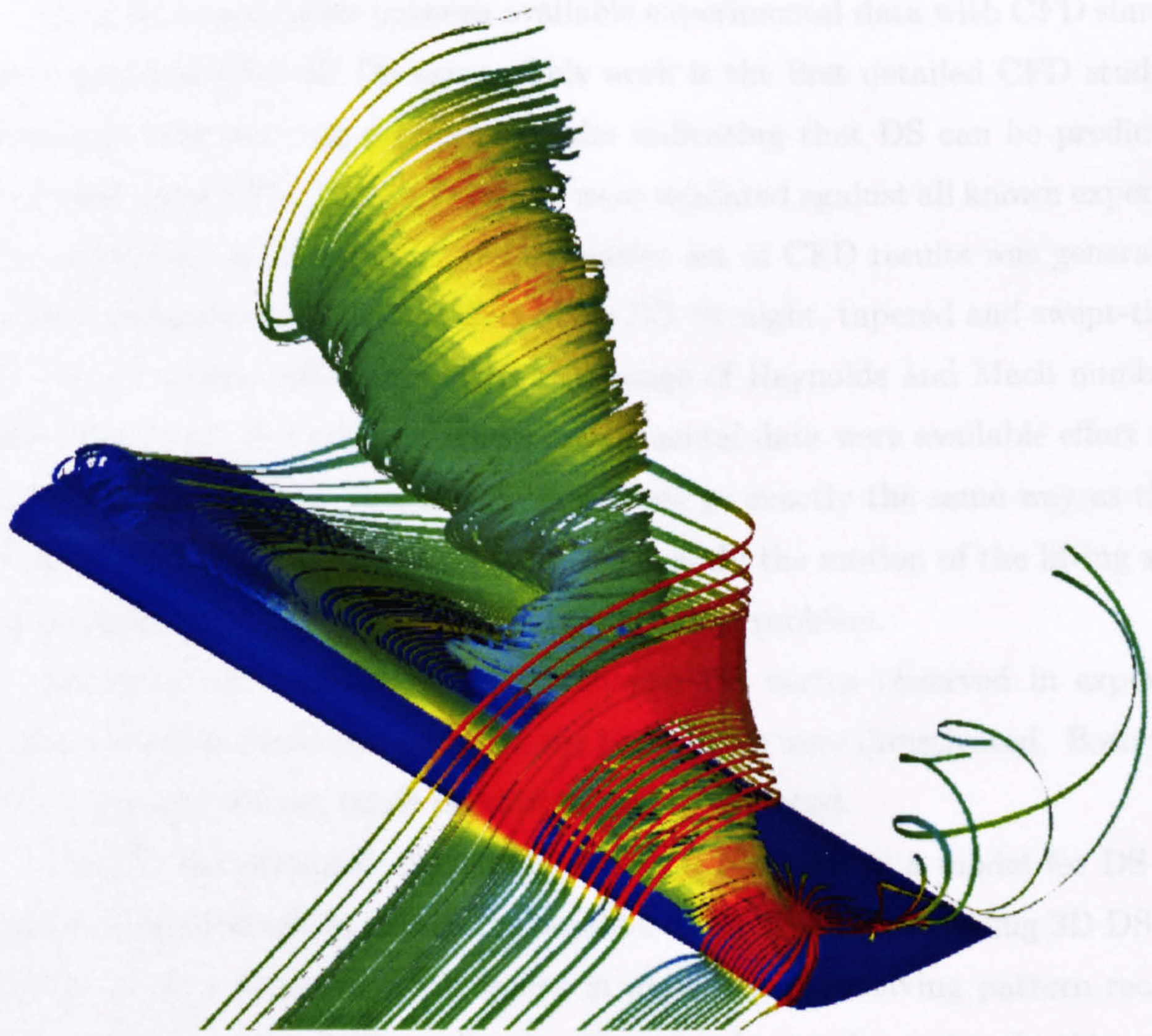

Abstract

Unlike fixed-wing aerodynamic design which incorporates significant Computational Fluid Dynamics (CFD), rotary-wing design utilises only a small fraction of the potential CFD has to offer. The main reason for this, is the nature of the flow near the lifting surfaces which is complex, unsteady and turbulent. The numerical modelling of such flows encounters two main problems due to a) the excessive CPU time required for computing and b) the lack of experimental data suitable for validation of the numerical computations.

Focusing on helicopter aerodynamics, it is known that the aerodynamic performance of the retreating side of a rotor disk is mainly dictated by the stall characteristics of the blade. Stall under dynamic conditions (Dynamic Stall) is the dominant phenomenon encountered on heavily loaded fast-flying rotors, resulting in extra lift and excessive pitching moments. Dynamic stall (DS) can be idealised as the pitching motion of a finite wing and this is the focus of the present work which includes three main stages.

At first, comparisons between available experimental data with CFD simulations were performed for 3D DS cases. This work is the first detailed CFD study of 3D Dynamic Stall and has produced results indicating that DS can be predicted and analysed using CFD. The CFD results were validated against all known experimental investigations. In addition, a comprehensive set of CFD results was generated and used to enhance our understanding of 3D DS. Straight, tapered and swept-tip wings of various aspect ratios were used at a range of Reynolds and Mach numbers and flow conditions. For all cases where experimental data were available effort was put to obtain the original data and process these in exactly the same way as the CFD results. Special care was put to represent exactly the motion of the lifting surfaces, its geometry and the boundary conditions of the problem.

Secondly, the evolution of the Ω-shaped DS vortex observed in experimental works as well as its interaction with the tip vortices were investigated. Both pitching and pitching/rotating blade conditions were considered.

Finally, the potential of training a Neural Network as a model for DS was assessed in an attempt to reduce the required CPU time for modelling 3D DS. Neural Networks have a proven track record in applications involving pattern recognition but so far have seen little application in unsteady aerodynamics. In this work, two different NN models were developed and assessed in a variety of conditions involving DS. Both experimental and CFD data were used during these investigations. The

dependence of the quality of the predictions of the NN on the choice of the training data was then assessed and thoughts towards the correct strategy behind this choice were laid out.

Declaration

The author hereby declares that this dissertation is a record of the work carried out in the Department of Aerospace Engineering at the University of Glasgow during the period from September 2002 to December 2005. This dissertation is original except otherwise indicated.

December 2005

Agis Spentzos

Acknowledgements

First and foremost, I would like to thank my supervisor Dr. George Barakos for his continuous help, patience and support. His technical knowledge, everlasting enthusiasm and integrity of character have provided invaluable contribution throughout this project.

I would also like to thank all the members of the CFD Lab, past and present, for creating the environment, within I have been very lucky to work. In particular, I would like to thank Prof. Bryan Richards and Prof. Ken Badcock for their contibutions to my supervision and Dr. Punit Nayyar for so unselfishly devoting time of his, on problems of mine.

I am also very thankful to Prof. R.A.McD Galbraith and Prof. F. Coton from University of Glasgow, Dr. A. Berton and Prof. D. Favier from LABM, Dr. M. Raffel and Dr P. Wernert from DLR, Dr S. Schreck from NREL and Mr A. Brocklehurst from Agusta Westland for very kindly providing an extensive amount of experimental data, representing many years of hard work.

Last but not least, I would like to thank my family for their encouragement and support during the many rainy days.

The financial support from EPSRC (Grant GR/R79654/01) is also gratefully acknowledged.

Dedication

To my dear friend K. Ziamas who was born to shake the world and vanished without a trace.

Publications

Journal Papers:

Spentzos A. *et al.*, 'CFD Investigation of 2D and 3D Dynamic Stall', AIAA Journal, 34(5), 1023-1033, May 2005.

Spentzos A. *et al.*, 'Study of Three-Dimensional Dynamic Stall of Various Planform Shapes', Submitted to Aerospace Science and Technology Journal, January 2005, 60 manuscript pages.

Spentzos A. and G. Barakos, 'Modelling 3D Dynamic Stall using CFD and Neural Networks', invited paper, submitted for publication, IMechE Journal of Aerospace Engineering, Part G, 40 manuscript pages.

Papers in Conference Proceedings:

Spentzos A. and Barakos G., 'Modelling 3D Dynamic Stall Using Experimental and CFD Data', AIAA paper 2006-45484, to be presented at the 44th Aerospace Sciences Meeting and Exhibit, Reno Nevada, USA, January 2006.

Spentzos A., Barakos G., Badcock K., Richards B., 'Numerical Investigation of 3D Dynamic Stall in Rotation Using CFD and Neural Networks', presented at the 31st European Rotorcraft Forum, Florence, Italy, Sept. 13-15 2005.

Spentzos A., Barakos G., Badcock K., Richards B., 'Numerical Simulation of 3D Dynamic Stall using Neural Networks and CFD', presented at the "Integrating CFD and Experiments in Aerodynamics" international symposium, Cranfield University, Defence Academy Shrivenham, Sept. 2005.

Spentzos A., Barakos G., Badcock K., Richards B., CFD Study of 3D Dynamic Stall, AIAA Paper AIAA-2005-1107, 43rd AIAA Aerospace Sciences Meeting and Exhibit, Reno Nevada, Jan. 10-13, 2005.

Spentzos A., Barakos G., Badcock K., Richards B., 'CFD Study of Three-Dimensional

Dynamic Stall of Various Planform Shapes', presented at the 30th European Rotorcraft Forum, Marseilles, France, Sept. 14-16 2004.

Spentzos A. and Barakos G., 'CFD Study of 2D Dynamic Stall of Various Planform Shapes', presented at the Burn Helicopter Study Weekend, Angus, April 2004

Spentzos A., Barakos G., Badcock K., Richards B., Wernert P., Schreck S. and Raffel M., CFD Investigation of 2D and 3D Dynamic Stall, presented at the AHS 4th Decennial Specialist's Conference on Aeromechanics, San Francisco, California, Jan. 21-23, 2004, Also, Report N 801/2004, French-German Research Institute of Saint Louis, ISL

Spentzos A., Barakos G., Badcock K. and Schreck S., 'Numerical Simulation of 3D Dynamic Stall', presented at the "Integrating CFD and Experiments in Aerodynamics" intenational symposium, Glasgow, 8-9 September 2003.

Spentzos A., Barakos G., Badcock K. and Richards B., 'CFD Study of Three-Dimensional Dynamic Stall', presented at the 12th Scottish Fluid Mechanics Conference, Dundee University, Dundee, Oct. 2003

Spentzos A. and Barakos G., 'CFD Study of Three-Dimensional Dynamic Stall', presented at the Burn Helicopter Stufy Weekend, Angus, April 2003

Contents

List of Figures

List of Tables

Nomenclature

$B()$	Notation for blending function
c	Chord length of the aerofoil
C_p	Pressure coefficient, $C_p = \frac{1}{2\rho U_{inf}^2 S}(p - p_{inf})$
C_L	Lift coefficient, $C_L = \frac{L}{2S\rho U_{inf}^2}$
C_μ	Closure coefficient for one-equation models
C_μ	$k-\varepsilon$ model coefficient
d	Distance along the normal to chord direction
e	Specific internal energy
E	Total energy of fluid
f_i	Body force vector
$\mathbf{F}$	Flux vector in the x-direction
F_1,F_2	Blending functions used in the Baseline $k-\omega$ and SST models
$\mathbf{G}$	Flux vector in the y-direction
$\mathbf{H}$	Flux vector in the z-direction
i	Inviscid component
k	Reduced frequency of oscillation, $k = \frac{\omega c}{2U_{inf}}$
k	Heat transfer coefficient
k	Specific turbulent kinetic energy
L	Lift force
M	Mach number
n	Current time-step
n	Nearest
$n+1$	Next time-step
N	Number of samples/measurements
p	Pressure
P_ω	Dissipation rate specific to k

q_i	(Favre-averaged) Heat flux vector
R	Reynolds stress
$R_{i,j,k}$	Flux residual
Re	Reynolds number, $Re = \rho U_{inf} c/\mu$
R_t	Turbulent Reynolds number for $k-\varepsilon$ model
R_ω	Turbulent Reynolds number for $k-\omega$ model
S_{ij}	Strain rate tensor of mean flow
t	Turbulent
t	Non-dimensional time
T	Integration time
T	Temperature
u	Local streamwise velocity
U_∞	Free-stream velocity
u_i	Velocity vector
u_τ	Frictional velocity
v	Viscous component
$\mathcal{V}_{i,j,k}$	Cell volume
w	Wall
$\mathbf{W}$	Vector of conserved variables
x_i	Position vector
x	Chord-wise coordinate axis (CFD)
y	Normal coordinate axis (CFD)
y	Distance
y_n	Distance to the nearest wall
z	Span-wise coordinate axis (CFD)
arg_1,arg_2	Arguments to blending functions F_1 and F_2

Greek

α	Instantaneous incidence angle
α_0	Mean incidence angle for oscillatory cases
α_1	Amplitude of oscillation
α^+	Nondimensional pitch rate, $\alpha^+ = \frac{d\alpha}{dt}\frac{c}{U_{inf}}$
β	Yaw angle
δ_{ij}	Kronecker delta
ε	Dissipation rate of k per unit mass of fluid
μ	Advance Ratio
μ_t	Dynamic eddy viscosity
ν	Kinematic molecular viscosity
ρ	Density
ρ_∞	Density at free-stream
τ	Frictional component
τ_w	Dynamic wall shear stress
τ_{ij}	Viscous stress tensor
ϕ	Phase angle
ϕ'	Fluctuating part of a quantity
$\overline{\phi}$	Mean part of a quantity
ψ	Azimuth angle
ω	Angular frequency

Acronyms

2D	Two-Dimensional
3D	Three-Dimensional
AoA	Angle of Attack
AR	Aspect Ratio
CFD	Computational Fluid Dynamics
DS	Dynamic Stall
DSV	Dynamic Stall Vortex
ELDV	Embedded Laser Doppler Velocimetry
FFBP	Feed Forward Back Propagation
LE	Leading Edge

LEV	Leading Edge Vortex
NN	Neural Network
RNN	Recursive Neural Network
TE	Trailing Edge
TEV	Trailing Edge Vortex
TV	Tip Vortex

Subscripts

i,j,k	Indices i,j,k=1,2,3...

Superscripts

$'$	Fluctuating part
$+$	Non-dimensionalised wall distance

Chapter 1

Introduction

1.1 Motivation

The Dynamic Stall (DS) of a lifting surface is one of the most interesting aerodynamic phenomena. It is encountered when a lifting surface is rapidly pitched beyond its static stall angle, resulting to an initial lift augmentation and its subsequent loss in a highly non-linear manner [1].

From an industrial point of view, the aerodynamics and the dynamic response of helicopter rotors, are two main unsteady flow phenomena appearing constantly in the industrial list of priorities. Helicopter rotor performance is limited by the effects of compressibility on the advancing blade and DS on the retreating blade. Figure 1.1 shows the calculated contours of the local angle of attack for a helicopter rotor at $\mu = 0.3$, in three different flight conditions (a) level flight, (b) climb at 1,000 fpm and (c) autorotation [2]. Figure 1.1 clearly shows that the rotor is very likely to encounter situations where the AoA of the retreating side blades may enter the DS regime. Consequently, the study and understanding of 3D DS flow phenomena will assist the rotorcraft industry in further pushing the design limits towards faster and more efficient rotors. Figure 1.2a shows the retreating side of a helicopter rotor with the shaded area where DS usually occurs. Figure 1.2b shows a schematic explaining the main aerodynamic constraints of a rotor during forward flight. High rotor loading conditions during helicopter flight, require high rotational speeds which in turn result to high advance ratios for a given forward flight speed. Thus, the high tip speeds on the advancing side of the rotor disk may result to shock formation and consequently, reduction of lift. On the other hand, the maximum loading of the helicopter during hover is compromised by the stalling of the blades on the

retreating side of the rotor. The optimum operating area is below the two areas shown in Figure 1.2b. In particular, if high forward speed is required, the point where the two lines cross (Figure 1.2b) is the optimum operating point.

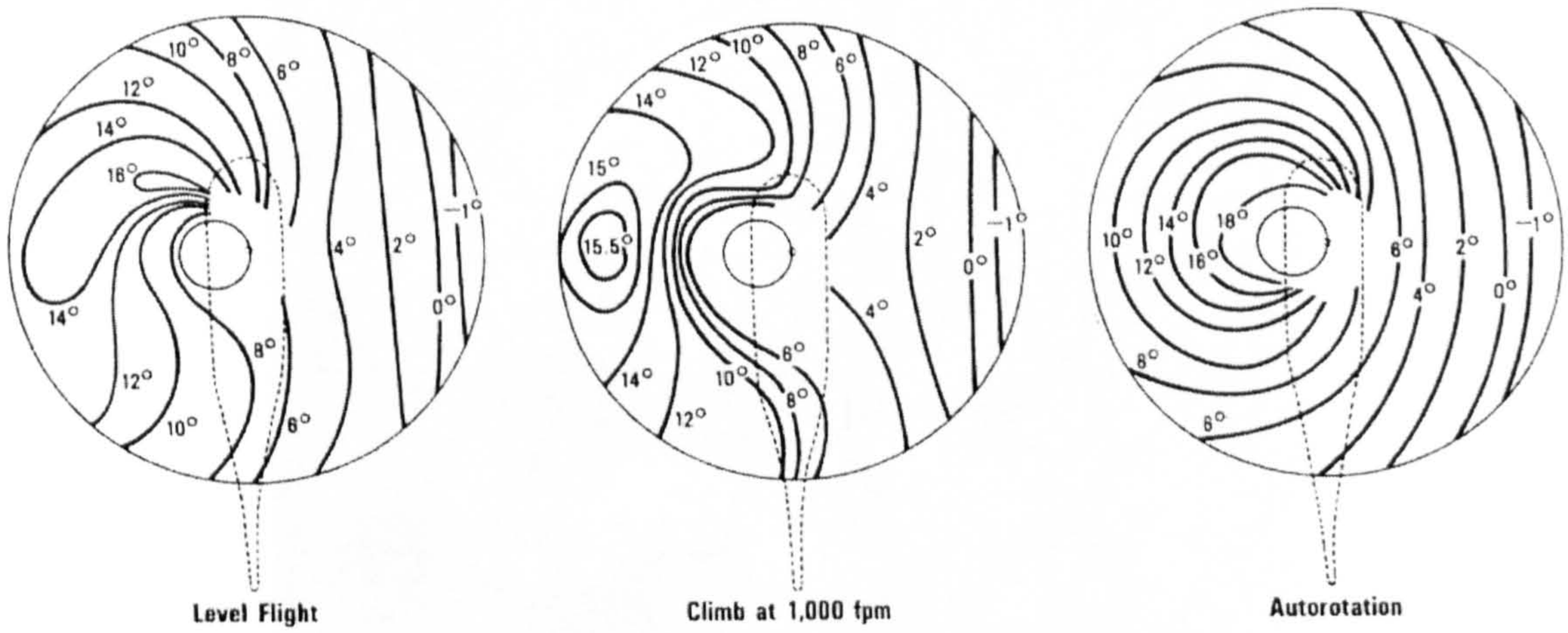

(a) (b) (c)

Figure 1.1: Calculated contours of the local angle of attack for a helicopter rotor at $\mu = 0.3$, in three different flight conditions, (a) level flight, (b) climb at 1,000 fpm and (c) autorotation. Picture taken from [2].

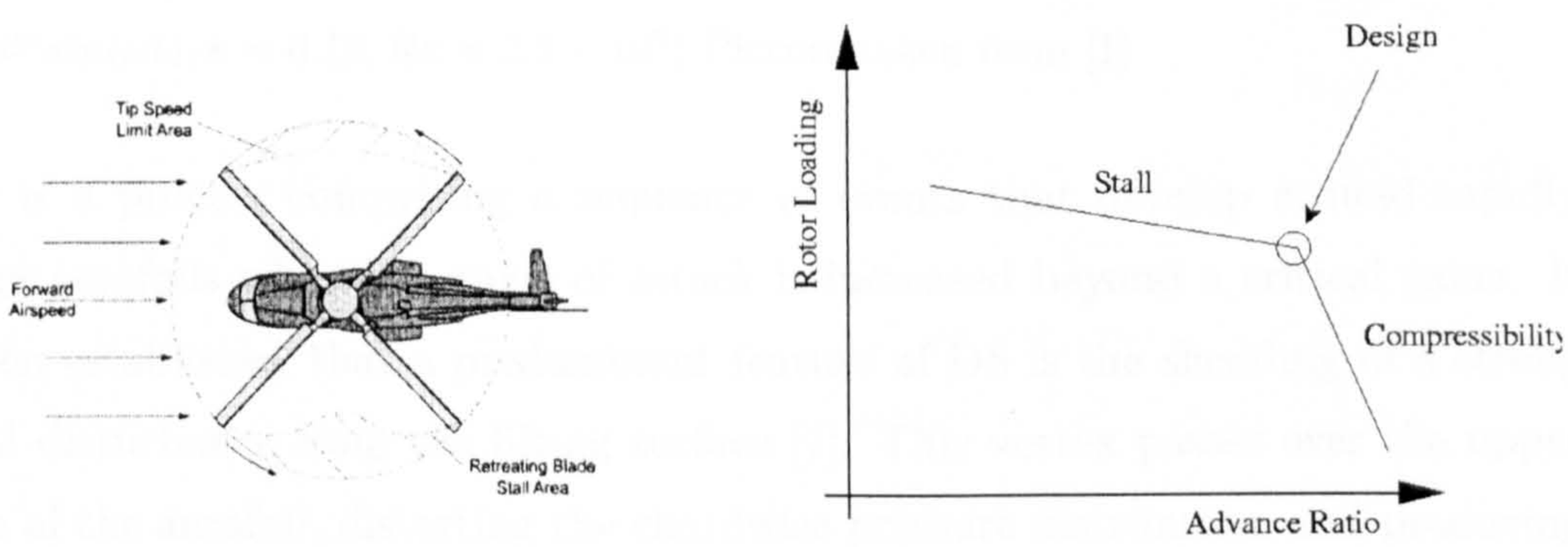

(a) (b)

Figure 1.2: Schematics showing (a) the retreating side of a helicopter rotor with the shaded area where DS usually occurs and (b) the optimum design point for a rotor during forward flight.

1.1. MOTIVATION

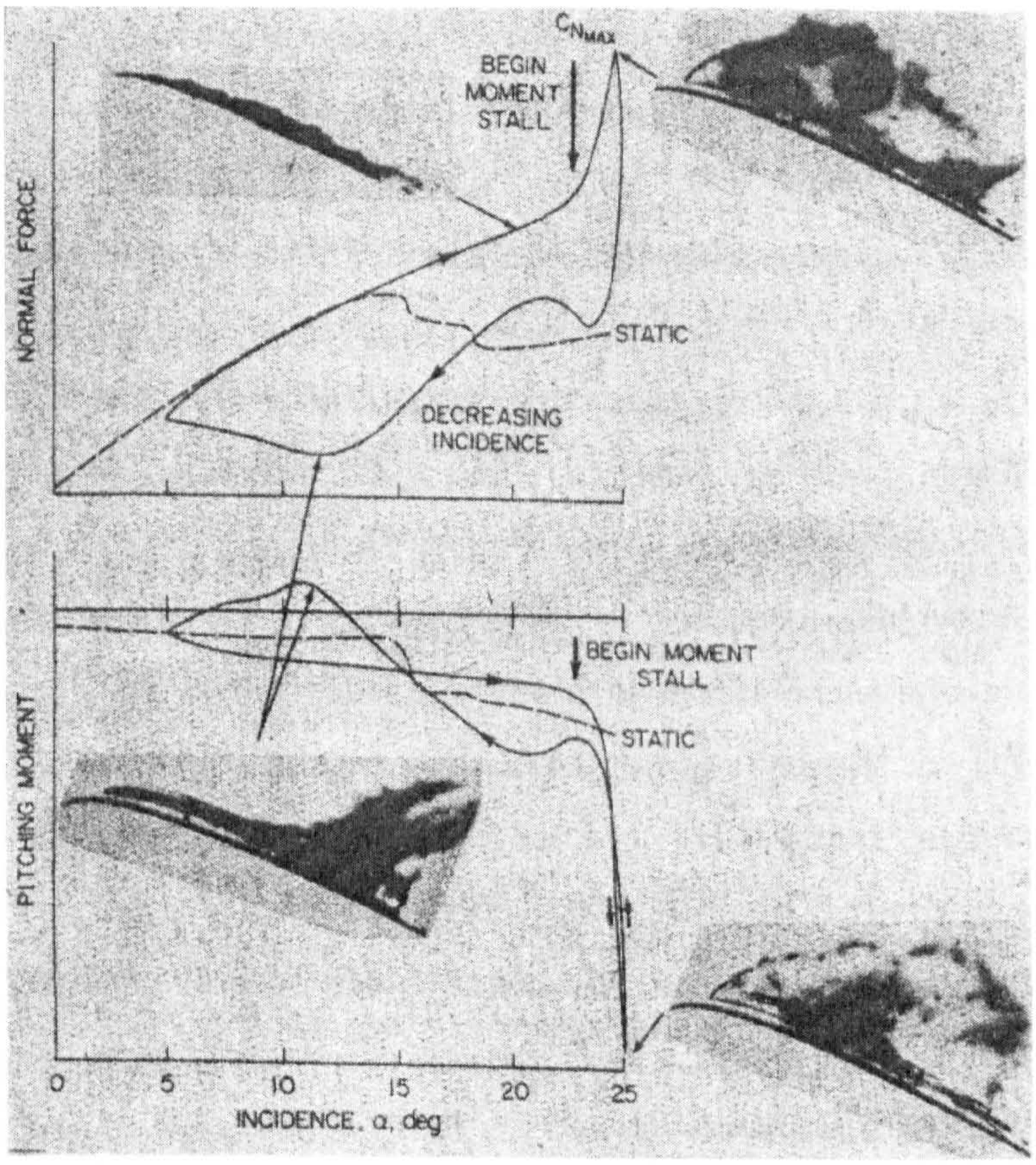

Figure 1.3: Normal force and pitching moment on NACA 0012 aerofoil during DS. ($\alpha = 15^o + 10^o sin(\omega t), k = 0.15, Re = 2.5 \times 10^6$) Picture taken from [1]

DS is a process comprising a sequence of events that develop around rapidly pitching aerofoils when the angle of attack is increased beyond a critical value. It has been established that a predominant feature of DS is the shedding of a strong vortical disturbance from the lifting surface [1]. This vortex passes over the upper surface of the aerofoil, distorting the chordwise pressure distribution and producing transient forces that are fundamentally different from their static counterparts (Figure 1.3, [1]). While the primary vortex is resident above the aerofoil, high values of lift are experienced which can be exploited for the design of highly maneuverable aircraft. The penalty, however, is that this primary vortex eventually detaches from the surface and is shed downstream producing a sudden loss of lift and a consequent abrupt nose down pitching moment. The phenomenon continues either with the generation of weaker vortices if the body remains above its static angle of attack, or terminated if the body returns to an angle sufficiently small for flow reattachement. During DS the flow field is characterised by a number of flow phenomena such as boundary-layer growth, separation, unsteadiness, shock/boundary-layer and invis-

cid/viscous interactions, vortex/body and vortex/vortex interactions, transition to turbulence and flow re-laminarisation. Such rich flow patterns are of primary importance both from theoretical and practical point of view. The phenomenon of DS appears in several applications including high maneuverable aircrafts and helicopters. The maneuverability of fighters could be enhanced if the unsteady airloads generated by DS were utilised in a controlled manner. Effective stall control of the retreating blade of a helicopter rotor could increase the maximum flight speed by reducing rotor vibrations and power requirements. Maximum speed of wind power-generator rotors could result in higher electricity production and less rotor vibration, therefore the useful life of the generator could be extended.

Due to the highly three-dimensional and unsteady nature of the DS phenomenon, an attempt to fully understand the sequence of events that lead to DS requires very detailed experimental analyses which can be difficult, expensive and frequently impossible to perform, due to the complication imposed by the nature of motion of the structures around which DS occurs. The obvious alternative is to perform numerical simulations using CFD which can be developed and assessed using experimental evidence available. However, the difficulties associated with CFD analyses for this particular application (computational cost, turbulence and transition modelling issues and scarcity of comprehensive three-dimensional data) makes such an investigation very demanding and also explains the fact why only one comprehensive three-dimensional computation has been undertaken to date [3].

From the viewpoint of applied aerodynamics, a comprehensive study of DS could lead to numerical models that comprise all its important flow characteristics but are much cheaper to compute. The additional lift that DS provides can be very useful in stretching the operating envelope of an aircraft or rotor/turbine. However, its catastrophic loss can potentially be disastrous, mainly due to structure fatigue. Therefore, computationally inexpensive methods that have the potential to predict such phenomena on-the-fly could provide the pilot with the ability to control his aircraft in a more efficient and safe way.

1.2 Literature Survey

This literature review has been structured in the following way: First an **overview** of DS is presented, detailing past efforts on 2D CFD simulations. This is followed by the **experimental** and **computational** works undertaken in 3D DS. As a result

of the high computational cost involved in the numerical solutions of 3D geometries, several attempts towards cheaper reduced models have been performed. A brief summary of such efforts is then presented. Finally, the **objectives** and the **outline** of this work are laid out. The findings of this survey have been sourced from the *Web of Knowledge* [4], the *NASA Technical Reports Server* [5] and the *AIAA* database [6].

1.2.1 Overview

The DS process has been under investigation for about three decades, and significant progress has been made towards understanding the physical processes associated with rapidly pitching an aerofoil beyond its static stall angle of attack.

In the seventies the study of the unsteady turbulent flows is dominated by the works of Telionis and McCroskey [7, 8]. The above efforts are mainly experimental studies and attempts to derive analytical solutions for unsteady boundary layers.

The earliest computational investigations of DS appeared in the 70s and early 80s with indicative efforts by Mehta [9], Gulcat [10] and McCroskey *et al.*[8]. Chyu *et al.*[11] employed an approximate factorisation scheme based on a pentadiagonal solver to perform calculations using the Baldwin-Lomax [12] model, while a year later Shamroth and Gibeling [13] employed a better $(k-l)$ model in conjunction with a collocated Briley-McDonald ADI-based solver.

In the 80's the rapid progress of computer technology allowed researchers to simulate unsteady flows using numerical techniques. In the middle 80s, the algorithm by Wu [14, 15] for incompressible flow provided results consistent with experimental data. Tuncer [16] extended the model for high Reynolds number flows, obtaining accurate and inexpensive results.

Furthermore the AGARD's efforts resulted in a comprehensive set of experimental data for the light stall regime [17]. The reviews of McCroskey [8] and Carr [18] provide good descriptions, on the basis of experiments, of the dynamic stall processes.

Compressibility effects started to be addressed during the last few years [19], and there are few numerical studies regarding high Reynolds number compressible flows [20]. The time delay between the appearance of incompressible and compressible Navier-Stokes solutions is primarily due to the increased computational requirements for the latter. From the simulation point of view, compressibility adds an additional

differential equation (for energy) to the system of equations. Furthermore, the solution must account for sharp flow-field gradients such as shock waves and contact discontinuities. During the same period, studies of unsteady flows and starting flows over lifting surfaces also started appearing [21].

In the 90's the effect of turbulence on the DS has been the subject of extensive experimental [22, 23] and numerical studies [24]. Ekaterinaris [25, 24] simulated transonic flows over harmonically oscillating aerofoils at high Reynolds numbers and low pitch rates. His results compared well with the experimental data by Lorber and Carta [26]. High Reynolds number flows not only increase the computing demands but also require careful modelling of turbulence. To date such modelling seems as much an art as a science. Eventhough most of the researchers focus on turbulent flows there is interest in the laminar flow regime as indicated by the work of Guo *et al.*[27].

Examination of the available literature reveals that detailed investigations of DS including high Mach and Reynolds number effects as well as lower pitch rates and more complex aerofoils, are rare. High pitch rates generally produce more straightforward, vortex-dominated flows where turbulence is less pronounced. Low pitch rate flow fields are usually more difficult to compute. Finally, complex aerofoils require complex grid generators and exhibit sharp edges, such as truncated trailing edges, which can produce numerical difficulties. Due to the number of parameters involved in the DS, the problem prevents any easy quantification of the phenomena and thus investigations are to be limited to certain parameters. Following McCroskey [28] the main parameters of the DS phenomenon are:

- free-stream Mach number (unsteady shock/ boundary layer interaction),
- free-stream Reynolds number,
- flow turbulence,
- flow transition,
- aerofoil shape (thickness, leading edge curvature, camber etc.),
- type of aerofoil motion (pitch amplitude, mean incidence, pitch rate, pitch axis location etc.),
- 3D effects (wing, blade tip shape, aspect ratio, planform, anhedral, spanwise loading distribution).

1.2.2 Turbulence modelling

The majority of works related to turbulent aerodynamic flows employ algebraic or one-equation turbulence models. Past research has revealed that the accuracy of the turbulent flow calculations is mainly dictated by the accuracy of the turbulence model. In addition, experience using zero-equation turbulence models [12] has shown that such modelling of turbulence does not provide satisfactory results in most cases. In this study, low Reynold number linear two equation eddy viscosity models will be used. This is necessary because first-order closure models of turbulence describe the Reynolds stresses as a simple function of the mean flow strain and, thus, result in large inaccuracies in the simulation of turbulent separated flows. Moreover, eddy-viscosity models work well only in cases with mild adverse pressure gradients and flowfields with small separation regions.

The $k-\epsilon$ model [29, 30] is one of the most popular two-equation turbulence models and in the past this model has been used in conjunction with wall-functions for the computation of a variety of flows [29, 31, 32, 33]. The $k-\epsilon$ model, however, exhibits numerical stiffness and inaccuracies when applied to near-wall turbulent flows as well as separated flows [31]. Various versions of the $k-\epsilon$ model have been proposed over the years in order to improve the accuracy of the model in various flow cases [31, 32, 33]. An alternative to the $k-\epsilon$ model, which has also received considerable attention, is the $k-\omega$ model by Wilcox [34, 35]. In the past, the model has been implemented in several flow cases by other authors [36, 37].

Linear EVM of turbulence assume an explicit algebraic relationship between Reynolds stresses and mean strain. The validity of these linear (Boussinesq) eddy-viscosity models is based upon theoretical justification in simple flows. Linear eddy-viscosity models give fair predictions for attached, fully developed turbulent boundary layers with weak pressure gradients and are relatively easy to be incorporated in CFD codes. However, the predictions of these models deteriorate when all components of the Reynolds stress tensor become dynamically significant. Linear low-Re two-equation models seem to offer the best balance between accuracy and computational cost, but are not able to capture effects arising from normal-stress anisotropy. Second-moment closure is not without risk mainly due to the extensive computer resources and sophistication that are necessary in implementing and numerically solving these equations.

At present, non-linear and Reynolds stress models seem to be one of the principal

routes for advanced modelling of turbulence beyond the linear eddy-viscosity models. However, the level of their complexity can be very high and, thus, their numerical implementation is difficult. In view of the above, only linear Eddy Viscosity Models of the $k-\omega$ family have been used in this work.

1.2.3 Experimental Work

Experimental data are of primary importance to numerical studies, in validating the realism of the numerical predictions. This section presents the experimental works performed so far in the field of 3D DS, which are presented in Table 1.1.

1. The Work of Wernert

Amongst the plethora of 2D experimental investigations Wernert *et al.*[38] conducted a PIV study on a pitching NACA 0012 aerofoil for a mean angle of incidence of 15 degrees and oscillation of amplitude equal to 10 degrees. The wing had an aspect ratio of 2.8 the reduced frequency of oscillation was set to 0.15 and the Re number of the flow was 3.75×10^5. The researchers used splitter plates on both ends of the wing to give nominally 2D flow. Although this was not a 3D experiment, it is the only one with PIV measurements revealed by this literature survey. Also, since this experiment was performed in the transitional regime, comparisons between measurements and CFD can provide useful insight into the importance of turbulence modeling in highly impulsive flows.

Experiments in 3D DS have been undertaken in chronological order, by Lorber [26], Freymuth [39], Horner [40], Piziali [22], Schreck [41], Moir and Coton [42], Tang [43], Coton and Galbraith [44] and the Aerodynamics Laboratory of Marseilles (LABM) [46].

2. The Work of Lorber

Lorber [26] performed a series of experiments to examine the influence of k, M and geometry in TV and DSV strength, in relevance to helicopter flight. He used a semi-span rectangular wing measuring $0.44m \times 1.22m$ based on a SIKORSKY SSC-A09 aerofoil with 9% thickness. The wing was pitched around its 1/4 chord in sinusoidal and ramping motions. The measurements taken were surface pressure readings from 112 transducers over 5 span-wise rakes ($z/c = 0.08,\ 0.32,\ 0.6,\ 1,05\ and\ 1.5$, measuring from the tip). The wing was tested at Mach numbers between 0.2 and

Table 1.1: Summary of the experimental works on 3D DS. Data for cases 4, 5, 7, 8, 9 and 10 were available for comparisons with CFD simulations.

Case	Reference	Conditions	Measurements
1	Wernert *et al.* [38]	Oscillatory motion	LSV and PIV
		$Re = 3.73 \times 10^5$, M 0.1	
		NACA0012, AR=2.8	
2	Lorber [26]	Oscillatory and ramping motions	Surface pressure
		$Re = M \times 10^7$, $M = 0.2 - 0.6$	
		SSC-A09, AR=3.0	
3	Freymuth [39]	Ramping motion	smoke visualisatons
		$Re = 6 \times 10^4$,$M = 2 \times 10^{-3}$	
4	Horner [40]	Oscillatory motion	LSV and PIV
		$Re = 10^5$,$M = 4.5 \times 10^{-3}$	
		Flat plate, AR=2	
5	Piziali [22]	Ramping and oscillatory motions	Surface pressure
		$Re = 2.0 \times 10^6, M = 0.278$	Flow visualisation
		NACA0015, AR=10	(micro-tufts)
6	Schreck and Helin [41]	Ramping motions	Surface pressure
		$Re = 6.9 \times 10^4, M = 2.6 \times 10^{-2}$	Flow visualisation
		NACA0012, AR=2	(dye injection)
7	Moir and Coton [42]	Ramping and oscillatory motions	Smoke visualisation
		$Re = 13 \times 10^3$,$M = 0.1$	
		NACA0015, AR=3	
8	Tang and Dowell [43]	Oscillatory motions	Pressure measurements
		$Re = 5.2 \times 10^5$,$M = 0.20$	
		NACA0012, AR=1.5	
9	Coton and Galbraith [44]	Ramping and oscillatory motions	Surface pressure
		$Re = 1.5 \times 10^6$,$M = 0.1$	
		NACA0015, AR=3	
10	Berton *et al.* [45, 46]	Oscillatory motion	Boundary layers
	(LABM)	$Re = 3 - 6 \times 10^6, M = 0.01 - 0.3$	Velocity profiles
		NACA0012	Turbulence quantities

0.6, β angles of 0^o,15^o and 30^o and the relationship between the Re and M was $Re = M \times 10^7$. Lorber's [26] findings addressed mainly three issues: a) TV effects, b) stall vortex propagation and c) separation locations. Lorber [26], concluded that before stall the TV lowers the effective angle of attack thus reducing lift and delaying the onset of stall. In the near the tip region, the TV produces an aft loading creating a nose down moment. During stall, interaction with the TV prolongs the residence of the stall vortex on the wing. Regarding the DSV propagation characteristics, Lorber [26], reported that unswept motions showed slower propagation characteristics due to the anchoring of the DSV in the LE region of the tip, However, for the swept motions, DSV anchoring was no longer taking place, therefore, the near the tip part of DSV propagated faster towards the trailing edge than its inboard section. Moreover, it was reported that the variation of Mach number and motion type (sinusoidal or ramping) do not alter the DSV propagation properties. Propagation speed for the uswept cases was found to be 0.25 times the freestream velocity. This measurement was performed by monitoring the aft motion of the global minima of the individual transducers placed at $z/c = 1.6$. Closer to the tip, at $z/c = 0.08$, this speed was reduced to 0.09 times the freestream velocity, due to its interaction with the TV. Regarding separation, Lorber [26] reported that he only observed LE separation phenomena. For low Mach numbers ($M < 0.3$), unsteady separation begun at the forward $5-10\%$ of chord and rapidly expanded to eliminate the LE suction peak to form a strong and concentrated stall vortex. For higher Mach numbers ($M \geq 0.3$) a mildly supersonic flow forms near the LE, causing an oscillation just downstream of it. This oscillation forces the flow in the LE to detach earlier than for the lower Mach number case.

3. The Work of Freymuth

Freymuth [39] published his efforts on investigating the applicability of Helmholtz's law to the vortex systems generated by rapidly pitching a rectangular and a delta wing. His experiments involved smoke visualisations introduced into areas of vorticity production. The rectangular half-wing was sinusoidally pitched at 5^o amplitude around a 20^o mean angle of attack. The conditions of the experiment were: $V_o = 0.61m/s$, $f = 0.67Hz$ and $c = 0.152m$. The major vortical structures produced by this motion (*ie* the TV, LEV and TEV) were identified as well as their tendency to connect in the near the LE region of the tip. However, this connection is not

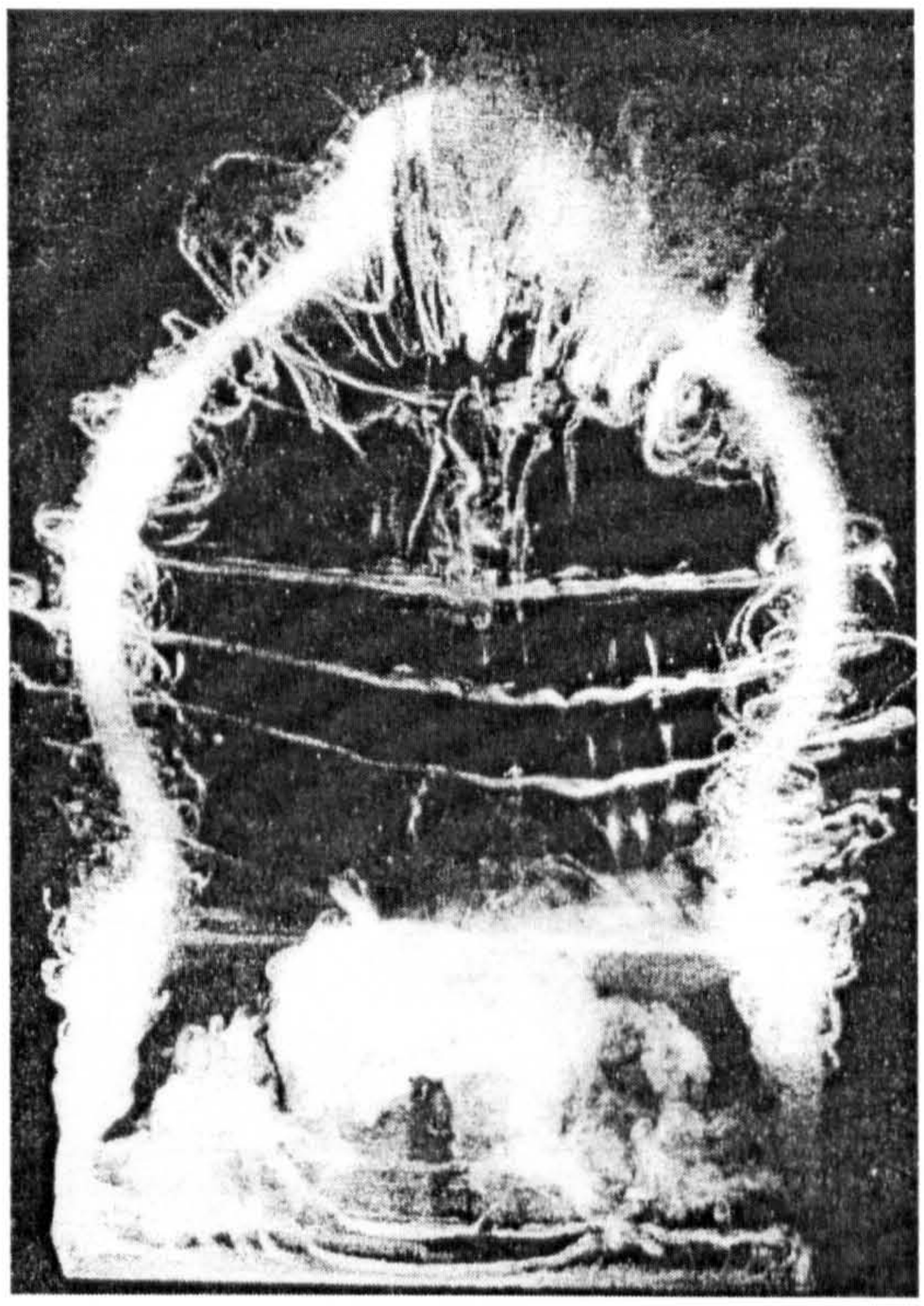

Figure 1.4: Top view of vortex system of a rectangular wing with aspect ratio 2 after a rapid pitch from 0^o to 60^o. Picture taken from [39].

very clear by the photos included in the report. Moreover, Freymuth [39] assumed that this connection confirms Helmholtz's law. However, this law has been stated in reference to inviscid flows and its validity cannot be confirmed unless measurements of the circulations of the individual vortices are performed. The Ω shape of the DSV, which has also been shown in this work, is evident in Figure 1.4, but it was Horner [40] who first introduced this term. The delta wing was periodically pitched between the angles of 0^o and 30^o at $r = 0.16$. The two counter-rotating vortices were shown to link near the front corner. The linked vortical system then convected downstream, while at the same time new LE vortices formed and underwent the same growth-decay cycle. Further downstream, these vortical structures were shown to attain irregular spiral shapes and they finally burst.

4. The Work of Horner

Horner *et al.*[40], performed smoke visualisation experiments by oscillating a flat plate of $12in$ span, $6in$ chord and $0.25in$ thickness in a $16in \times 16in$ wind tunnel. The flat plate oscillations were driven by a DC motor coupled to the plate through a flywheel and crank linkage. Reduced frequencies of 1.0 and 2.0 and mean angles

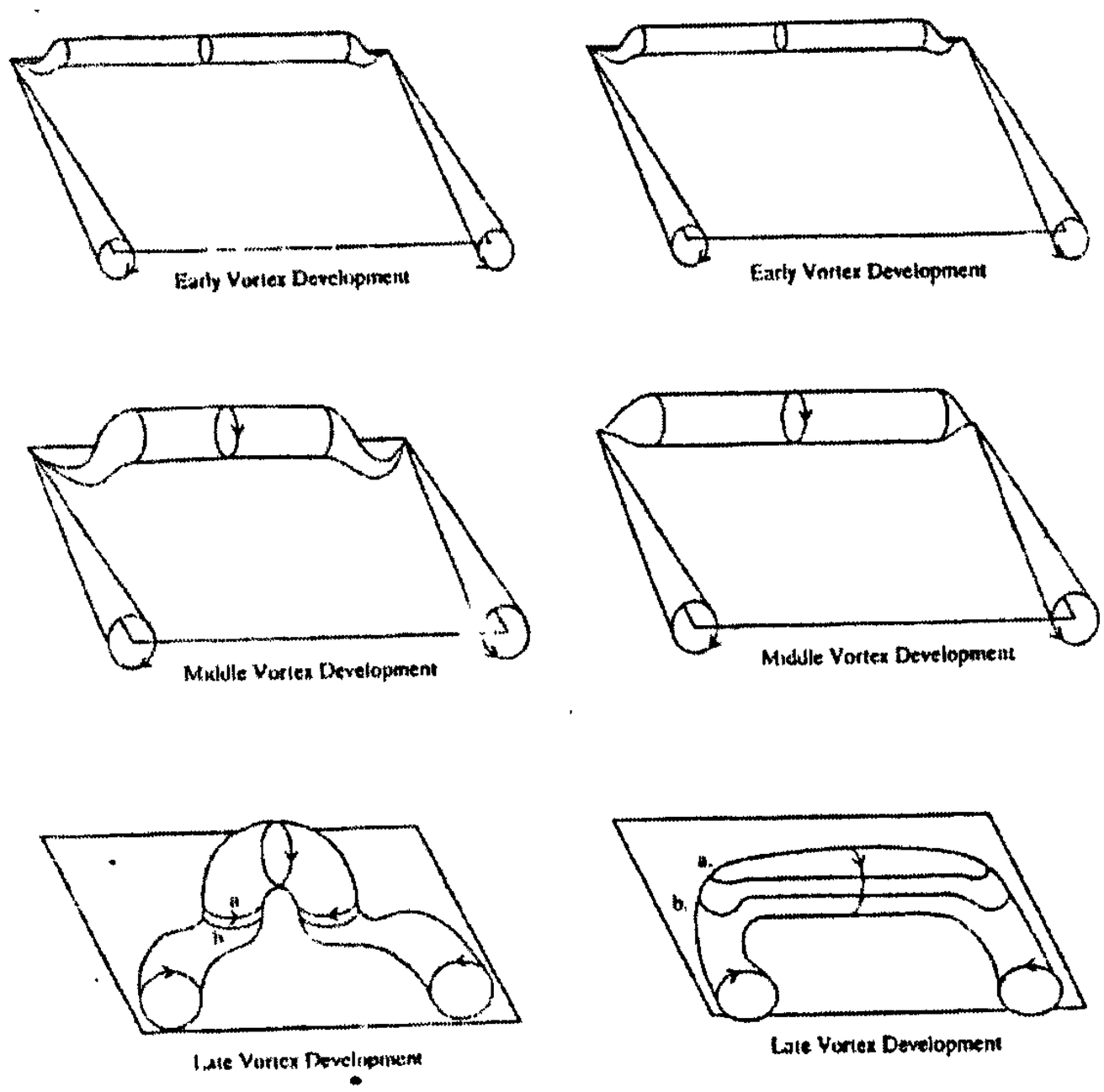

Figure 1.5: Caricatures of LEV development under 3D test conditions (left) and 2D test conditions (right). Picture taken from [40].

of 10^o and 20^o were selected, while the freestream velocity and oscillation amplitude was held at $5ft/s$ and 10^o respectively. Two different tip conditions were investigated to allow for both 2D and 3D flow configurations. Firstly the flat plate was positioned at the centre of the section leaving $2in$ gaps from either side. In the second arrangement, the test section was narrowed by inserting a clear acrylic plate. Then, the flat plate was re-centered and small woven cellulose tip extensions were inserted to ensure a tight seal against the wall sections. However, only partial sealing was achieved and the three dimensionality of the flow was only reduced rather than eliminated, as flow visualisations clearly demonstrated the existence of the tip vortices. Therefore what the experimentalist termed as 2D flow conditions as opposed to 3D flow conditions was not entirely accurate. Visualisation was performed across vertical and horizontal smoke planes. Vertical planes of smoke were introduced at several locations to provide smoke visualisations along several span sections and above the wing. Horner *et al.*[40], summarised their findings in a series of sketches (Figure 1.5) that exhibit the behaviour of the vortical structures on the suction side of the flat plate, for both their 3D and 2D cases. These sketches depict the vortical structures during their early, middle and late development. In the early stage, a vortex along the leading edge of the wing is formed which connects to the TVs at

a point on the leading edge forming a flat Π structure. In the 2D configuration, the initiation of the leading edge vortex occurred earlier than in the 3D case. As the angle of attack increased, the 2D case LEV gradually grew in size, remaining attached to the LE of the flat plate. In the 3D case, the LEV started growing at a similar manner but also started moving up and towards the TE. In both cases, the ends of the LEV remained pinned to the TV. Finally, following the stall of the TVs, in the 3D case the Π structure was forced to attain an Ω shape, while in the 2D case, the Π structure attained a horseshoe shape.

5. The Work of Piziali

Piziali [22] performed extensive experimental investigations of the pressure distribution over a semispan wing undergoing pitching motions. He then presented the cycle-averaged coefficients for lift, drag and pitching moment as well as limited flow visualisations using arrays of micro-tufts distributed over the suction side of the wing. The wing used was based on a NACA 0015 aerofoil section, had a rectangular planform of $60in\ x\ 12in$ and was used in both 3D and 2D configurations. A square and a round tip cap were used, extending the span to a further $0.62in$. The pressure taps were located at nine spanwise locations, at $y/s = 0.25, 0.475, 0.8, 0.9, 0.957, 0.966, 0.976$ and 0.995. The wing was mounted horizontally in the wind tunnel's test section. A splitter plate was positioned at the wing's root to eliminate the wind tunnel wall boundary effect. At the wing's 70% span, an additional wing support was used consisting of a crossed pair of floor to ceiling streamlined aircraft wires. Leakage from the lower to the upper surface was prevented by sealing the wing wire mounting points. The pitch oscillation of the wing was generated by a crank mechanism consisting of a variable speed feedback-controlled DC motor connected to a flywheel. The oscillating amplitude was achieved via a pin with adjustable offset and finally the connecting rod and pitch arm were attached to the wing's quarter chord axis. The amplitude of oscillation was adjustable from 0^o to 10^o, the mean angle could vary from -12^o to $+27^o$ and the reduced frequency range of the oscillation was adjustable from 0.04 to 0.2. Piziali [22], published a very large number of sectional integral loads for c_l, c_d and c_m spanning the entire range of 2D and 3D measurements.

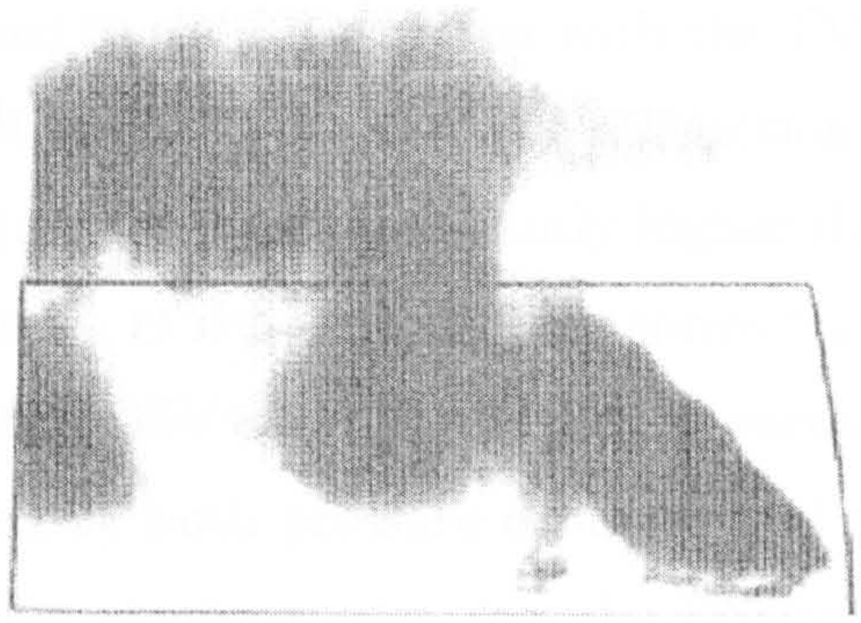

Figure 1.6: Dye visualisation in water tunnel showing the Ω vortex. Picture taken from [41].

6. The Work of Schreck and Helin

Schreck and Helin [41] used a NACA 0015 profile on a half wing of aspect ratio 2, mounted in a $0.91 \times 0.91 - m$ wing tunnel. The wing had a rectangular planform of $0.1524m$ chord and $0.291m$ span, made of hollow aluminum NACA 0015 aerofoil stock. A circular splitter plate $0.3048m$ in diameter and with a NACA 0015 cutout was located at the wing's root. The wing had a single chordwise row of 15 pressure transducers fitted in the hollow section, that effectively covered 11 spanwise positions, by means of adding wing sections to the wing's tip and sliding the splitter plate over the wing span. The effective spanwise locations were surface pressure measurements were recorded were located at 0.0, 0.05, 0.10, 0.15, 0.25, 0.375, 0.5, 0.625, 0.70 and 0.80 span outboard the splitter plate. The nondimensional pitch rates were 0.05, 0.10 and 0.20, while the Re number was 6.9×10^4. Wing pitch axis was located at $0.25c$ for the experimental range of nondimensional pitch rate and at $0.33c$ for the nondimensional pitch rate 0.10. Ensemble averaged values were recorded over 20 consequetive wing pitch motions. Additionally, water tunnel flow visualisations were provided for the same wing-splitter plate arrangement, using dye injection. The Re for the visualisation experiment was kept at 5.6×10^4 for the nondimensional pitch rates of 0.05, 0.10 and 0.20. Schreck and Helin [41], used a series of suction-side pressure contours together with dye visualisations (Figure 1.6) corresponding to the same instances, in order to investigate the process of vortex generation and evolution throughout the ramping motions.

The authors [41] identified the inception of a vortical structure near the leading edge, extending from the tip to wing-plate juncture. As the angle of attack increased, this structure started growing and moving towards the TE. Close to the

tip, the vortex was pinned to the LE together with the TV, while towards the wing-plate juncture it moved freely. However, the convection speed of the vortex-end close to the wing-plate juncture was significantly higher than the convection further outboard. The consequence of this non uniform convection speed was a vortex disruption, which caused the DSV to arch and flex towards the surface of the wing. This effect was identified by both pressure contours and dye visualisation. The reported effect of increasing ramping rate, was the DSV disruption occurring closer to the LE. The work by Schreck and Helin [41] was interesting as it was the first to provide both surface measurements and flow visualisation in 3D DS. However, the splitter plate used had probably surface imperfections which allowed boundary layer development. This was evident throughout their measurements and visualisations, since the flow near the wing-splitter plate juncture appeared to have a strong spanwise component.

7. The Work of Moir and Coton

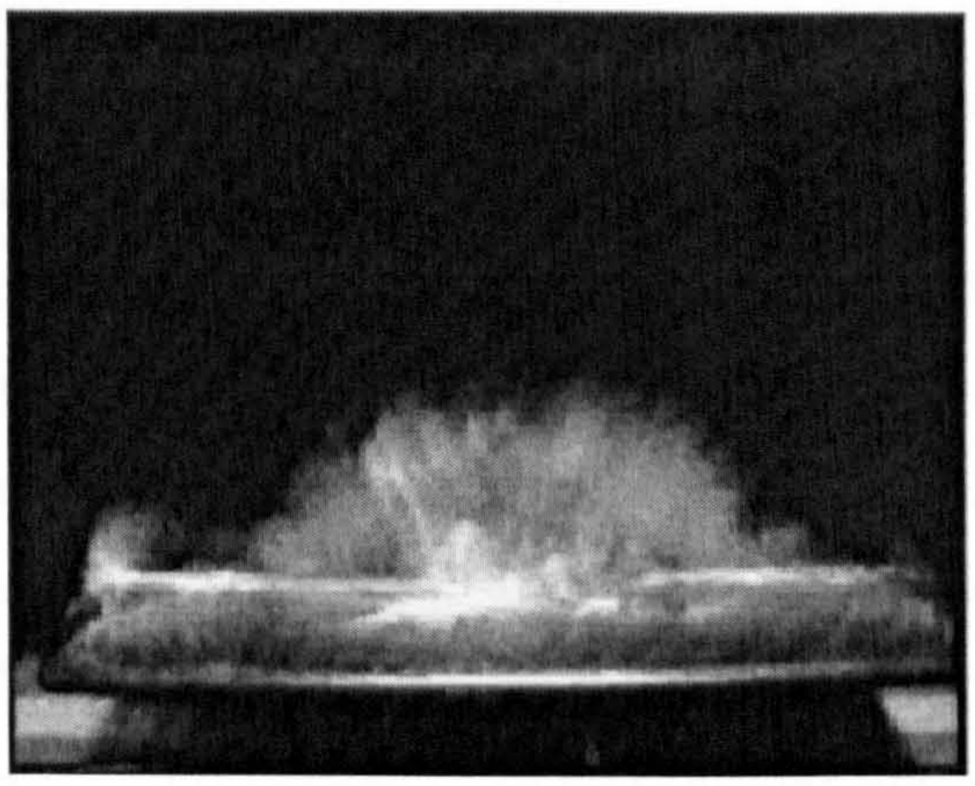

Figure 1.7: Front view smoke visualisation of Ω vortex. Picture taken from [42].

Moir and Coton [42] performed a series of visualisation experiments using two different wing planforms, a rectangular of $AR = 3$ and a swept back cut-out of the former with 60^o swept tips. Both wings were based on NACA 0015 aerofoils. The pitching motion of the models was achieved with a stepper motor/lead screw system. The stepper motor was programmed using LABVIEW running on a Macintosh LCIII computer. Smoke was produced by vaporising Ondina oil in a Taylor scientific smoke generator and was introduced to the flow either through small holes in the model surface or from smoke-rake positioned upstream of the model. Images were recorded with a camcorder, subsequently transferred to digital format using a Macintosh

grabbing system. Each model was pitched about its quarter chord from 0° to 40° at a reduced pitch rate of $\alpha^+ = 0.08$ and the Re number was 12,000. The experiments conducted with the rectangular wing planform indicated the presence of two major vortical structures; the DSV emanating from the leading edge region and the tip vortices. A secondary vortex forming following trailing edge separation had also been identified. The flowfield in the mid-span region was shown to be two-dimensional. The DSV was observed to form uniformly along the span but quickly assumed an arched shape, as downstream convection in the mid span region took place. However, the outboard ends of the DSV were pinned to the LE of the tip region. Moir and Coton [42] argued that the faster growth of the DSV along the mid-span region is a product of two effects, a) the higher effective α away from the tips due to downwash and b) the vortex enhancement in the mid-span region aided by the entrainment of the TE vortex. The combined effect of the above according to Moir and Coton caused the buckling of the DSV. This buckling shape was the same as identified by Horner [40] (who coined the term 'Ω vortex) and Schreck and Helin [41] (Figure 1.7). The swept back wing created flow configurations very similar to those of the rectangular wing, [42]. A weaker DSV has been reported and attributed to the smaller effective planform area leading to lower lift. However, the tip vortices were reported to be larger and with an orientation which directly affected a larger portion of the wing. This observation has an interesting consequence regarding the validity of Helmholtz's theorem with respect to flows involving DS. If a different planform produces stronger tip vortices but weaker DSV, then although the DSV appears to be connected with the TVs, their circulations might be different. Another difference that Moir and Coton [42] found between the rectangular and swept wing cases, was that in the mid span area, the DSV produced by the swept wing attained a higher distance from the wing surface that in the case of the rectangular wing. It also had the tendency to remain above the mid chord region, rather than be convected downstream as in the case of the rectangular wing.

8. The Work of Tang and Dowell

Tang and Dowell [43] used a NACA 0012 square wing of $AR = 1.5$ oscillating in pitch and took measurements along three span-wise locations ($0.5z/c$, $0.75z/c$ and $0.9z/c$) for various reduced pitch rates and angles of attack. These experiments aimed to extend the 2D ONERA model to 3D. The unsteady experiments involved

sinusoidal motions of mean angle $9^o - 28^o$, amplitude $1^o - 6^o$ and freestream velocities of $8.51m/s - 20.56m/s$. The oscillation frequency varied from $2Hz$ to $14Hz$. Two sets of experiments were conducted, below and above stall. The experimentalists [43] have presented a very limited number of sectional integrated loads while their focus had been on the extension of the ONERA model rather than the analysis of the three dimensionality of the flow. However, their claim that their results were qualitatively similar with the 2D case, appears rather peculiar given the high three-dimensionality and complexity of the near the tip flow. Tang and Dowel [43] did not present measurements at the $z/c = 0.9$ span position for the above-stall experiments.

9. The Work of Coton and Galbraith

Coton and Galbraith[44] used a NACA 0015 square wing with $AR = 3$ in ramp-up, ramp-down and harmonic oscillation in pitch. A relatively high Reynolds number of 1.5×10^6 has been used for various angles of incidence, pitch and ramp rates. The experiments took place in the university of Glasgow's 'Handley Page' low speed wind tunnel. The actuation force was produced using a hydraulic actuator and a crank mechanism which allowed a variation of angle of attack from -26^o to 40^o. The model's aerofoil section was that of a NACA 0015 and the tips were solids of revolution. The dimensions of the wing were $126cm$ x $42cm$. An overall of 192 pressure transducers were placed predominantly on the wing's starboard side. There were six chordal distributions with 30 transducers each (on both the upper and lower surface of the wing). Additional pressure transducers were placed in the region of the tip. A small number of transducers were also placed at the port side of the wing to enable checks on the symmetry of the wing loading. Data acquisition was carried out by a PC using 200 channels, each capable of a maximum sampling rate of $50kHz$. The experimentalists [44], presented integrated sectional loads and moments as well as C_p histories for six ramping cases with α^+ between 0.00043 and 0.027. The sectional gradients and peak values of the normal force curves *vs* angle of attack, were found to be higher in the mid wing sections than to those near the tip. When compared to the 2D case, the full wing 3D normal force curves exhibited lower peaks and gradients, however, the 2D and 3D curves were found to be broadly very similar.

The authors argued that the 2D flow is initially similar to the mid-wing sections of the 3D case. In their 3D cases [44], a leading edge vortex was identified to develop

uniformly across the leading edge. Shortly after its formation, it was observed that the DSV losses its uniformity under the influence of the tip vortices. The flow near the tip region was influenced by the downwash of the tip vortices who pin down the DSV in the LE of the tip region. The combined effect of the unconstrained growth of the DSV in the mid-span region and its pin-down at the tips cause the DSV to buckle attaining the Ω shaped first reported by Horner [40]. It has also been reported [44] that the mid-span segments initially moved faster downstream than those outboard. However, the downstream convection was not uniform as the passage of the vortex system over the trailing edge occurred almost simultaneously across the span. The same observations were made in all but the lowest reduced pitch rates, which in effect where in the quasi steady regime and no DSV presence was reported. The authors [44] drew very similar conclusions regarding the shape and global evolutionary characteristics of the DSV with previous works [40, 41], however, their experiments were conducted in realistic high *Re* regime.

10. The Work in LABM

The work undertaken by the Aerodynamics Laboratory of Marseilles (LABM) [46] employed an embedded Laser Doppler Velocimetry (ELDV) technique in order to provide detailed velocity measurements inside the boundary layer during DS. The experiment was designed to assist CFD practitioners with their efforts in turbulence modelling. A schematic from the experimental apparatus is shown in Figure 1.8. The model used for simulating the steady and unsteady flow configurations consisted of a swept half wing, mounted vertically within the test section of the S1L high subsonic wind tunnel. The wing's section was that of a NACA 0012 aerofoil and the half-wing had a root chord of $0.24m$ and a parallel to the tip chord of $0.06m$. The leading edge angle was 84^o and the trailing edge angle was 72.5^o. The wing was mounted on a turntable and pivoted around its quarter chord root point via a crank mechanism. The optical head was also mounted on the same turntable. The experimental apparatus was able to produce sinusoidal motions with mean angles in the range 0^o to 25^o and amplitudes of 3^o and 6^o. The velocity of the freestream varied from $50m/s$ to $100m/s$ and the oscillation frequencies from $1Hz$ to $5Hz$.

Measurements were taken at fifteen vertical distances ($0.8mm$-$90mm$) off the surface of the wing, at three chordwise locations ($0.4c$, $0.5c$ and $0.6c$) at 50% of span and two chordwise locations ($0.4c$ and $0.57c$) at 70% of span. Surface pressure

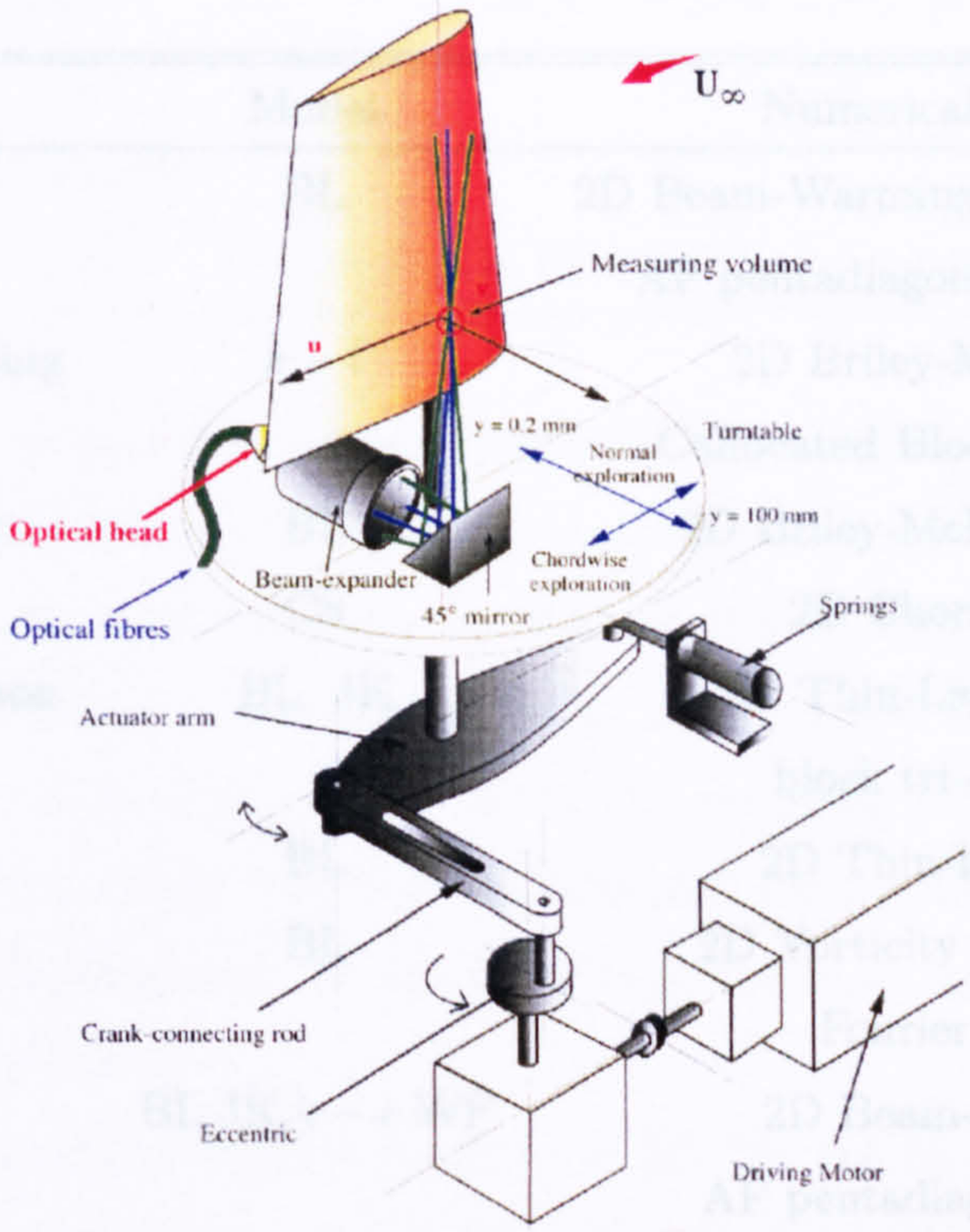

Figure 1.8: The ELDV experimental setup. Picture taken from [46].

measurements were also taken at sixteen chordwise positions and at both sides of the wing at 50% of span. The wing model used for the pressure measurements had the same shape but twice the chord ($0.48m$ at the root). Data acquisition was performed through a computer from two Burst Spectrum Analysers, delivering the Doppler frequencies for each velocity component as well as the arrival validation time for each frequency measurement. The arrival validation time was counted from a time origin delivered by a photoelectric cell mounted on the oscillating device which provided the exact aerofoil position in terms of phase angle (ωt) during the oscillation.

1.2.4 Computational Work

A summary of the 2D numerical simulations appeared so far in the literature is given in Table 1.2. As can be seen, only recently the simulation of unsteady flows with low-Re turbulence models beyond the algebraic ones has been attempted. On the

other hand, efforts to model 3D unsteady turbulent flow using advanced turbulence models have not been undertaken by other authors. A summary of trends in the research of unsteady aerodynamic flows is given in [47]. CFD studies have so far

	Reference	Model	Numerical Scheme
1	Chyu *et al.*	BL	2D Beam-Warming, Thin-Layer NS, AF pentadiagonal block solver
2	Shamroth & Gibeling	$k-l$	2D Briley-McDonald, Collocated Block solver ADI
3	Tassa & Sankar	BL	2D Briley-McDonald, ADI
4	Hegna	CS	2D Chorin SOR
5	Rumsey & Anderson	BL, JK	2D Thin-Layer NS AF block tri-diagonal
6	Visbal	BL	2D Thin-Layer AF
7	Tuncer *et al.*	BL	2D Vorticity formulation Fourier, SOR
8	Wu *et al.*	BL,JK,$k-\epsilon$ WF	2D Beam-warming AF pentadiagonal solver
9	Dindar & Kaynak	BL,JK	2D AF LU-ADI, Pulliam-Chaussee
10	Rizzetta & Visbal	BL,$k-\epsilon$	2D AF Beam-Warming Pentadiagonal
11	Srinivasan *et al.*	BL,JK,CS,SA,BB	2D AF Beam-Warming Pentadiagonal
13	Ekatarinaris & Menter	BL,SA,$k-\omega$	2D Steger-Warming AF
14	Yang	BL,$k-\epsilon$	2D Collocated Pressure Correction
15	Niu *et al.*	BL	2D Steger-Warming
16	Guilmineau *et al.*[48]	BB,SST $k-\omega$	2D PISO CPI

BL: Baldwin-Lomax algebraic turbulence model [12] CS: Cebesi-Smith algebraic turbulence model [49] JK: Johnson-King algebraic turbulence model [50] SA: Spalart-Allmaras one-equation turbulence model [51, 52] BB: Baldwin-Barth one-equation turbulence model [53] AF: Approximate Factorization LU: Lower-Upper (decomposition) SOR: Successive Over-Relaxation ADI: Alternating Direction Implicit PISO: Pressure-Implicit Solution by Splitting of Operators CPI: Consistent Physical Interpolation

Table 1.2: Summary of past 2D DS calculations.

concentrated on 2D DS cases with the earliest efforts to simulate DS performed in the 1970s by McCroskey *et al.*[1], Lorber and Carta [26] and Visbal [19]. Initially, compressibility effects were not taken into account due to the required CPU time for such calculations. However, in the late 1990s, the problem was revisited by many

Table 1.3: Summary of the computational works on 3D DS.

Case	Reference	Comparisons with Experimental Works by:
1	Newsome [58]	Schreck and Helin [41]
2	Ekaterinaris [54]	Piziali [22]
3	Morgan and Visbal [59]	-
4	Spentzos *et al.*[3]	Schreck and Helin [41] and Wernert *et al.*[38]

researchers [54, 20, 55, 56] and issues like turbulence modelling and compressibility effects were assessed. Still, due to the lack of computing power and established CFD methods, most CFD work done until now focused on the validation of CFD codes rather than the understanding of the flow physics. Barakos and Drikakis [56] have assessed several turbulence models in their 2D study, stressing their importance in the realistic representation of the flow-field encountered during DS. More recently, the same researchers [57] presented results for a range of cases and have analysed the flow configuration in 2D.

The only 3D CFD works published to date on 3D DS are by Newsome [58] in the compressible laminar flow regime and Ekaterinaris [54] and Spentzos *et al.*[3] in the turbulent. A summary of the 3D CFD works performed to date on DS are presented in Table 1.3.

The only comprehensive 3D study of DS performed to date is the work by Spentzos *et al.*[3]. Spentzos, used the parallel multiblock solver (PMB) of the university of Glasgow to simulate several ramping motions based on the experiments by Schreck [41] and the sinusoidal motion of the PIV experiment by Wernert, [38]. A detailed description of the PMB code can be found in chapter 2 and comparisons with the experimental works ([41] and [38]) can be found in chapter 4 of the present work respectively. In both cases, a standard $\kappa\omega$ turbulence model was used. Although the PIV experiments by Wernert *et al.*[38] where not 3D, they were the only ones found in the literature incorporating measurements of the flow field in the area above the wing's surface during DS. The authors [3] presented streamline maps as well as velocity distributions for several locations in the flow field which matched very closely the experimental measurements. They then went on to compare with the 3D surface pressure measurements of the experiments by Schreck and Helin [41] and produced a series of pressure contour maps and vortex visualisations, that matched very closely the measurements and visualisations by Schreck [41]. The computations by Spentzos *et al.*, were the first CFD simulations to provide detailed visualisations of the size and shape of the DSV and its interactions with the TVs.

1. The work of Newsome

Newsome [58] used NASA Langley's computer code CFL3D as the flow solver. This code is an upwind-biased, finite volume approximate factorisation algorithm employing either Van Leer's flux vector splitting or Roe's flux difference splitting. The diagonalised algorithm was generalised for unsteady flows with moving grids and the Navier-Stokes equations were solved with respect to the inertial coordinates at the coordinate locations determined by the moving grid. Newsome [58], used the same geometry and conditions with Schreck's and Helin's [41] experimental work. His computational grid simulated a wing of $AR = 2$ with a splitter (inviscid) plate at the root, however, he used a rounded tip instead of the square tip Schreck and Helin [41] used, in order to model the whole computational domain by a single block. The Re number used in the computations was $RE = 5.6 \times 10^4$ for ramping motions between 0^o and 60^o with reduced ramp rates of α=0.1 and 0.2. A higher than the experimental M of 0.2 (instead of $M = 0.03$) was used to speed convergence. The minimum normalised wall spacing was 5×10^{-5} and the wing surface was defined by 152 circumferential points. No information was provided concerning the num-

ber of points across the wing's span. Finally, the non-dimensional time was set to $0,002$. Newsome [58], concentrated his analysis of the flow in the splitter plate - wing juncture area. He provided comparisons with Schreck's experiments [41] in the form of surface pressure contours for the case of the high ramp rate of 0.2 and sectional normal force coefficients for both the computed reduced ramp rates. The agreement with experiments was better for the higher ramp rate of 0.2, while for the lower ramp rate of 0.1 the inception and evolution of the DSV was 5^o to 10^o premature. Newsome [58] attributed this discrepancy to the M mismatch between CFD and experiments.

2. The work of Ekaterinaris

Ekaterinaris [54] used a solver based on the thin layer approximation of the conservative form of the compressible, Reynolds-averaged Navier-Stokes equations for a body-fitted coordinate system. The inviscid fluxes were evaluated using Osher's upwinding scheme and the viscous fluxes where computed by using central differencing. Ekaterinaris [54] used a baseline 2D grid with 181×121 points to simulate two light stall experiments by Piziali [22] ($15^o + 4.2^o sin(t)$ and $15^o + 4.2^o sin(t)$, $Re = 1.99 \times 10^6$, $M = 0.299$). He compared the Baldwin-Lomax and Baldwin-Barth turbulence models and found that the B-B models provided better results. He then went on to compute the light stall 3D case ($15^o + 4.2^o sin(t)$, $Re = 1.99 \times 10^6$, $M = 0.299$) by using the same grid (per 2D section) and time resolution that gave the best results in the 2D study case. Ekaterinaris [54] performed the 3D computation with a single block C-H type grid of $181 \times 51 \times 71$ points (37 points along the wing's span), $16,000$ time steps per cycle and the B-B turbulence model. Ekaterinaris [54] presented comparisons between measured [22] and computed sectional integral loads (c_l, c_d and c_m) along three spanwise locations ($y/s = 0.47$,$y/s = 0.80$ and $y/s = 0.98$). The comparisons between the experiments of Piziali [22] and the computations of Ekaterinaris [54] were in very good agreement in all three locations for both the upstroke and downstroke parts of the hysteresis loops. However, as the hysteresis loops indicate, no evidence of the existence of DSV can be seen. In fact the maximum angle of 19.2^o during the fast sinusoidal motion ($k = 0.1$) was probably too low to produce separation and the subsequent inception of the DSV. However, with this work, Ekaterinaris [54] demonstrated that 3D computations are possible.

3. The work of Morgan and Visbal

Additional work by Morgan and Visbal [59] also discussed the 3D aspects of DS. The objective of the researchers was the simulation of the flow around a wing spanning the test section of a tunnel without any tips exposed to the free stream. The wing was based on a NACA 0012 aerofoil, had an $AR = 4$, was pitched from 0^o to 60^o at a constant ramp rate of $\alpha^+ = 0.2$ and the Reynolds and Mach numbers were $Re = 1.2 \times 10^4$ and $M = 0.1$ respectively. One end of the wing was modelled with symmetry boundary conditions and the other with Euler slip conditions. The flow was solved [59] with a parallel laminar compressible solver in 64 processors and for two grid sizes with 4.24million and 8.44million points respectively. Although the intentions of the authors were to explore the three-dimensionality of the flow, their choice of the boundary conditions deprived the flow from the most important source of three-dimensionality in pitching wings, which is the effect of the tips. In fact the authors reported on the remarkable similarity between their 3D solutions and the 2D solutions of a NACA 0012 aerofoil undergoing the same ramping motion. The work by Morgan and Visbal [59] did not address the 3D nature of DS, but can be seen as a successful exercise of carrying out big parallel computations of pitching wings.

1.2.5 Reduced Models

CFD studies of 3D DS produce results of varied level of accuracy depending on the employed turbulence and transition models. Computations can be expensive in terms of computing time and the computing power presently available, is far from being adequate to provide with real time solutions of the 3D flow-fields encountered in practical applications. A variety of alternative approaches have been undertaken, aiming to produce reduced models that are computationally efficient yet capable to characterise the flowfield across the parameter space. Efforts along these lines include the ONERA model based on a non-linear indicial method [60, 61], the heuristic Leishman-Bedoes [62, 63] model, a model based on Lagrangian functions devised by Vepa [64] as well as simulation of DS by Neural Networks [65, 66]. The major drawback of such models [62, 63, 60, 61] is the large number of assumptions and tuning of parameters they require. That impedes their generalising ability and makes them suitable only for a narrow operating envelope. Therefore, a large number of aerodynamic data is required for their fine tuning.

On the other hand, NNs offer improved performance over conventional technologies in areas which include: Machine Vision, Pattern Recognition, Signal Filtering, Virtual Reality, Data Segmentation, Data Compression, Data Mining, Text Mining, Adaptive Control, Optimisation, Complex Mapping etc. and hence they constitute a very promising candidate as simple yet efficient DS calculators.

Past experience has shown that NNs can recreate histories of unsteady aerodynamic loads on the suction side of pitching aerofoils, following appropriate training. The principles behind NN models are described in detail in chapter 3. Faller *et al.*[65, 66], used sets of the experimental data produced by Schreck and Helin [41] to train a Recursive NN (RNN) that was able to predict the Cp readings of 15 pressure transducers along each of three spanwise positions (0%, 37.5% and 80% span) on the upper surface of a ramping-up and ramping-down wings. For all motions, the angle of attack α ranged between 0^o and 60^o, the Reynolds number was $Re = 6.9 \times 10^4$ the Mach number was $M = 0.026$ and the reduced ramp rates were 0.01, 0.02(t), 0.05(t), 0.075(v), 0.10(t), 0.15(v) and 0.20(t), were (t) denotes a dataset used for 'training' and (v) denotes a dataset used for 'validation'. Furthermore, a sinusoidal motion with a reduced frequency of 0.25(v) and mean angle and amplitude of 10^o completed the dataset used for training and validation of the RNN model. Each dataset comprised of 200 time steps. This RNN model [65, 66] had an input layer of 47 neurons, an output layer of 45 neurons and two hidden layers with 32 neurons each. The 45 neurons of the output layer corresponding to the C_p transducers distributed on the three spanwise rakes were fed-back to the input layer. The remaining two neurons of the input layer represented the instantaneous values of the angle of attack α and acceleration $d\alpha/dt$.

Following training of the RNN with all the training datasets, results were presented [65, 66] in the form of predicted C_p histories for the validation cases. Comparisons between the measured and predicted C_p histories were provided only for the spanwise location of 35% span for the two interpolated cases corresponding to $\alpha^+ = 0.075$ and 0.15. The RNN model managed to capture the overall shape of the individual transducer C_p time histories and the magnitude as well as the phase of the footprint of the DSV were predicted well. However, the very limited comparison that was provided is not adequate to assess their RNN model more conclusively.

1.3 Objectives

This literature review has shown that although the problem of DS has been studied extensively in 2D configurations, there are very few experimental works and only one comprehensive numerical 3D study [3] performed to date. It has been shown that the full 3D DS on finite wings produces flow phenomena markedly different than the ones created from infinite wings. From the industrial point of view, understanding 3D DS is of primary importance in the effective rotorcraft design. However, prior to using CFD for the analysis of such flows, CFD practitioners have to establish that their models can provide accurate results. Thus, comparisons with experiments in a variety of conditions are extremely important in building confidence on the particular simulation tool of choice. During this work, experimental data in electronic format became available for the works summarised in Tablé 1.1. Although this table does not include all of the experimental works encountered in the literature, it provides data from a wide range of motion types, wing shapes and flow conditions. Therefore, one can trust results produced by a CFD methodology successful in reproducing these experiments.

Also, 3D unsteady flow simulations tend to be computationally very expensive and reduced models can provide a useful compromise between accuracy and speed. A real-time calculator of DS moments and loads would be of considerable benefit to most rotorcraft applications. Neural networks can be seen as universal calculators, which following the appropriate training, could perform this task on-the-fly and with good accuracy.

Based on the above facts, the objectives of this work are the following:

- (1) establish confidence on the ability of CFD to accurately simulate 3D DS
- (2) investigate the flow topology during 3D DS
- (3) assess the possibility of using neural networks as a means of an accurate real-time DS computer.

1.4 Outline

The remaining of this thesis is organised as follows:

- in chapter 2 a brief description of the PMB flow solver used in this study is given. The code is capable of solving flow conditions from inviscid to fully tur-

bulent using the Reynolds Averaged Navier-Stokes (RANS) equations in three dimensions. Detached eddy simulation and large eddy simulation options are also available. Due to the flow conditions considered in this work, simple, two-equation turbulence models have been employed. Most of the results presented in this thesis have been obtained using the baseline $k-\omega$ model [35]. Good results throughout the Reynolds number range ($Re = 6,9 \times 10^4 - 2,0 \times 10^6$) indicate that turbulence modelling is of secondary importance in highly impulsive flows. To solve the RANS equations, multi-block grids were generated around the required geometries, and the equations were discretised using the cell-centered finite volume approach. For the discretisation of the convective fluxes, Osher's scheme has been used. A formally third-order accurate upwind scheme is achieved using a MUSCL interpolation technique. Viscous fluxes were discretised using central differences. Boundary conditions were set using two layers of halo cells. The solution was marched in time using an implicit second-order accurate scheme and the final system of algebraic equations was solved using a preconditioned Krylov subspace method. For this work, multi-block structured grids have been used and care has been taken in accurately representing the tip shape of each wing considered. As explained in [3] flat wing tips cannot be modelled with single-block grids and several multi-block topologies have been assessed to ensure that the quality of the CFD grids is adequate and the geometry of the wing is represented exactly.

- in chapter 3 the two different NN models used in this work are presented. Firstly, the principles of the basic FFBP approach are explained and the reader is walked through the FORTRAN code in APPENDIX A. Then a variation of the FFBP model with recursive feedback is described. The FORTRAN implementation of the latter is presented in APPENDIX B. These two models are tested for various ramping cases in chapter 6.

- in chapter 4 the comparisons between CFD and the selected experiments (Table 1.1) are shown, addressing objective (1). These tests take place over a large range of parameters. The experiments with which CFD simulations are compared with, use different wing and tip shapes, planform geometries as well as Reynolds and Mach numbers. Even more interestingly, due to the different experimental methodologies, not only surface pressure measurements are considered but also flow velocities as well as visualisations of the DSV. Collec-

tively, these comparisons provide a very good understanding concerning the potential CFD has to offer in the problem of 3D DS and it is the only such work done to date.

- the work described in chapter 4 has been a successful confidence building exercise which allowed for further explorations of 3D DS phenomenon. Furthermore, this work establishes CFD as a very promising candidate for exploring 3D DS free from the costs and limitations encountered in the experimental investigations. Chapter 5 contains the attempts for further understanding of 3D DS. The only available visualisations of the DSV in the literature, have been performed at the low *Re* regime [39, 40, 41, 42]. The DSV and the TV are the two major vortical structures in 3D DS and they seem to interact in an interesting way. All these works [39, 40, 41, 42] indicated that the DSV and the TV connect in the tip region. This raises two questions, a) why? and b) is this always the case? Also, what are the effects of *Re*, *M*, planform, yaw and rotation in 3D DS? Answers to these questions are critical to a better understanding of 3D DS and are the first step towards better industrial designs.

- in chapter 6 the two NN models described in chapter 3 are tested for a variety of ramping motions. Their behaviour, training requirements and potential to predict the basic characteristics of 3D DS are then discussed. Both the NN and RNN models were found capable of predicting the inception and propagation of the DSV. However, the NN model outperformed the RNN model in terms of numerical stability and accuracy in predictions within the training envelope. The NN model approach also benefits from the inclusion of the spatial information in the training and predicting stages which is useful in tackling 3D problems. Therefore, the NN was the preferred choice for conducting further tests in different geometries and types of motions. These tests involved predictions of contours of surface pressures and C_p time histories for ramping, yawed and rotating geometries. The FFBP NN model used was found to be a very promising alternative to the ONERA, Vepa and Beddoes models.

- Finally, in chapter 7 the concluding remarks of this work as well as suggestions for future work are laid out.

Chapter 2

Mathematical Model I - CFD Solver

2.1 CFD Solver

All computations were performed using the Parallel Multi-Block (PMB) flow solver [67] developed at the University of Glasgow. The flow solver has been continually revised and updated over a number of years and has been successfully applied to a variety of problems including cavity flows, hypersonic film cooling, spiked bodies, flutter and delta wing flows amongst others. The PMB code is a 3D multi-block structured-grid solver which solves the Navier-Stokes equations in the 3D Cartesian frame of reference. The Navier-Stokes equations consist of Partial Differential Equations (PDEs) describing the laws of conservation for:

- Mass (continuity equation).
- Momentum (Newton's 2nd Law).
- Energy (1st Law of Thermodynamics).

The continuity equation simply states that the mass must be conserved. In Cartesian coordinates, x_i, this is written as

$$\frac{\partial \rho}{\partial t} + \frac{\partial (\rho u_i)}{\partial x_i} = 0 \tag{2.1}$$

where ρ is the density of the fluid, t is the time and u_i is the velocity vector. In the above, tensor notation is used, which implies summation for repeated indices.

The second conservation principle states that momentum must be conserved. It is written in Cartesian coordinates as

$$\frac{\partial(\rho u_i)}{\partial t} + \frac{\partial(\rho u_i u_j)}{\partial x_j} = \rho f_i - \frac{\partial p}{\partial x_i} + \frac{\partial \tau_{ij}}{\partial x_j} \tag{2.2}$$

where f_i represents the body forces, p the pressure and τ_{ij} the viscous stress tensor, which is defined as

$$\tau_{ij} = \mu\left[\left(\frac{\partial u_i}{\partial x_j} + \frac{\partial u_j}{\partial x_i}\right) - \frac{2}{3}\delta_{ij}\frac{\partial u_k}{\partial x_k}\right] \tag{2.3}$$

μ is the molecular viscosity and δ_{ij} represents the Kronecker delta, which is defined as

$$\delta_{ij} = \begin{cases} 1 & \text{if i=j} \\ 0 & \text{otherwise} \end{cases} \tag{2.4}$$

The third principle can be written in Cartesian coordinates as

$$\frac{\partial \rho E}{\partial t} + \frac{\partial}{\partial x_j}\left[u_i(\rho E + p)\right] - \frac{\partial}{\partial x_j}\left(u_i \tau_{ij} - q_j\right) = 0. \tag{2.5}$$

where E is the total energy of the fluid, defined as

$$E = \rho\left[e + \frac{1}{2}u_i u_i\right] \tag{2.6}$$

and e is the specific internal energy with $u_i u_i$ representing the kinetic energy.

The heat flux vector, q_i, is calculated using Fourier's Law

$$q_i = -k\frac{\partial T}{\partial x_i} \tag{2.7}$$

where k is the heat transfer coefficient and T is the temperature of the fluid.

These three laws of conservation can be combined and written in the equation shown below, which is referred to as the Navier-Stokes equation of viscous flow. For brevity, vector notation is used

$$\frac{\partial \mathbf{W}}{\partial t} + \frac{\partial(\mathbf{F}^i + \mathbf{F}^v)}{\partial x} + \frac{\partial(\mathbf{G}^i + \mathbf{G}^v)}{\partial y} + \frac{\partial(\mathbf{H}^i + \mathbf{H}^v)}{\partial z} = 0 \tag{2.8}$$

where $\mathbf{W}$ is the vector of conserved variables and is defined by

$$\mathbf{W} = (\rho, \rho u, \rho v, \rho w, \rho E)^T \tag{2.9}$$

with the variables ρ, u, v, w, p and E having their usual meaning of density, the three components of velocity, pressure and total energy, respectively. The superscripts i and v in Equation 2.8 denote the inviscid and viscid components of the flux vectors

F (in the x-direction), **G** (in the y-direction) and **H** (in the z-direction). The inviscid flux vectors, $\mathbf{F}^i$, $\mathbf{G}^i$ and $\mathbf{H}^i$, are given by

$$\begin{aligned}
\mathbf{F}^i &= \left(\rho u, \rho u^2 + p, \rho uv, \rho uw, u\left(\rho E + p\right)\right)^T, \\
\mathbf{G}^i &= \left(\rho v, \rho uv, \rho v^2 + p, \rho vw, v\left(\rho E + p\right)\right)^T, \\
\mathbf{H}^i &= \left(\rho w, \rho uw, \rho vw, \rho w^2 + p, w\left(\rho E + p\right)\right)^T.
\end{aligned} \tag{2.10}$$

while the viscous flux vectors, $\mathbf{F}^v$, $\mathbf{G}^v$ and $\mathbf{H}^v$, contain terms for the heat flux and viscous forces exerted on the body and can be represented by

$$\begin{aligned}
\mathbf{F}^v &= \frac{1}{\mathrm{Re}}\left(0, \tau_{xx}, \tau_{xy}, \tau_{xz}, u\tau_{xx} + v\tau_{xy} + w\tau_{xz} + q_x\right)^T, \\
\mathbf{G}^v &= \frac{1}{\mathrm{Re}}\left(0, \tau_{xy}, \tau_{yy}, \tau_{yz}, u\tau_{xy} + v\tau_{yy} + w\tau_{yz} + q_y\right)^T, \\
\mathbf{H}^v &= \frac{1}{\mathrm{Re}}\left(0, \tau_{xz}, \tau_{yz}, \tau_{zz}, u\tau_{xz} + v\tau_{yz} + w\tau_{zz} + q_z\right)^T.
\end{aligned} \tag{2.11}$$

where the term τ_{ij} represents the viscous stress tensor and q_i the heat flux vector.

Although the Navier-Stokes equations completely describe turbulent flows, the large number of temporal and spatial turbulent scales associated with high Reynolds numbers make it difficult to resolve all the turbulent scales computationally. In such circumstances, small turbulent scales are eliminated by time averaging the Navier-Stokes equations to give the Reynolds-Averaged Navier-Stokes equations (RANS). This results in additional unknowns (called Reynolds stresses) which are modelled by the turbulence model. The viscous stress tensor mentioned in Equation 2.11 is then approximated by the Boussinesq hypothesis, more description of which is provided in the following sections.

The PMB flow solver uses a cell-centred finite volume approach combined with an implicit dual-time stepping method. In this manner, the solution marches in pseudo-time for each real time-step to achieve fast convergence. According to the finite volume method, the RANS equations can be discretised for each cell by

$$\frac{d}{dt}\left(\mathbf{W}_{i,j,k}\mathcal{V}_{i,j,k}\right) + \mathbf{R}_{i,j,k} = 0. \tag{2.12}$$

where $\mathcal{V}_{i,j,k}$ denotes the cell volume and $\mathbf{R}_{i,j,k}$ represents the flux residual.

The implicit dual-time stepping method proposed by Jameson [68] is used for time-accurate calculations. The residual is redefined to obtain a steady-state equation which can be solved using acceleration techniques. The following system of equations are solved in the implicit scheme during the time integration process

$$\frac{\Delta V\mathbf{W}^{m+1}_{i,j,k} - \Delta V\mathbf{W}^{m}_{i,j,k}}{\Delta V\Delta\tau} + \frac{\Delta V\mathbf{W}^{n+1}_{i,j,k} - \Delta V\mathbf{W}^{n}_{i,j,k}}{\Delta V\Delta t} = \mathbf{R}^{n+1}_{i,j,k} \tag{2.13}$$

where ΔV is the change in cell volume, $\Delta\tau$ is the pseudo time-step increment and Δt is the physical time-step increment. The flux residual $\mathbf{R}^{n+1}_{i,j,k}$ is approximately defined by

$$\mathbf{R}^{n+1}_{i,j,k} \approx \mathbf{R}^{n}_{i,j,k} + \frac{\partial \mathbf{R}^{n}_{i,j,k}}{\partial \mathbf{W}^{n}_{i,j,k}} \left(\mathbf{W}^{n+1}_{i,j,k} - \mathbf{W}^{n}_{i,j,k}\right) \tag{2.14}$$

By substituting Equation 2.14 into Equation 2.13, the linear system can be approximated to

$$\left(\frac{1}{\Delta t} + \frac{\partial \mathbf{R}^{n}}{\partial \mathbf{W}}\right) \Delta \mathbf{W} = -\mathbf{R}^{n} \tag{2.15}$$

where the subscripts i, j, k have been dropped for clarity and ΔW is used for $\left(\mathbf{W}^{n+1}_{i,j,k} - \mathbf{W}^{n}_{i,j,k}\right)$.

Osher's upwind scheme [69] is used to evaluate the convective fluxes although Roe's flux-splitting scheme [70] is also available. The MUSCL variable extrapolation method is employed in conjunction to formally provide third-order accuracy. The van Albada limiter is also applied to remove any spurious oscillations across shock waves. The central differencing spatial discretisation method is used to solve the viscous terms. The linear system of equations that is generated as a result of the linearisation is then solved by integration in pseudo-time using a first-order backward difference. A Generalised Conjugate Gradient (GCG) method is then used in conjunction with a Block Incomplete Lower-Upper (BILU) factorisation as a pre-conditioner to solve the linear system of equations, which is obtained from a linearisation in pseudo-time.

The flow solver can be used in serial or parallel mode. To obtain an efficient parallel method based on domain decomposition, different methods are applied to the flow solver [71]. An approximate form of the flux Jacobians resulting from the linearisation in pseudo-time is used which reduces the overall size of the linear system by reducing the number of non-zero entries. Between the blocks of the grid, the BILU factorisation is also decoupled thereby reducing the communication between processors. Each processor is also allocated a vector that contains all the halo cells for all the blocks in the grid. Message Passing Interface (MPI) is used for the communication between the processors in parallel. All computations undertaken for the 3D DS analysis have been performed on the Beowulf Pentium 4 100-processor workstations of the CFD Laboratory at the University of Glasgow. The two-equation Wilcox $k-\omega$ [72] turbulence model was used. This model is described in more detail in the following sections.

2.2 General Description of Turbulence and its Modelling

Turbulent flows are irregular in the sense that they contain structures which show rapid fluctuations in time and space. A broad range of scales are observed to exist at high Reynolds numbers where turbulence develops as an instability of the laminar flow. Starting with the laminar flow, fluid layers slide smoothly past each other and the molecular viscosity dampens any high-frequency small-scale instability. At high Reynolds number, the flow reaches a periodic state. The character of the flow also changes and becomes more diffusive and dissipative. This flow has increased mixing friction, heat transfer rate and spreading rate. Boundary layers consequently become thicker and less susceptible to separation.

The non-linearity of the Navier-Stokes equations leads to various interactions between the turbulent fluctuations of different wavelengths and directions. Wavelengths extend from a maximum comparable to the width of the flow to a minimum fixed by viscous dissipation scale of energy. A key process that spreads the motion over wide range of wavelengths is called vortex stretching. Turbulent structures in the flow gain energy if the vortex elements are primarily orientated in a direction which allows the mean velocity gradients to stretch them. This mechanism is called **production of turbulence**. The kinetic energy of the turbulent structures is then convected, diffused and dissipated.

Most of the energy is carried by the large scale structures, the orientation of which is sensitive to the mean flow. The large eddies cascade energy to the smaller ones via stretching. Small eddies have less pronounced preference in their orientation and statistically appear to be isotropic. For the shortest wavelengths, energy is dissipated by viscosity. This description corresponds to what is known as **isotropic turbulence**. For this flow, the ratio of the largest to smaller scale increases with Reynolds number.

If the unsteady Navier-Stokes equations are used to calculate the flow, a vast range of length and time scales would have to be computed. This would require a very fine grid and a very high resolution in time. This approach known as **Direct Numerical Simulation of turbulence (DNS)** is by today's computing speeds applicable only to flows at very low Reynolds number. One technique called **Large-Eddy Simulation** explicitly resolves the scales away from the wall and exploits

modelling in the near-wall regions. A sub-grid scale (SGS) model is used to model the smaller scales which are assumed to be more isotropic. Although less computationally intensive than DNS, this is still expensive, especially for higher Reynolds number flows.

A turbulence model therefore needs to account for some part of the fluctuating motion in order to keep the computing cost down. The optimum model should therefore be simple to implement, general and derived out of the flow physics. It is equally important that the model is computationally stable and co-ordinate invariant. These statistical turbulence models are applied to a special form of the equations of motion called the Reynolds-Averaged Navier-Stokes (RANS) equations. These are obtained by Reynolds averaging the Navier-Stokes equations.

2.3 Reynolds Averaging

In a turbulent flow, the fields of pressure, velocity, temperature and density vary randomly in time. Reynold's averaging approach involves separating the flow quantities into stationary and random parts. The quantities are then presented as a sum of the mean flow value and the fluctuating part

$$\phi = \overline{\phi} + \phi' \tag{2.16}$$

This formulation is then inserted into the conservation equations and a process known as **Reynolds averaging** is performed. Three averaging methods are possible:

- Time averaging.
- Spatial averaging.
- Ensemble averaging.

2.3.1 Time Averaging

Time averaging is the most common averaging method. It can be used only for statistically stationary turbulent flows, i.e. flows not varying with time on the average. For such flows, the mean flow value is defined as

$$\overline{u_i} = \lim_{T\to\infty} \frac{1}{T} \int_i^{i+T} u_i(t)\,\mathrm{d}t \tag{2.17}$$

In practice, $T \rightarrow \infty$ means that the integration time T needs to be long enough relative to the maximum period of the assumed fluctuations.

2.4 Boussinesq-Based Models

The Boussinesq approximation is based on an analogy between viscous and Reynolds stresses and expresses the Reynolds stresses as a product of the eddy viscosity (μ_t) and the velocity gradient. The Boussinesq's eddy viscosity hypothesis states that

$$-\rho\overline{u_i'u_j'} = \mu_t \left[\left(\frac{\partial u_i}{\partial x_j} + \frac{\partial u_j}{\partial x_i} \right) - \frac{2}{3}\delta_{ij}\frac{\partial u_k}{\partial x_k} \right] - \frac{2}{3}\rho\delta_{ij}k \tag{2.18}$$

where k represents the specific kinetic energy of the fluctuations and is given by

$$k \equiv \frac{u_i'u_i'}{2} \tag{2.19}$$

The key idea behind Boussinesq's hypothesis is that the Reynolds stresses can be calculated as a product of the dynamic eddy-viscosity, μ_t, and the strain-rate tensor of the mean flow, i.e.

$$-\rho\overline{u_i'u_j'} = 2\mu_t S_{ij} - \frac{2}{3}\delta_{ij}k \tag{2.20}$$

where

$$S_{ij} = \frac{1}{2}\left(\frac{\partial u_i}{\partial x_j} + \frac{\partial u_j}{\partial x_i} - \frac{2}{3}\delta_{ij}\frac{\partial u_k}{\partial x_k} \right) \tag{2.21}$$

Eddy viscosity, μ_t, is a scalar and consequently the Reynolds stress components are linearly proportional to the mean strain-rate tensor. What is implied here is that compressibility plays a secondary rate in the development of the turbulent flow-field. According to Morkovin's hypothesis [73], compressibility affects turbulence only at hypersonic speeds.

To compute μ_t, further modelling is required and it is at this point that turbulence models come into play. Turbulence models are classified into categories based on the number of transport equations required to calculate μ_t. According to the number of transport equations needed for the calculation of the eddy viscosity, the Boussinesq-based models are classified as:

- **Algebraic** or **zero-equation** models, such as the Cebeci-Smith [49] and Baldwin-Lomax [12] models.

- **One-equation** models, such as the Spalart-Allmaras [52] and Baldwin-Barth [53] models.

- **Two-equation** models, such as the $k-\varepsilon$ [30], $k-\omega$ [72], , $k-\omega$ SST [74] and $k-g$ [75] models.

An additional family of models exists, which solves equations for all components of the Reynolds stress tensor. These are also known as **Reynolds Stress Models (RSM), second-order closures** or **second-moment closures.**

2.5 Viscosity-Dependent Parameters

Non-dimensionalised wall distances for turbulent flow, y^*, and non-turbulent flow, y^+, are defined as follows

$$y^* \equiv \frac{y_n k^{1/2}}{\nu}, \qquad y^+ \equiv \frac{y_n u_\tau}{\nu}, \tag{2.22}$$

where y_n is the distance from the nearest wall, $u_\tau \equiv \sqrt{\tau_w/\rho}$ is the frictional velocity and τ_w represents the dynamic wall shear stress. Turbulent Reynolds numbers for the $k-\varepsilon$ model (denoted by R_t) and for the $k-\omega$ model (denoted by R_ω) are given by the following equation

$$R_t \equiv \frac{k^2}{\nu\varepsilon}, \qquad R_\omega \equiv \frac{k}{\nu\omega}. \tag{2.23}$$

2.6 One-Equation Models

This type of turbulence models were designed to improve the ability of algebraic models to account for the convection and diffusion of turbulence. This was accomplished by employing a transport equation, usually for the realisation of the kinetic energy of turbulence, k . The general form of this transport equation takes the following form

$$\frac{\partial k}{\partial t} + u_j \frac{\partial k}{\partial x_j} = \tau_{ij}\frac{\partial u_i}{\partial x_j} - \varepsilon + \frac{\partial}{\partial x_j}\left[\frac{\mu}{\rho}\frac{\partial k}{\partial x_j} - \frac{1}{2}\overline{u_i' u_i' u_j'} - \frac{1}{\rho}\overline{p' u_j'}\right] \tag{2.24}$$

The first term in Right-Hand Side (RHS) ($\tau_{ij}\frac{\partial u_i}{\partial x_j}$) represents the **production of turbulence.** From the terms in the square brackets, the first ($\frac{\mu}{\rho}\frac{\partial k}{\partial x_j}$) is the **molecular diffusion** term, the second ($\overline{u_i' u_i' u_j'}$) is the **turbulent flux of the turbulent kinetic energy** and the third ($\frac{1}{\rho}\overline{p' u_j'}$) is the **pressure diffusion** term, which is

usually neglected due to its small contribution. The term ε is the **dissipation rate** of k per unit mass of fluid, and is usually defined by

$$\varepsilon = \frac{\mu}{\rho}\overline{\frac{\partial u_i'}{\partial x_k}\frac{\partial u_i'}{\partial x_k}} \tag{2.25}$$

Eddy viscosity for one-equation turbulence models is usually calculated by

$$\mu_t = \rho C_\mu l_{mix}\sqrt{k} \tag{2.26}$$

where C_μ is a coefficient specific to the model.

The Baldwin-Barth [53] and Spalart-Allmaras [52] one-equation models are the most common types of one-equation models. History effects of the turbulent kinetic energy profile are better accounted for in one-equation models due to the additional differential equation. This can be particularly important in non-equilibrium flows and consequently provides better results than algebraic models. Specifically tuned for aerodynamic flows with adverse pressure gradients and transonic flow conditions, one-equation models also work well for flow regions where the mean velocity gradient is zero. Better modelling of near-wall effects and transition, for instance, can simply be integrated into the model's formulation by adding extra relevant terms because of its modular design. For these reasons, one-equation models have gained much popularity in aerospace applications. The disadvantage of one-equation models is the absence of a mechanism for the computation of the length scale, l, is included making the prediction of highly turbulent flows (with a broad range of length scales) difficult. In that respect, one-equation models are still similar to algebraic models.

2.7 Two-Equation Models

By far the most popular type of turbulence model used is of the two-equation type. Two-equation models are 'complete', i.e. can be used to predict properties of a given flow with no prior knowledge of the turbulence structure or flow geometry. Two transport equations are used for the calculation of the turbulent kinetic energy, k , and turbulence length scale, l, or a function of it. The choice of the 2nd variable is arbitrary and many proposals have been presented. The most popular involves using:

- ε — dissipation rate of turbulence.
- ω — k-specific dissipation rate.

- τ — turbulent time-scale.

A description of the different types of two-equation models is provided in Table 2.1 below. As well as indicating the variable used for the second transport equation, Table 2.1 includes the equation used to calculate the eddy viscosity.

Table 2.1: Different types of two-equation turbulence models and the corresponding second variable used

Two-Equation Model	Equation	2nd Variable Used
Kolmogorov (c. 1942) [76]	$k^{1/2}l^{-1}$	ω (Frequency Length Scale)
Rotta (c. 1950)	l	
Harlow-Nakayama (1968) [77]	$k^{3/2}l^{-1}$	ε (Energy Dissipation Rate)
Spalding (1969) [78]	kl^{-2}	ω'^2 (Vorticity fluctuations squared)
Speziale (1992) [79]	$lk^{-1/2}$	τ (Time-Scale)
Nee	kl	kl (k times length scale)
Harlow-Nakayama	$lk^{-1/2}$	ν_t (Eddy viscosity)

One of the most widely used two-equation turbulence models is the $k-\varepsilon$ model. One of the original versions of this model was developed by Jones and Launder [30] in 1972. The turbulent scale in the $k-\varepsilon$ model is calculated using a second transport equation for the turbulent dissipation rate, ε. The eddy viscosity for the $k-\varepsilon$ model is typically derived from

$$\mu_T = C_\mu \rho \frac{k^2}{\varepsilon} \tag{2.27}$$

where C_μ is a model coefficient. The advantage of the $k-\varepsilon$ model is that it performs well for attached flows with thin shear layers and jets but fails to predict the correct flow behaviour in many flows with adverse pressure gradients, extended separated flow regions, swirl, buoyancy, curvature generated secondary flows and unsteady flows.

The other class of two-equation turbulence models that is widely used is the $k-\omega$ model. In 1988, Wilcox [72] developed the famous $k-\omega$ model originally conceived by Kolmogorov. The $k-\omega$ model is similar to the $k-\varepsilon$ model but instead uses the k -specific dissipation rate as a second variable to compute the turbulent length

scale. The eddy viscosity is obtained by

$$\mu_T = \rho \frac{k}{\omega} \tag{2.28}$$

Although the $k-\omega$ model provides better performance in adverse pressure gradient flows, it suffers largely from the same problems as the $k-\varepsilon$ model. Hybrid versions of the $k-\omega$ and $k-\varepsilon$ models called the Baseline $k-\omega$ (which improves free stream dependancy) and SST models were later introduced by Menter [74]. In particular, the SST model, performs well in separated flows. The idea behind the Baseline $k-\omega$ model is to exploit the robust and accurate formulation of the $k-\omega$ model near the wall but to also take advantage of the lack of sensitivity to free-stream values of the $k-\varepsilon$ model away from the wall. Menter [74] achieved this by transforming the $k-\varepsilon$ model into the same form as the $k-\omega$ formulation. This process generated an additional cross-diffusion parameter in the ω transport equation. For the SST model [74], the idea was to improve the Baseline $k-\omega$ model by including terms to account for the transport of the principal shear stress. This term is incorporated in Reynolds Stress Models (RSM) and was also used by Johnson-King [50] to produce the so called half-equation model that solved an ode for the maximum shear stress transport. Its importance was realised based on the significantly improved results for adverse pressure gradient flows [74].

2.7.1 Model Equations: Linear $k-\omega$ Model

Mathematical formulations of the different types of the linear $k-\omega$ two-equation turbulence models discussed in the previous sections are described here. More information on the $k-\varepsilon$ and $k-g$ models can be obtained from Ref. [80].

Since the introduction of the linear $k-\omega$ model by Wilcox in 1988 [72], the other notable modification to the $k-\omega$ model came from Menter in 1994 [74] who proposed the hybridisation of the $k-\omega$ model with the $k-\varepsilon$ model, as described previously. Table 2.2 lists the four notable versions of the $k-\omega$ models and further describes if they include parameters to compute the low Reynolds number properties.

The turbulence transport equations used in the formulation of the $k-\omega$ models are:

$$\frac{\partial}{\partial t}(\rho k) + \frac{\partial}{\partial x_j}(\rho U_j k) = \frac{\partial}{\partial x_j}\left[\left(\mu + \frac{\mu_t}{\sigma_k}\right)\frac{\partial k}{\partial x_j}\right] + \rho\left(P - \beta^* \omega k\right) \tag{2.29}$$

Table 2.2: Different types of linear $k-\omega$ turbulence models

Type of Model	Low-Re
Wilcox (1988) [72]	Yes
Wilcox (1994) [81]	Yes
Menter (1994) [74] — (i) Baseline Model	Yes
Menter (1994) [74] — (ii) SST Model	Yes

$$\frac{\partial}{\partial t}(\rho\omega)+\frac{\partial}{\partial x_j}(\rho U_j\omega)=\frac{\partial}{\partial x_j}\left[\left(\mu+\frac{\mu_t}{\sigma_\omega}\right)\frac{\partial\omega}{\partial x_j}\right]+\rho\left(\frac{\alpha}{\nu_t}P-\frac{\beta}{\beta^*\omega^2}\right)+\rho S_l \quad (2.30)$$

In the transport equation for k and ω above, the production of turbulence, P, and the dissipation rate specific to k , P_ω, are defined by:

$$P_k=\tau_{ij}^R\frac{\partial u_i}{\partial x_j}, \qquad P_\omega=\rho\frac{\alpha}{\nu_t}P_k. \quad (2.31)$$

Values for the coefficients used in all the four types of linear $k-\omega$ models discussed here are given in the Tables 2.3 and 2.4.

Table 2.3: Values of constants used in linear $k-\omega$ models (continued)

Type of Model	α^*	β^*	α	β
Wilcox (1988) [72]	1	$\frac{9}{100}$	$\frac{5}{9}$	$\frac{3}{40}$
Wilcox (1994) [81]	$\frac{\frac{1}{40}+\frac{R_\omega}{6}}{1+\frac{R_\omega}{6}}$	$\frac{9}{100}\frac{\frac{5}{18}+\left(\frac{R_\omega}{8}\right)^4}{1+\left(\frac{R_\omega}{8}\right)^4}$	$\frac{5}{9}\frac{\frac{1}{10}+\frac{R_\omega}{2.7}}{1+\frac{R_\omega}{2.7}}$	$\frac{3}{40}$
Menter (1994) [74] *(Baseline)*[1]	1	0.09	$B\begin{pmatrix}0.553\\0.440\end{pmatrix}$	$B\begin{pmatrix}0.075\\0.083\end{pmatrix}$
Menter (1994) [74] *(SST)*[2]	$\min\left(1,\frac{0.31}{F_2}\frac{\omega}{\bar{\omega}}\right)$	0.09	$B\begin{pmatrix}0.553\\0.440\end{pmatrix}$	$B\begin{pmatrix}0.075\\0.083\end{pmatrix}$

Menter's models [74] are constructed as a 'blend' of the $k-\omega$ and $k-\varepsilon$ models. Here the $k-\varepsilon$ model is cast in the same form as the $k-\omega$ model so as to exploit its independence of free-stream values. Blending of the $k-\varepsilon$ and $k-\omega$ model values for α, β, σ_k^{-1} and σ_ω^{-1} is (in this notation) given by the following equation

$$B\begin{pmatrix}a\\b\end{pmatrix}\equiv F_1 a+(1-F_1)\,b. \quad (2.32)$$

Table 2.4: Values of constants used in linear $k-\omega$ models (concluded)

Type of Model	σ_k	σ_ω	S_l
Wilcox (1988) [72]	2	2	0
Wilcox (1994) [81]	2	2	0
Menter (1994) [74]*(Baseline)*[1]	$\frac{1}{B\begin{pmatrix}0.5\\1.0\end{pmatrix}}$	$\frac{1}{B\begin{pmatrix}0.5\\0.856\end{pmatrix}}$	$B\begin{pmatrix}0\\\frac{1.71}{\omega}\nabla k\cdot\nabla\omega\end{pmatrix}$
Menter (1994) [74]*(SST)*[2]	$\frac{1}{B\begin{pmatrix}0.85\\1.0\end{pmatrix}}$	$\frac{1}{B\begin{pmatrix}0.5\\0.856\end{pmatrix}}$	$B\begin{pmatrix}0\\\frac{1.71}{\omega}\nabla k\cdot\nabla\omega\end{pmatrix}$

The blending function is defined by

$$F_1 = \tanh\left(\arg_1^4\right), \tag{2.33}$$

where

$$arg_1 = min\left[\max\left(\frac{k^{1/2}}{\beta^*\omega y}, \frac{500\nu}{y_n^2\omega}\right), \frac{2k\omega}{y_n^2\max\left(\nabla k\cdot\nabla\omega, 0.0\right)}\right]. \tag{2.34}$$

The SST model places an additional vorticity-dependent limiter on the shear stress

$$F_2 = \tanh\left(arg_2^2\right), \qquad arg_2 = \max\left(\frac{2k^{1/2}}{\beta^*\omega y}, \frac{500\nu}{y^2\omega}\right). \tag{2.35}$$

Note that this model also uses a slightly different value of σ_k.

For low-Reynolds number versions of the $k-\omega$ model and Menter's Baseline $k-\omega$ and SST models, the following boundary conditions are assumed for a direct integration to the wall

$$\text{For } k: \quad k_w = 0, \qquad flux(k)_w = 0. \tag{2.36}$$

$$\text{For } \omega: \quad \omega = \infty, \qquad flux(\omega)_w = -\nu\nabla\omega. \tag{2.37}$$

where the subscript w denotes the value *at* the wall.

Chapter 3

Mathematical Model II - Neural Network

3.1 Introduction

A Neural Network (NN) is an information processing machine, inspired by the way biological nervous systems, such as the brain, work. NNs are composed of a large number of highly interconnected processing elements (neurons) working in unison to solve specific problems. NNs, like the brain, learn by example. An NN is configured for a specific application, such as pattern recognition, through a learning process. Learning in biological systems involves adjustments to the synaptic connections that exist between the neurons. NNs have a remarkable ability to derive meaning from complicated or imprecise data and can be used to extract patterns and detect trends that are too complex to be noticed by either humans or other computer techniques [82, 83, 84]. A trained neural network can be thought of as an "expert" in the category of information it has been given to analyse. This expert can then be used to provide predictions given new situations of interest. The architecture of NNS facilitate parallel as well as dedicated hardware implementations. Therefore, NNs can also be extremely fast in their operation. NNs, have been so far used to very diverse applications, from market forecasting to industrial process control and risk management. More recently, Faller *et al.*[65, 66] have also used them in unsteady aerodynamics for the prediction of DS. In this chapter, the reader is firstly walked through the basic principles of NNs. Then the details of two algorithms based on a standard feed-forward back-propagation (FFBP) model are presented: (a) a standard FFBP NN (Figure 3.1) and (b) a FFBP NN with feedback (RNN) (Figure

3.2). The RNN approach was first tested for DS by Faller *et al.*[65, 66].

3.2 Generic FFBP NN

A NN can be seen as a universal approximator with the capacity to simulate any mapping of the type:

$$z = z(x_1, x_2, ..., x_n) \tag{3.1}$$

or in the case of the wing surface pressure distribution during DS:

$$C_p = C_p(t, \alpha, \alpha^+, x, y) \tag{3.2}$$

The theoretical justification for the suitability of a FFBP NN to approximate such mappings, comes from the existence theorem put forward by A. N. Kolmogorov [85]: *For every integer dimension* $d > 1$, *there exist continuous real functions* $h_{ij}(x)$ *defined on the unit interval* $U = [0, 1]$, *such that for every continuous real function* $f(x_1, ..., x_d)$ *defined on the* $d-$*dimensional unit hypercube* U^d, *there exist real continuous functions* $g_i(x)$ *such that:*

$$f(x_1, ..., x_d) = \sum_{i=1}^{2d+1} g_i \sum_{j=1}^{d} h_{ij}(x_j) \tag{3.3}$$

The above equation can be interpreted as a NN with 3 layers and a total of $(2d+1)d$ neurons in the hidden layer. Figure 3.1 shows the topology of a generic NN model.

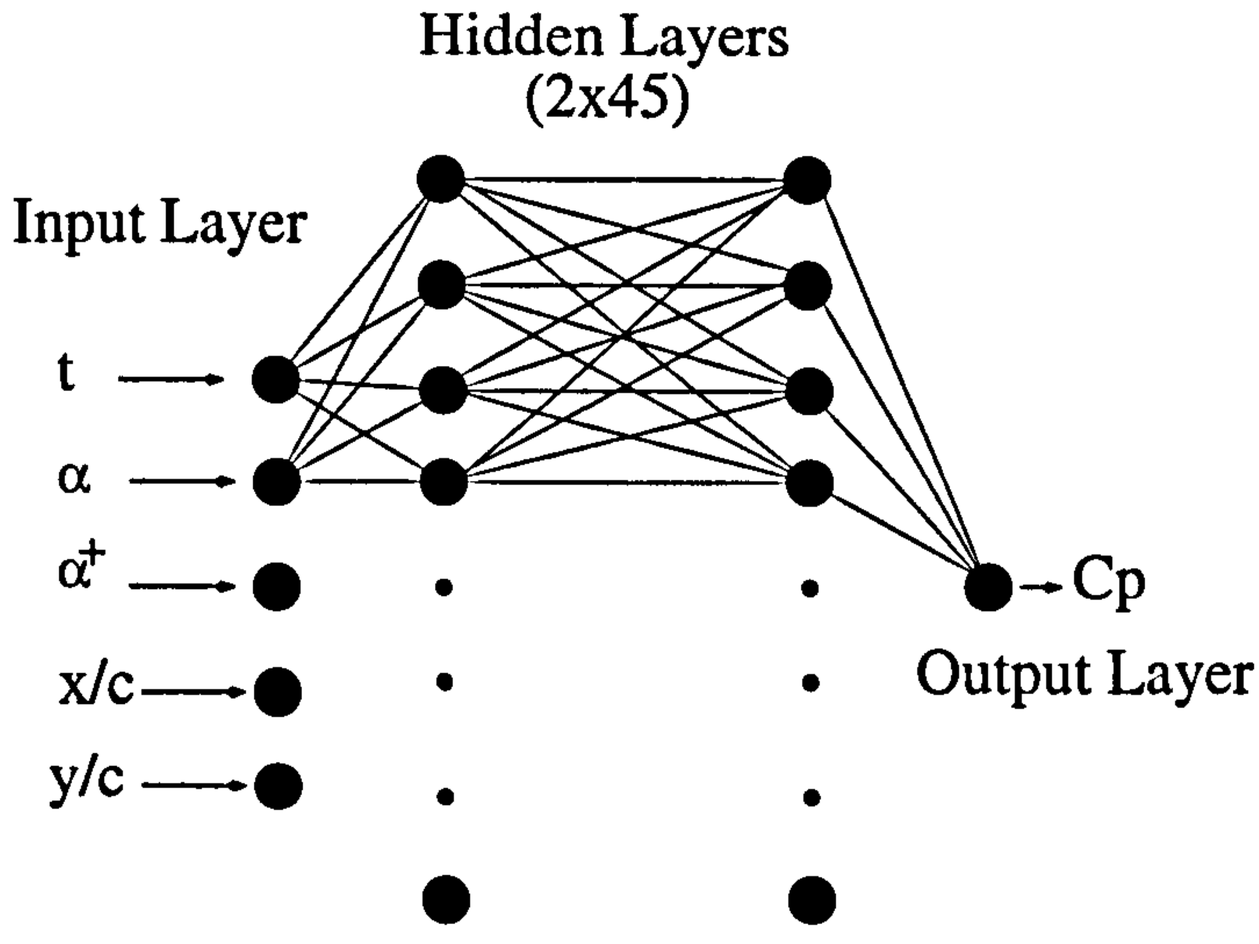

Figure 3.1: Generic Neural network model.

This NN consists of an input layer with 5 neurons, 2 hidden layers and an output

layer with 1 neuron. Each neuron is connected to all the neurons of the previous layer and to all the neurons of the next layer. All neurons are exactly the same, the only distinguishing characteristics between them being the number of inputs and outputs they have. Each inter-neural connection (shown as a straight line) is defined by a particular real number, a *weight* w_{ij}. The total number of these weights is the degrees of freedom (DoF) of the NN and it is precisely in these connections were the 'knowledge' of a trained NN resides. Each neuron can be seen as a 'black box' which internally performs two basic operations:

- a combination which computes a linear summation over its input signals
- a scaling through an activation function which bounds the result of the summation to a required interval.

The most commonly used activation function is the non linear sigmoid:

$$y(x) = \frac{1}{1+e^{-x}} \tag{3.4}$$

whose range of values is the interval $[0, 1]$.

To illustrate how the values propagate through successive layers, we can imagine that the 5 input layer neurons of the NN of Figure 3.1 are fed with the values x_i $(i = 1, 2, ...5)$ respectively. Each of the input neurons will pass this value through the sigmoid function of eqn (3.4), to yield the following output:

$$y_i = \frac{1}{1+e^{-x_i}},\ i = 1, 2, ..., 5 \tag{3.5}$$

We can assume that the first hidden layer of the NN shown in Figure 3.1 has n neurons. Each of these neurons is connected with all 5 input layer neurons via the weights w_{ij} $(i = 1, 2, ..., 5$ and $j = 1, 2, ..., J)$. Therefore, each of the J neurons on the first hidden layer receives a signal equal to:

$$h_j^{in} = \sum_{i=1}^{5} y_i \times w_{ij},\ j = 1, 2, ..., J \tag{3.6}$$

which will consequently pass through their activation function, to give the following value at their output:

$$h_j = \frac{1}{1+e^{-h_j^{in}}},\ j = 1, 2, ..., J \tag{3.7}$$

The process described above is repeated until the values reach the output layer. In that manner, the NN can be seen as a 'tree' which 'propagates forward' the input

signals to the output. Each one of the branches of this tree as seen in figure 3.1, is essentially a 'synaptic weight' that defines the connection magnitude of each neuron at a given layer to each neuron at the layer ahead. Thus, if all synaptic weights are known, a given combination of input values will yield a single value at the output of the NN. It should be stressed that the optimal number of hidden layers as well as the number of neurons on each hidden layer is currently more an issue of art than it is of science. The numbers of input and output neurons are always dictated by the physics of the problem at hand, however, the number of neurons in the hidden layers (or perceptron) is not at all well defined. An excellent summary of the behaviour and the fine-tunning particulars of FFBP NNs can be found in [86]. Mather and Kavzoglu [86] argue that the choice behind the number of hidden layers as well as the number of neurons on each hidden layer is not straight forward and greatly depends on the complexity of the physics of the problem and the number of patterns used for training. A pattern is a pair of an input and an output vector. It seems that the effect of increasing the number of layers is to make a NN 'smarter' and the effect of increasing the number of neurons per layer, makes a NN more accurate.

The process described so far is essentially the NN's predictive mode (Feed Forward), were all synaptic weights are assumed to be known. Hence, the resulting z at the output of the NN is a function of the input values. It is evident that the predictive mode is very cheap, as the process from input to output involves a very small number of operations. A FFBP NN is trained by a sufficient number of patterns. The training process starts with a random distribution of the synaptic weights w_{ij} between layers. Via the process described above, a unique and wrong solution vector is yielded at the output of the NN, for a particular pattern. However, since the right vector corresponding to the input vector for this pattern is known, a measure of the error can be calculated:

$$E = \sum_{k=1}^{m} |y_k - t_k| \tag{3.8}$$

or in order to simplify the algebra (see Eqn (3.10) on the next page):

$$E = \frac{1}{2} \sum_{k=1}^{K} (y_k - t_k)^2 \tag{3.9}$$

where K is the number of output neurons and y_k and t_k are the components of their corresponding output and target values respectively. Clearly, the error function E is a function whose variables are all the different weights w_{ij} in the NN. The aim of the Back Propagation (BP) algorithm is to find the particular distribution of weights

that minimise the value of E. The method used here is the Gradient Descent with Momentum (GDM) algorithm [87]. Without loss of generality, it is assumed that the NN has one only hidden layer. To avoid confusion, the indices k, j, i refer to the output, hidden and input layers respectively and K, J, I are the total number of neurons of these layers. The BP algorithm is explained below, step by step:

- The derivative of Eqn (3.9) is calculated. This derivative represents the rate of change of the error function E, subject to a change of the k-th component of the output vector:

$$\frac{\partial E}{\partial y_k} = y_k - t_k \tag{3.10}$$

- This change is then propagated backwards to the input of the k-th neuron of the output layer. Thus, the effect that a change of the output vector has on the input values of the neurons on the output layer is calculated:

$$\Delta y_k = \frac{\partial E}{\partial x_k} = \frac{\partial E}{\partial y_k} \times \frac{dy_k}{dx_k} = (y_k - t_k) \times y_k \times (1 - y_k) \tag{3.11}$$

  where y_k is the transfer function defined in Eqn (3.4).

- The next step is to propagate Δy_k backwards, across the inter-layer connections w_{jk} and the transfer function of the neurons of the hidden layer, to the input of the hidden layer. Thus,

$$\Delta h_j = \sum_{k=1}^{K} [w_{j,k} \times \Delta y_k] \times h_j \times (1 - h_j) \tag{3.12}$$

  where h_j is defined in Eqn (3.6).

- Δh_j in Eqn (3.12) above, represents the magnitude of change of the values h_j at the input of the hidden layer neurons, subject to a change of the output vector. At this point, a change of the weights w_{ij} between the input and hidden layers can be computed using the generalised delta rule:

$$\Delta^n w_{ij} = \eta \times \Delta h_j + \alpha \times \Delta^{n-1} w_{ij} \tag{3.13}$$

  consequently,

$$w_{ij} = w_{ij} + \Delta^n w_{ij} \tag{3.14}$$

  where η is the learning rate, α the learning momentum and n is the global iteration level.

- The final step of the BP method, is the amendment of the weights w_{jk} between the hidden and the output layers:

$$\Delta^n w_{jk} = \eta \times \Delta y_k + \alpha \times \Delta^{n-1} w_{jk} \tag{3.15}$$

and

$$w_{jk} = w_{jk} + \Delta^n w_{jk} \tag{3.16}$$

At this stage, all the weights in the NN have been re-approximated towards values that provide a smaller error E. However, this process has been so far applied to a single pattern and only once. Next, the procedure is repeated for all patterns and thus an 'epoch' is completed. The procedure is then iterated over the necessary number of epochs to satisfy a convergence criterion based on a limiting value of E. It is critical that during every epoch, the patterns are introduced at a random order. This ensures faster learning rates, avoids 'memorising' and increases the capability of the NN to tackle situations it has not been trained for. Appendix A, contains the Fortran source code of the standard FFBP NN, as explained above. The starting file 'input' is read (lines 33-43) providing the name of the pattern file, the values for the size of the NN, the running parameters (refresh rate, error threshold, η and α). Then in lines 45-69, the weights of the networks are initialised with small random values. Finally the file containing the training patterns is read (lines 71-86). This file must have an ASCII format and as many columns as the number of input neurons plus the number of the output neurons. Each line represents a different pattern and is of the form **I,O**, where **I** and **O** are the input and output vectors correspondingly. Best results will be obtained if all input and output vector components are scaled linearly in the range [0,1]. The preferred method of scaling is local scaling, within individual columns at a time. The main training loop starts at line 89. Line 93 generates a random integer between 1 and the total number of training patterns. Of course, in this way there is no guarantee that during an epoch all patterns will be used once, however, it is expected that over many epochs, all patterns will appear with the same frequency. The code between lines 96 and 103 performs the forward propagation of the input values to the output of the neurons of the first hidden layer. Note, that since the input values are already scaled in [0,1], the sigmoidal transfer function is not applied on the input neurons. Then in (lines 106-115) the exit of the first hidden layer neurons is further propagated to the exit of the last hidden layer neurons. Finally, the forward propagation terminates at the exit of the NN

(lines 119-135) where the output value is compared to the target value and thus an accumulated error value is calculated (line 130). The part of the code performing the BP algorithm is contained between the lines 133 and 213 as described in the steps above. More specifically, the quantity Δy_k is calculated at line 133 and Δh_j on line 162 (note that this code supports an arbitrary number of hidden layers). The first array of weights (between the input layer and the first hidden layer) is re-approximated on line 177 and the weight arrays between the hidden layers on line 194. Finally, the BP ends when the last array of weights (between the last hidden layer and the output layer) is re-approximated on line 210. The loop over all the patterns terminates on line 214 and the global loop over all the epochs, on line 216.

3.3 Recursive NN

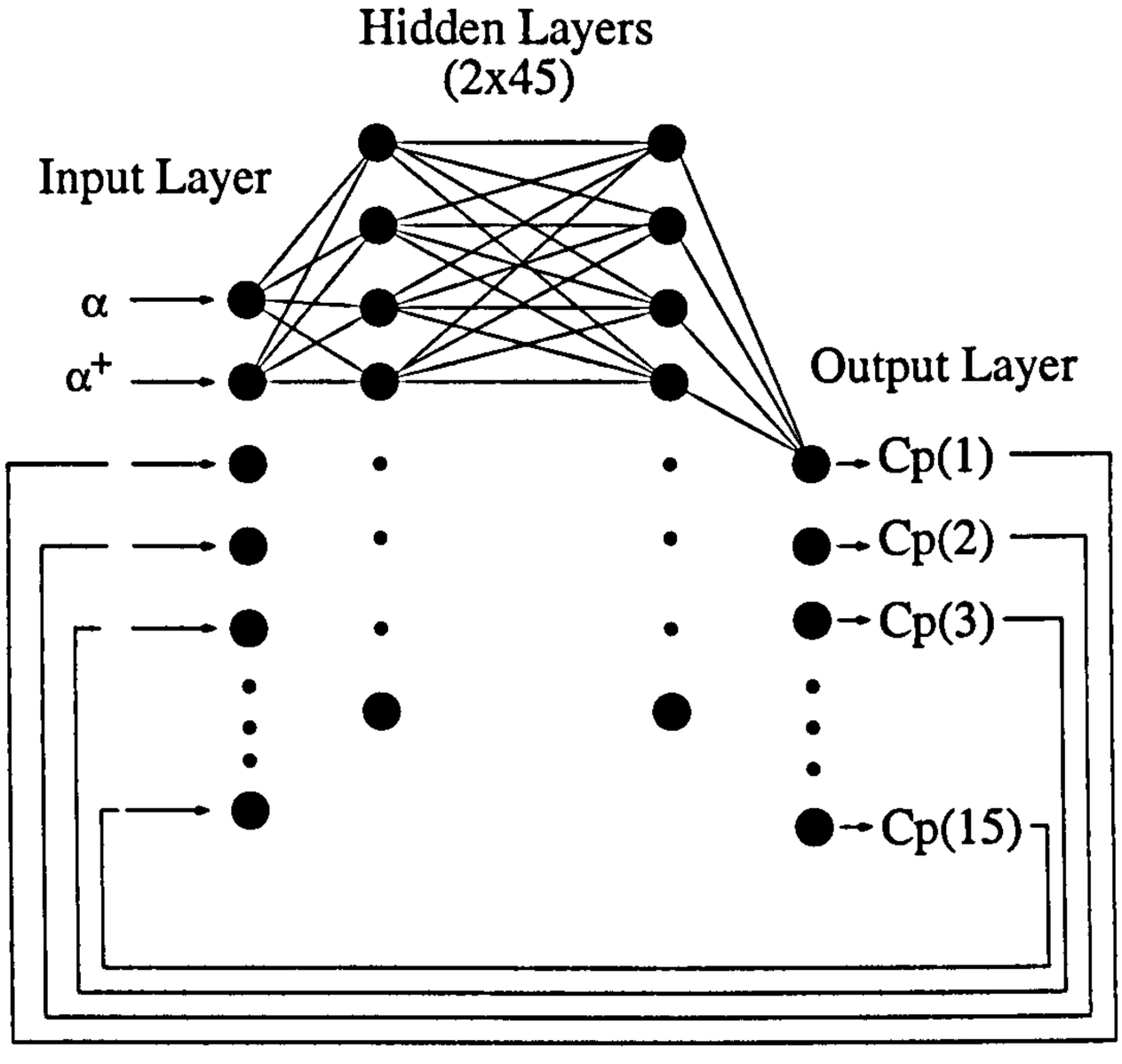

Figure 3.2: Neural network model with feedback.

The second NN model used (Figure 3.2) is a variation of the standard FFBP NN model described in the previous section. In this model, every C_p transducer on the wing has a dedicated neuron (15 in this case) both at the input and output layers. Therefore, it is no longer necessary to include the spatial information x, y of the transducers to the training sequence. Also, during training, the C_p values for every motion are fed to their corresponding neuron on the input layer in their true time sequence. These values are then propagated to the output layer in exactly the same

way as in the standard FFBP NN model. We can assume that the $C_p(t_0)$ values corresponding to time $t_0 = 0$ are fed into the input, together with their corresponding $\alpha(t_0)$ and $\alpha^+(t_0)$. A random starting distribution of weights propagates these values to the output layer. These output values are then compared to the actual $C_p(t_1)$ values and an error value based on their difference is generated. Based on this error, the BP algorithm re-evaluates all the network weights in the same manner as in the standard FFBP NN implementation. The sequence is repeated, but now the $C_p(t_1)$ values that are fed to the input are the output values of the previous step, via the feedback loop. The NN is trained after a sufficient number of epochs. A successfully trained NN should be able to predict the $C_p(t)$ histories of a particular motion, by the starting $C_p(t_0)$ values as well as the sequence of $\alpha(t)$ and $\alpha^+(t)$ corresponding to this motion.

Appendix B, contains the Fortran source code of the FFBP NN with feedback, as explained above. Since the code of the RNN is largely identical to the standard NN code, only their differences will be described here. The pattern file is read on line 70 and it consists of the same number of columns as the input layer neurons. The number of lines is equal to the sum of the timesteps of all the training cases, each presented in their true time sequence. During training, the different sets should be randomly presented every time. Therefore, the user is required to input the information regarding the number of sets as well as their corresponding starting and ending lines (lines 79-91). Then in lines 93-107, the target file is constructed from the input file, according to the requirement:

$$Target[C_p^i(t_n)] = C_p^i(t_{n+1}) \tag{3.17}$$

where n denotes timestep and i denotes the C_p identity number. Finally, in lines 132-136 the feedback connection is applied by setting the next input equal to the previous output. The FF as well as the BP stage of the NN model with feedback are identical to the generic NN model described previously.

Chapter 4

CFD Validation

4.1 Introduction

To validate CFD against experiments care must be taken to ensure that the same boundary conditions and geometry are used. Due to the flow conditions considered here, simple two-equation turbulence models have been employed. The results presented in this dissertation have been obtained using the baseline $k-\omega$ model [35]. Meshing finite wings encounters a problem in the tip region as a single-block grid will (a) render flat tips topologically impossible and (b) lead to skewed cells in the case of rounded tips. To counter these problems, three different blocking strategies were considered as shown in Figure 4.1. In a first attempt, shown in Figure 4.1a, the tip end is formed by a 2D array of collapsed cells resulting in a C-H single-block topology. Although this is adequate for thin, sharp tips, it fails to satisfactorily represent the tip geometry of wings with thicker sections or flat tips. For wings with flat tips, good results can be obtained by using a true multi-block topology. As shown in Figure 4.1b, the tip plane constitutes one of the six sides of a new block extending to the far-field. This topology can generate both flat and rounded tips and produces no collapsed cells in the vicinity of the tip region. A modification of this topology is shown in Figure 4.1c where 4 blocks were used next to the flat tip plane to promote cells with a better aspect ratio than in the previous case. Other approaches including H-H and C-O topologies have also been investigated. The latter is shown in Figure 4.1d and is suitable for truncated wings with rounded tips. In this case, the C- topology used around the leading edge curves around the tip resulting in a very smooth distribution of the radial mesh lines around the entire wing and in particular at the wing-tip interface, which is no longer treated as a block

boundary. This blocking produces the smoothest mesh around the tip region as none of the emerging grid cells is skewed. Apart from the single-block C-H method all other topologies can be used for both rounded and flat wing tips. Figure 4.2 shows the full blocking strategy corresponding to grid (c) of Figure 4.1. This blocking was eventually used for all runs and planforms in this work in three variations: (a) half wings with symmetry plane on the root plane (Figures 4.2a and b), (b) half wings with viscous wall on the root plane (Figure 4.2c) and (c) full wings. In the case of full wings, the blocking shown in Figure 4.2a was simply mirrored in respect to the root plane to produce the full wing blocking topology. In addition to the wing geometry, the selection of end-plates, tunnel walls and kinematics of the moving surface are also important. In paragraphs 4.3.1 and 4.5.2 respectively, the effects of splitter plates and accurate, non-idealised motion profiles have been accounted. In the latter case, an accurate ramping profile was recreated from the experimental measurements of the AoA of the wing using Fourier Transform. Table 4.1 presents all the experimental cases for which comparisons with CFD computations have been performed, in ascending *Re*. Case 3 of Table 4.1, is an exception, as strictly speaking, it should not be among the 3D experimental works. However it is the only work where PIV measurements have been collected for DS and therefore presented a chance for flow field comparisons. The remaining of this chapter is divided into three parts:

(A) the validations of the low *Re* cases (cases 1 and 2) of Table 4.1

(B) the validation of the 2D case (case 3 of Table 4.1) and

(C) the validation of the high *Re* cases (cases 4,5 and 6) of Table 4.1.

The details of all grids used in this study are presented in Table 4.2.

4.1. INTRODUCTION

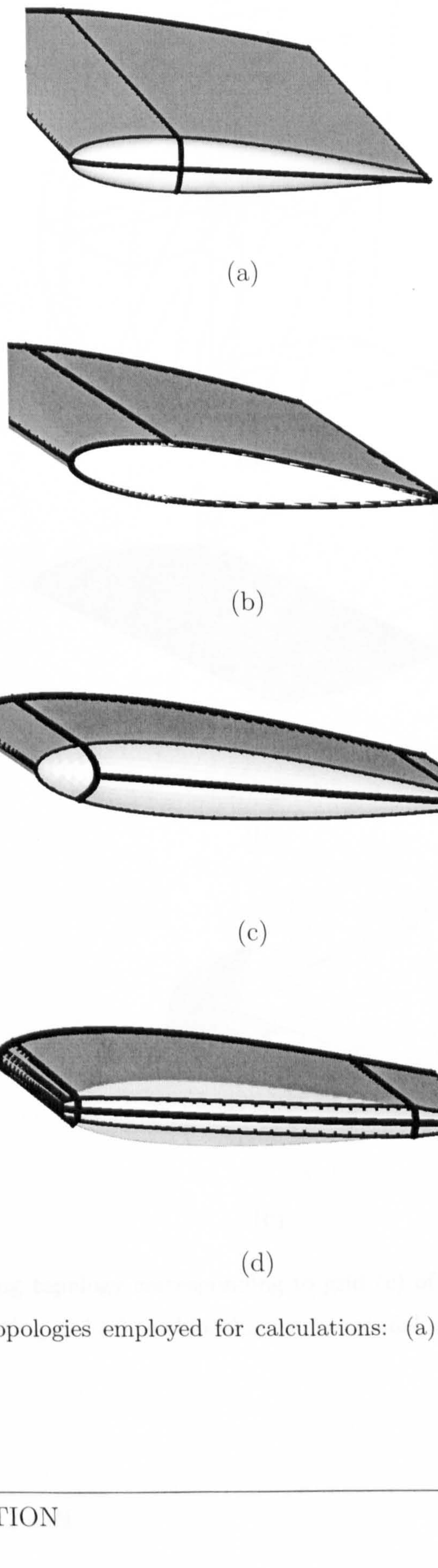

(a)

(b)

(c)

(d)

Figure 4.1: Grid topologies employed for calculations: (a) 'collapsed' tip, (b,c,d) 'extruded' tips.

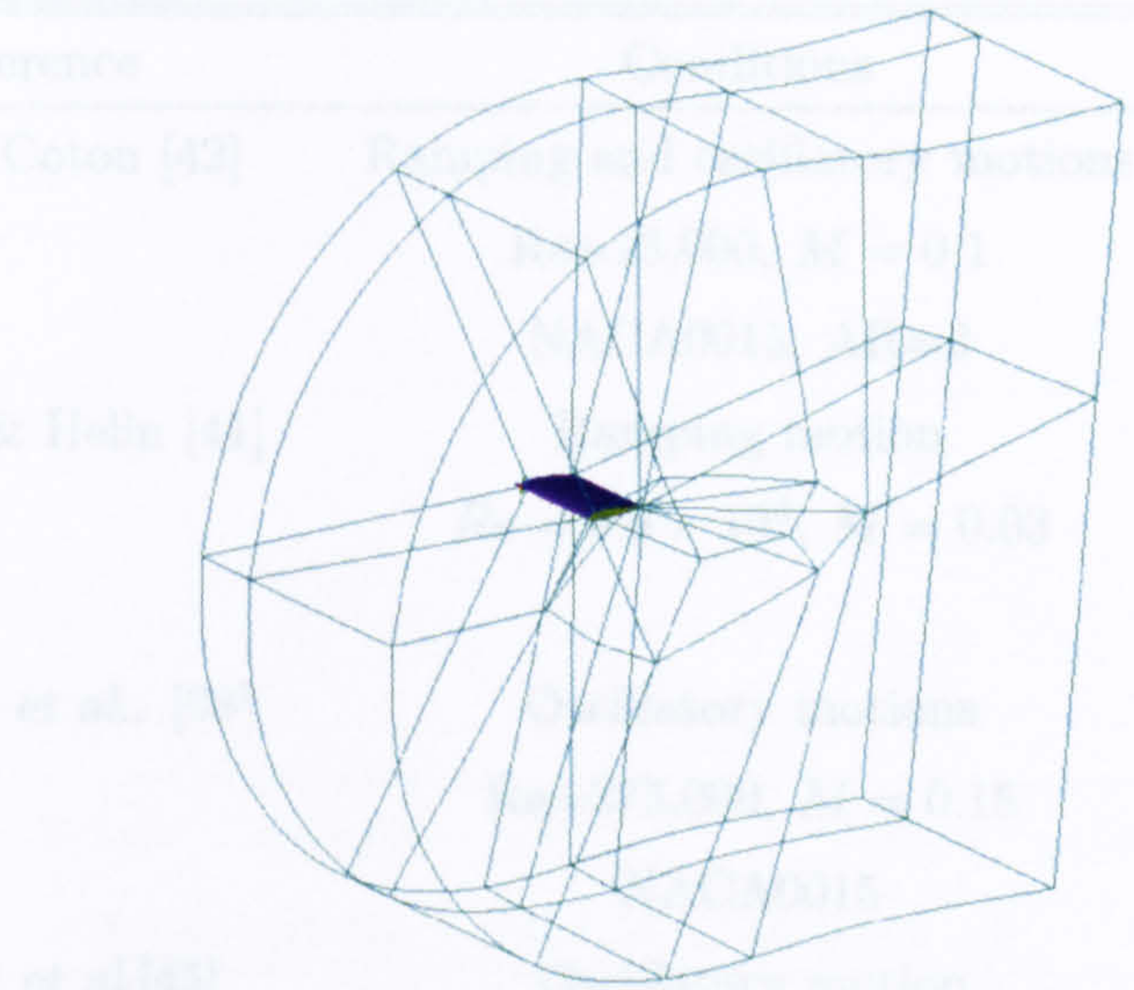

(a)

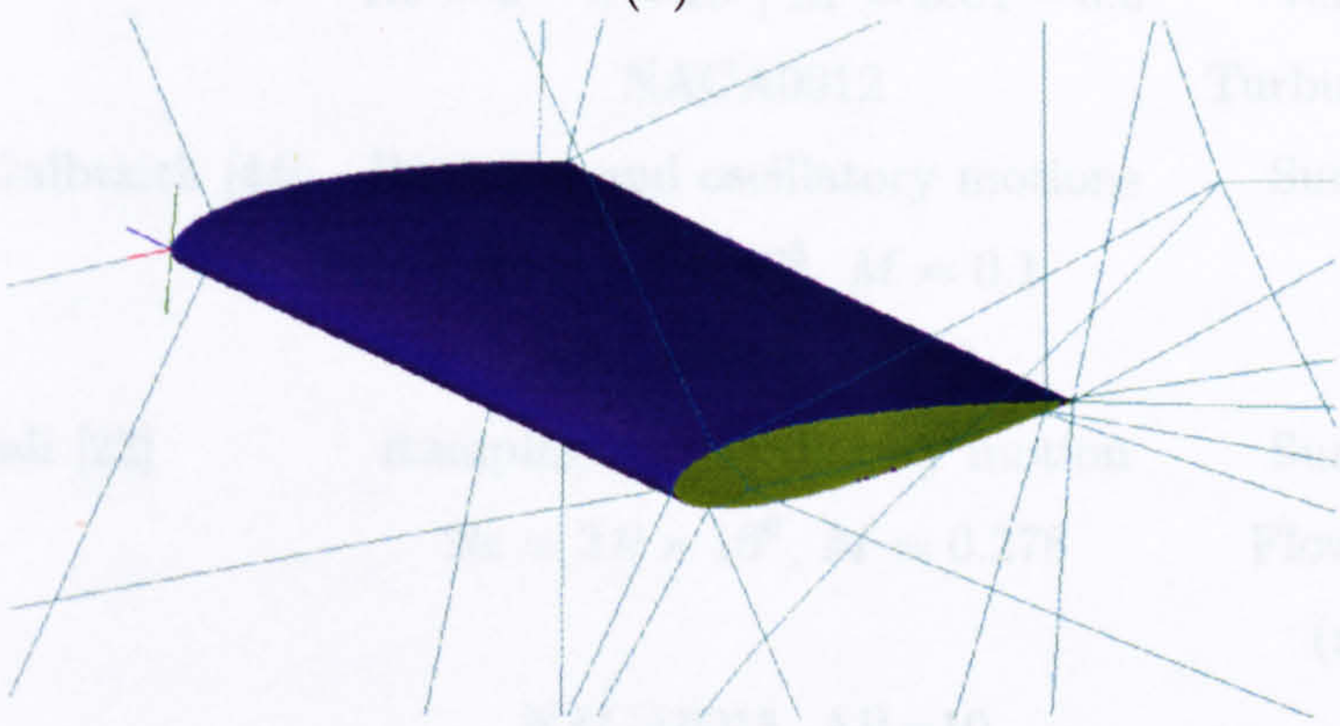

(b)

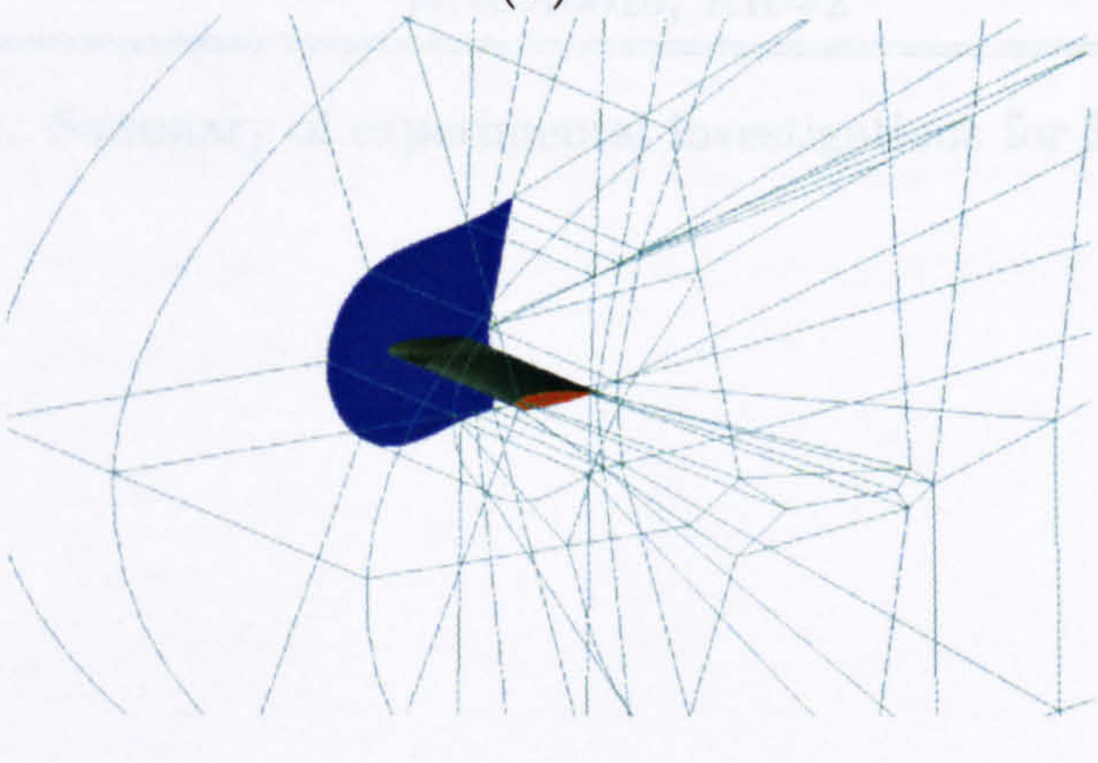

(c)

Figure 4.2: Blocking topology corresponding to grid (c) of Figure 4.1. (a) full grid, (b) details close to the wing and (c) the blocking used to model the viscous plate on the wing's root.

4.2 Tables

Case	Reference	Conditions	Measurements
1	Moir & Coton [42]	Ramping and oscillatory motions	Smoke visualisation
		Re=13,000, $M = 0.1$	
		NACA0015, AR=3	
2	Schreck & Helin [41]	Ramping motion	Surface pressure
		$Re = 6.9 \times 10^4$, $M = 0.03$	Flow visualisation
			(dye injection)
3	Wernert *et al.*. [38]	Oscillatory motions	PIV
		Re=373,000, $M = 0.15$	
		NACA0015	
4	Berton *et al.*[45]	Oscillatory motion	Boundary layers
		$Re = 3 - 6 \times 10^6$, $M = 0.01 - 0.3$	Velocity profiles
		NACA0012	Turbulence quantities
5	Coton & Galbraith [44]	Ramping and oscillatory motions	Surface pressure
		$Re = 1.5 \times 10^6$, $M = 0.1$	
		NACA0015, AR=3	
6	Piziali [22]	Ramping and oscillatory motion	Surface pressure
		$Re = 2.0 \times 10^6$, $M = 0.278$	Flow visualisation
			(micro-tufts)
		NACA0015, AR=10	
		NACA0015, AR=2	

Table 4.1: Summary of experimental investigations for 3-D DS.

Case	Blocks	Points on wing	Points on tip	Size (nodes)	Wall distance (c)	CPU time (hrs)	Number of CPUs
1	40	6,750	1,800	2,268,000	10^{-5}	305	12
2a	13	6,222	820	420,000	10^{-4}	255	1
2b	20	7,100	900	729,000	10^{-4}	31.1	8
2c	44	8,400	900	1,728,000	10^{-4}	111.1	8
2d	64	18,900	4,500	2,727,000	10^{-5}	100	24
3a	6	240	n/a	62,400	10^{-5}	17.5	1
3b	6	360	n/a	108,000	10^{-5}	38.9	5
4	36	7,800	7,200	1,828,000	10^{-5}	319	8
5	20	3,375	1,800	1,134,000	10^{-5}	63	9
6	28	7,800	7,200	2,632,000	10^{-5}	320	16

Table 4.2: Details of the employed CFD grids and time required for the calculations. For all cases the far-field boundary of the computational domain was located at 8-10 chord lengths away from the wing surface. All calculations were performed on a Linux Beowulf cluster with 2.5GHz Pentium-4 nodes.

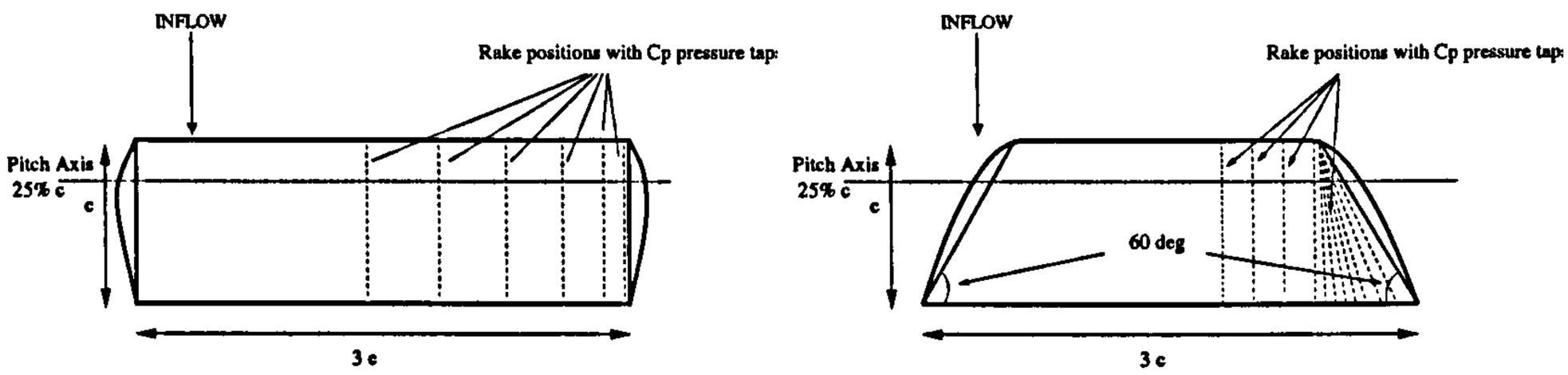

(a) Moir and Coton [42] and Coton and Galbraith [44] (left), and Coton and Galbraith [44] swept wing (right). Both utilise a NACA 0015 section.

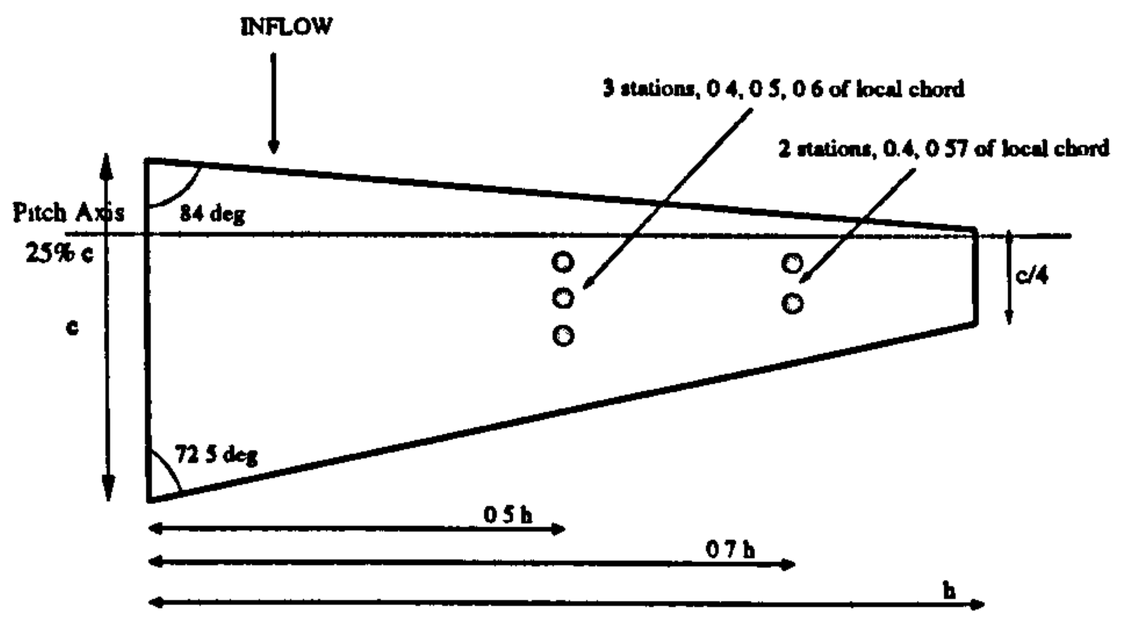

(b) Berton *et al.*[45] (NACA 0012 wing section)

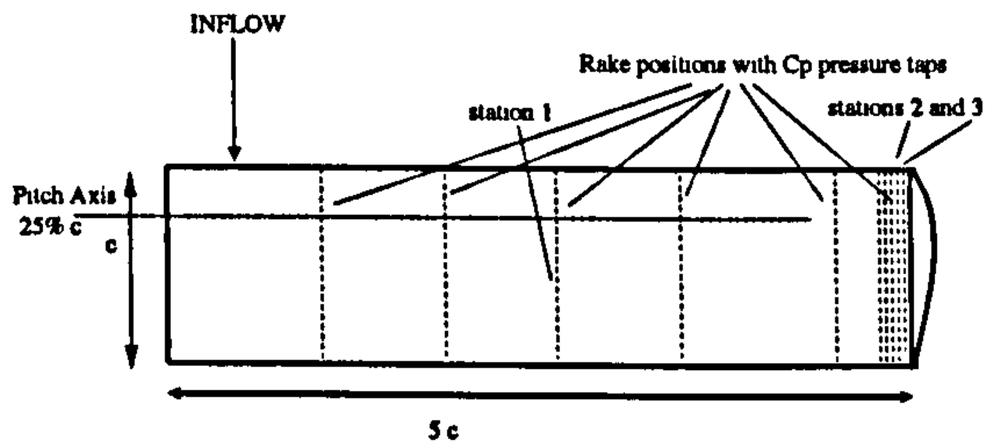

(c) Piziali [22] (NACA 0015 wing section)

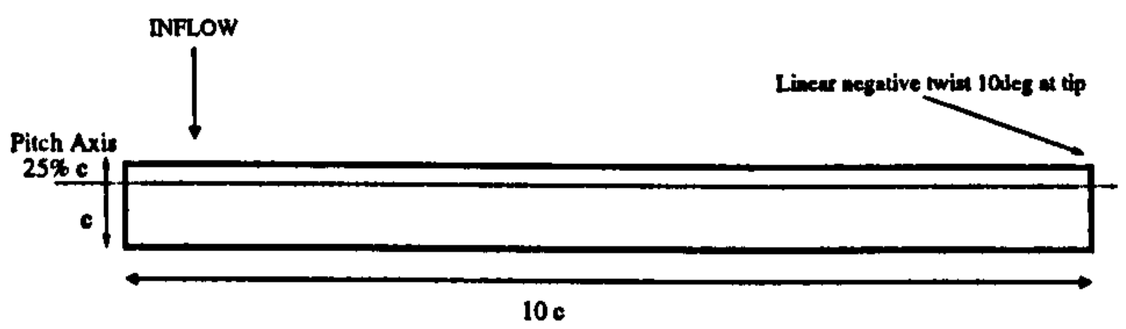

(d) High aspect ratio wing (NACA 0015 wing section)

Figure 4.3: Wing planforms employed for calculations. (a) Cases 3 and 4 of Table 4.1 by Moir and Coton [42] and Coton and Galbraith [44]. (b) Case 5 of Table 4.1 by Berton *et al.*[45]. (c) High aspect ratio wing with linear twist of -10°.

4.3 The low *Re* regime validation cases

The appeal of the experiments performed at low *Re* is that turbulence modelling issues are secondary. Furthermore, grid sizes can be smaller leading to cheaper computations. In addition, the employed ramping rates were high so that the flow is mainly driven by the forced motion of the body. At slower ramping rates, it is expected that the influence of turbulence, transition and viscous effects will be stronger. The required CPU time for calculating the 2D and 3D flow cases is reported in Table 4.2. All calculations were performed on a Beowulf cluster with 2.5 GHz Pentium-4 nodes. In this section CFD simulations are compared against two experimental data sets:

(A) The flow visualisation experiments of Moir and Coton [42]

(B) The surface pressure experiments of Schreck and Hellin [41]

4.3.1 The experiments of Schreck

The first set of calculations in the low *Re* regime simulated the experiment of Schreck *et al.* [41]. S. Schreck from NREL kindly provided the data used here. As for the flow visualisation experiments of Moir and Coton [42] described in the following paragraph, Schreck's experiment was conducted at low Reynolds numbers so turbulence modelling issues were secondary. For this work both laminar and turbulent flow calculations have been performed. It has to be noted that the flow conditions of Newsome's study [58] are close but not the same as the ones used here. This is due to the fact Newsome's calculations were compared against water-tunnel visualisation and pressure data from Schreck [88] at lower Reynolds number, while the current set of experimental data comes from wind-tunnel experiments [41]. In contrast to the previous laminar flow study by Newsome [58] where rounded tips were used instead of sharp ones, the present work preserves the real geometry of the wing using multi-block grids as explained in the previous sections. This was found to be necessary since there is a strong interaction between the tip and the DS vortices. Three CFD grids were constructed, the coarse grid has 0.7 million cells, the medium 1.7 million cells and the fine 2.7 million cells. The medium grid was found to be adequate following comparisons of the integral loads of the wing between the three grids and was employed for the rest of the calculations. Even results on the coarse grid were found to be close to those obtained on finer meshes for incidence angles

below stall.

A time-step sensitivity study was subsequently conducted by halving the original time-step. The results of the two calculations were practically the same and therefore the original time-step was considered as adequate. This dimensionless time-step of 0.058 corresponds to a real time-step of 10^{-3} seconds and results in four unsteady flow solutions per degree of incidence.

Comparisons against measurements are presented in Figure 4.4 where Cp contours on the upper surface of the wing are plotted. Measurements are only available on part of the wing area [41], bounded by a dashed box on the CFD plots. Three sets of calculations are shown including laminar flow results with the inboard boundary plane of the computational domain assigned a viscous wall boundary condition, turbulent flow results with symmetry plane condition and turbulent flow results with viscous wall condition. The same number of contours and at the same levels were drawn for experiments and CFD. The concentration of the contour lines near the mid-chord corresponds to the location of the DSV. One can clearly see that at 30 degrees of incidence the simulation results with viscous wall condition are in much better agreement with the experiments. It is difficult to decide which of the laminar and turbulent flow results are in better agreement with experiments, however, towards the tip region of the wing the simulation with the turbulence model provides a better comparison predicting more accurately the location of the DSV. Overall, the shape and level of the contours corresponds to the measured data with the agreement getting better at higher incidence angles. The reason for any minor discrepancies towards the mid-span of the wing lies in the fact that the experiment used a splitter plate on the wing root with surface qualities that do not exactly match the idealisations made by either symmetry or viscous boundary conditions. The size of the plate is comparable with the DSV size (the splitter plate diameter was equal to two chord lengths) and thus the effectiveness of the plate may not be good especially at high incidence angles. Due to the size of the splitter plate, results with viscous wall condition at mid-span are closer to the experiments for low incidence, however, symmetry plane results tend to be better at higher angles. This is because the DSV moves away from the surface of the wing and expands beyond the splitter plate.

Further calculations were performed for different ramp rates and the pivot point of the wing was also changed from $x/c = 0.33$ to $x/c = 0.25$. The comparison between the CFD results and measurements for the surface pressure on the wing is

shown in Figure 4.5. One can see that at the higher ramp rate the comparison is better since the character of the flow is more impulsive and driven predominantly by the motion of the wing. It appears however, that the suction corresponding to the DSV extends up to the wing tip where it is joined with the low pressure region dominated by the tip vortex. This can be seen in Figure 4.5(b) in the area outside the dashed box which marks the region where pressure measurements were made. To further assist a quantitative comparison between measurements and CFD results, the Cp distribution at two spanwise stations (z/c=1.0 and 1.6) and for two incidence angles (30 and 40 degrees) were extracted and the comparisons are presented in Figure 4.6. The footprint of the DSV can be seen in all stations while the evolution of dynamic stall appears to be slightly faster in the experiment than the CFD especially near the leading edge region.

The ability to predict the integral loads on the wing during the unsteady maneuver is paramount for design. CFD results for the C_L, C_D and C_M coefficients are presented in Figure 4.7. For the sake of comparison, 2D calculations have also been performed at the same conditions. As can be seen, results at a higher ramp rate indicate a more impulsive behaviour and delayed stall in the 2D case. Overall, the 3D calculations reveal a smoother variation of the integral loads with a more gradual stall in comparison to the 2D results. Apart from potential flow and dynamic stall effects, this is a direct result of the interaction between the tip and the DS vortices. As the incidence increases, the strength of the tip vortex also increases but the effect of the vortex is reduced as it approaches the tip and bends towards the leading edge of the wing. This has a strong effect especially for the moment and drag coefficients and highlights the problem engineers have to face when scaling 2D measurements for use in 3D aerodynamic models.

4.3. THE LOW *RE* REGIME VALIDATION CASES

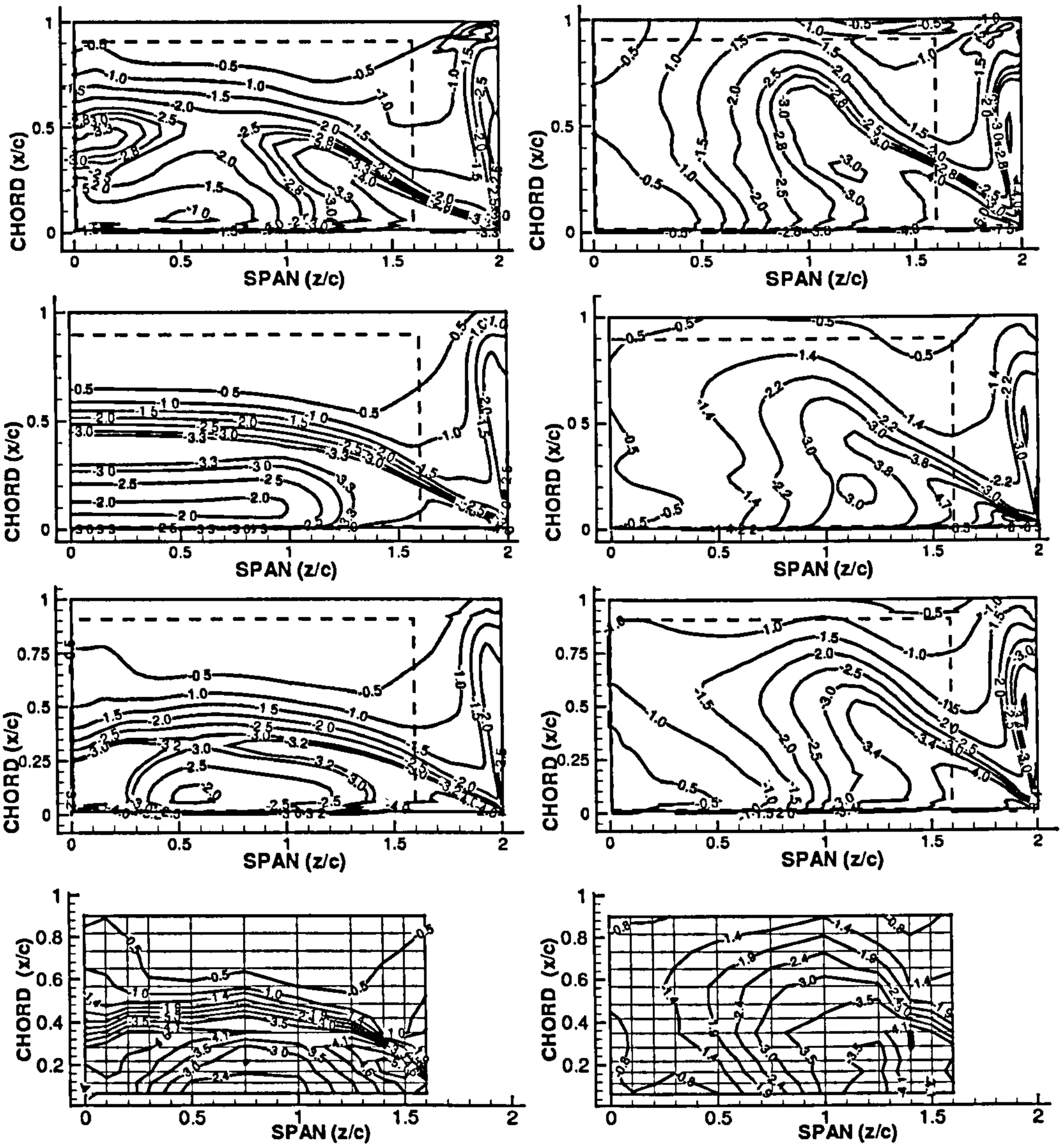

(a) 30.0 deg (b) 40.9 deg

Figure 4.4: Comparison between experiments by Schreck and Helin [41] and CFD results for the surface coefficient distribution on the suction side of the square NACA-0015 wing. Flow conditions are: $a^+ = 0.1$, $Re = 6.9 \times 10^4$, $M = 0.2$, $x/c_{rot} = 0.33$, ramping motion between 0 and 60 degrees of incidence. From top to bottom: CFD with splitter plate as a viscous wall and laminar conditions, CFD with splitter plate as symmetry plane (sp), CFD with splitter plate as viscous wall (vw) and experimental values.

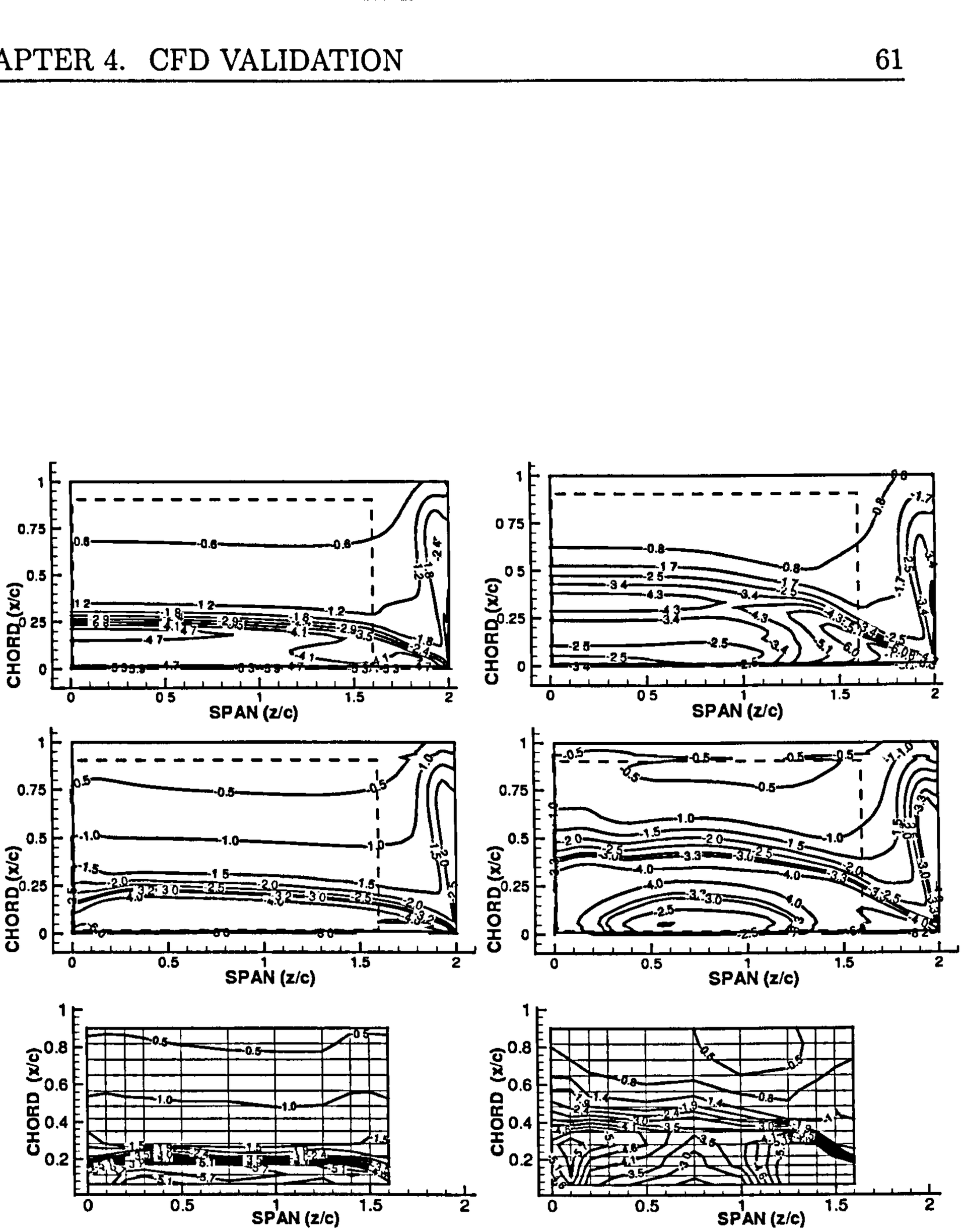

(a) 29.5 deg (b) 40.3 deg

Figure 4.5: Comparison between experiments by Schreck and Helin [41] and CFD results for the surface coefficient distribution on the suction side of the square NACA-0015 wing. From top to bottom: CFD with splitter plate as symmetry plane (sp), CFD with splitter plate as viscous wall (vw) and experimental values ($a^+ = 0.2$, $Re = 6.9 \times 10^4$, $M = 0.2$, $x/c_{rot} = 0.25$, ramping motion between 0 and 60 degrees of incidence).

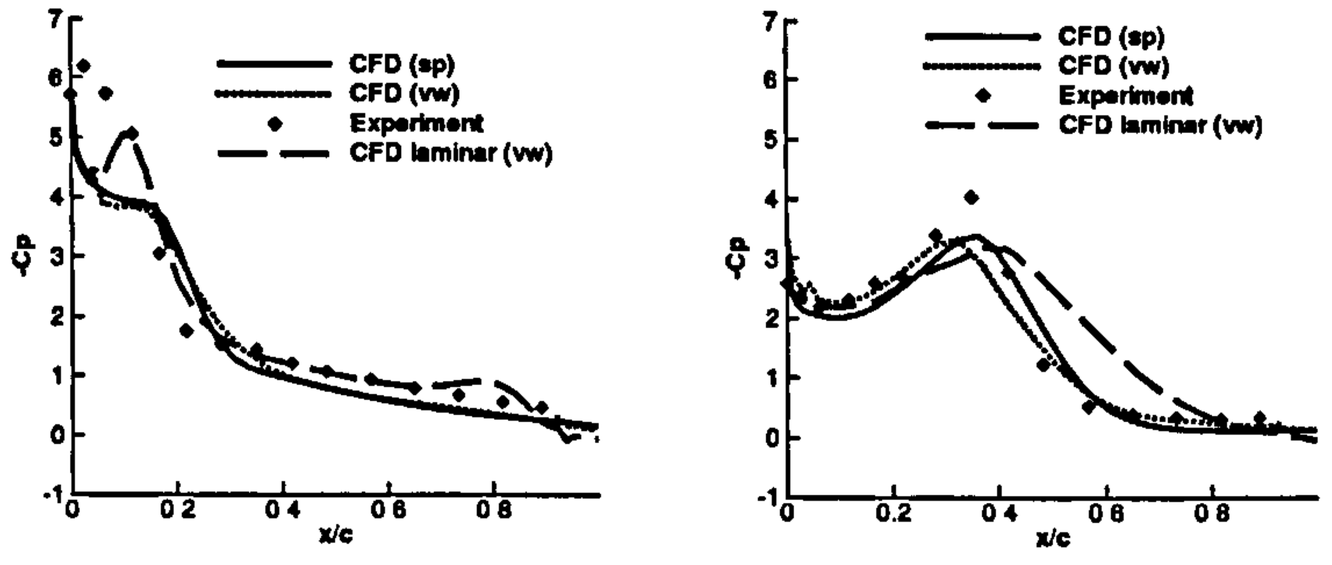

$z/c = 1.0,\ a^+ = 0.1$

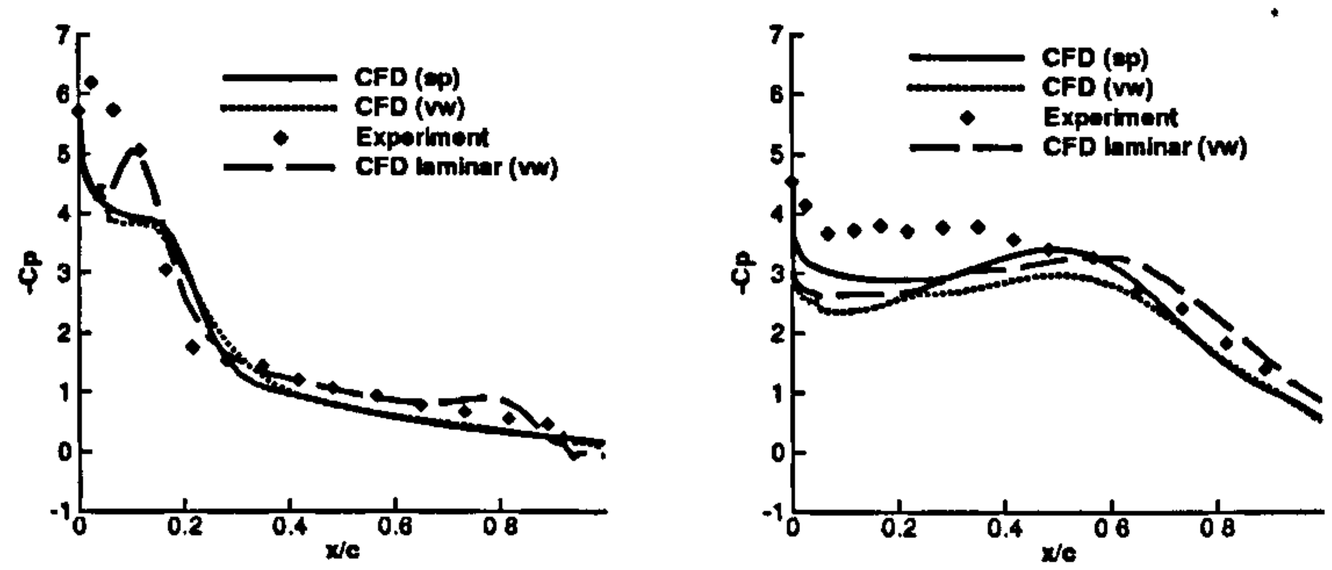

$z/c = 1.6,\ a^+ = 0.1$

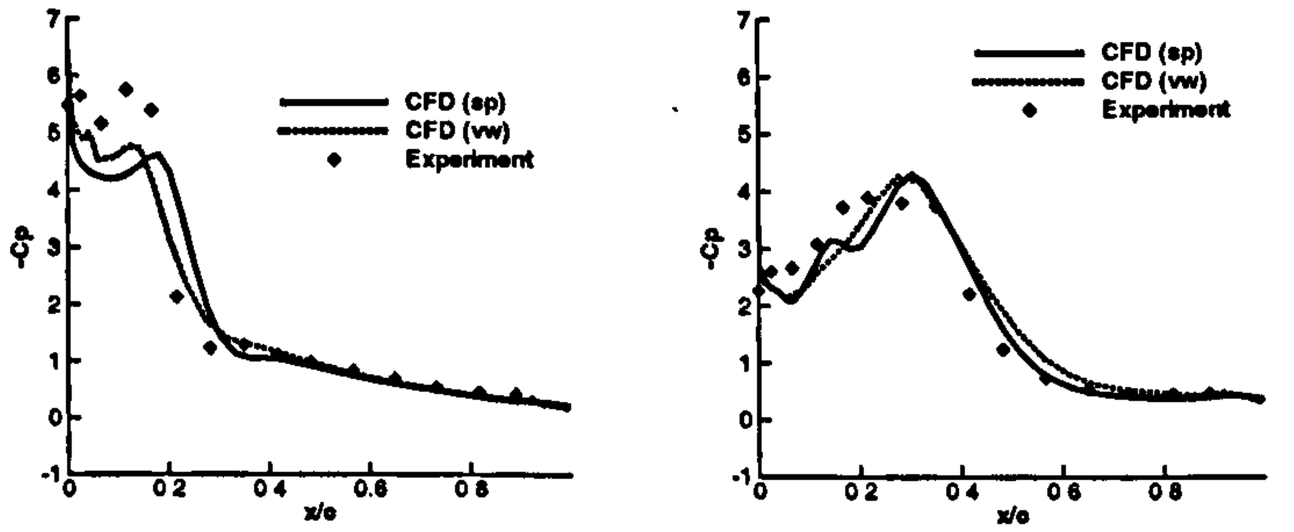

$z/c = 1.0,\ a^+ = 0.2$

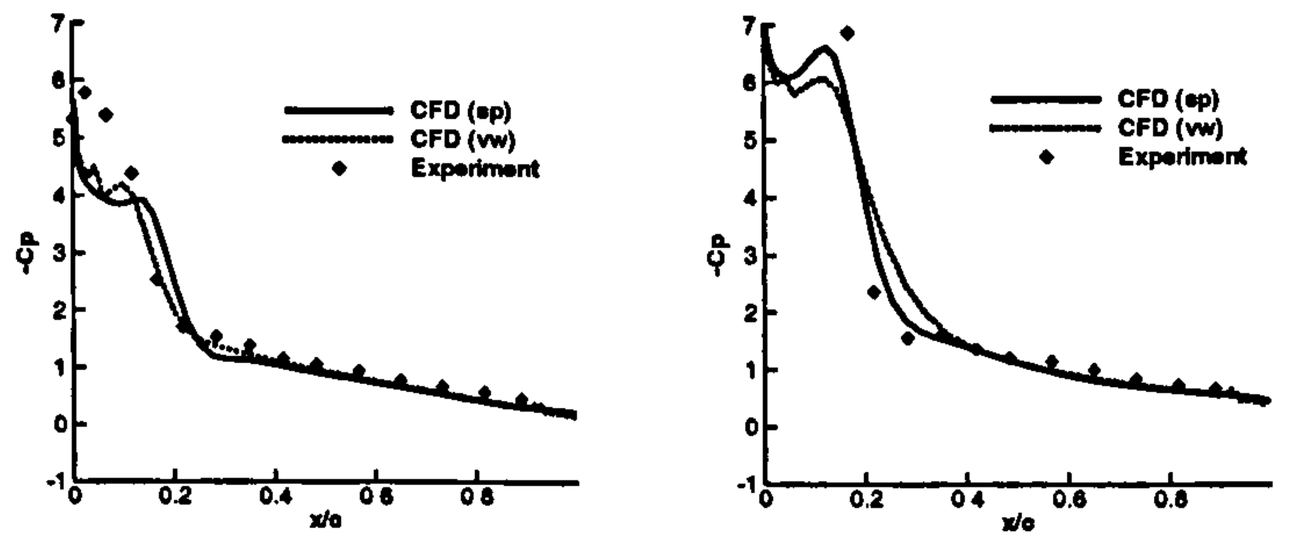

$z/c = 1.6,\ a^+ = 0.2$

Figure 4.6: Comparison between experiments and simulation for the surface pressure coefficient distribution at incidence angles of 30° (left) and 40° (right). Both cases with a splitter plate as a symmetry plane (sp) and splitter plate as a viscous wall (vw) are shown. ($Re = 6.9 \times 10^4$, $M = 0.2$, $x/c_{rot} = 0.25$, ramping motion between 0 and 60 degrees of incidence).

4.3. THE LOW *RE* REGIME VALIDATION CASES

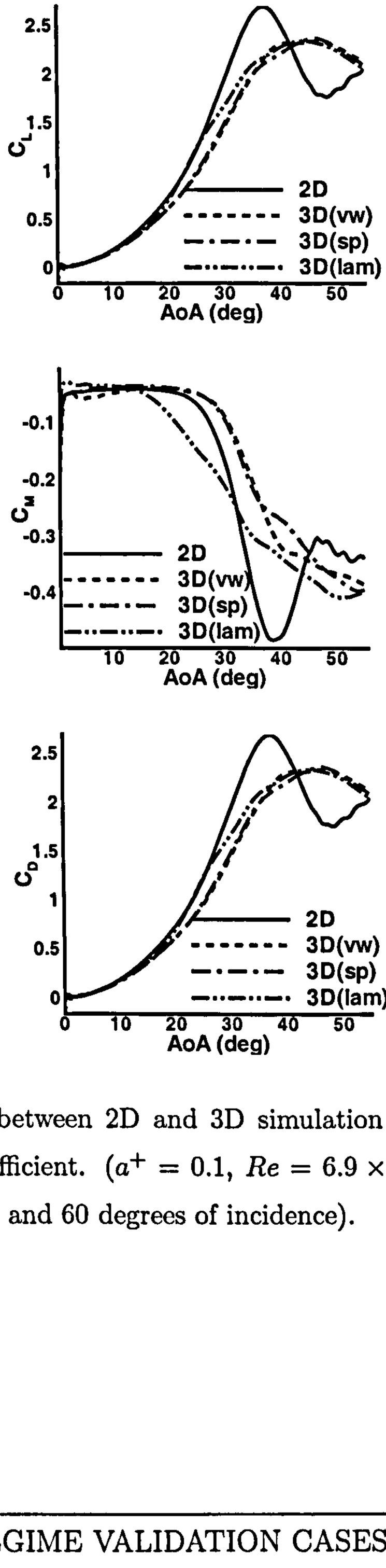

Figure 4.7: Comparison between 2D and 3D simulation results for the lift, drag and quarter-chord moment coefficient. ($a^+ = 0.1$, $Re = 6.9 \times 10^4$, $M = 0.2$, $x/c_{rot} = 0.25$, ramping motion between 0 and 60 degrees of incidence).

4.3. THE LOW *RE* REGIME VALIDATION CASES

4.3.2 The flow visualisation experiments by Moir and Coton

The next step in the validation process is the qualitative comparison between CFD and the flow visualisation experiments by Moir and Coton [42] at the smoke tunnel of the University of Glasgow. Moir and Coton [42], provided detailed account of the initiation and evolution of the DS vortex at laminar flow conditions ($Re = 13,000$). The employed wing was of rectangular planform with rounded tips and an aspect ratio of 3. Prof F. Coton from University of Glasgow kindly provided the extensive video footage from these experiments. A schematic showing the wing used in these experiments can be seen in Figure 4.3a. The wing had a NACA 0015 section, constant along the span. CFD calculations have been performed for a ramping case, at a reduced ramping rate of $\alpha^+ = 0.16$ which corresponds to the test conditions used by Moir and Coton [42]. The low Reynolds number of this experiment was beneficial since smoke visualisation can be made clearer at lower wind speeds and from the point of view of CFD no turbulence modelling was necessary. A set of still images has been extracted from the video tapes recorded during the experiments and were consequently used for comparisons with the CFD simulation. Figure 4.8 presents the comparison between experiments and simulation at incidence angles where, the most important features of the 3-D DS are shown. Figure 4.8a, shows the plan view of the wing at an incidence angle of 30°. At this stage, the DSV is well formed and its inboard portion is located at approximately 1/3 of chord from the leading edge, running parallel to the pitch axis of the wing. The portion however, of the DSV close to the tips, is deflected towards the leading edge, and appears to interact with the tip vortices. Further aft, one can also see the trailing edge vortex, whose ends tend to merge with the DSV and the tip vortices. At this stage, the trailing edge vortex is of comparable size with the DSV. Figure 4.8b, shows the same time instance from a different viewing angle, in order to show the merging of the DSV with the tip vortices, as well as the backwards tilted arch-like shape of the DSV resembling that of an inclined Ω. One can see that the streamlines closer to the surface of the wing have the same pattern as the smoke streaks of the visualisation. This points to the fact that that the DSV impinges on the surface of the wing at a distance of a chord length inboards from the tips in the spanwise direction, and at half a chord's length in the chordwise direction. The trailing edge vortex can no longer be seen, pushed by a continuously growing in size DSV, which is constantly fed with momentum by the free stream and the wing motion.

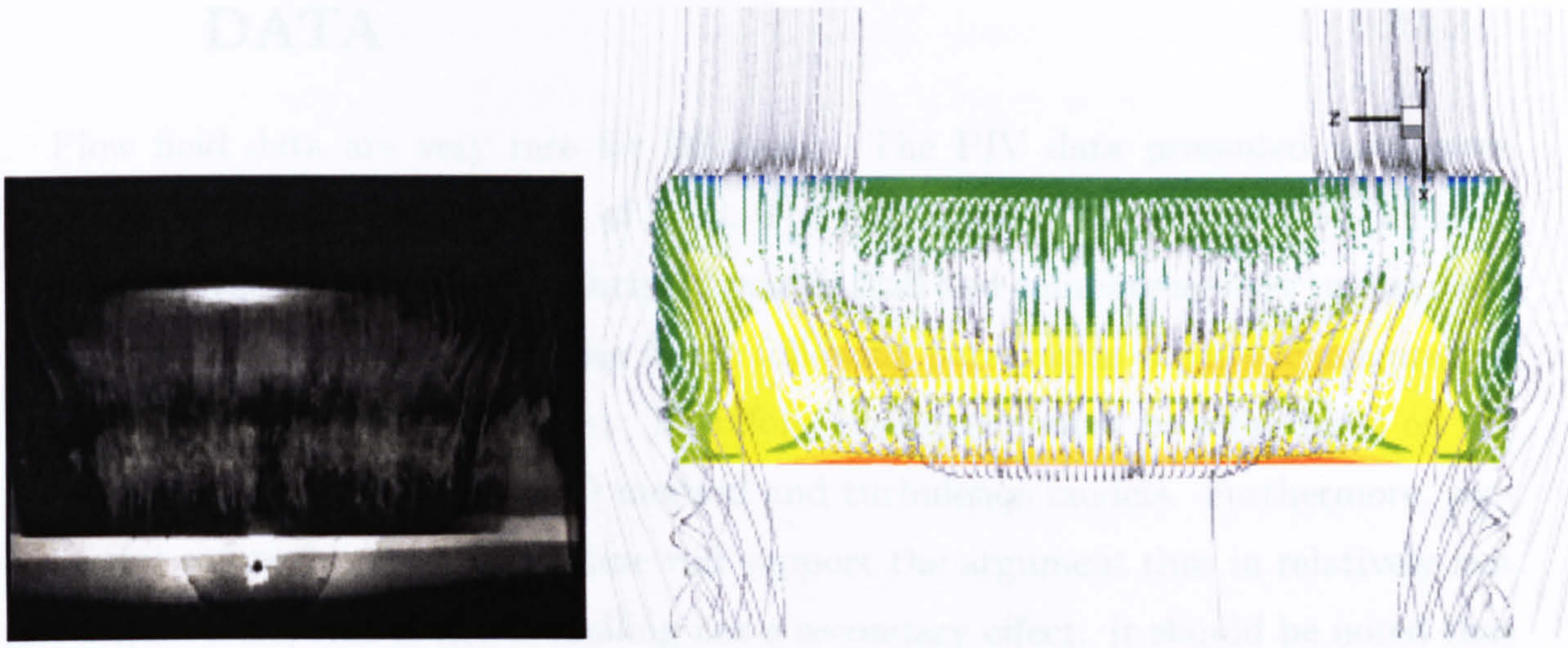

(a)

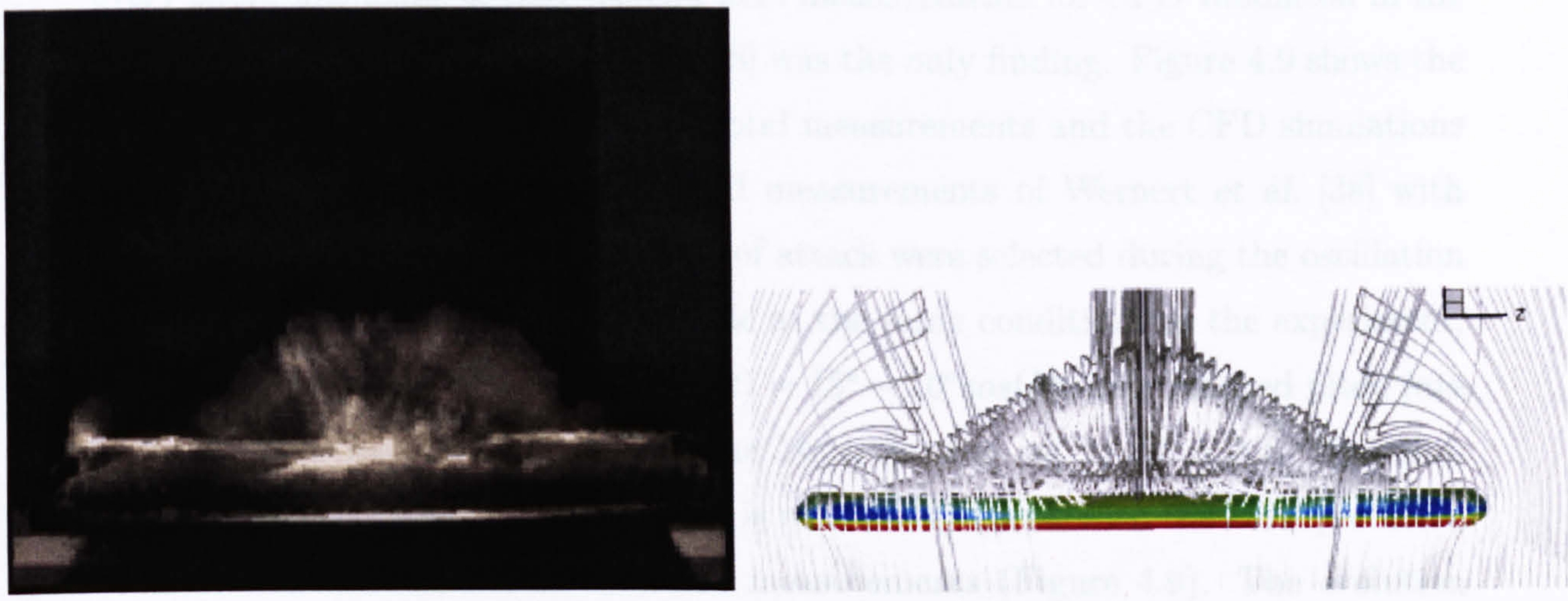

(b)

Figure 4.8: Smoke visualisation by Moir and Coton [42] (left) and CFD predictions (right) for the short aspect ratio wing of case 3 of Table 4.1. Ramping motion between 0^o and 40^o, Re=13,000, M=0.1, α^+=0.16. (a) Plan view and (b) view from the leading edge of the DS vortex and the trailing edge vortices at an incidence angle of 30^o.

4.4 Prediction of the Flow Field around an Oscillating Aerofoil: Comparison Against PIV DATA

Flow field data are very rare for DS cases. The PIV data presented here, were kindly provided by P. Wernert of DLR. The next stage of the validation work is to compute the 2D velocity field during dynamic stall and compare against tunnel measurements. This is essential since in the following paragraphs the flow configuration during 3D DS is to be analysed. Therefore, confidence must be established on the accuracy of the employed CFD method and turbulence models. Furthermore, successful comparisons in this regime will support the argument that in relatively fast wing motions, turbulence modelling has a secondary effect. It should be noted that 2D simulations tend to be more sensitive to the influence of turbulent structures since there is no mechanism to aid dissipation in the third dimension. Although every effort was made to find velocity field measurements for CFD validation in the literature, the case by Wernert *et al.* [38] was the only finding. Figure 4.9 shows the streamlines generated by the experimental measurements and the CFD simulations and Figure 4.10 compares the flowfield measurements of Wernert *et al.* [38] with the present CFD results. Three angles of attack were selected during the oscillation cycle. The CFD calculations were made at the same conditions as the experiment, with a sinusoidal pitch of the form: $\alpha(t) = 15° - 10°cos(kt)$ at a reduced pitch rate of $k = 0.15$, a Re of 3.73×10^5 and the Mach number set to $M = 0.1$. The comparison between CFD and experiments is remarkably good, with the DSV predicted at almost the same position as in the measurements (Figure 4.9). The evolution of DS is similar to that described by previous authors [57]. A trailing edge vortex appears at high incidence angles and below the DSV a system of two secondary vortices is formed. Despite the lack of measurements of the surface pressure, the PIV study of Wernert *et al.* [38] provides the rare opportunity for comparing the computed velocity field against quantitative measurements. In this work, velocity profiles were extracted at three chordwise stations corresponding to $x/c = 0.25$, 0.5 and 0.75. With the exception of the work reported by Barakos and Drikakis in [46] this is the only other comparison of velocity profiles during DS appearing in the literature. As shown in Figure 4.10 the comparison between experiments and CFD is remarkably good at the lowest incidence angle (Figure 4.10a) and remains favourable

even at higher incidence angle (Figure 4.10c). The experimentalists [38], have reported that at the angles of 23° and 24° the flowfield was no longer reproducible during the experiments, which explains the discrepancies observed. The agreement is better closer to the wall while a constant shift appears towards the outter part of the boundary layer. The shape of the profile is however well predicted. Further comparisons of the turbulent flow quantities in this unsteady flow are not possible due to the lack of near-wall resolution of the PIV measurements. As can be seen in Figure 4.10b, the effect of the spatial and temporal results is strong. Three plots are shown corresponding to the coarse grid with coarse time (cc), fine grid with fine time (ff) and fine grid with coarse time (fc). The details of the grids are given in Table 4.2. Grids 3a and 3b where used for the prescribed cases and the final results where obtained on grid 3b. The coarse time discretisation corresponds to 80 time steps per cycle whereas the fine time discretisation corresponds to 200 time steps per cycle. The resolution even of the coarse time step corresponds to 3 unsteady calculations per degree of incidence.

4.4. PREDICTION OF THE FLOW FIELD AROUND AN OSCILLATING AEROFOIL: COMPARISON AGAINST PIV DATA

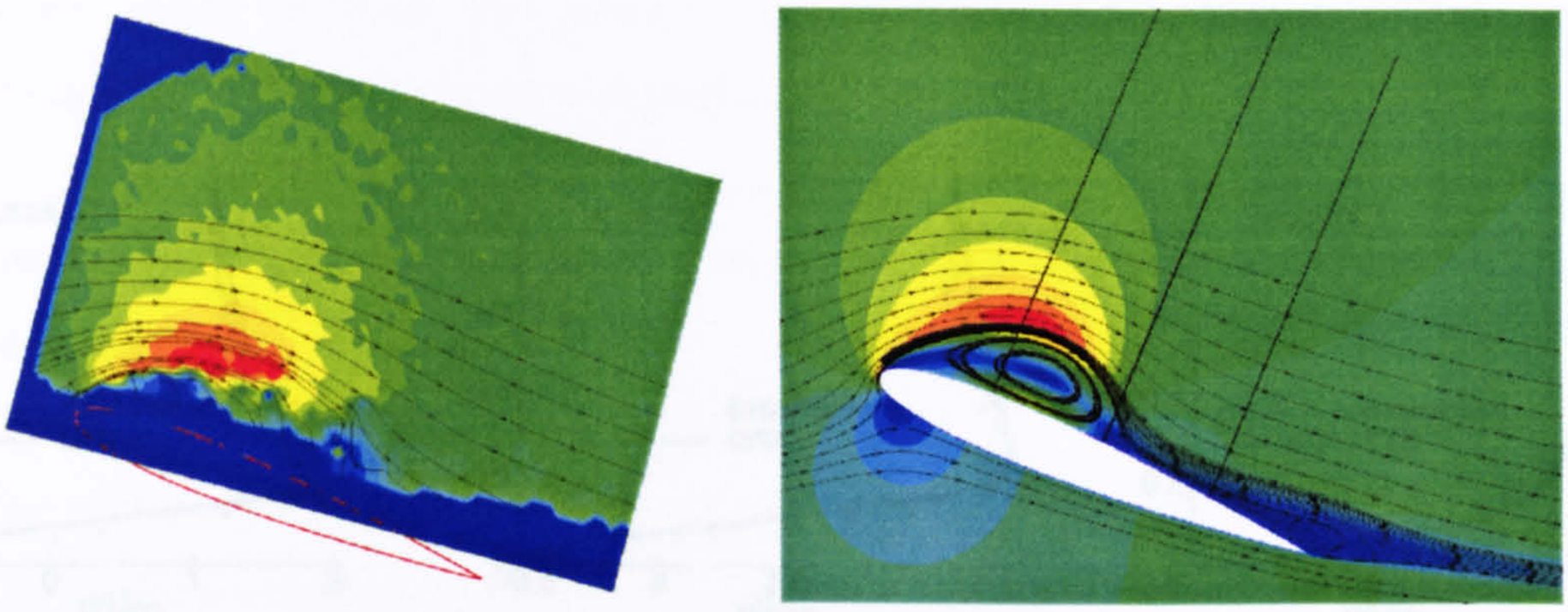

(a) AoA=22 deg upstroke

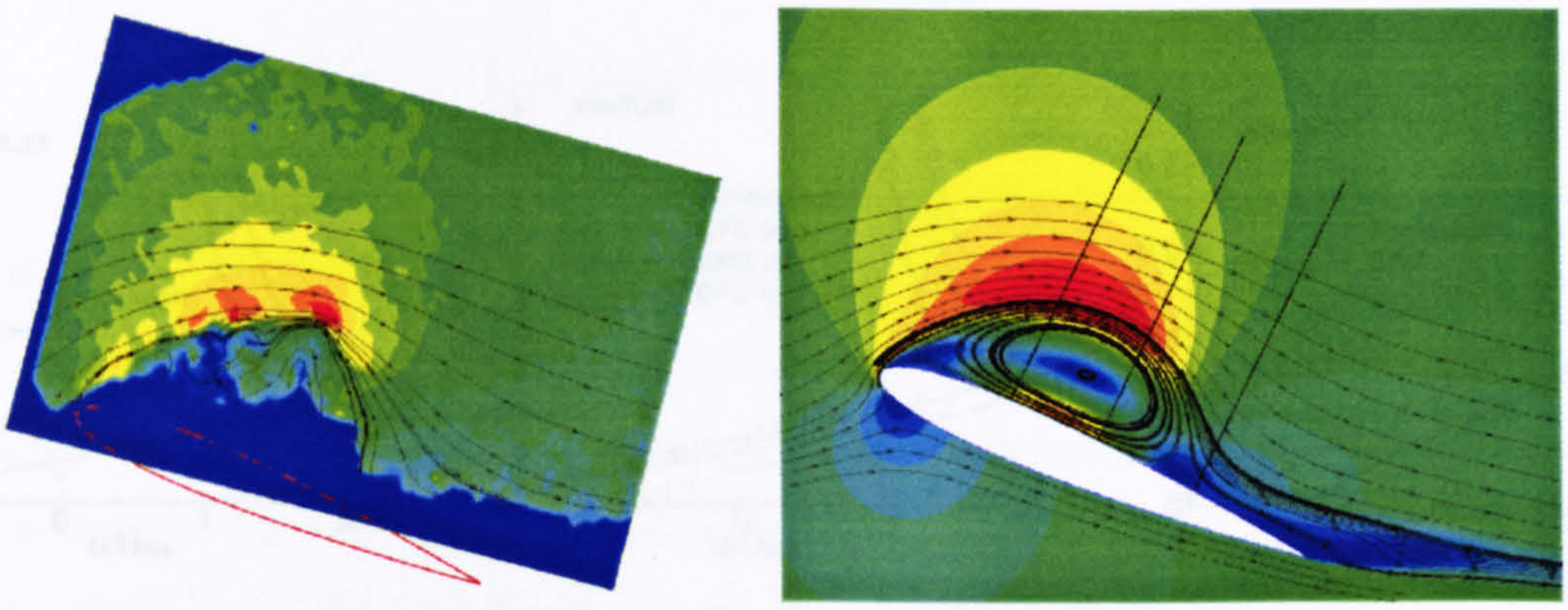

(b) AoA=23 deg upstroke

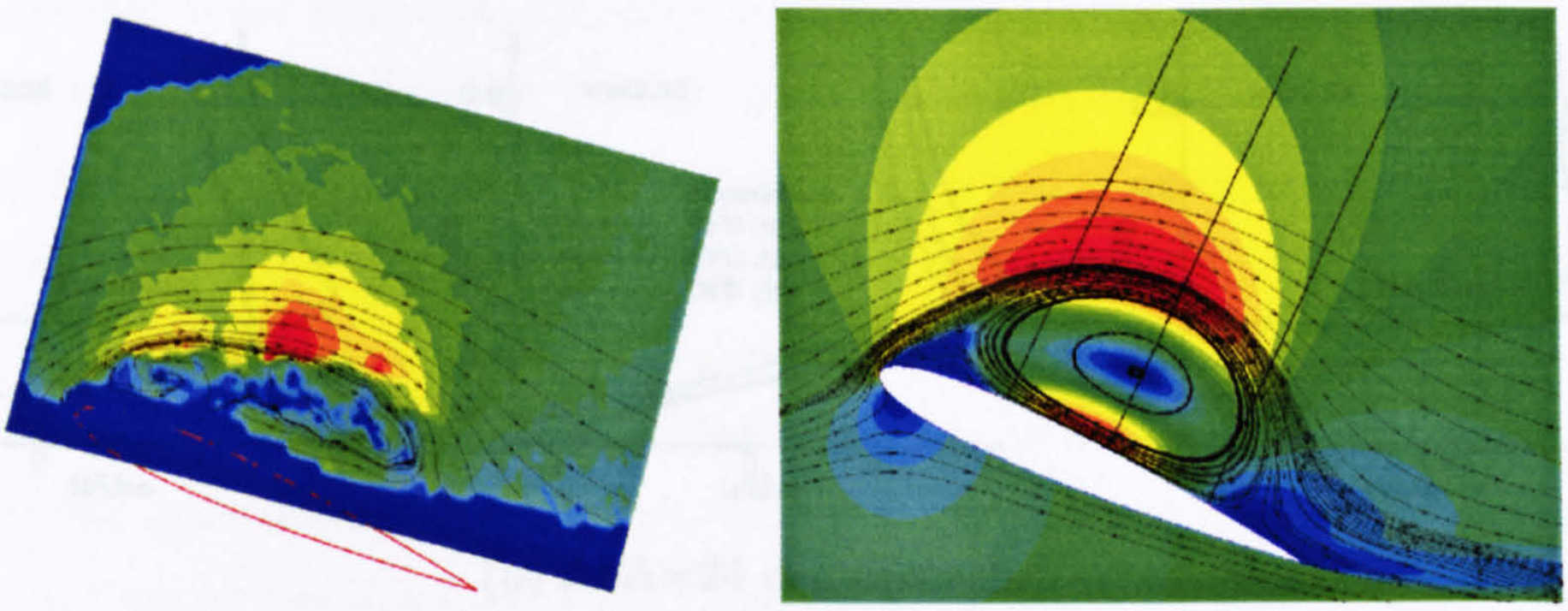

(c) AoA=24 deg upstroke

Figure 4.9: Comparison between experiments (left) by Wernert *et al.*[38] and CFD (right): The streamlines have been superimposed on colour maps of velocity magnitude. The experimental values are based on PIV data. ($\alpha(t) = 15° - 10°cos(kt)$, $k = 0.15$, $Re = 3.73 \times 10^5$, $M = 0.1$, $x/c_{rot} = 0.25$).

4.4. PREDICTION OF THE FLOW FIELD AROUND AN OSCILLATING AEROFOIL: COMPARISON AGAINST PIV DATA

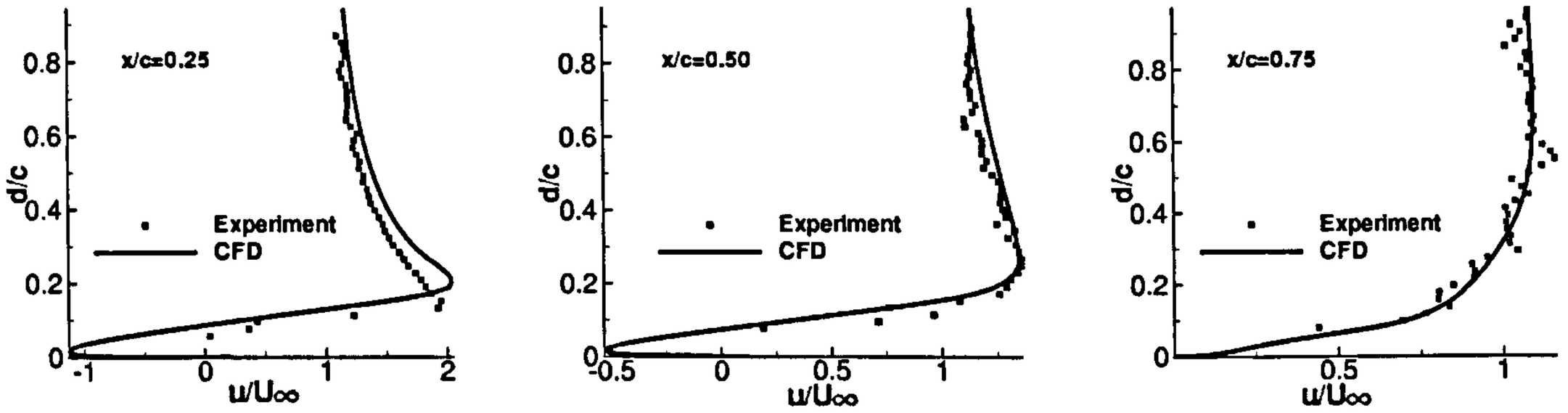

(a) AoA=22 deg upstroke

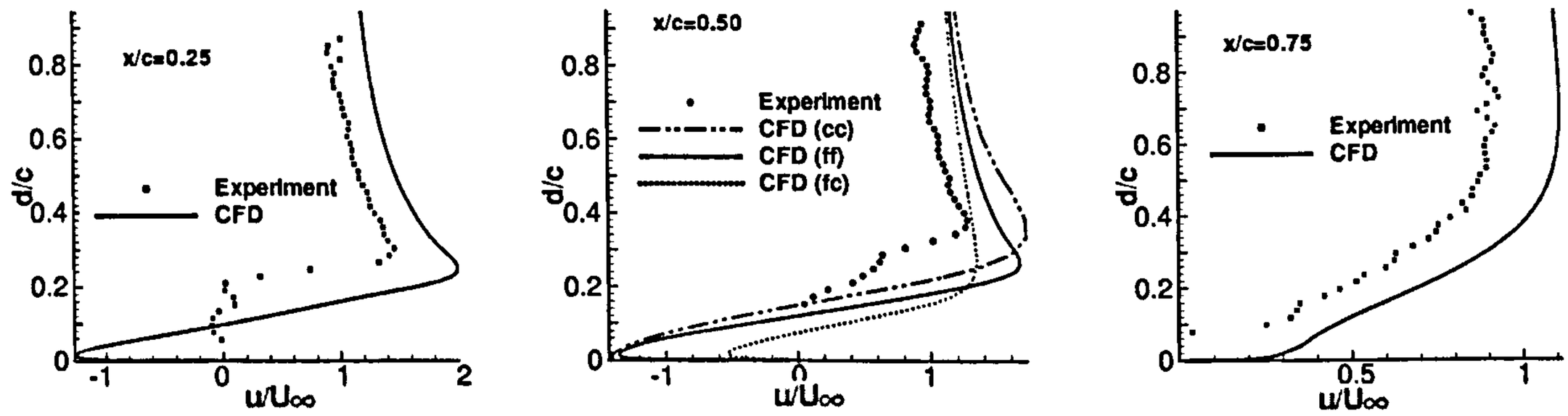

(a) AoA=23 deg upstroke

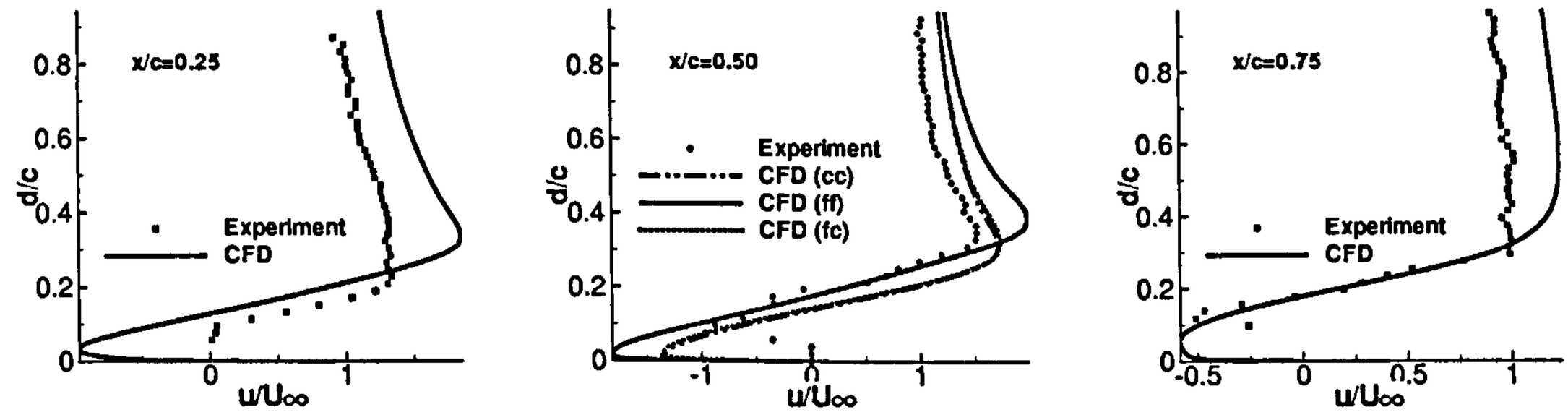

(b) AoA=24 deg upstroke

Figure 4.10: Comparison between CFD and experiments by Wernert *et al.*[38]: The experimental values are based on PIV data. ($\alpha(t) = 15° - 10°cos(kt)$, $k = 0.15$, $Re = 3.73 \times 10^5$, $M = 0.1$, $x/c_{rot} = 0.25$). (cc)-coarse grid coarse time, (ff)-fine grid fine time and (fc)-fine grid coarse time.

4.4. PREDICTION OF THE FLOW FIELD AROUND AN OSCILLATING AEROFOIL: COMPARISON AGAINST PIV DATA

4.5 High *Re* regime validation cases

In realistic rotor motions, the effective *Re* is of the order of few millions. The remaining validation cases involve experiments performed n the *Re* range of $10^6 - 2\times 10^6$

This section contains the comparisons between CFD simulations and the experiments by:

(A) The ELDV measurements by Berton *et al.*[45].

(B) The surface pressure measurements of Coton and Galbraith [44].

(C) The surface pressure measurements of Piziali [22].

4.5.1 The ELDV measurements by Berton *et al.*

The DS of an oscillating, tapered, low aspect ratio wing has been studied by Berton *et al.*[45, 46]. This is a very interesting case for two reasons: i) velocity data have been obtained at various phase angles during the oscillation and at several spanwise and chordwise locations and ii) the wing planform represents an idealisation of an active control surface similar to the ones encountered in modern super-maneuverable aircraft. Prof. D Favier and Dr A. Berton from LABM kindly provided us with the experimental data presented here. The experiments [45] were conducted in the S1L high subsonic wind tunnel of the Aerodynamics Laboratory of Marseilles using a novel Embedded Laser Doppler Velocimetry (ELDV) technique. According to this method the laser probe is mounted on the same circular rotating disc which also supports the wing [45, 46]. The shape and dimensions of this planform can be seen in Figure 4.3(b). The employed wing had a root chord length of 0.24m and was mounted in the axisymmetric wind tunnel octagonal cross section of width equal to 3m. For the cases selected here the freestream velocity was 62.5m/s. Experimental results [46] are available for oscillatory motion of the wing for several mean angles, amplitudes of oscillation between 3^o and 6^o and reduced frequencies in the range of 0.02 to 0.1. Two cases were computed both having a mean angle $\alpha_o = 18^o$ and amplitude $\Delta\alpha = 6^o$, while the reduced frequencies considered were k=0.048 and k=0.06. Comparisons of u-velocity profiles at four different phase angles during the oscillation cycle can be seen in Figures 4.11-4.13 for k=0.048 and in Figures 4.14-4.16 for k=0.06 respectively. Overall, CFD was found to be in excellent agreement with the experimental data. In each of these figures, one can see an embedded plot

of the cross spanwise section where the probing station is also shown. The chordwise location of the probe, streamlines, as well as the pressure distribution are presented at the corresponding phase angle. For each of the two reduced frequencies selected for this work, velocity profiles were extracted at three stations ($x/c = 0.4$, $z/c = 0.5$), ($x/c = 0.6$, $z/c = 0.5$) and ($x/c = 0.4$, $z/c = 0.7$) for four phase angles (ϕ) of 0, 90, 180 and 270 degrees. The velocity profiles at phase angles of 0 and 270 degrees reveal a fully attached flow at all spanwise and chordwise stations. In contrast, the velocity profiles at 90 and 180 degrees show massive recirculation of the flow. This can also be seen from the embedded plots at Figures 4.11 to 4.16. The CFD solution predicted the onset and the extend of the separation very well. It is only for the inboard station at $x/c = 0.6$ that the CFD slightly under-predicts the separation at a phase angle of 180 degrees. It is also interesting that the CFD results predict very well the velocity profiles at the outboard station of $z/c = 0.7$ for all phase angles and employed reduced frequencies. As will be discussed in subsequent paragraphs, the flow near the tip is highly 3-D. In this region, the DS vortex appears to interact with the tip vortex resulting in a very complex flow field. For this case the CPU time was found to be higher apparently due to the extra resolution required near solid boundaries and the overhead of the employed turbulence model.

4.5. HIGH *RE* REGIME VALIDATION CASES

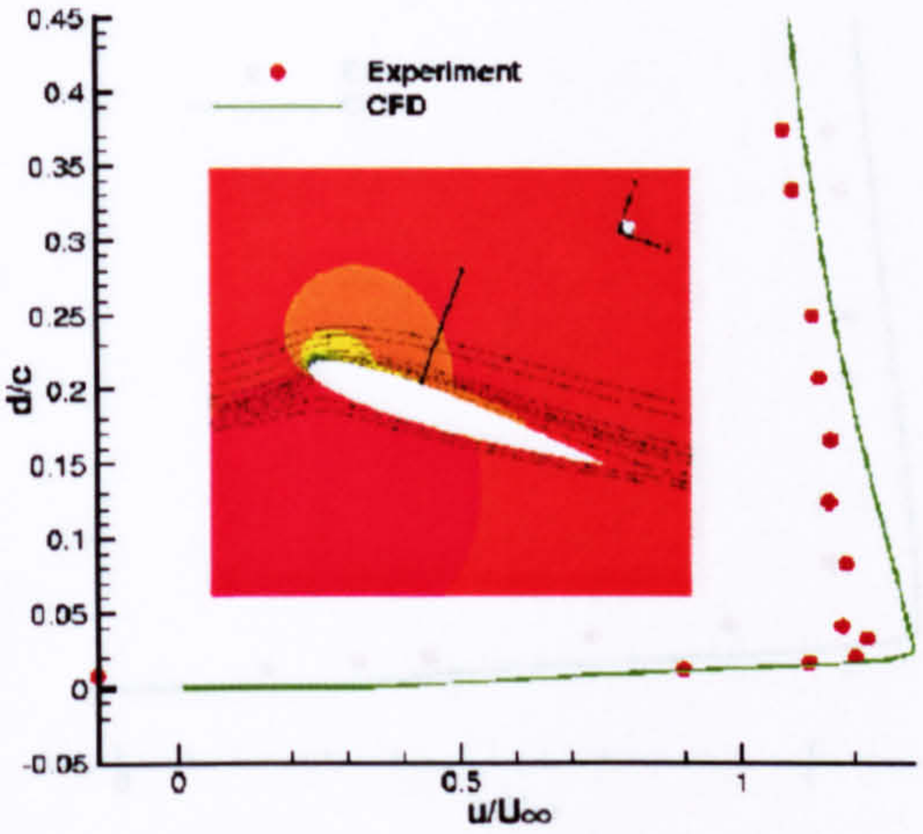

ϕ=0°, $\alpha = 12^o up$

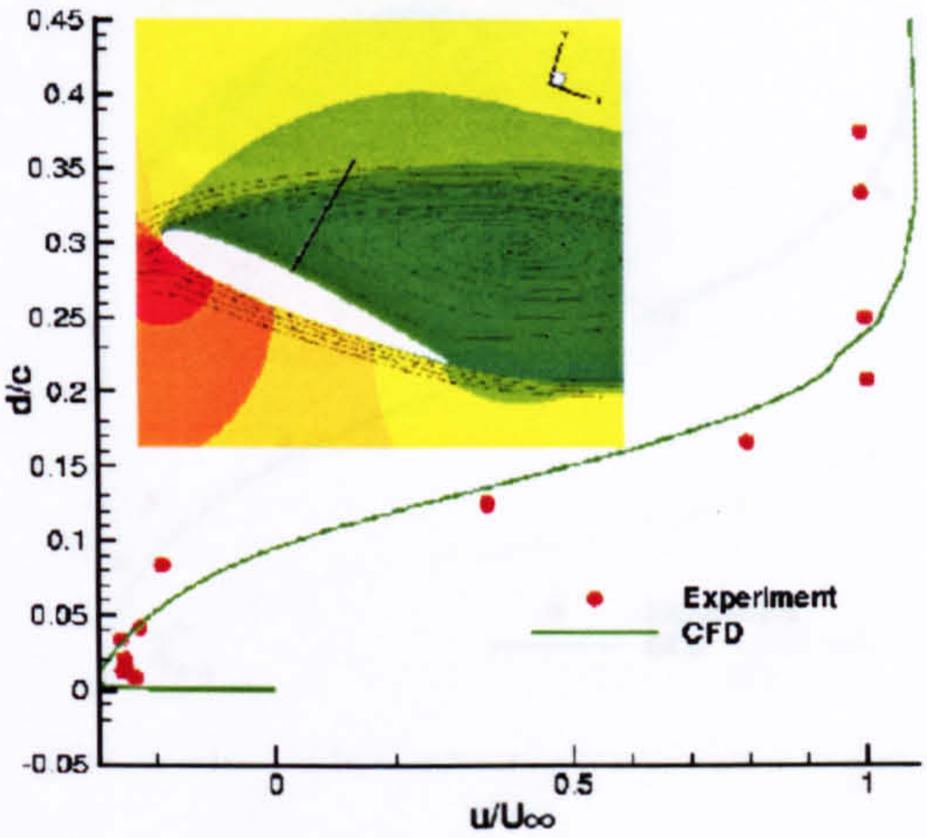

ϕ=90°, $\alpha = 18^o$

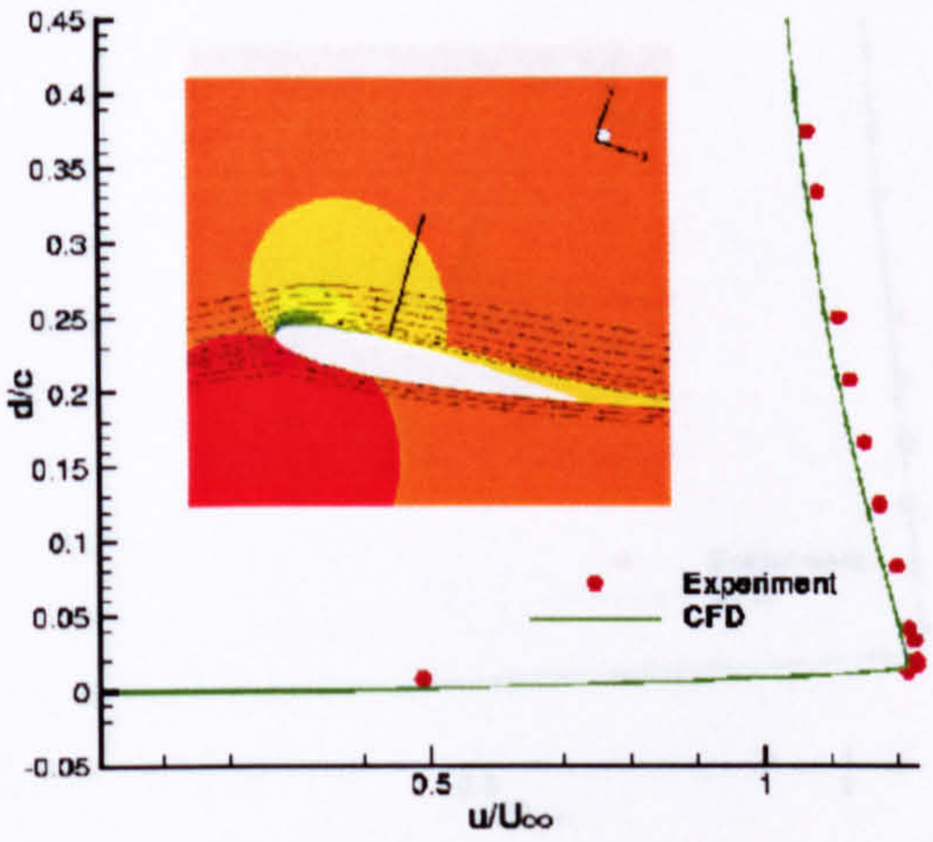

ϕ=270°, $\alpha = 6^o$

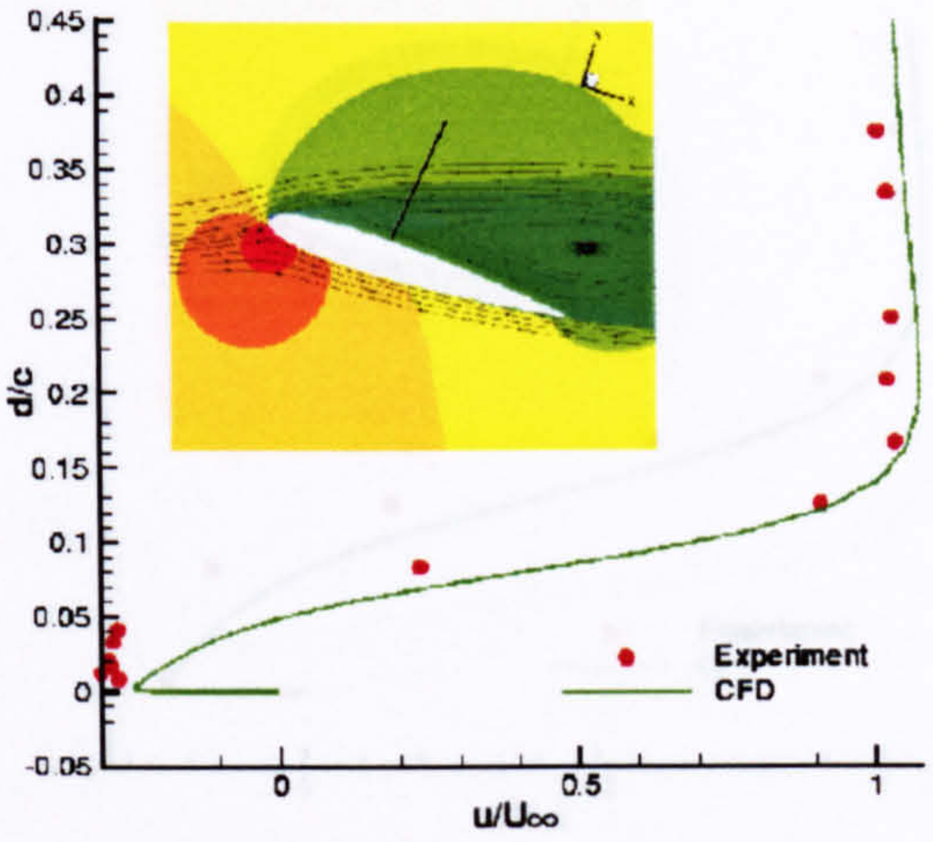

ϕ=180°, $\alpha = 12^o down$

Figure 4.11: Comparison between CFD and ELDV measurements by Berton *et al.*[45] for the u-velocity profiles during DS. Oscillatory motion of a tapered wing, $\alpha(t) = 12^o + 6^o sin(kt)$, $k = 0.048$, $Re = 10^6$, $M = 0.2$. The line on the inserted plot corresponds to the direction of the ELDV probing, superimposed on pressure contours. The profiles were extracted at a spanwise station of $z/c = 0.5$ and chordwise station of $x/c = 0.4$ (see Figure 4.3b).

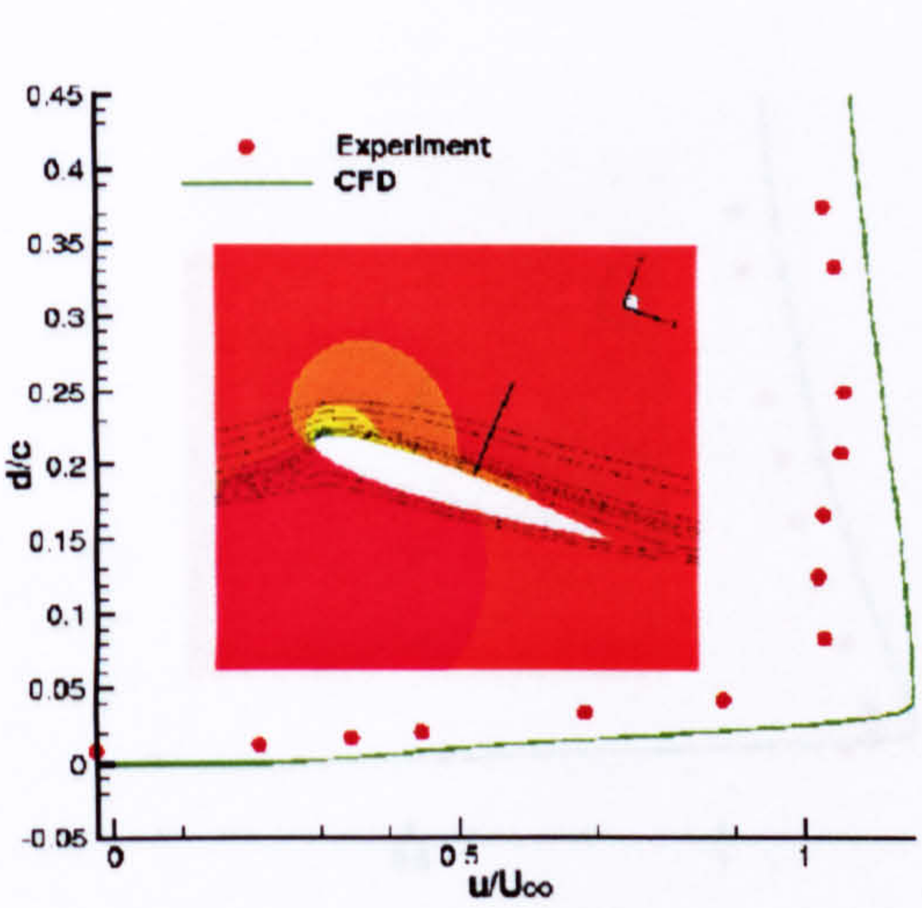

ϕ=0°, $\alpha = 12^o up$

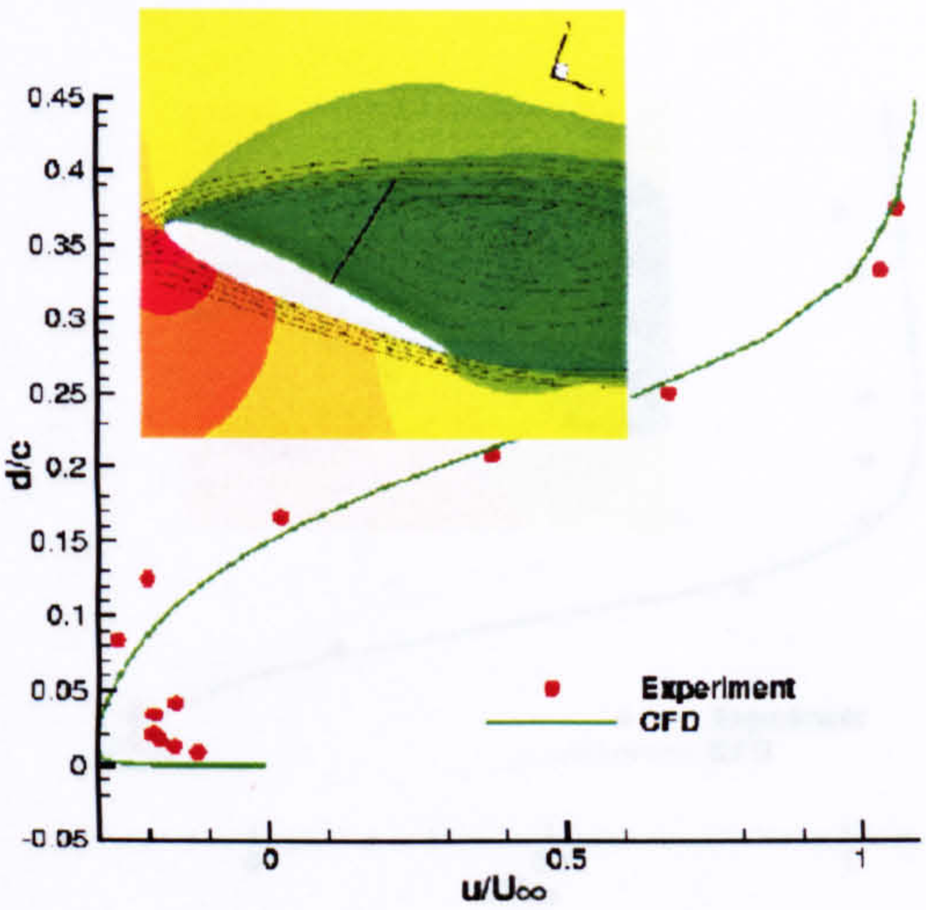

ϕ=90°, $\alpha = 18^o$

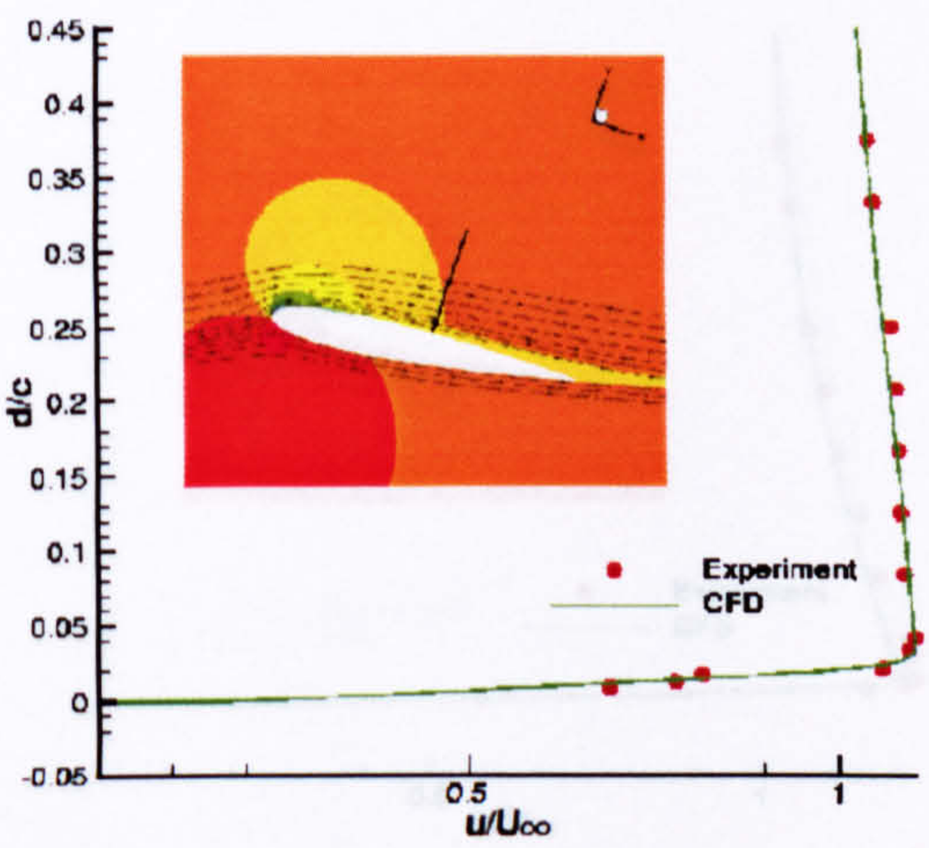

ϕ=270°, $\alpha = 6^o$

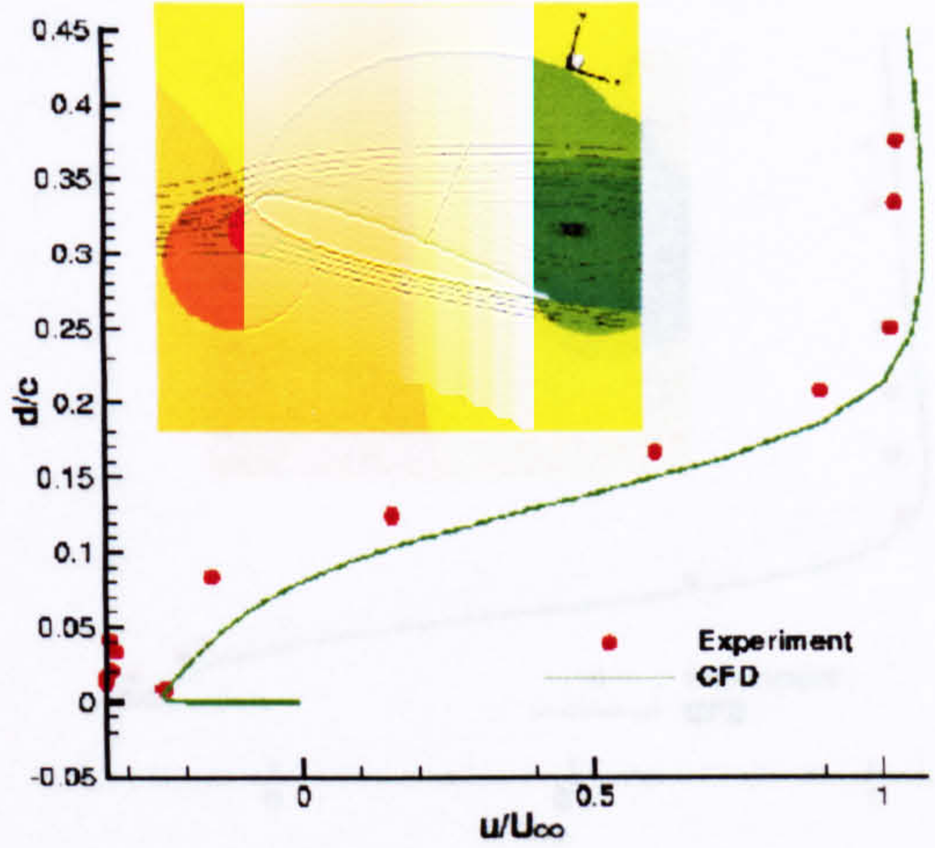

ϕ=180°, $\alpha = 12^o down$

Figure 4.12: Comparison between CFD and ELDV measurements by Berton *et al.*[45] for the u-velocity profiles during DS. Oscillatory motion of a tapered wing, $\alpha(t) = 12^o + 6^o sin(kt)$, $k = 0.048$, $Re = 10^6$, $M = 0.2$. The line on the inserted plot corresponds to the direction of the ELDV probing, superimposed on pressure contours. The profiles were extracted at a spanwise station of $z/c = 0.5$ and chordwise station of $x/c = 0.6$ (see Figure 4.3b).

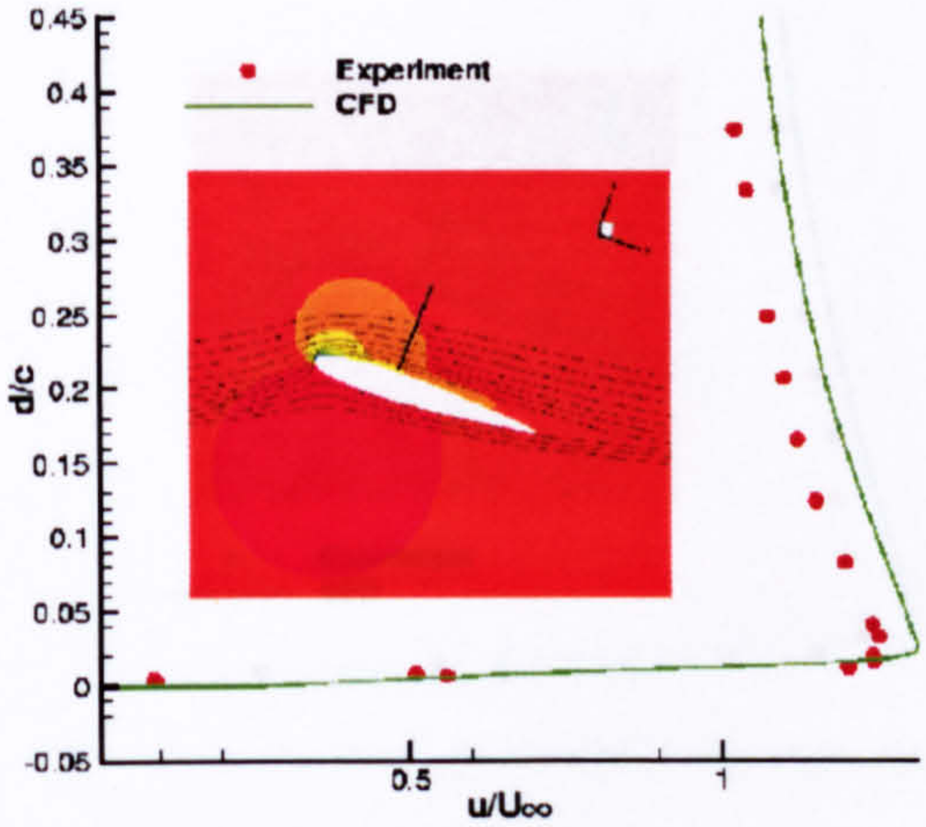

ϕ=0°, $\alpha = 12^o up$

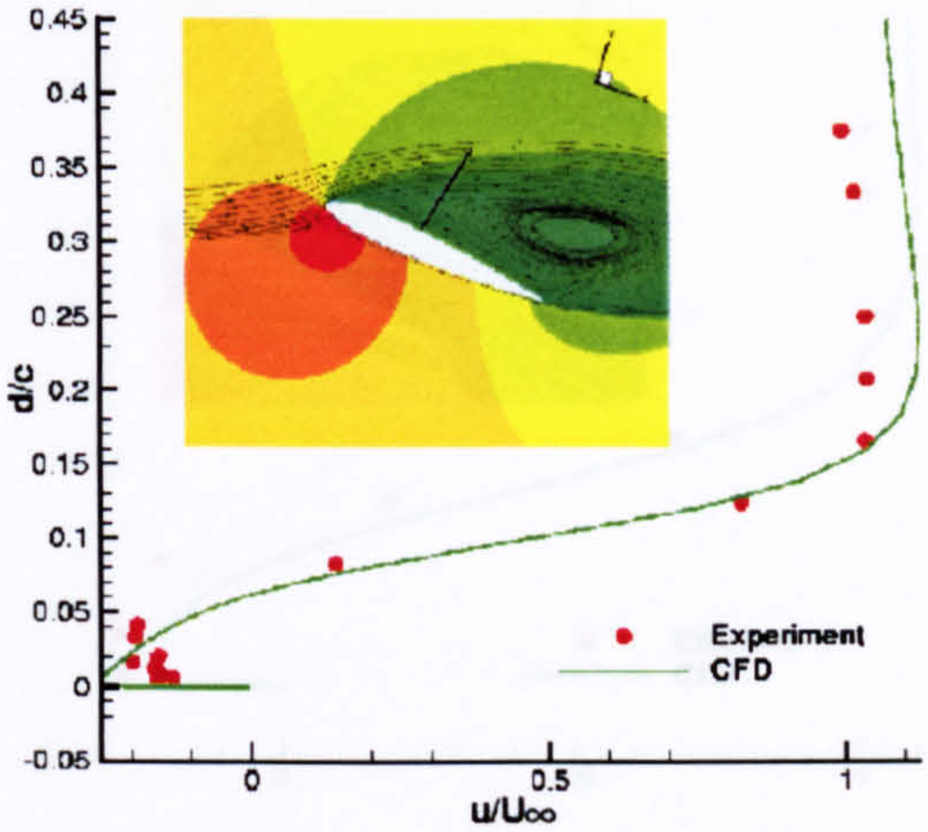

ϕ=90°, $\alpha = 18^o$

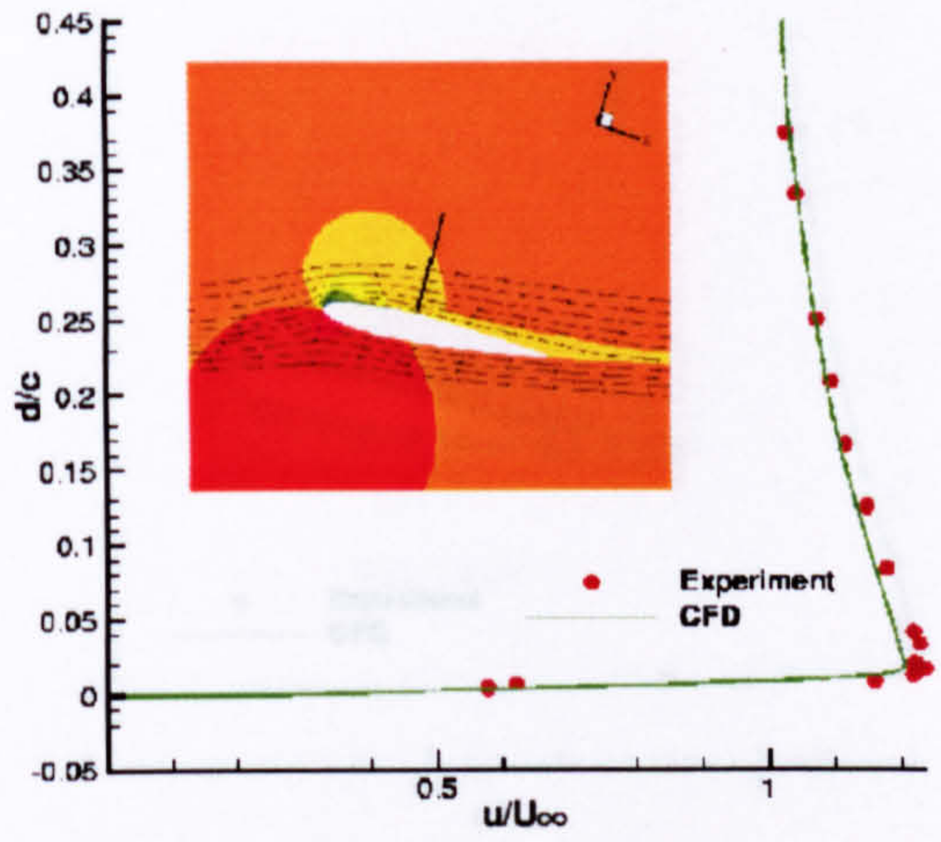

ϕ=270°, $\alpha = 6^o$

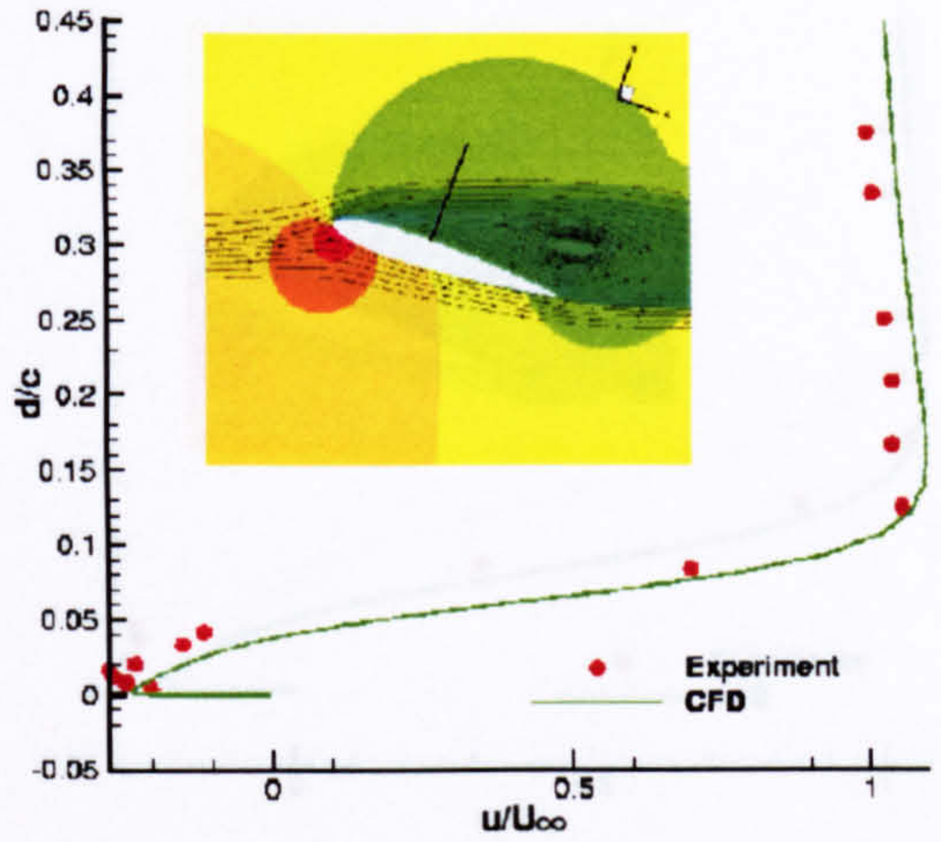

ϕ=180°, $\alpha = 12^o down$

Figure 4.13: Comparison between CFD and ELDV measurements by Berton *et al.*[45] for the u-velocity profiles during DS. Oscillatory motion of a tapered wing, $\alpha(t) = 12^o + 6^o sin(kt)$, $k = 0.048$, $Re = 10^6$, $M = 0.2$. The line on the inserted plot corresponds to the direction of the ELDV probing, superimposed on pressure contours. The profiles were extracted at a spanwise station of $z/c = 0.7$ and chordwise station of $x/c = 0.4$ (see Figure 4.3b).

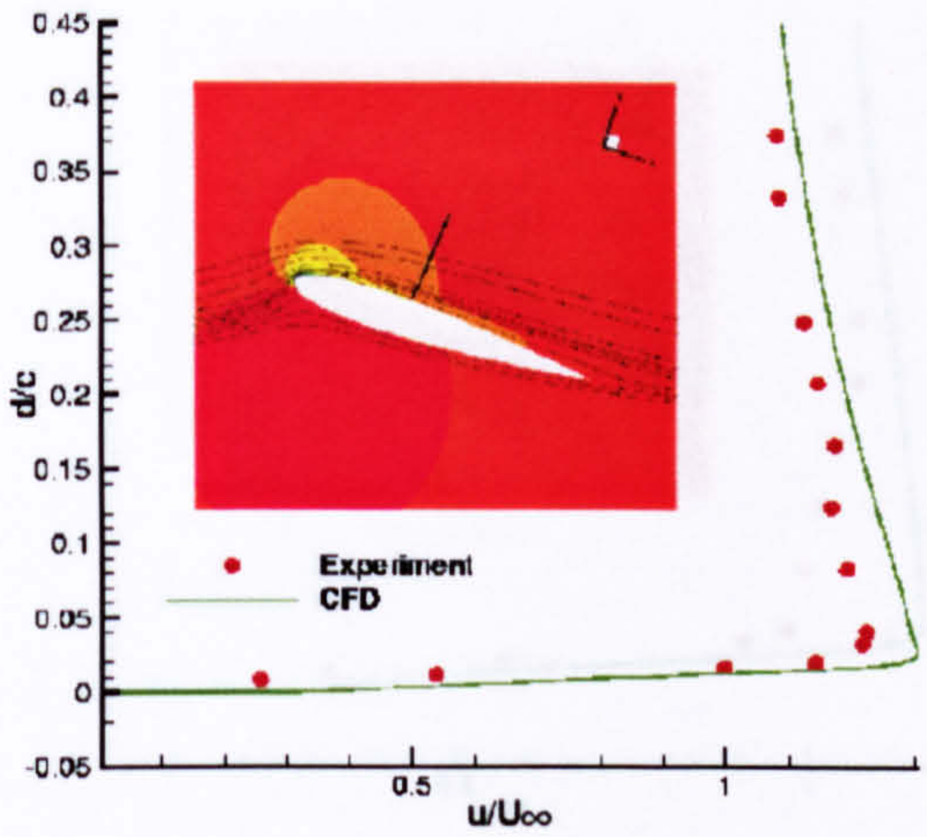

ϕ=0°, $\alpha = 12°up$

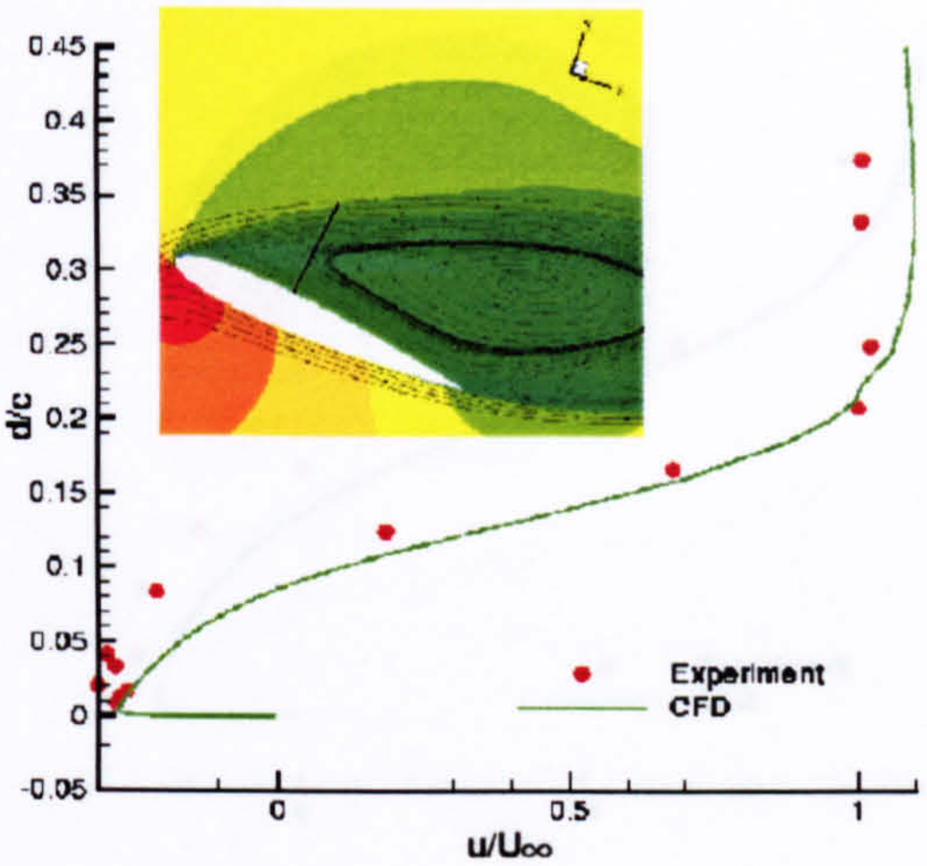

ϕ=90°, $\alpha = 18°$

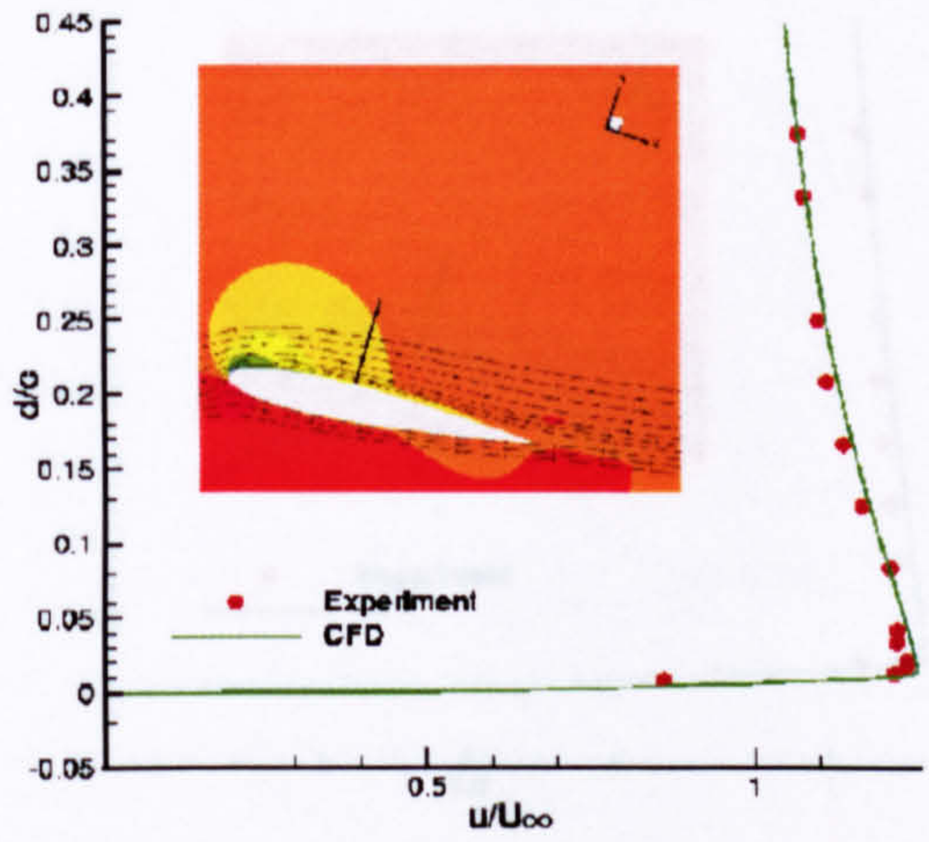

ϕ=270°, $\alpha = 6°$

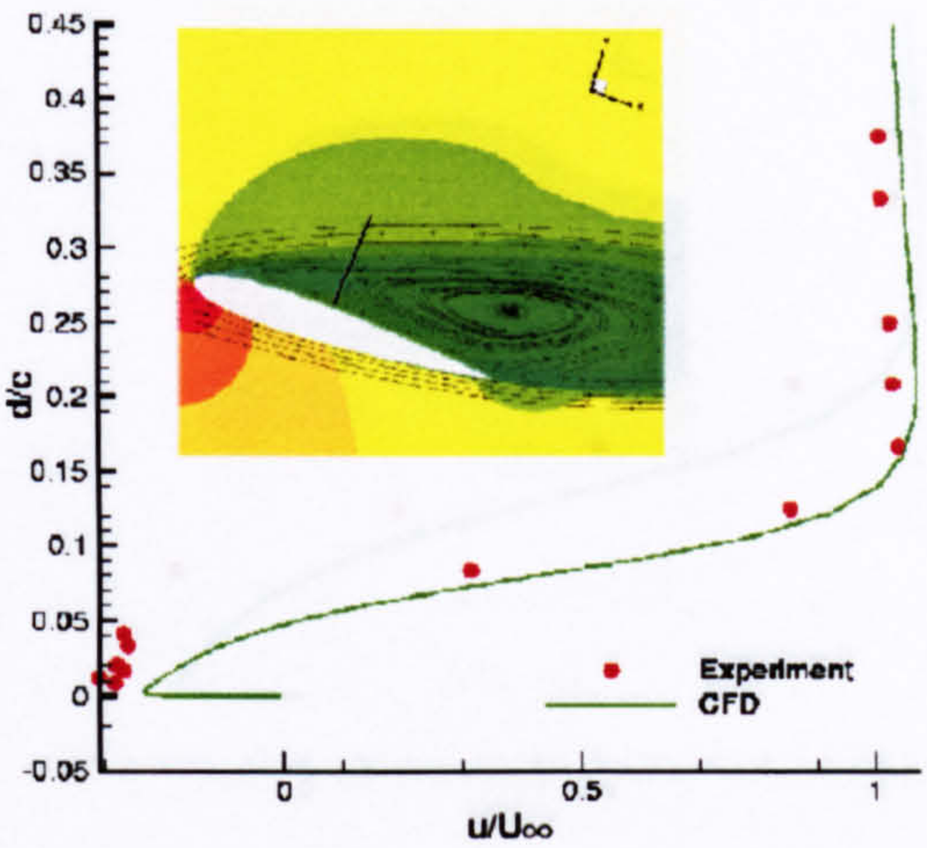

ϕ=180°, $\alpha = 12°down$

Figure 4.14: Comparison between CFD and ELDV measurements by Berton *et al.*[45] for the u-velocity profiles during DS. Oscillatory motion of a tapered wing, $\alpha(t) = 12° + 6°sin(kt)$, $k = 0.06$, $Re = 10^6$, $M = 0.2$. The line on the inserted plot corresponds to the direction of the ELDV probing, superimposed on pressure contours. The profiles were extracted at a spanwise station of $z/c = 0.5$ and chordwise station of $x/c = 0.4$ (see Figure 4.3b).

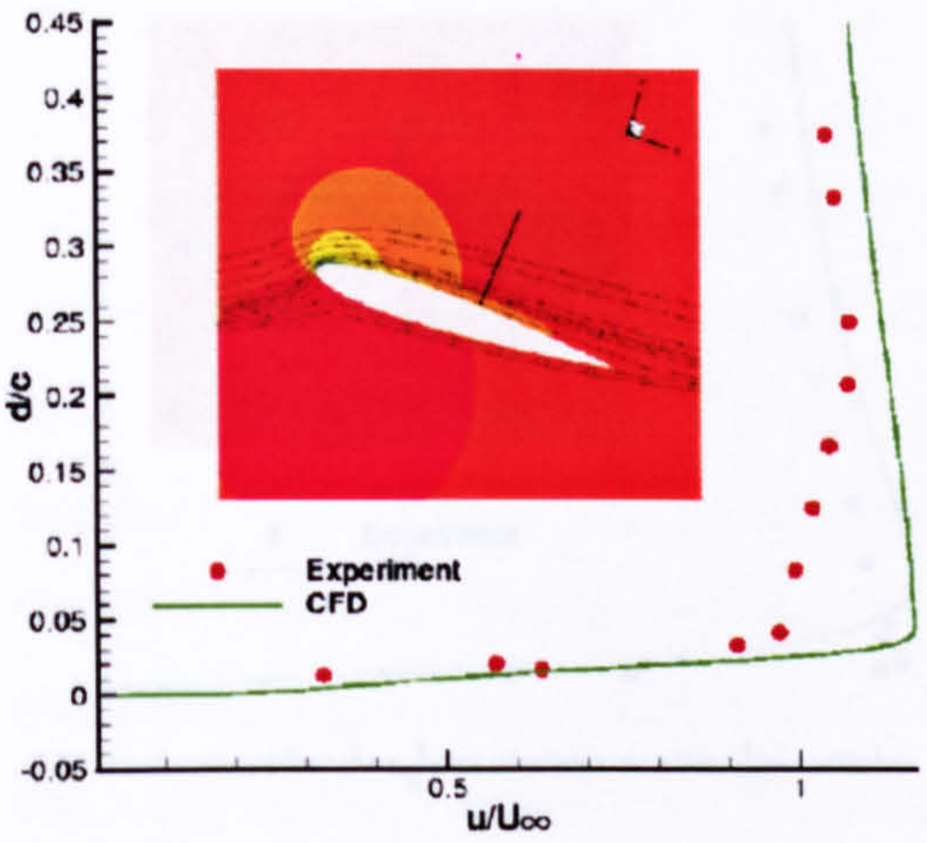

ϕ=0°, $\alpha = 12°up$

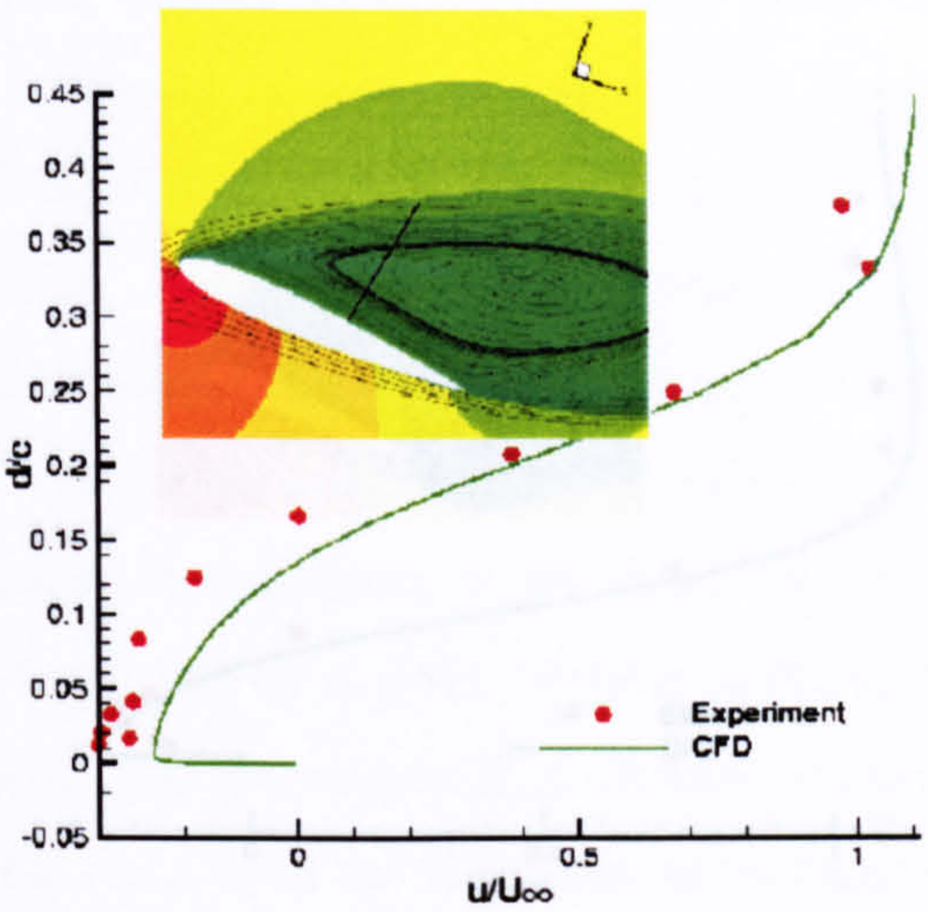

ϕ=90°, $\alpha = 18°$

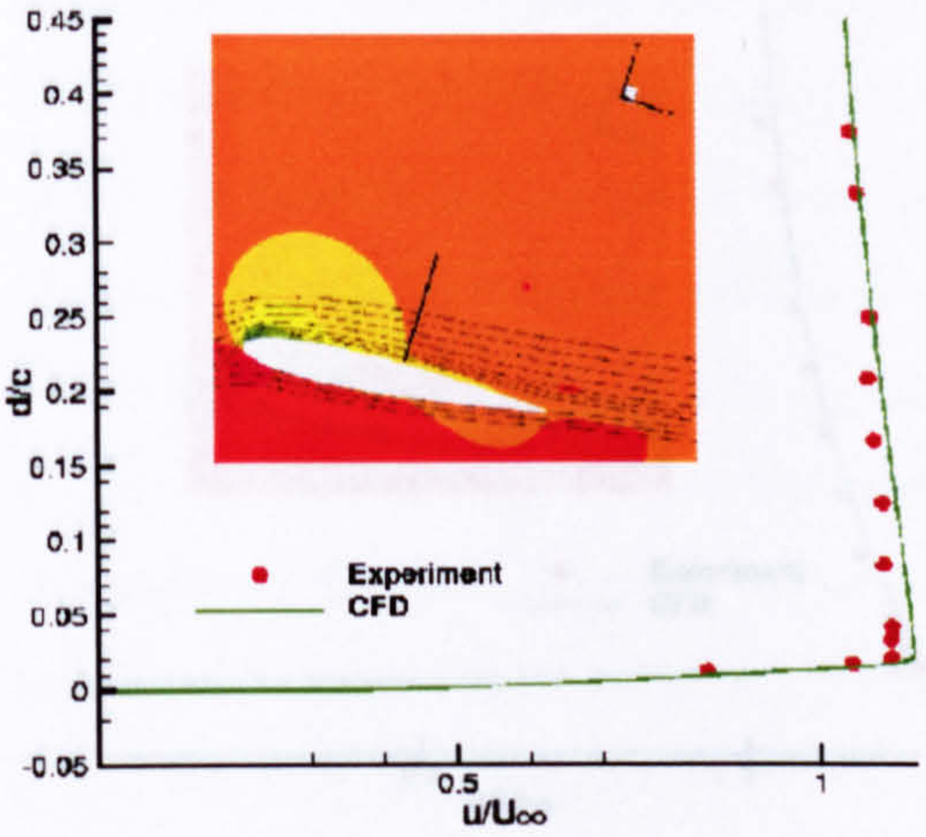

ϕ=270°, $\alpha = 6°$

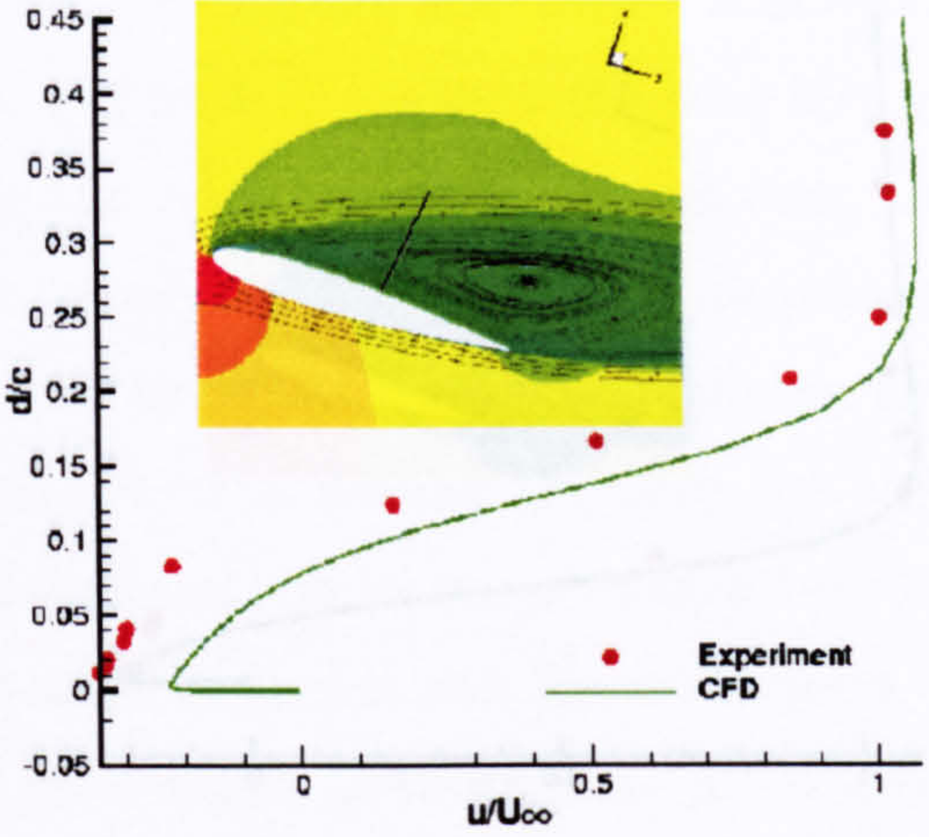

ϕ=180°, $\alpha = 12°down$

Figure 4.15: Comparison between CFD and ELDV measurements by Berton *et al.*[45] for the u-velocity profiles during DS. Oscillatory motion of a tapered wing, $\alpha(t) = 12^o + 6^o sin(kt)$, $k = 0.06$, $Re = 10^6$, $M = 0.2$. The line on the inserted plot corresponds to the direction of the ELDV probing, superimposed on pressure contours. The profiles were extracted at a spanwise station of $z/c = 0.5$ and chordwise station of $x/c = 0.6$ (see Figure 4.3b).

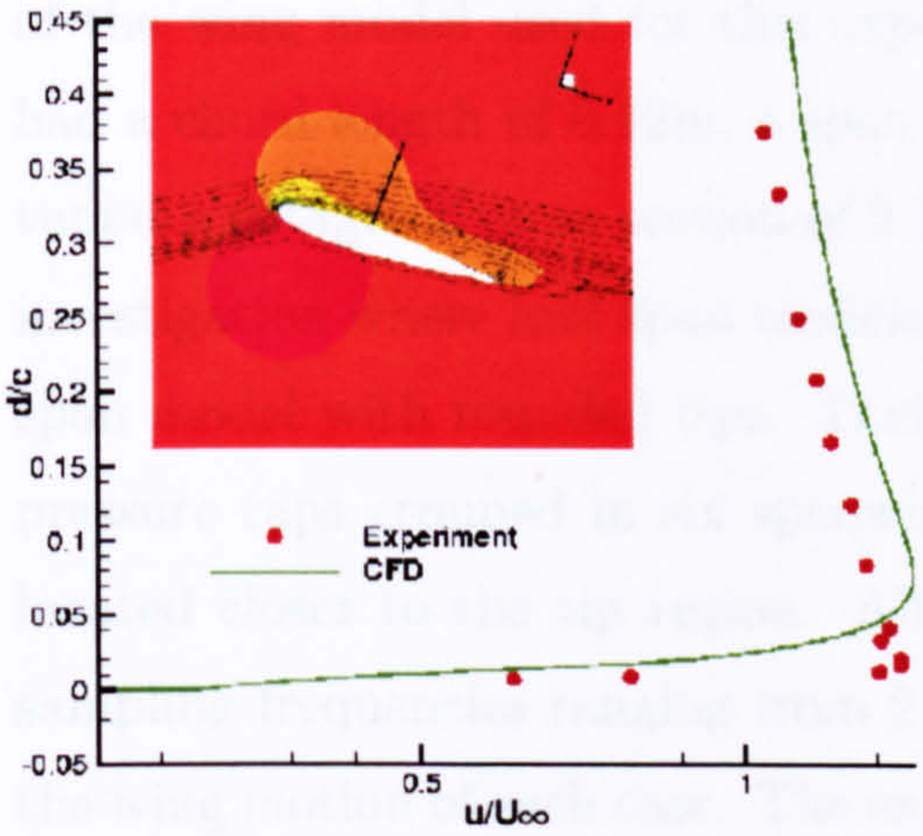

ϕ=0°, $\alpha = 12^o up$

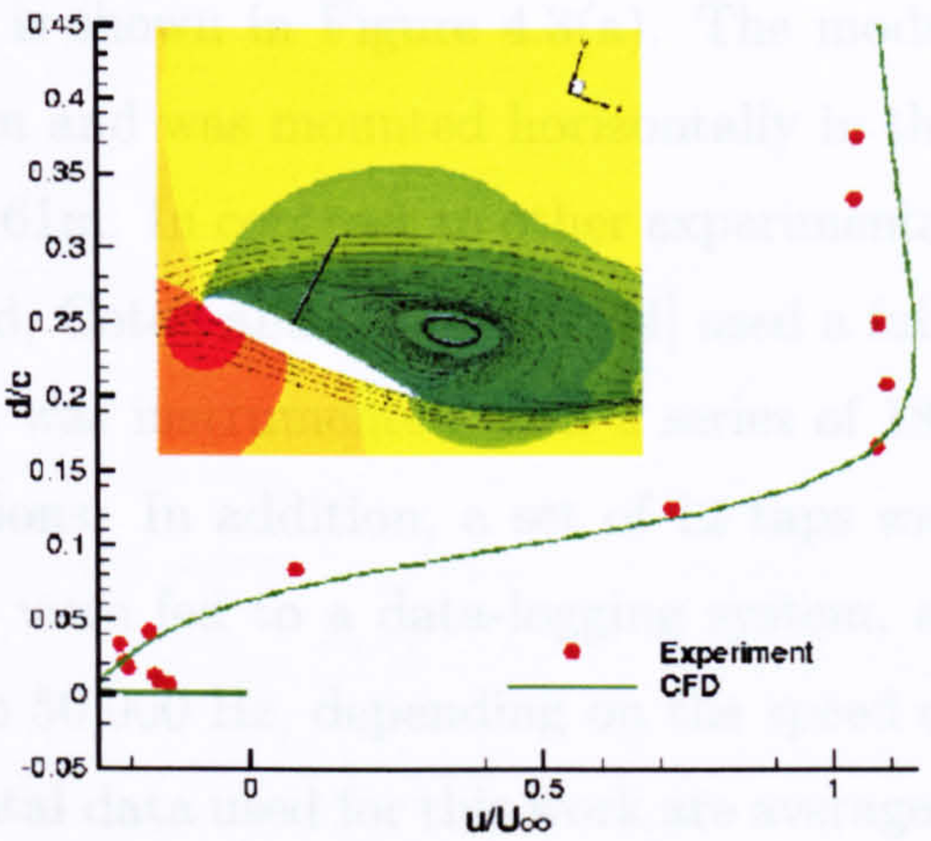

ϕ=90°, $\alpha = 18^o$

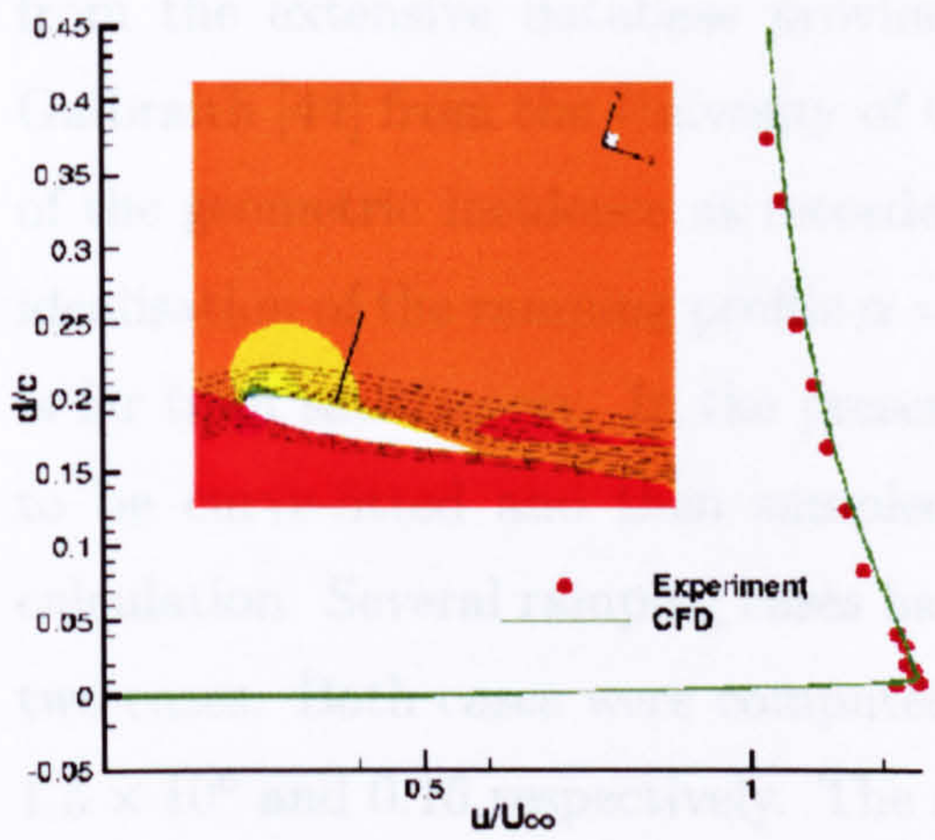

ϕ=270°, $\alpha = 6^o$

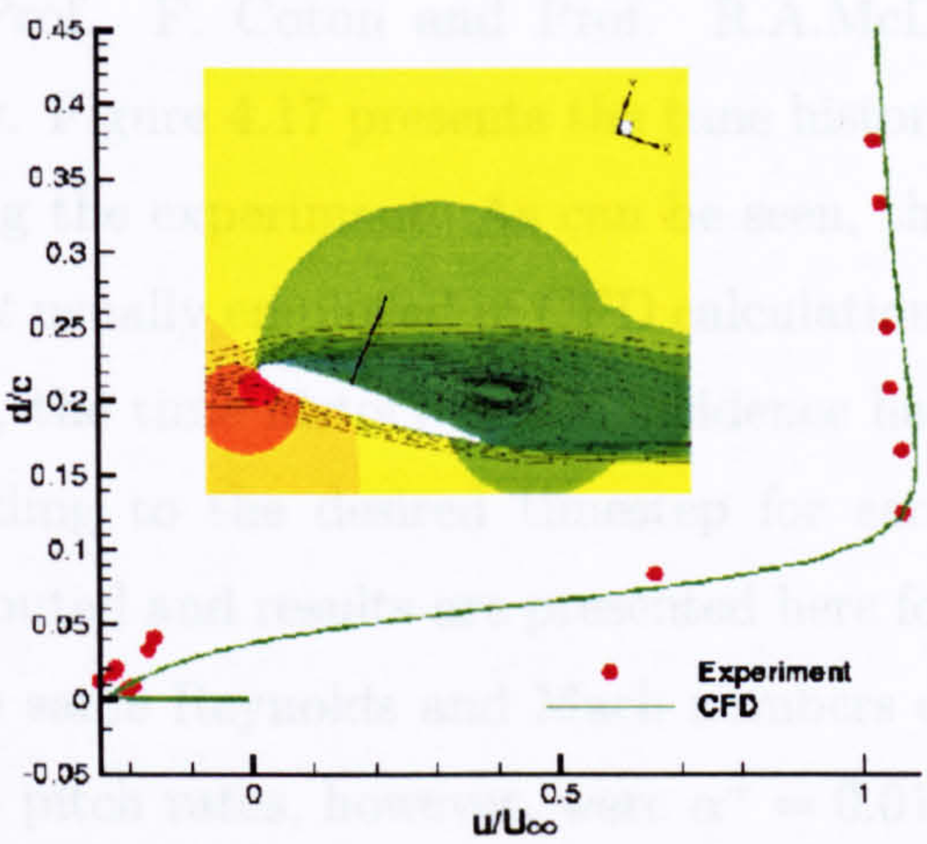

ϕ=180°, $\alpha = 12^o down$

Figure 4.16: Comparison between CFD and ELDV measurements by Berton *et al.*[45] for the u-velocity profiles during DS. Oscillatory motion of a tapered wing, $\alpha(t) = 12^o + 6^o sin(kt)$, $k = 0.06$, $Re = 10^6$, $M = 0.2$. The line on the inserted plot corresponds to the direction of the ELDV probing, superimposed on pressure contours. The profiles were extracted at a spanwise station of $z/c = 0.7$ and chordwise station of $x/c = 0.4$ (see Figure 4.3b).

4.5.2 The pressure measurements of Coton and Galbraith

The tests described here [44], were carried out in the 'Handley Page' wind tunnel of the University of Glasgow which is of low speed closed-return type. The planform of the wing model used for this experiment is shown in Figure 4.3(a). The model had a chord length of 0.42m, a span of 1.26m and was mounted horizontally in the tunnel's octagonal cross section of 2.13m x 1.61m. In contrast to other experimental investigation where half-span models are used, Coton and Galbraith [44] used a full-span model with rounded tips. Their model was instrumented with a series of 180 pressure taps grouped in six spanwise locations. In addition, a set of 12 taps was located closer to the tip region. All signals were fed to a data-logging system, at sampling frequencies ranging from 218 Hz to 50,000 Hz, depending on the speed of the wing motion of each case. The experimental data used for this work are averaged from a number of consecutive cycles.

For the CFD investigation both ramping and oscillatory cases have been selected from the extensive database provided by Prof. F. Coton and Prof. R.A.McD. Galbraith [44] from the Univesity of Glasgow. Figure 4.17 presents the time history of the geometric incidence as recorded during the experiment. As can be seen, the idealisation of the ramping profile $\alpha = \alpha_o + \dot{\alpha}t$ usually employed in CFD calculations is far from satisfactory. In the present work, the time history of the incidence had to be curve-fitted and then sampled according to the desired timestep for each calculation. Several ramping cases have computed and results are presented here for two cases. Both cases were computed at the same Reynolds and Mach numbers of 1.5×10^6 and 0.16 respectively. The reduced pitch rates, however, were $\alpha^+ = 0.011$ and $\alpha^+ = 0.022$. For both cases the incidence varied between -5 and 39 degrees.

Figure 4.17(b) suggests that a similar treatment is required for the oscillatory cases. The ideal case $\alpha = \alpha_o + \alpha_1 sin(kt)$ had to be generalised so that the imposed wing actuation corresponds the experimental one. It was found that about ten harmonics were necessary and the resulting actuation was described by

$$\alpha = \alpha_o/2 + \sum_{i=1}^{i=10} \alpha_i sin(ikt) + \beta_i cos(ikt).$$

Table 4.3 presents the bias α_o as well as the amplitudes (a_i, b_i) of the in- and out- phase components used for the CFD simulations.

To allow comparisons with the ramping cases the Reynolds and Mach numbers were kept the same. Again, two reduced frequencies were used as fundamental

harmonics of the oscillation, namely, $k = 0.092$ and $k = 0.17$. Comparisons between experiments and CFD results for the surface pressure coefficient are presented in Figure 4.18 for the ramping and Figure 4.20 for the oscillatory case.

Figure 4.18 presents the comparison at two incidence angles. One cannot fail to notice that at low incidence (20^o in Figure 4.18a) the experiments and CFD agree quite well. The shape of the Cp contours corresponds to attached flow and the suction peak near the leading edge as well as the pressure recovery along the chordwise direction are adequately captured. Since the wing is loaded, the Cp contours near the tip are distorted due to the presence of the tip vortex. Unfortunately, the number of pressure taps used for the experiment does not allow for detailed comparison in the near tip region. A dashed line on the Cp plot of the CFD solution indicates the area covered by the pressure taps. A grid is shown on the experimental plot which indicates the location of the pressure taps on the wind tunnel model. At higher incidence angles, the agreement between experiments and CFD was less favourable. A correction of the incidence angle of about 5^o was necessary in order to have a similar loading of the wing. As can be seen in Figure 4.18b both experiments and CFD indicate the presence of a massive vortical structure over the wing. This can be seen near the centre of the plot at a spanwise location z/c of 0.75 where a local suction peak is present. This peak is due to the DS vortex impinging on the wing surface. At this high incidence, a strong tip vortex dominates the near tip region of the wing. This is now captured by both experiments and CFD and appears as a secondary suction peak at z/c of about 1.4. This secondary peak corresponds to Cp values of about -3, which is much less than the peak due to the DS vortex which reaches Cp values of -1.2. The experimentalists reported an upwash of 0.5 deg in the tunnel's test section, possibly attributed to the supporting struts of the wing as well as the tunnel wall effects. For the case shown in Figure 4.18b, a correction of 4^o was necessary. This also points out to deficiencies in the calculation since it is known from 2-D cases [57] that slower actuations of the wing are harder to simulate than rapid ones. This is due to the fact that viscous flow effects are more dominant for low ramp rates, especially as static stall conditions are approached.

Figure 4.19 compares the time history of the surface pressure coefficient at 8 locations on the wing. As can be seen, the initial part of the curves is close for all stations but discrepancies occur at higher incidence angles. For all cases the magnitude of C_p is predicted well and the only necessary correction is on the phasing. Similar remarks can be made for the oscillatory cases for which CFD results are

presented in Figure 4.20. Comparisons are shown only for a phase angle of 90° which corresponds to the highest incidence encountered during the oscillation. Again the suction peaks induced by the DS and the tip vortices are predicted at almost the same magnitude provided a 4° correction of the incidence was applied.

A separate set of calculations has been conducted for the swept tip planform which was tested at the same conditions as the square wing. Results for this case are shown in Figure 4.21 again at two incidence angles. For this case, a similar number of pressure taps was used and the CFD solution was supplied at the locations of these taps. Since the pressure tap locations where not spread out in a structured manner, a Delaunay triangulation was used to construct a sampling mesh. The data were subsequently used to reconstruct the pressure field in exactly the same way as the experiments. Again a correction was need for the wing loadings to match. This correction was constant for all the cases considered and the possible sources for this discrepancy are the tunnel wall effects, the experimental support mechanisms which were not modelled in the CFD runs and/or the turbulence modelling. Interestingly, although there was a phase difference between experiments and CFD, the actual C_p magnitude compared well.

$k = 0.092$	$\alpha_o = 0.169892$				
i	1	2	3	4	5
α_i	-0.0717488	-0.00809223	-0.00416931	-0.00230814	0.001161
β_i	0.157438	-0.00194330	0.00219548	0.000897672	-0.00197636
i	6	7	8	9	10
α_i	-1.61438E-05	0.000539150	3.0956E-05	-0.000122833	-0.000159201
β_i	0.000977314	0.000387543	-0.000113408	-0.00037934	-6.75040E-05

$k = 0.17$	$\alpha_o = 0.155459$				
i	1	2	3	4	5
α_i	-0.101697	0.0161334	0.00914202	-0.00169119	-0.000486481
β_i	0.125778	-0.0129037	-0.000836860	-0.00164984	-0.00231397
i	6	7	8	9	10
α_i	0.000773430	-0.000166552	0.000357502	1.5609E-05	6.5348E-05
β_i	0.000218741	-0.000135753	-0.000478472	-1.08930E-05	-0.000338885

Table 4.3: Fourier expansion coefficients for the two oscillating cases by Coton & Galbraith [44].

4.5. HIGH *RE* REGIME VALIDATION CASES

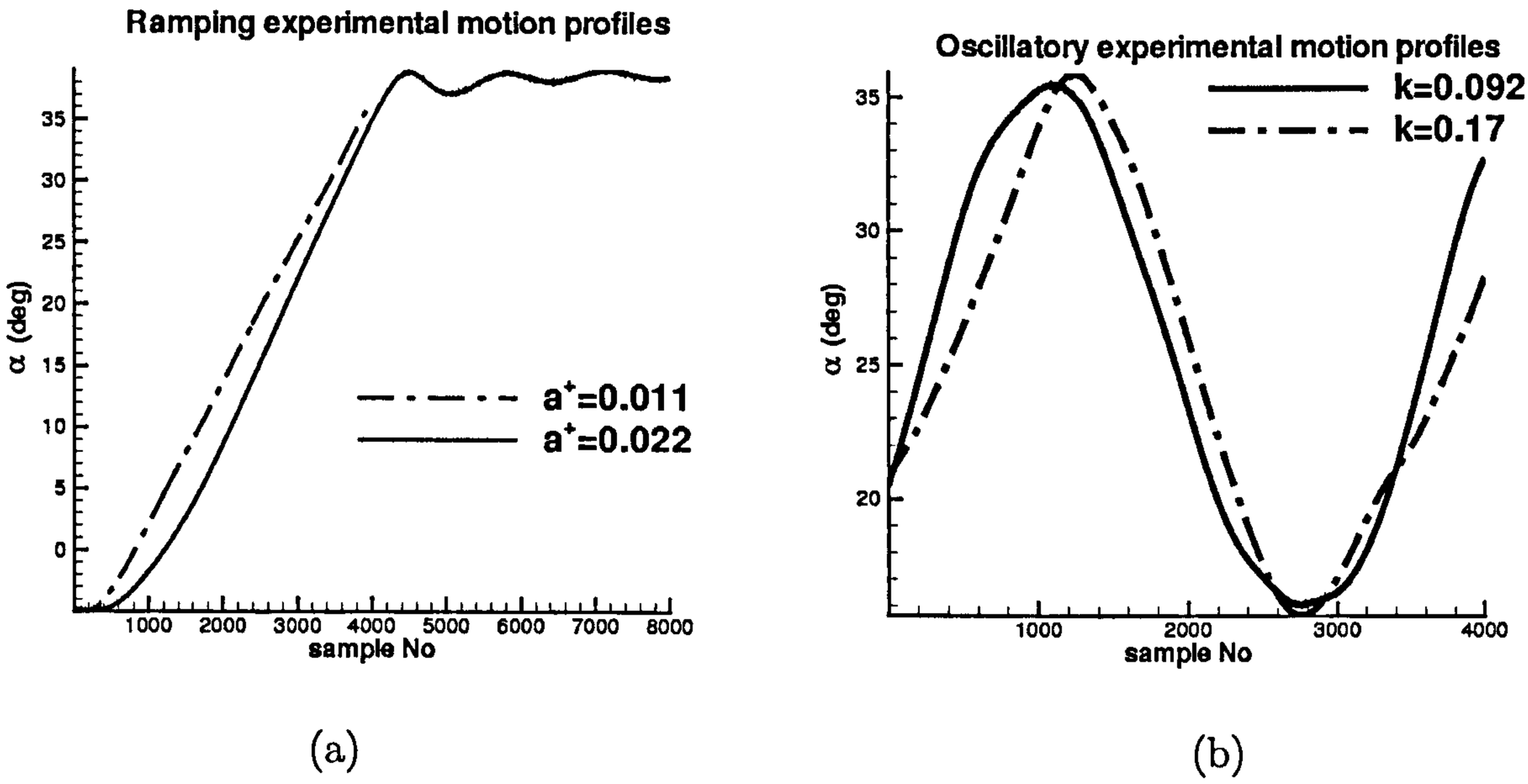

(a) (b)

Figure 4.17: Geometric angle vs sample number of the wing motion for the case by Coton and Galbraith [44]. (a) Ramping cases at $\alpha^+ = 0.011$ and $\alpha^+ = 0.022$. (b) Oscillatory cases at $k = 0.092$ and $k = 0.17$.

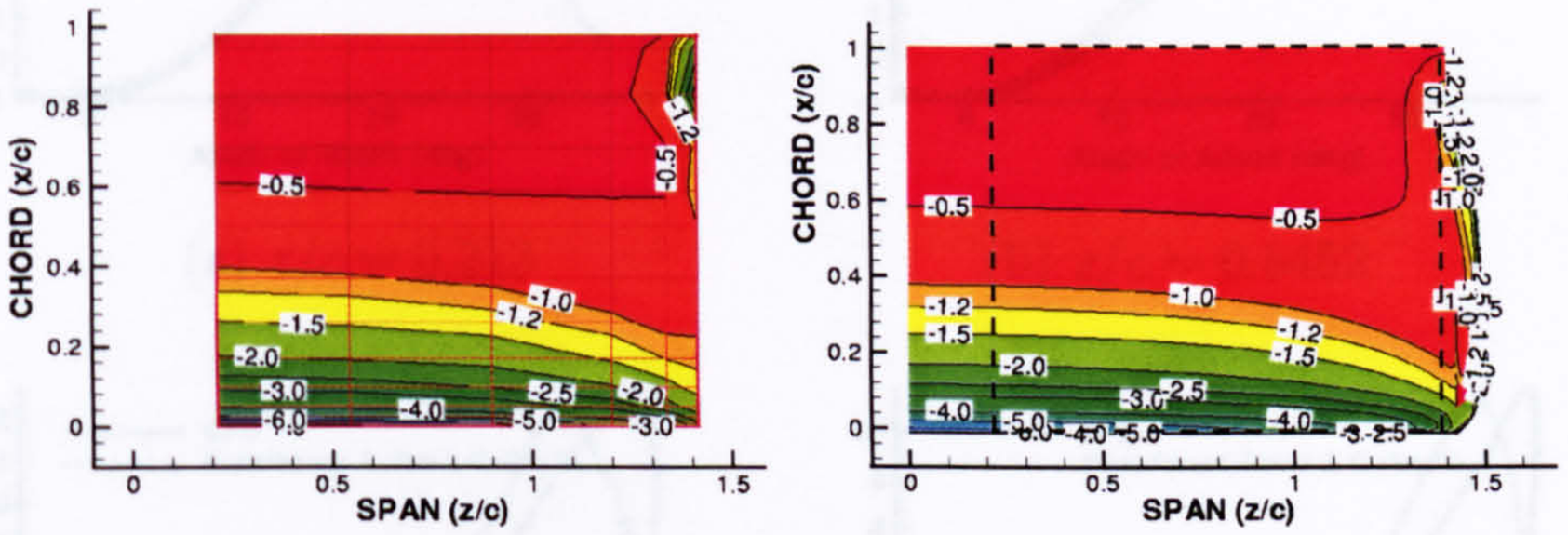

(a)

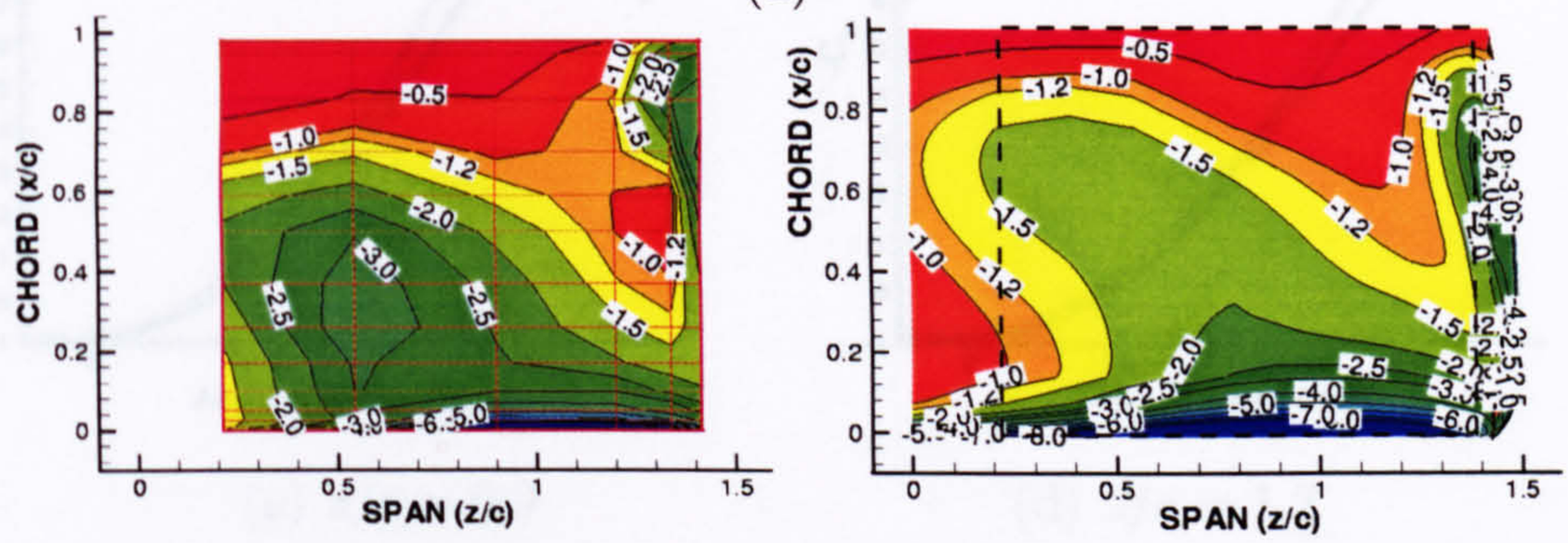

(b)

Figure 4.18: Comparison between experimental (left) and CFD (right) surface pressure distributions for the case 4 of Table 4.1 [44]. Ramping wing motion between -5^o and 39^o, $\alpha^+ = 0.022$, $Re = 1.5 \times 10^6$, $M = 0.16$. (a) $\alpha = 20^o$ and (b) $\alpha = 37^o$ (CFD), $\alpha = 33^o$ (Experiment).

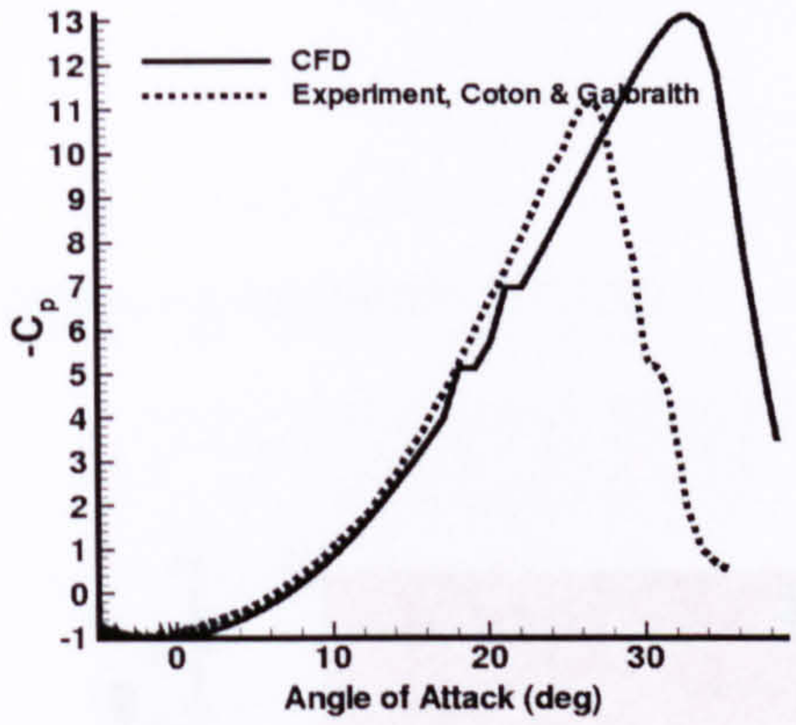

(a) $z/c = 0.213$

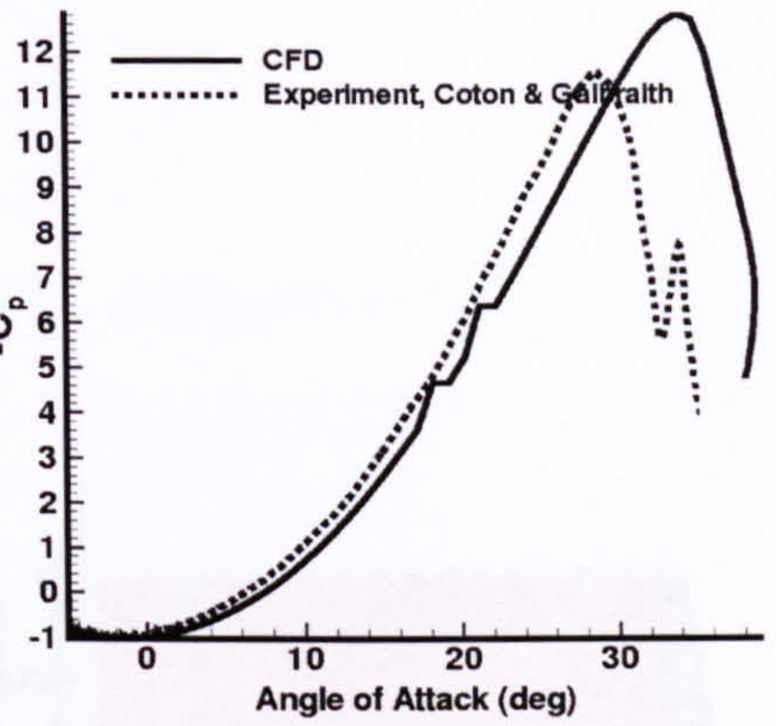

(b) $z/c = 0.5452$

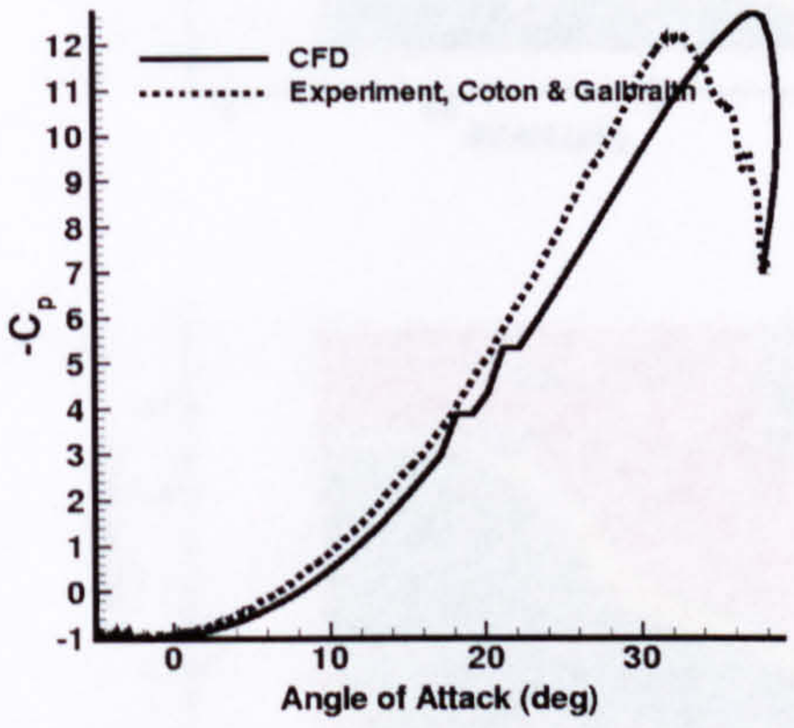

(c) $z/c = 0.9$

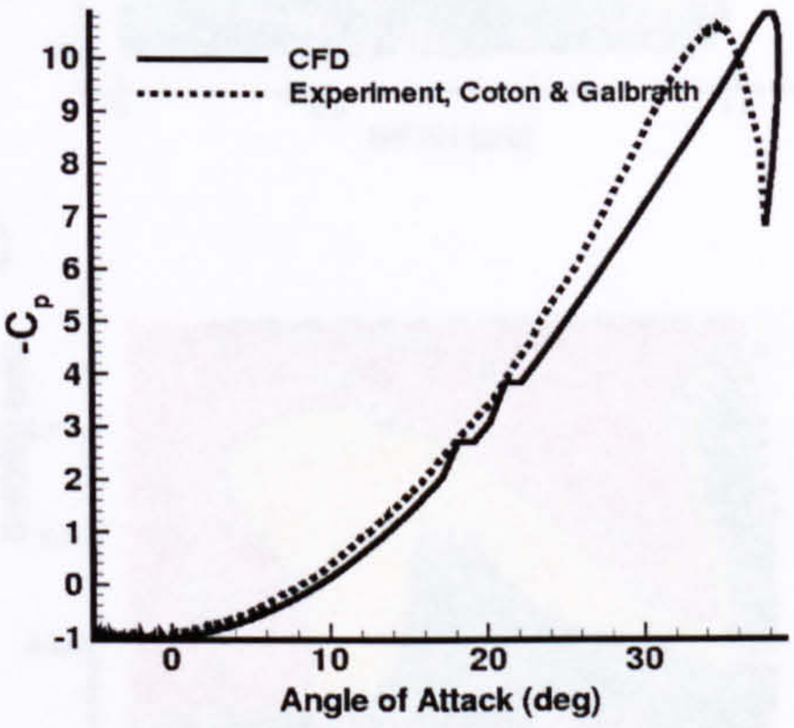

(d) $z/c = 1.2$

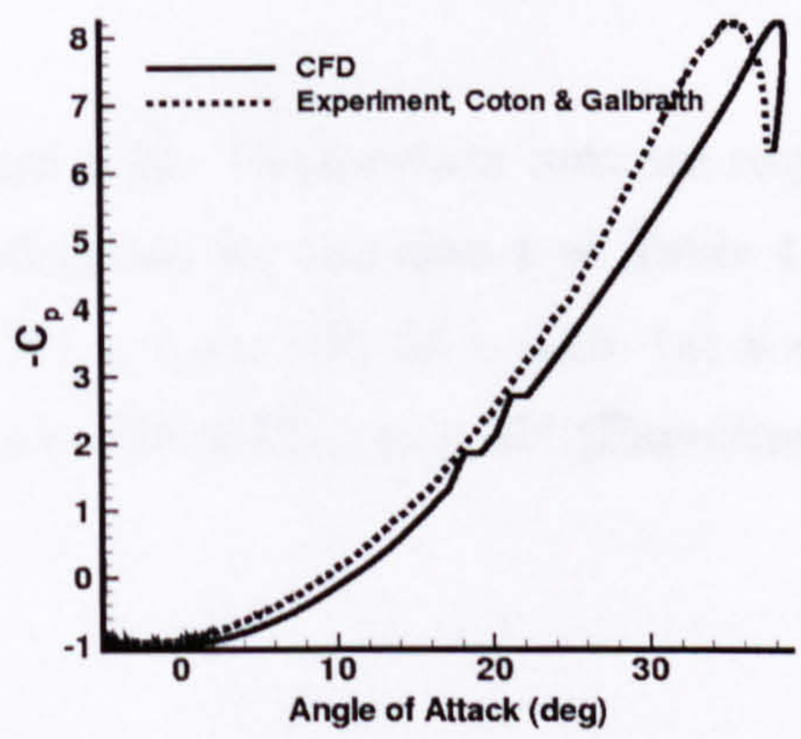

(e) $z/c = 1.34$

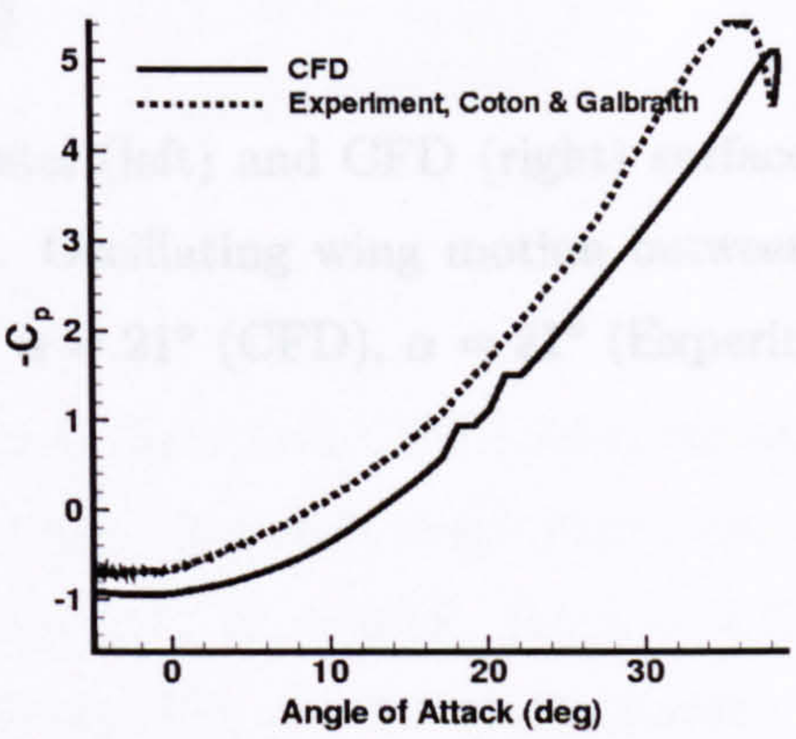

(f) $z/c = 1.416$

Figure 4.19: Cp vs angle of attack for a single rake of pressure transducers at $x/c = 0.00025$ for the ramping case with $\alpha^+ = 0.022$, $Re = 1.5M$, $M = 0.16$, $\alpha = -5^o$ *to* 40^o.

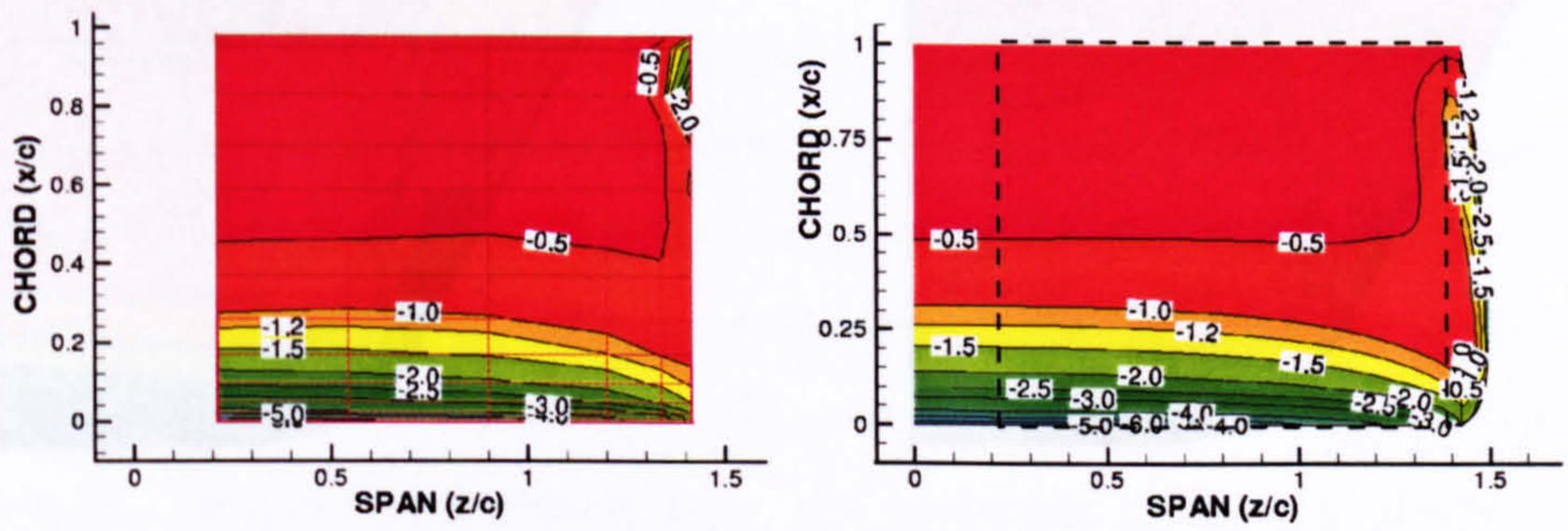

(a)

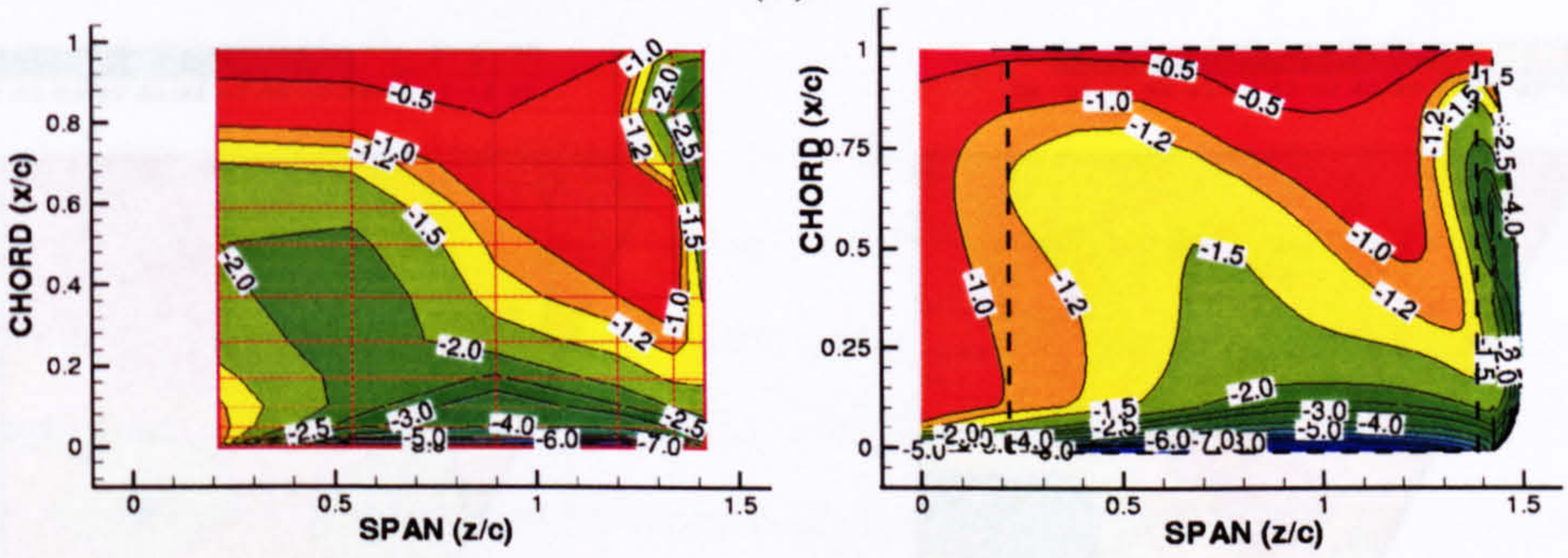

(b)

Figure 4.20: Comparison between experimental (left) and CFD (right) surface pressure distributions for the case 4 of Table 4.1 [44]. Oscillating wing motion between 15^o and 35^o, $Re = 1.5 \times 10^6$, $M = 0.16$. (a) $k = 0.17$, $\alpha = 21^o$ (CFD), $\alpha = 21^o$ (Experiment) and (b) $\alpha = 35^o$ (CFD), $\alpha = 31^o$ (Experiment).

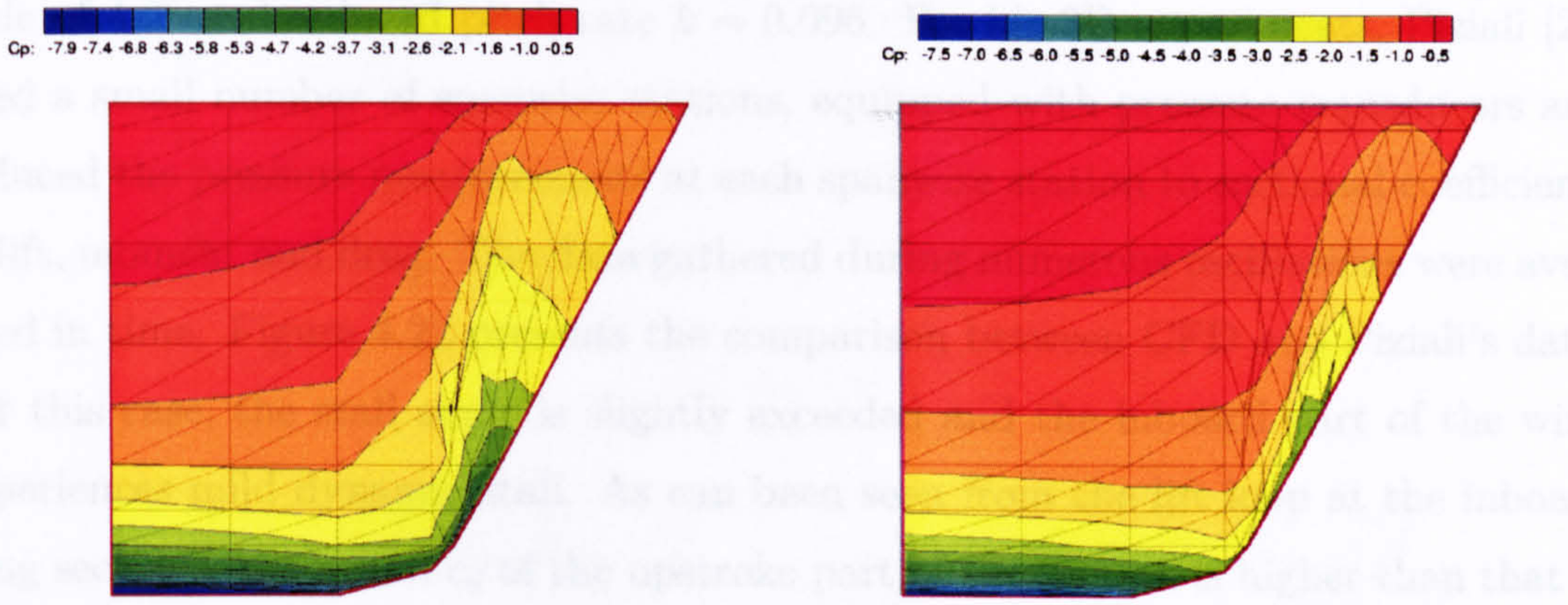

(a)

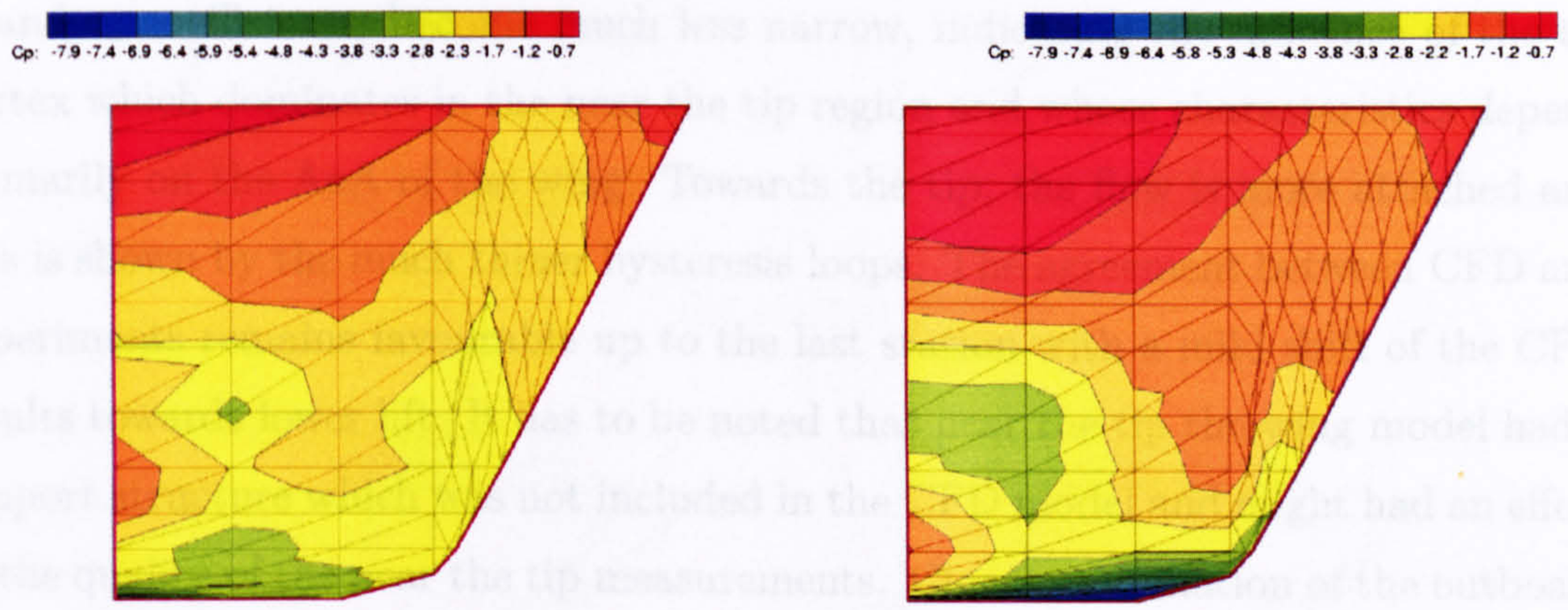

(b)

Figure 4.21: Comparison between experimental (left) and CFD (right) surface pressure distribution for the case 5 of Table 4.1 [44] for the wing with swept back tips. Oscillating wing motion between 15^o and 35^o, $Re = 1.5 \times 10^6$, $M = 0.16$. (a) $k = 0.17$, $\alpha = 21^o$ (CFD), $\alpha = 25^o$ (Experiment) and (b) $\alpha = 39^o$ (CFD), $\alpha = 35^o$ (Experiment).

4.5.3 The experiments by Piziali

The experiments by Piziali have been used by several authors in their studies of 2D DS. Regardless of their popularity, Ekaterinaris [54] was the only author who attempted the calculation of the 3D case. The case considered by Ekaterinaris has also been used in this work and is an oscillatory motion with a mean angle of 11^o, amplitude of 4.2^o and reduced pitch rate $k = 0.096$. For his 3D experiments, Piziali [22] used a small number of spanwise stations, equipped with pressure transducers and reduced the pressure measurements at each spanwise station to sectional coefficients of lift, moment and drag. The data gathered during numerous oscillations were averaged in time. Figure 4.22 presents the comparison between CFD and Piziali's data. For this case, the stall angle is slightly exceeded and the inboard part of the wing experiences mild dynamic stall. As can been seen from the lift loop at the inboard wing sections, the c_l and c_d of the upstroke part of the motion is higher than that of the downstroke motion. At the same time, the hysteresis of the c_d coefficient is much larger than that of the c_l. As the tip is approached, the hysteresis loops of both the c_l and c_d coefficients, become much less narrow, indicating the influence of the tip vortex which dominates in the near the tip region and whose characteristics depend primarily on the AoA of the wing. Towards the tip, the flow is more attached and this is shown by the much thiner hysteresis loops. The agreement between CFD and experiments remains favourable up to the last station with a mild shift of the CFD results towards lower lift. It has to be noted that near the tip the wing model had a support structure which was not included in the CFD model and might had an effect to the quality of the near the tip measurements. Closer examination of the outboard loops indicates that the shift between the CFD results and the experiments is of the order of 1 degree which could also be attributed to wing flex during the experiment.

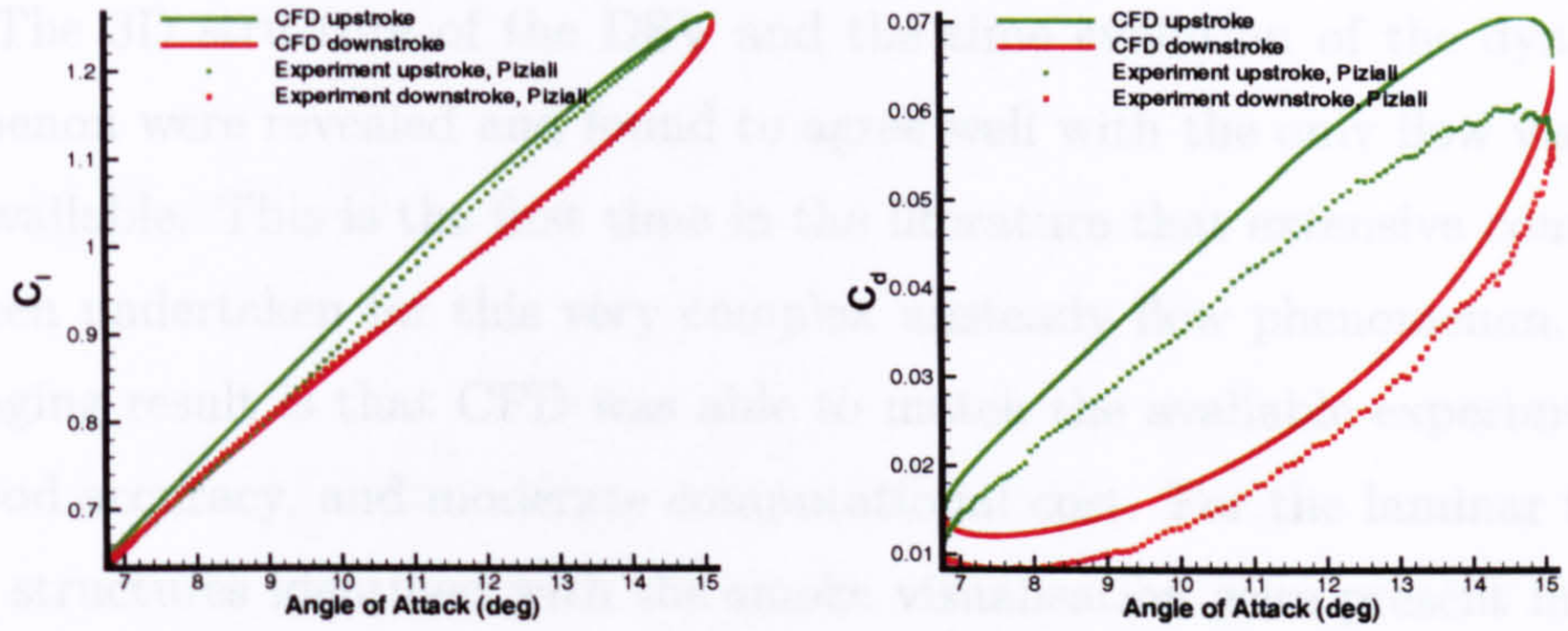

(a) station 1

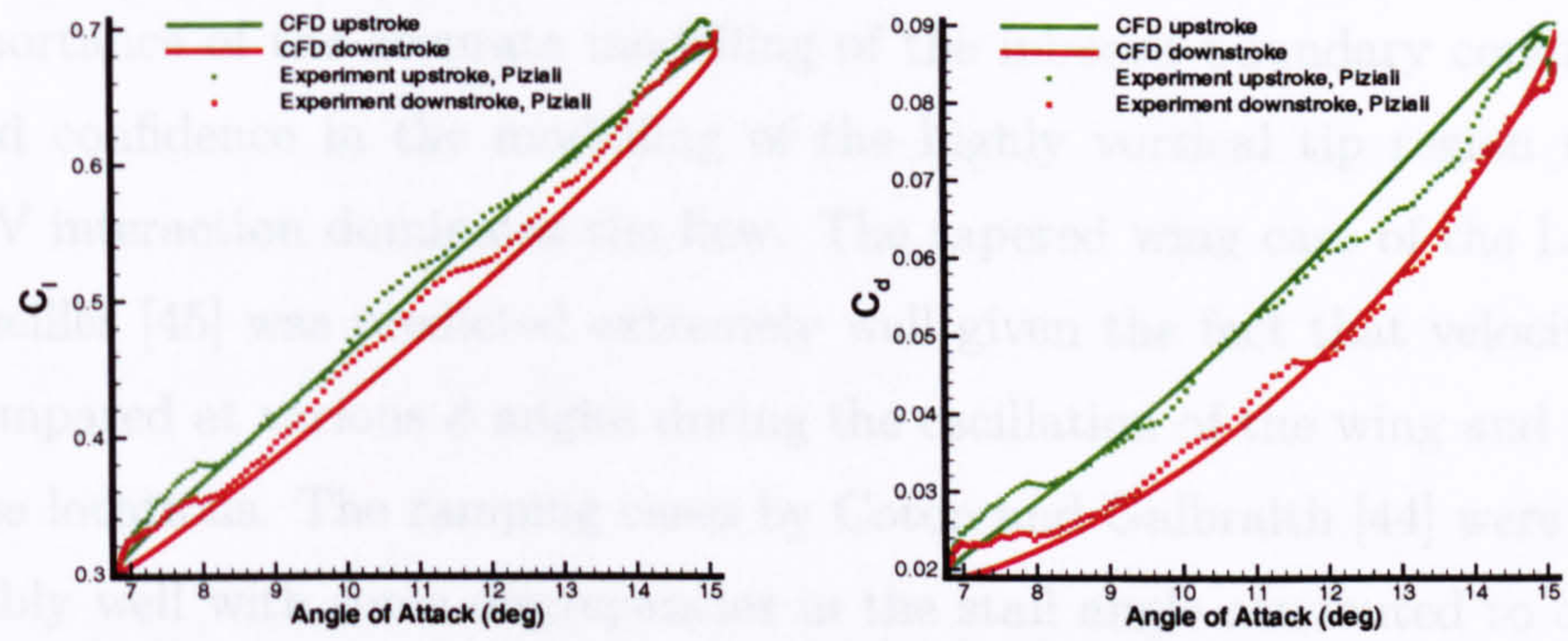

(b) station 2

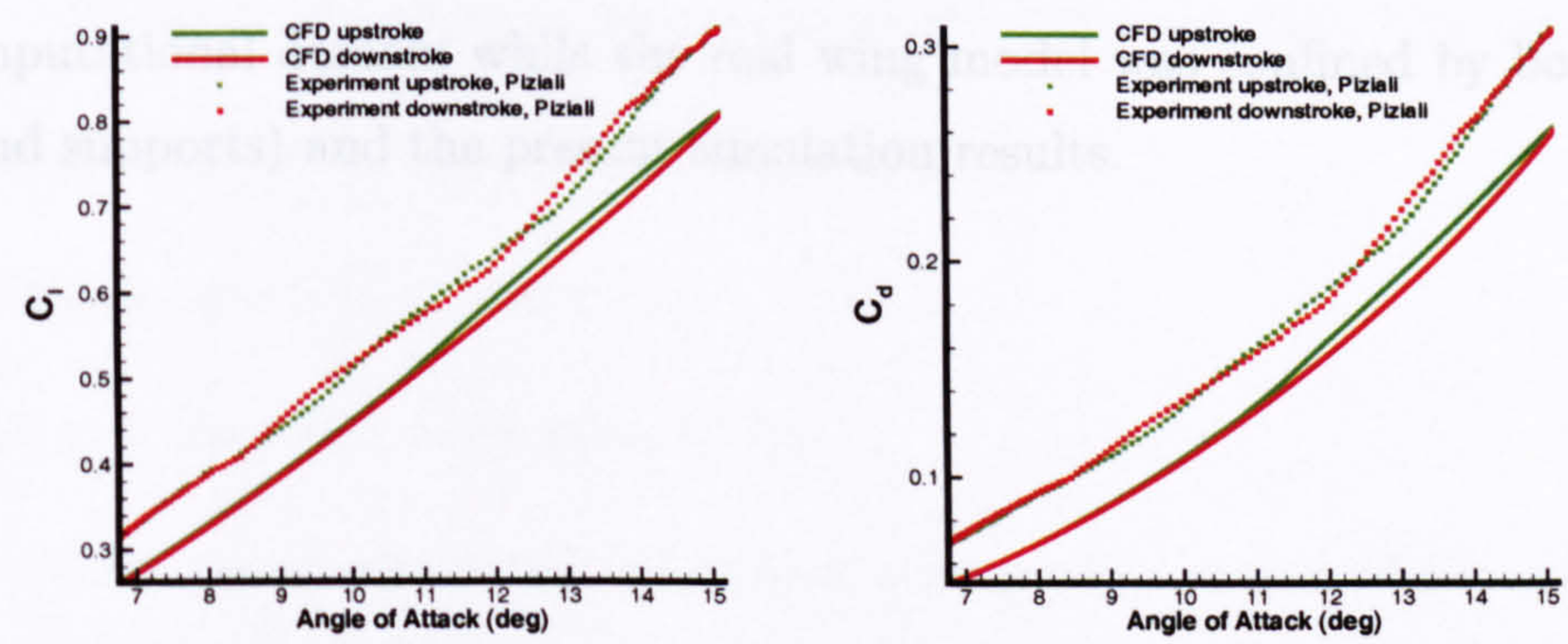

(c) station 3

Figure 4.22: Comparison between experimental and CFD hysteresis loops for the sectional loads at three stations (a) z/s=0.47, (b) z/s=0.966 and (c) z/s=0.995. The conditions correspond to run r0329 of Piziali [22]. Oscillating wing motion between 7^o and 15^o, $Re = 2.0 \times 10^6$, $M = 0.3$.

4.6 Summary

Detailed validation of a CFD method has been undertaken for 3D dynamic stall cases. The 3D structure of the DSV and the time evolution of the dynamic stall phenomenon were revealed and found to agree well with the only flow visualisation study available. This is the first time in the literature that extensive computations have been undertaken for this very complex unsteady flow phenomenon. The first encouraging result is that CFD was able to match the available experimental data with good accuracy, and moderate computational cost. For the laminar test cases, all flow structures identified with the smoke visualisation were present in the CFD solutions and the flow topology was found to be predicted with remarkable precision. The comparisons with the experiments performed by Schreck and Helin [41], revealed the importance of the accurate modelling of the inboard boundary conditions and provided confidence in the modelling of the highly vortical tip region where the DSV-TV interaction dominates the flow. The tapered wing case of the Laboratory of Marseilles [45] was predicted extremely well given the fact that velocity profiles were compared at various ϕ angles during the oscillation of the wing and at various spanwise locations. The ramping cases by Coton and Galbraith [44] were predicted reasonably well with some discrepancies in the stall angle attributed to differences between the conditions of the experimental investigation (for example, the CFD computations have been performed with free-stream conditions at the far field of the computational domain while the real wing model was confined by both tunnel walls and supports) and the present simulation results.

Chapter 5

Flow Topology During DS

5.1 Introduction

Having established confidence on the CFD method, further computations were attempted. The questions addressed in this chapter are:

- What is the overall topology of the DSV?
  - What is the effect of inboard conditions to the topology of the DSV ?
  - What is the topology of the DSV/TV interaction?
  - What is the effect of Re number to the DSV and DSV/TV interaction?
  - What is the effect of M number to the DSV and DSV/TV interaction?
- What is the effect of planform shape to DS?
- What is the effect of yaw to DS?
- What is the effect of rotation to DS?

The questions raised above will be, where appropriate, answered in a qualitative manner, since appropriate experimental data do not currently exist. Therefore, flow visualisation will play a primary role in this process. DS produces impulsive, highly three-dimensional vortex dominated flows. It is clear, that in order to be able to draw meaningful conclusions on issues like the shape, trajectory and interactions of these vortical structures, we need to trust our visualisation methods. When an experimentalist releases dye in a water tunnel or smoke in a wind tunnel, an impression of the flowfield is generated by the motion of coloured particles in a transparent background. A similar 'particle tracking' technique exists in CFD, where

the test fluid particles follow the numerical solution of the vector field through successive unsteady solutions (also known as Streaklines). However, in the case of 3D flows this method can be computationally very expensive for two reasons: (a) for every CFD run a large number of unsteady solutions need to be stored to ensure smooth and accurate tracking leading to excessive storage requirements and (b) the actual process of tracking is numerically intensive, requiring machines with fast CPUs and high RAMs. An alternative and far more convenient way of re-creating the flowfield from the numerical solution is to use instantaneous streamlines. Streamlines are the locii of the tangents of the velocity vectors at a given solution timestep. Streamlines and streaklines are identical in the case of steady flows, however, in unsteady flows the flowfields they re-create can be considerably different. In the case of flows involving DS, the degree of similarity between the 'true' streaklines and the 'virtual' streamlines depends on two parameters: (a) the Re and (b) the frequency of the wing's motion. The lower the Re is, the longer it will take to the fluid particles to travel from the leading edge to the trailing edge. Therefore, the higher the chance for the instantaneous flowfield to change during this time interval. Also, the higher the frequency of the motion is, the higher the unsteadiness of the flowfield will be, thus causing even more deviation to the flow pattern based on streamlines from the actual flow pattern based on streaklines. Figures 5.1(a and b) show the two flowfields for $\alpha = 60^o$ (case 1 of Table 5.1), generated by streaklines and streamlines respectively. The size, shape and positioning of the DSV appears to be identical in both cases. Since this motion represents the lower Re and higher k considered in this study and streamlines appear to be a good approximation of the streaklines, it is expected that flowfields based on streamlines can adequately represent the flowfields for all other cases in the present study.

5.1. INTRODUCTION

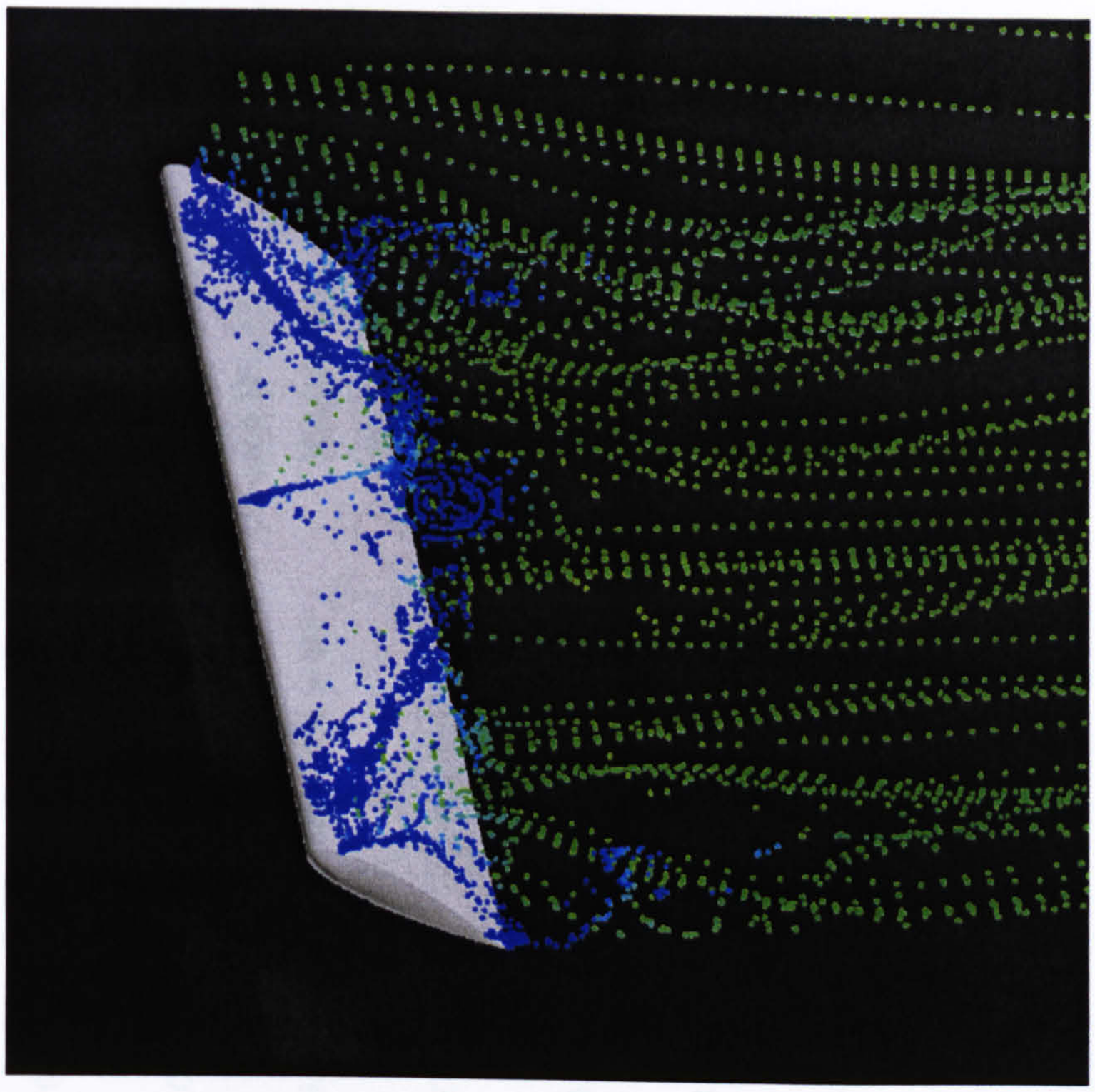

(a)

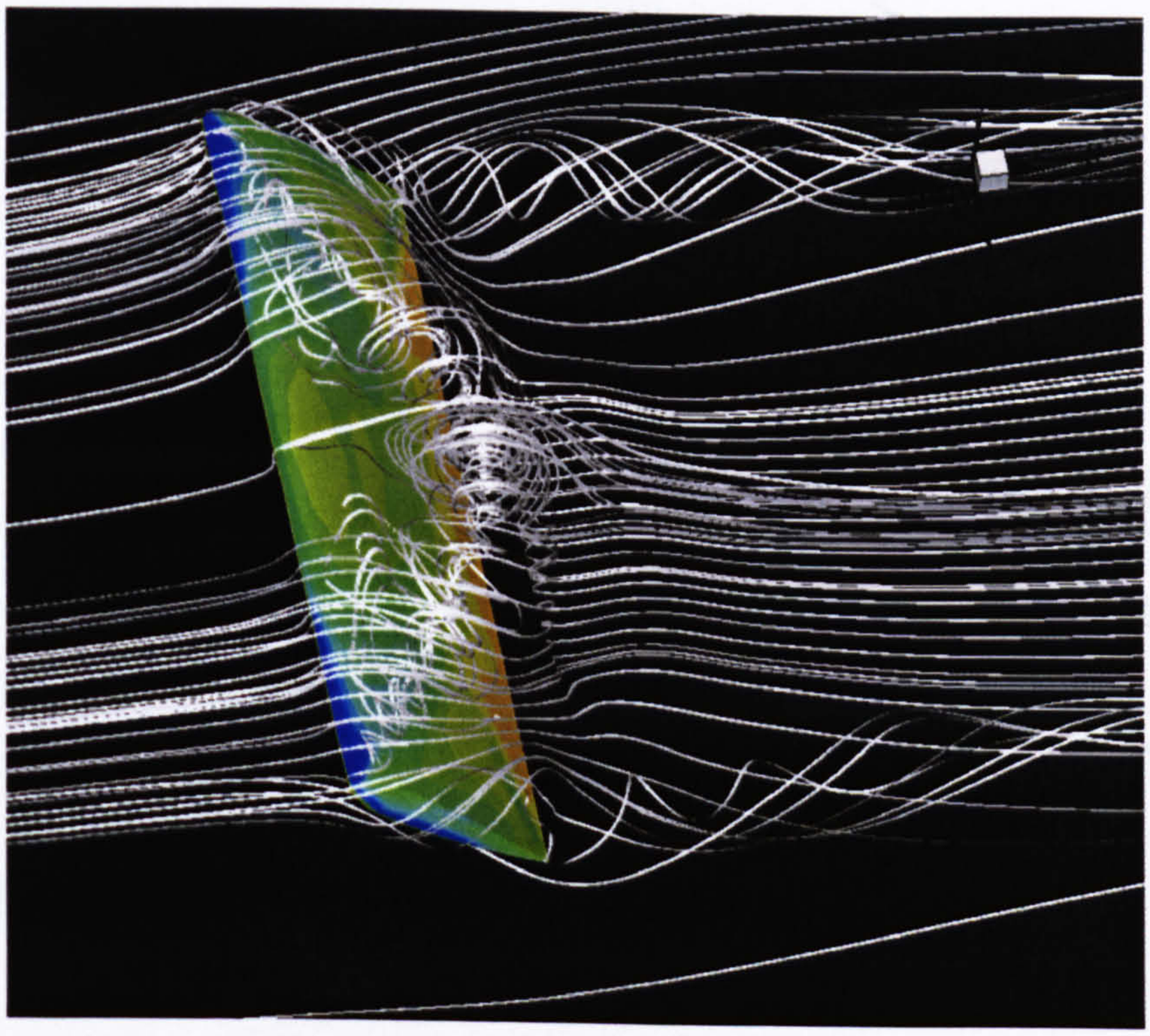

(b)

Figure 5.1: DSV shown at 60^o with (a) streaklines and (b) streamlines. Case 1 from Table 5.1. $\alpha^+ = 0.2$.

Case	Grid Size	Motion	k/α^+	β	M	Re	Wing Model
1	2,268,000	ramping	0.2	0^o	0.1	1.3×10^4	NACA 0015
		$\alpha = 0^o - 60^o$					F,$AR = 3$
2	729,000	ramping	0.2	0^o	0.2	6.9×10^4	NACA 0015
		$\alpha = 0^o - 60^o$					HS,$AR = 4$
3	1,728,000	ramping	0.2	0^o	0.1	6.9×10^4	NACA 0015
		$\alpha = 0^o - 60^o$					HN,$AR = 4$
4	1,828,000	oscillation	0.06	0^o	0.2	10×10^6	NACA 0012
		$\alpha = 18^o + 6^o sin(kt)$					tapered,HS,$AR = 3.6$
5	1,134,000	ramping	0.02	0^o	0.16	$1.5 \times 10^6 - 9.4 \times 10^4$	NACA 0015
		$\alpha = -5^o - 40^o$					HS,$AR = 3.0$
6	2,632,000	ramping	0.2	0^o	0.1	6.9×10^4	HS NACA 0015
		$\alpha = 0^o - 60^o$					twisted,HS,$AR = 10.0$
7	1,134,000	ramping	0.02	0^o	0.16	1.5×10^6	NACA 0015
		$\alpha = -5^o - 40^o$					swept-back,HS,$AR = 3.0$
8	1,000,000	oscillation	0.1	0^o	0.25/0.55	10×10^6	NACA 0015
		$\alpha = 10^o + 10^o sin(kt)$					F,$AR = 5.0$
9	1,000,000	oscillation	0.05/0.1/0.15	$0^o/15^o$	0.25	10×10^6	NACA 0012
		$\alpha = 10^o + 10^o sin(kt)$					F,$AR = 10$
10	1,000,000	rotation with pitch	0.1	n/a	0.25	10×10^6	NACA 0015
		$\alpha = 10^o + 10^o sin(kt)$					F,$AR = 5.0$
		$beta = 0^o - 180^o$					

F: Full wing model H: Half wing model S: Symmetry boundary condition on root plane N: Non-slip boundary condition on root plane

Table 5.1: Details of the CFD runs performed. In runs that involved rotational motion, the rotating and pitching cycles were in phase. The yaw angle β is defined as the angle of the freestream with the root chord.

5.2 Shape of the DSV and the DSV-TV Interaction

Figure 5.2 shows the vortex cores (left) and the streamlines (right) from the CFD calculations for case 3 of Table 5.1. The phenomenon starts inboards with the formation of a vortex at the leading edge which is subsequently detached from the wing and grows in size. The growth reduces as one moves towards the tip of the wing (Figure 5.2a) and the core of the vortex bends upstream towards the leading edge of the wing tip (Figure 5.2b). Further on during the cycle, one cannot fail to notice that on the mid-span of the wing (Figure 5.2c) the flow evolves in a similar manner to the 2D case [20]. However, as the DSV is formed, the core of the vortex stays bound to the LE region of the wing-tip while the main part of the DSV is convected downstream. As the DSV grows in size and its core moves above the surface of the wing, however, near the wing-tip the vortex is still bound. The result of the DSV pinning is to cause buckling leading to the Ω shape described in [39] and termed in [40]. The phenomenon becomes more and more interesting as the tip vortex grows with increasing α, leading to a Π-Ω vortex configuration which is a combination of the two well-established vortical systems: the tip-vortex which appears for all wing tips and the DSV which is unique to unsteady flows. The outboard part of the wing is exposed to the downwash created by the tip, and therefore is subjected to lower AoA than the rest of the wing span. The area above the wing's surface is also exposed to the inboards circulation of the TV. The effect of the downwash is to reduce the size of the DSV near the tip and the combined effect of the inboards directed blow of the TV and the reduced size of the DSV near the tip is to create the characteristic Ω arching of the DSV. The flow near the LE of the wing tip is complex and the streamtraces originating just upstream of the tip are directed either towards the tip-vortex or the dynamic stall vortex. Apart from the main vortices all secondary vortices appearing during 2D dynamic stall are present in the 3D case. Interestingly, the secondary vortices formed below the DSV also appear to take the same Ω shape and bend at the LE of the wing tip, however, these are terminated on the wing's surface. It therefore appears, that the LE of the tip is a singularity point where the $\Pi-\Omega$ system stays attached on the solid surface. At this point the free stream can feed both vortices with momentum. Thinking in terms of Helmholtz's vortex theorems, this flow configuration is very interesting. The DSV

and the secondary vortices cannot end up in the freestream, but are forced to either join the tip vortex or end on a solid surface. Figures 5.3a-f show 2D spanwise slices of streamlines superimposed on contours of w-velocity for the same case as in Figure 5.1. Figure 5.3a corresponds to a location very close to the tip ($z/s = 1.11$) and Figure 5.3f corresponds to a location very close to the wing's half-span ($z/s = 0.03$). The wing in this case has an $AR = 3$ and the convention used is that $z/s = 0$ corresponds to the mid-span section, while $z/s = 1.5$ corresponds to the edge of the tip. The boundary between the green-blue and green-yellow regions is where the w-velocity changes sign. Negative w corresponds to crossflow directed inboards and positive w corresponds to crossflow directed outboards. Figure 5.3a shows a section of the DSV close to the LE. The flow across most of the $z/c = 2.22$ plane is positive with the exception of the blue-shaded area which dominates almost half a chord's length above the wing's surface. Interestingly enough, underneath the negative crossflow exists a positive, occupying a very thin region just over the surface of the wing. However, the crossflow through the section of the DSV which can be seen at approximately $x = c/4$, is entirely negative. Further inboards, in Figure 5.3b, the DSV has moved downstream and so has the area of negative w-velocity. The two counter-rotating LEV's occupy entirely a positive crossflow region. However, Figures 5.3c-f, suggest that increasingly, a part of the DSV section enters a positive crossflow area, thus inducing shear forces within its core. These shear forces could be partly responsible for the complex arching shape of the DSV shown in Figure 5.1.

5.2. SHAPE OF THE DSV AND THE DSV-TV INTERACTION

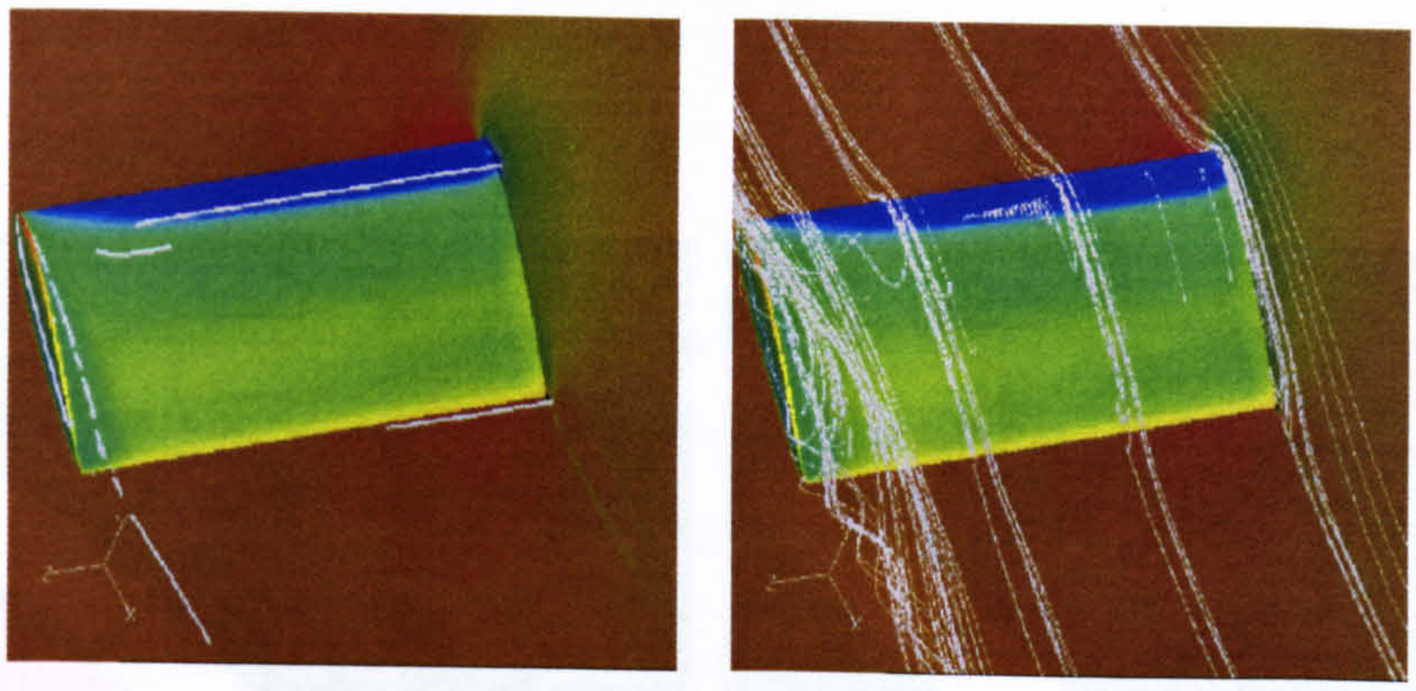

(a) 13 deg

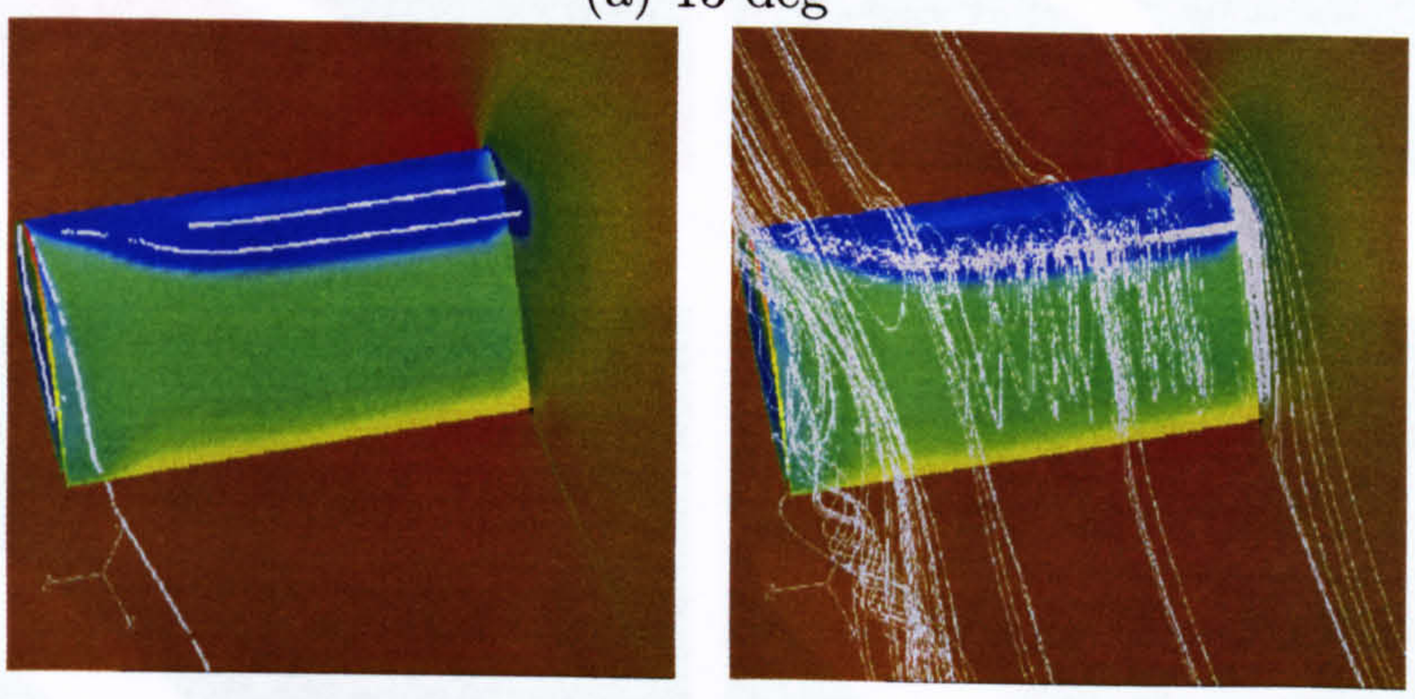

(b) 20 deg

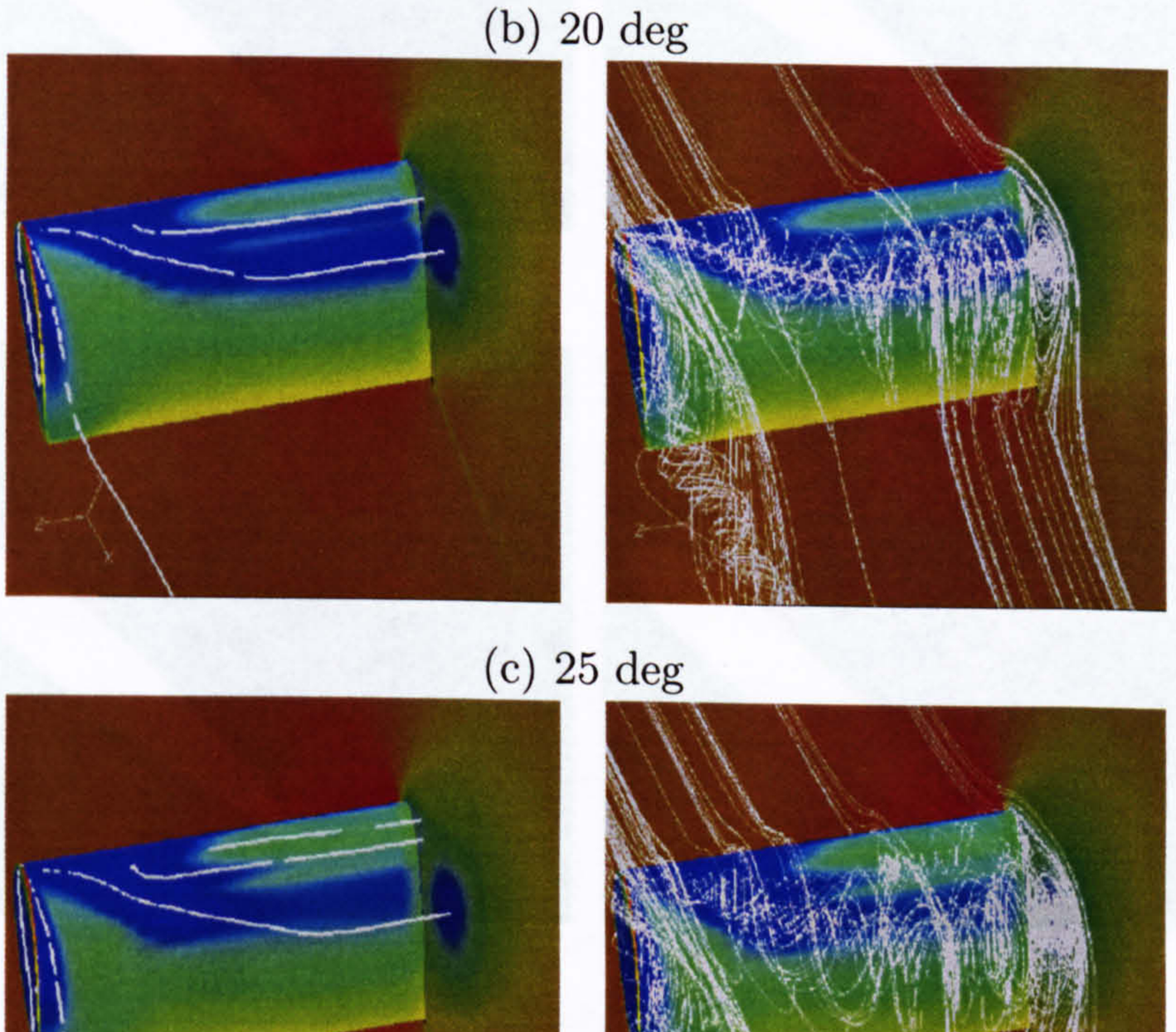

(c) 25 deg

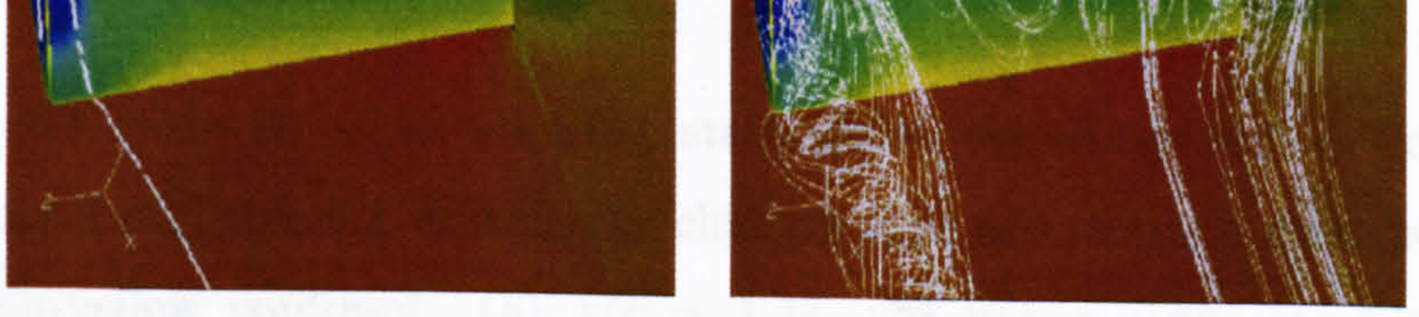

(d) 28 deg

Figure 5.2: Vortex cores (left) and streamtraces (right) for case 2 of Table 5.1. (a) 13^o, (b) 20^o, (c) 25^o and (d) 28^o.

5.2. SHAPE OF THE DSV AND THE DSV-TV INTERACTION

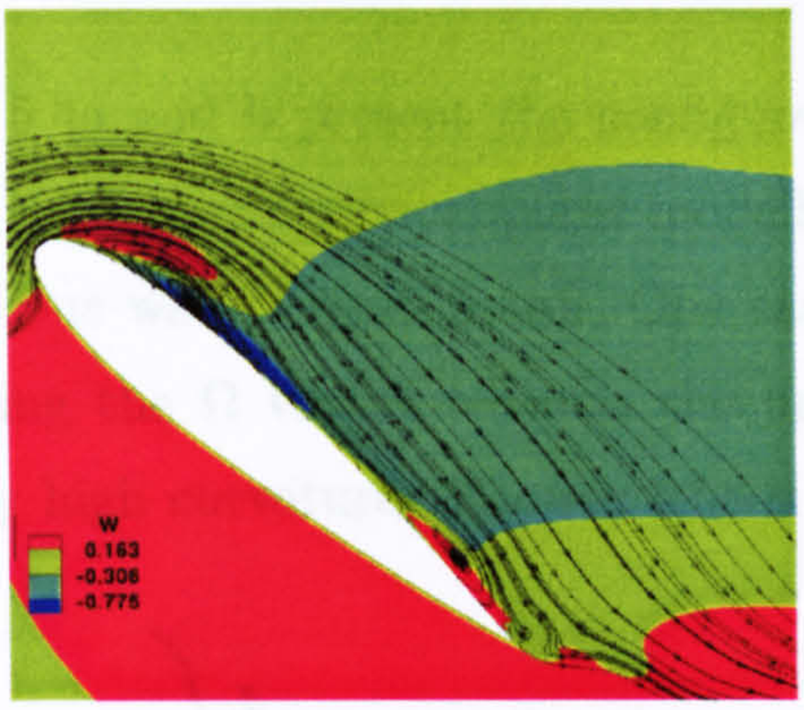

(a)

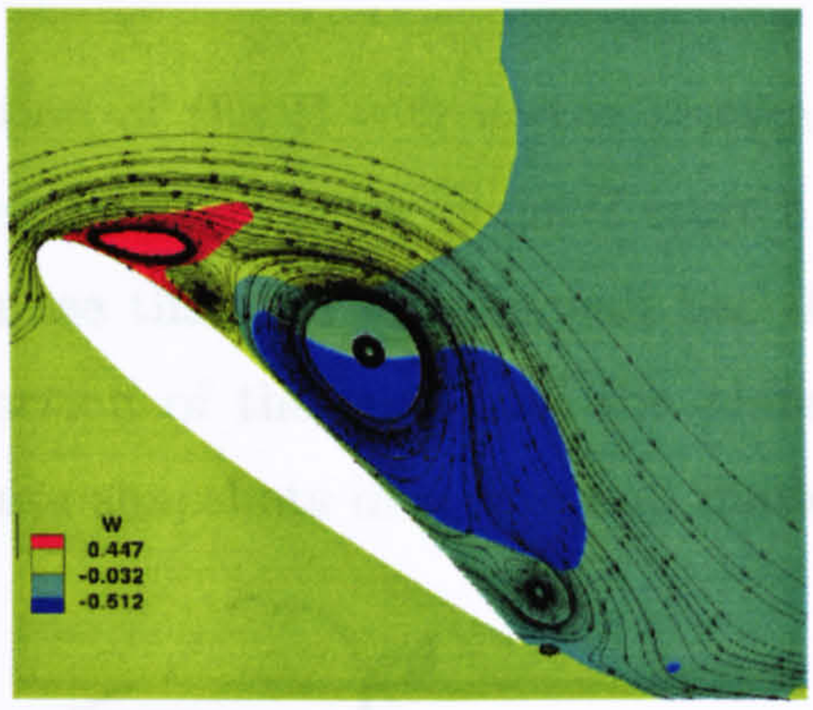

(b)

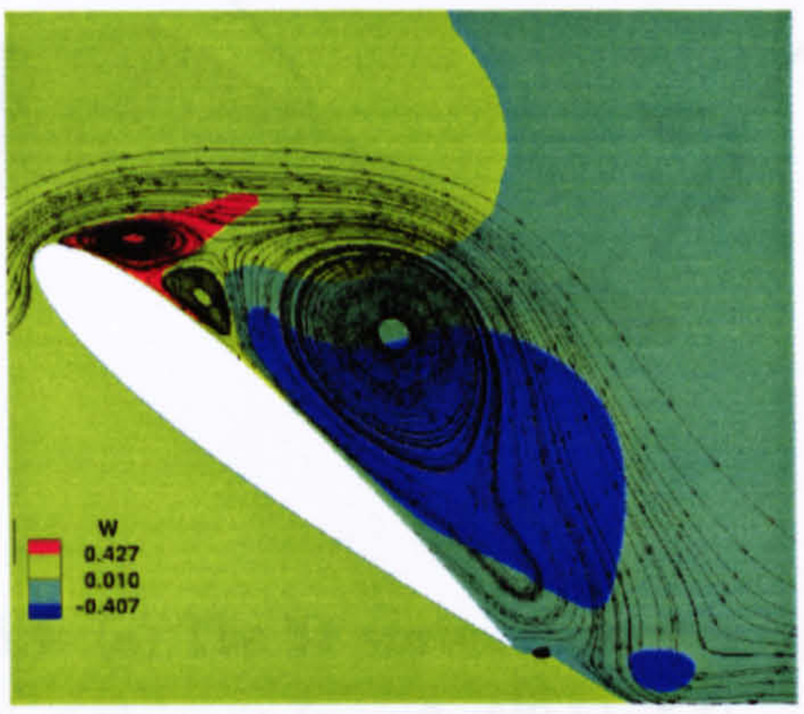

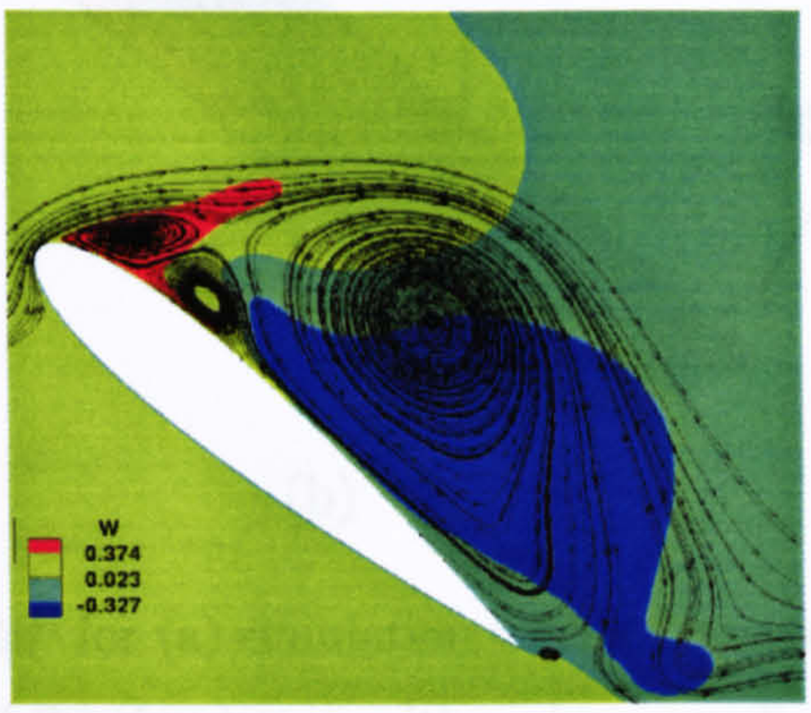

(c)

(d)

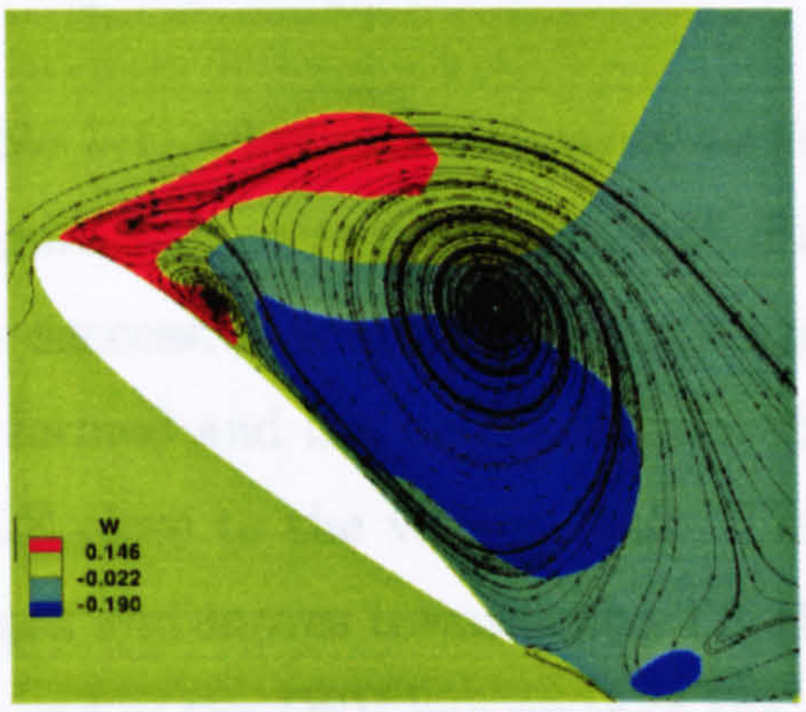

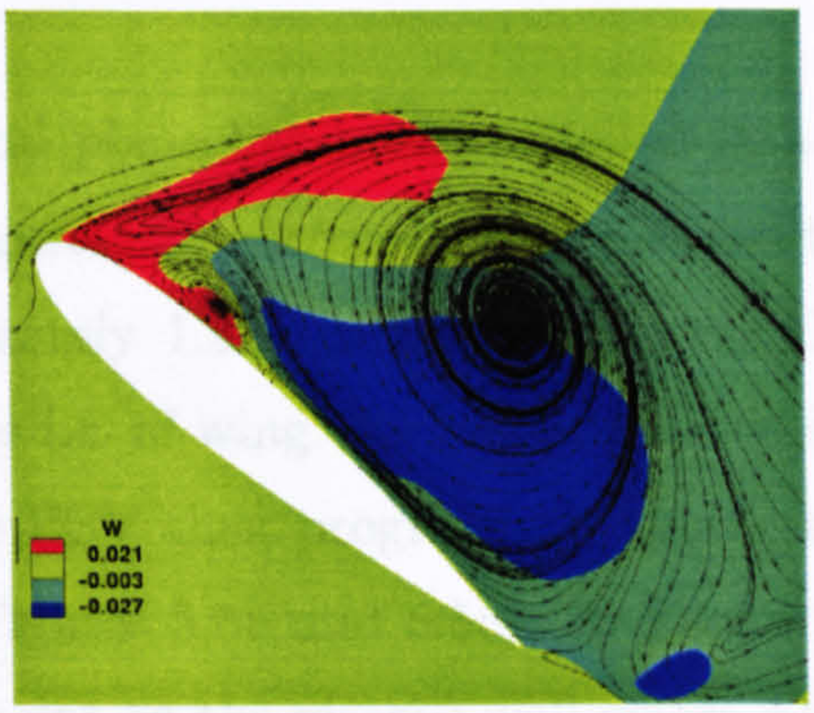

(e)

(f)

Figure 5.3: 2D spanwise slices showing streamlines superimposed on contours of w-velocity for case 1 of Table 5.1. w-velocity changes sign across the border between green-blue and green-yellow contours. (a) $z/c = 1.11$, (b) $z/c = 0.66$, (c) $z/c = 0.57$, (d) $z/c = 0.48$, (e) $z/c = 0.21$ and (f) $z/c = 0.03$.

5.3 Effect of the Inboard Boundary Conditions to the Shape of the DSV

Figures 5.4a and b present the configuration of the $\Pi - \Omega$ vortex system for the cases of the inboard vertical plane modelled as a symmetry plane (Figure 5.4a) and as a viscous wall (Figure 5.4b). One can see that the viscous wall has the effect of bending the Ω vortex towards the junction of the wing and the plate, giving it a very high curvature. Figures 5.5a-h are snapshots of a ramp-up motion (case

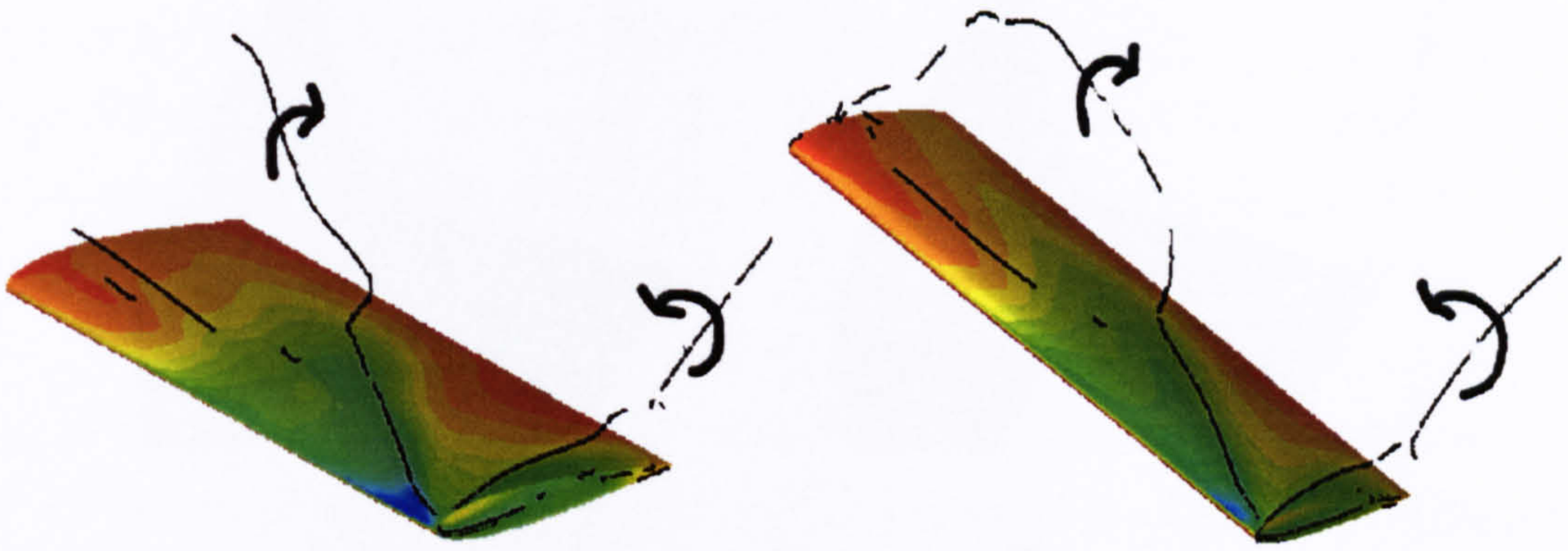

(a) (b)

Figure 5.4: (a) The 'Ω' vortex cores at $\alpha = 44^o$ for (a) simulation with a symmetry plane condition at the root (case 2 of Table 5.1) and (b) simulation with a viscous wall condition at the mid-span plane (case 3 of Table 5.1).

3 of Table 5.1) where the inboards vertical plane has been modelled as a viscous wall. Figure 5.5a corresponds to 26.5^o, Figure 5.5h corresponds to 37^o and the AoA between successive snapshots is approximately 1.5^o. In Figure 5.5, the DSV has already formed and has detached from the LE of wing. Its inboard end is attached to the LE close to the viscous wall. The DSV then progressively moves up while its inboard end moves towards the TE (Figures 5.5b and 5.5c). In Figure 5.5d the inboard end of the DSV has reached the point on the viscous wall where $x/c = 0.25$ which is the PA of the motion. It is remarkable that while the DSV further grows and buckles upwards, its inboard end stays close to the Pitch Axis (PA) for the part of the motion corresponding from 29.5^o to 35^o. Shortly after that, it detaches from the PA location of the viscous wall and continues in a backwards and upwards trajectory. Modelling the mid-span as a viscous wall, induces a vortical structure whose centre is the trace of the Pitch Axis (PA) onto the mid-span plane, and angular velocity, the angular velocity of the wing's rotation. However, during the

early stages of the formation of the DSV, the DSV and this 'viscous wall vortex' are of comparable strength and during the DSV's downstream motion they tend to merge. The consequence of this interaction is the tendency of the inboard part of the DSV to stick to the PA location. In the case of the mid-span plane being modelled as a symmetry plane, no such relation seems to exist between the PA and the appearing location of the DSV.

5.3. EFFECT OF THE INBOARD BOUNDARY CONDITIONS TO THE SHAPE OF THE DSV

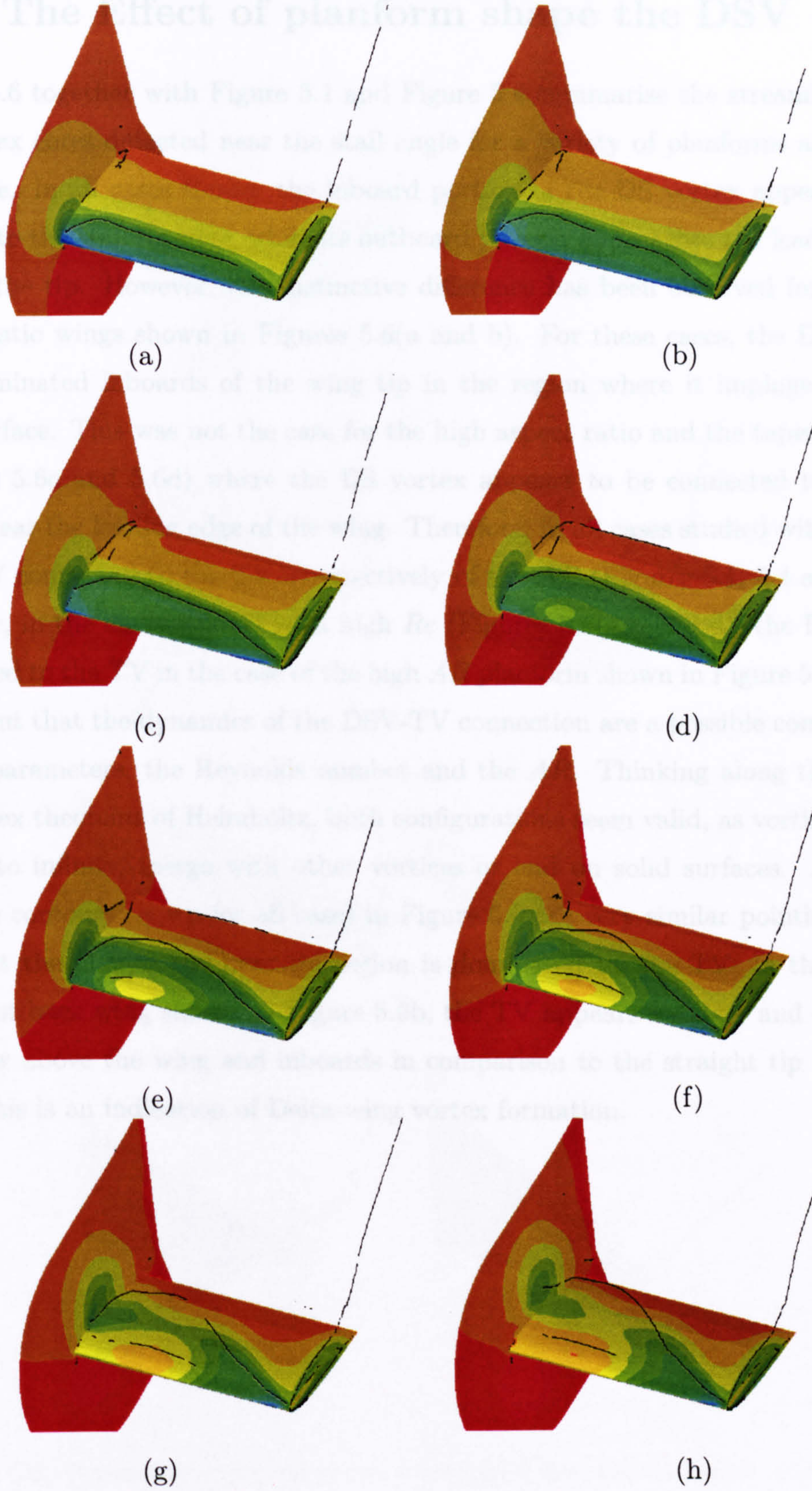

Figure 5.5: (a) The 'Ω' vortex cores for 8 different angles of attack (case 3 of Table 5.1). The root plane is modelled with non-slip conditions. (a) 26.5^o, (b) 28^o, (c) 29.5^o, (d) 31^o, (e) 32.5^o, (f) 34^o, (g) 35.5^o and (h) 37^o.

5.3. EFFECT OF THE INBOARD BOUNDARY CONDITIONS TO THE SHAPE OF THE DSV

5.4 The Effect of planform shape the DSV

Figure 5.6 together with Figure 5.1 and Figure 5.4 summarise the streamlines and the vortex cores detected near the stall angle for a variety of planforms across the *Re* range. In all cases shown, the inboard portion of the DS vortex appears to be parallel to the trailing edge, while its outboard portion approaches the leading edge part of the tip. However, one distinctive difference has been observed for the low aspect ratio wings shown in Figures 5.6(a and b). For these cases, the DS vortex was terminated inboards of the wing tip in the region where it impinged on the wing surface. This was not the case for the high aspect ratio and the tapered wings (Figures 5.6c and 5.6d) where the DS vortex appears to be connected to the tip vortex near the leading edge of the wing. Therefore, in all cases studied with low *Re* the DSV connected to the TV irrespectively of the *AR* (Figures 5.1, 5.4 and 5.6c). However, in the cases studied with high *Re* (Figures 5.6(a,b and d), the DSV only connected to the TV in the case of the high *AR* planform shown in Figure 5.6d. This points out that the dynamics of the DSV-TV connection are a possible combination of two parameters, the Reynolds number and the *AR*. Thinking along the line of the vortex theorems of Helmholtz, both configurations seem valid, as vortices either extend to infinity, merge with other vortices or end on solid surfaces. Also, the pressure contours shown for all cases in Figure 5.6 are very similar pointing to the fact that the flow in the near tip region is dominated by the TV. In the case of the swept back wing shown on Figure 5.6b, the TV appears stronger and is formed somehow above the wing and inboards in comparison to the straight tip of Figure 5.6a. This is an indication of Delta-wing vortex formation.

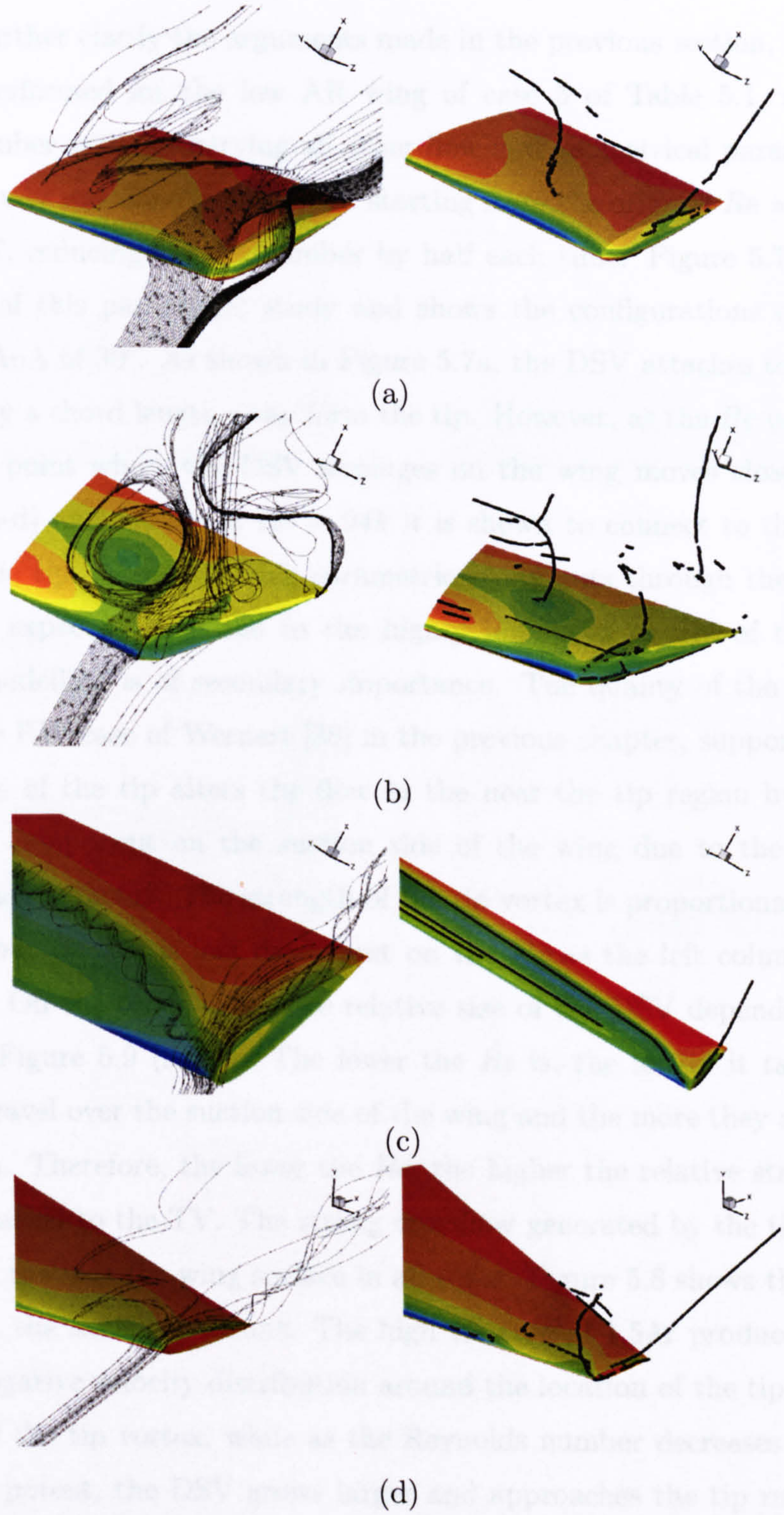

Figure 5.6: Streamlines (left) and vortex cores (right) near the stall angle. (a) Low aspect ratio wing with rounded tips (case 5 of Table 5.1), (b) swept back tip (case 7 of Table 5.1), (c) large aspect ratio wing with 10^o negative twist and flat tip (case 6 of Table 5.1), and (d) tapered wing with flat tip (case 4 of Table 5.1).

5.5 Effect of Re on the DSV-TV interaction

In order to further clarify the arguments made in the previous section, a parametric study was performed for the low AR wing of case 5 of Table 5.1, reducing the Reynolds number while preserving all other flow and geometrical parameters. This parametric study was done in five steps, starting from the original $Re = 1.5M$ down to $Re = 94K$, reducing the Re number by half each time. Figure 5.7 summarises the findings of this parametric study and shows the configurations of the vortex cores for an AoA of 30^o. As shown in Figure 5.7a, the DSV attaches to the wing at approximately a chord length away form the tip. However, as the Re is successively reduced, the point where the DSV impinges on the wing moves closer to the tip (Figures 5.7b-d) and finally, at $Re = 94k$ it is shown to connect to the TV at the LE part of the tip. Although, this parametric study cuts through the transitional regime, it is expected that due to the highly impulsive nature of the flow, the turbulence modelling is of secondary importance. The quality of the comparisons shown for the PIV case of Wernert [38] in the previous chapter, supports this view. The existence of the tip alters the flow in the near the tip region by inducing a negative $w-$ component on the suction side of the wing due to the direction of rotation of the tip vortex. The strength of the tip vortex is proportional to the AoA of the wing but its size is less dependent on the Re as the left column of Figure 5.9 suggests. On the other hand, the relative size of the DSV depends on the Re, as shown in Figure 5.9 (right). The lower the Re is, the longer it takes for fluid particles to travel over the suction side of the wing and the more they are energized by its motion. Therefore, the lower the Re, the higher the relative strength of the DSV is in relation to the TV. The strong crossflow generated by the tip, forces the DSV to bend towards the wing surface in all cases. Figure 5.8 shows the w-velocity magnitude at the same conditions. The high Re case of $1.5M$ produces an almost symmetric negative velocity distribution around the location of the tip showing the dominance of the tip vortex, while as the Reynolds number decreases and the TV becomes less potent, the DSV grows larger and approaches the tip region causing the w-velocity distribution to assume positive values.

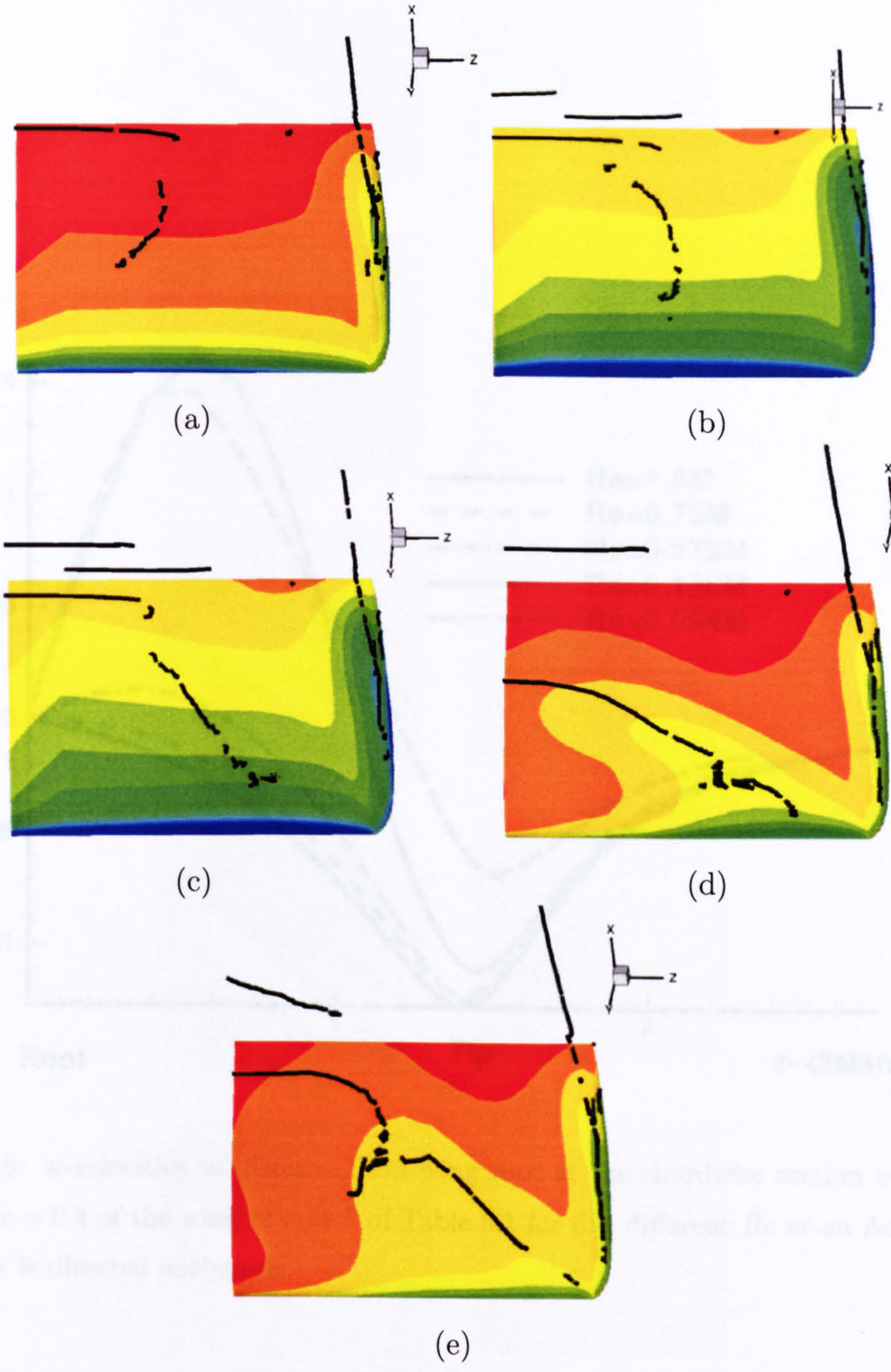

Figure 5.7: Plan view of the wing of case 5 of Table 5.1, showing the locations of the DSV for four different Reynolds numbers, at an AoA of 30^o. (a) $Re = 1.5M$, (b) $Re = 750k$, (c) $Re = 375K$, (d) $Re = 188K$, (e) $Re = 94K$.

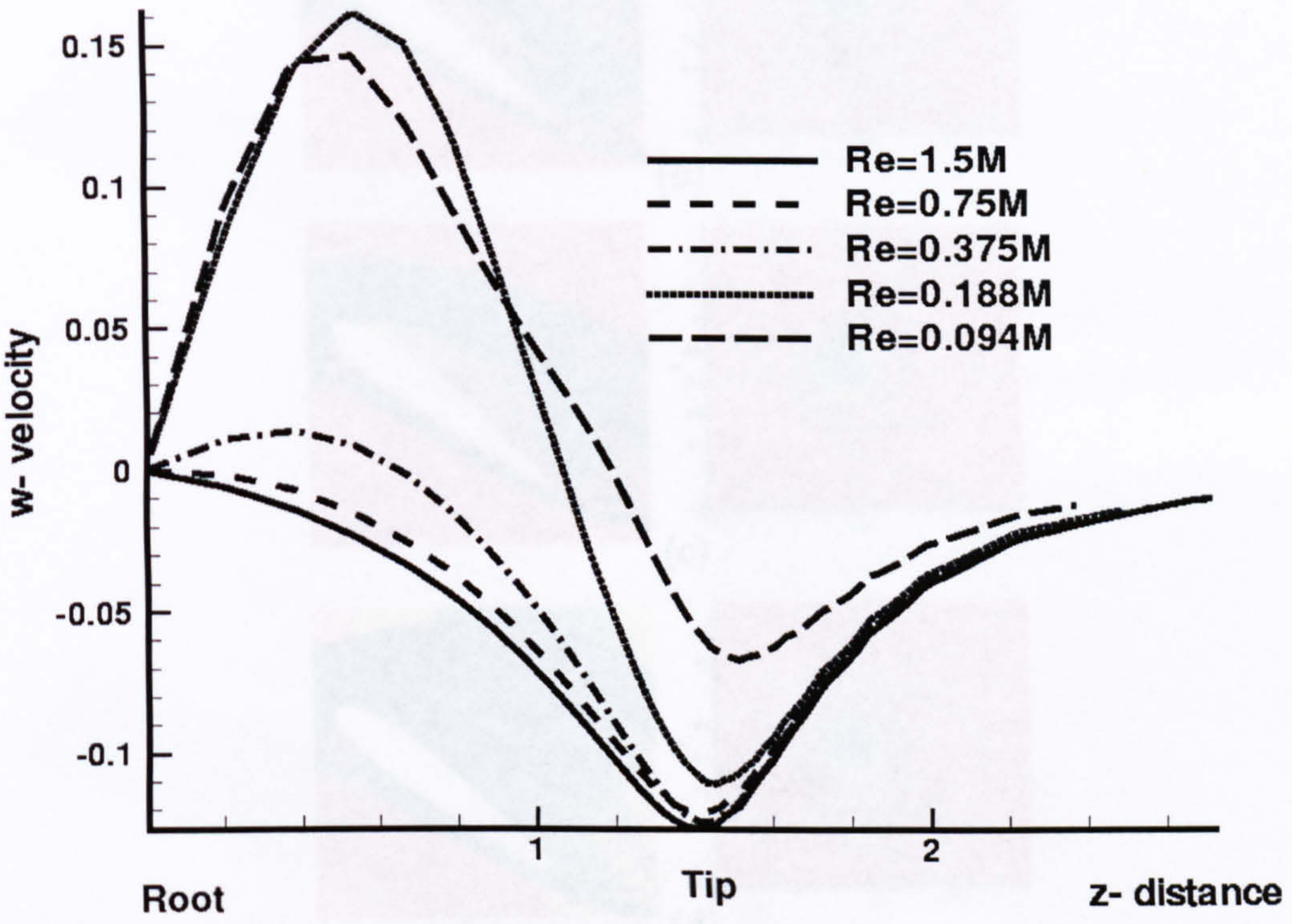

Figure 5.8: w-velocities vs distance from wing root at the chordwise section $x/c = 0.25$ and at $y/c = 0.4$ of the wing of case 5 of Table 5.1 for five different Re at an AoA of 30^o. Positive w is directed outboards.

5.5. EFFECT OF *RE* ON THE DSV-TV INTERACTION

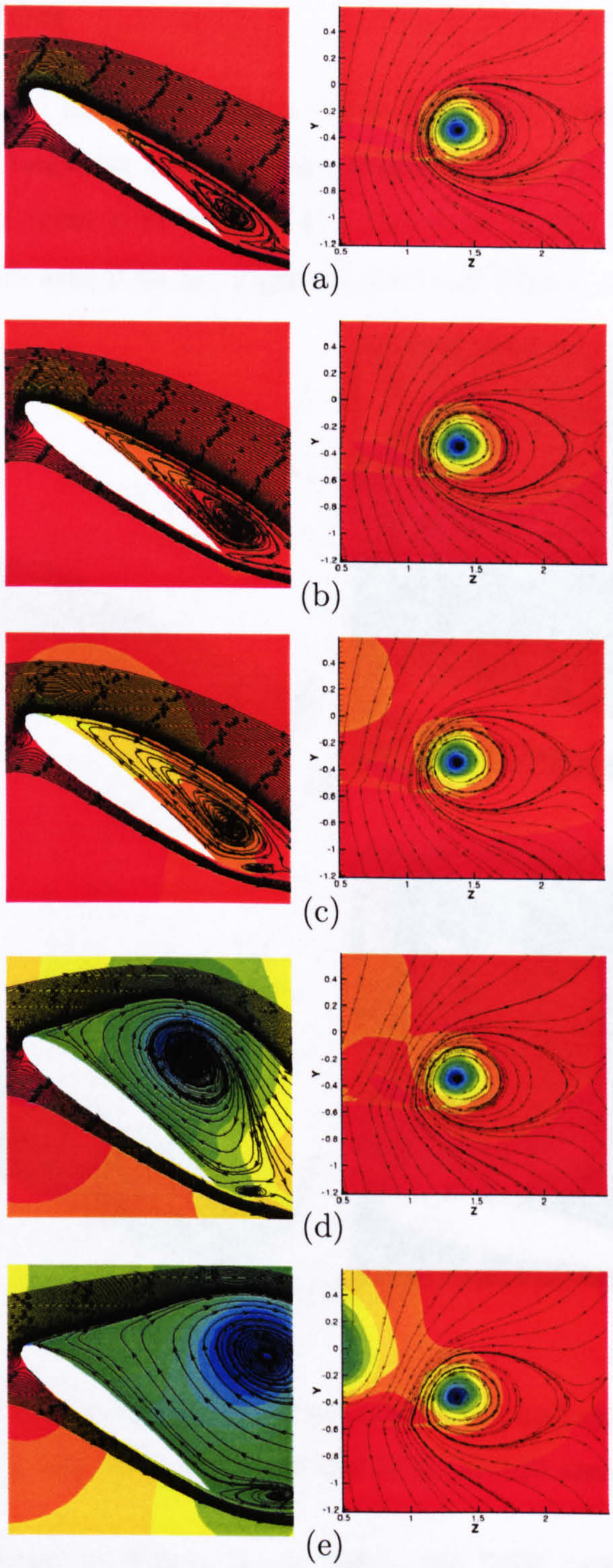

(a) (b) (c) (d) (e)

Figure 5.9: Chordwise section at half-span (left) and spanwise section close to the TE (right) of the wing of case 5 of Table 5.1, showing the locations and sizes of the DSV (left) and TV (right) for five different Re, at an AoA of 30^o. (a) $Re = 1.5M$, (b) $Re = 750k$, (c) $Re = 375K$, (d) $Re = 188K$, (e) $Re = 94K$.

5.6 Effect of Mach Number on the DSV-TV interaction

Figures 5.10(a and b) show the vortex cores (left) and streamlines over absolute z-vorticity contour maps on the mid-span (right) for an $AR = 5$ wing undergoing a sinusoidal motion (case 8 of Table 5.1). The AoA is 20^o the Re is 10^6 and the M numbers are 0.25 and 0.55 for Figure 5.10a and Figure 5.10b, respectively. In

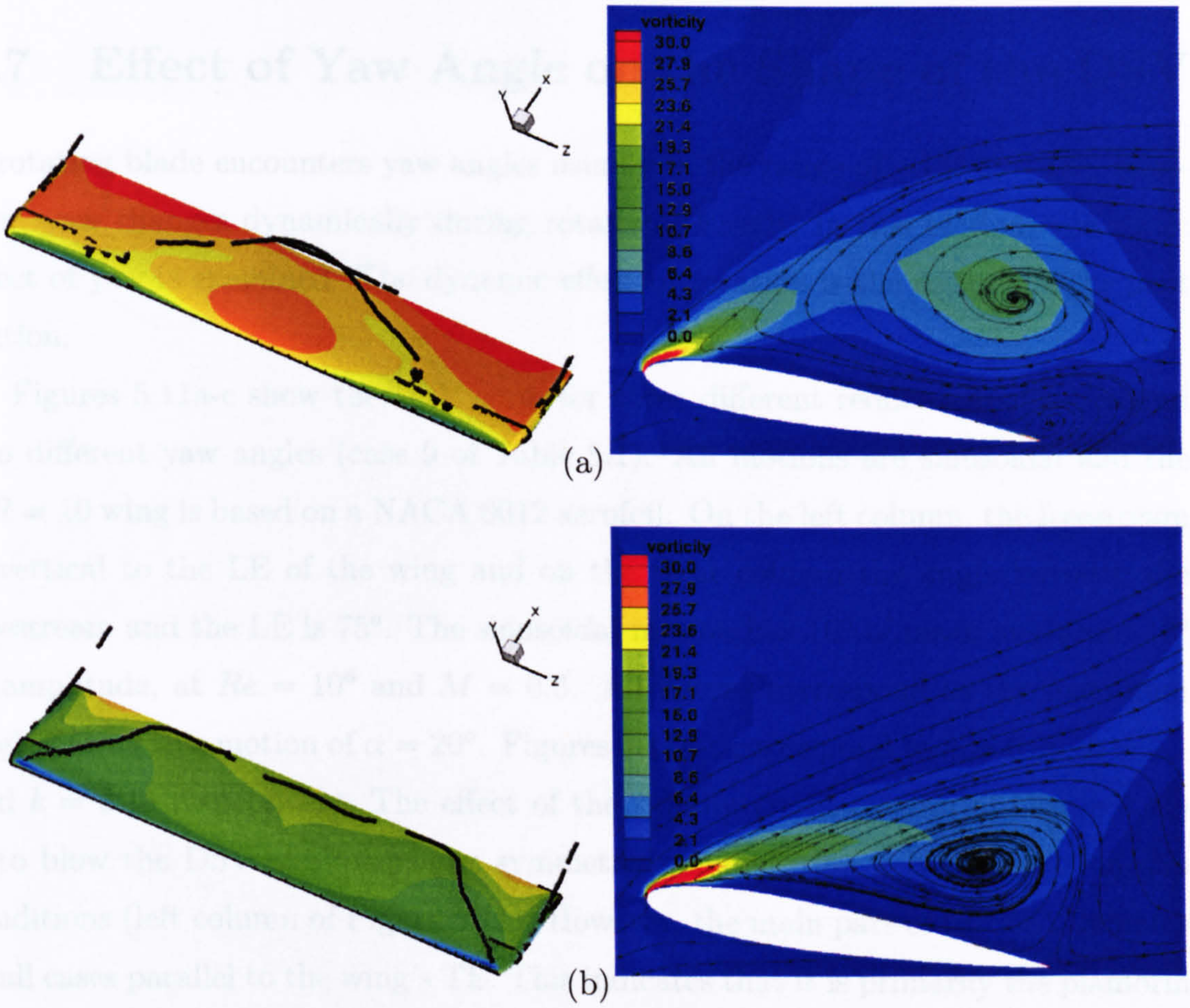

Figure 5.10: Vortex cores (left) and 2D slices at the wing's half span (right) corresponding to case 8 of Table 5.1. The AoA is 20^o and the M is (a) 0.25 and (b) 0.55.

the low M case shown in Figure 5.10a (left), the DSV terminates on the wing's surface approximately 1.5 chord lengths from the tip, indicating a low AR effect as explained in the previous section. However, in the case of the higher M case shown in Figure 5.10b (left), the DSV is shown to terminate at the LE part of the tip. Also, the right column of Figures 5.10a and 5.10b suggests that the DSV in the low M case attains a higher distance off the wing's surface compared to the high M

case. The right column of Figure 5.10 show higher vorticity values in the area of the DSV corresponding to the low M case (Figure 5.10a) as opposed to the high M case (Figure 5.10b). Therefore the less compressible flow of the low M results to a more energised DSV which grows larger in size, attains a higher position over the wing's surface, and becomes more exposed to the inboards spanwise flux generated by the TVs. This in turn causes the DSV to arch at a steeper angle than in the high M case of Figure 5.10b and detach from the tips.

5.7 Effect of Yaw Angle on the Shape of the DSV

A rotating blade encounters yaw angles usually in the range of -15^o to $+15^o$. However, yaw changes dynamically during rotation. Firstly, in this section, the static effect of yaw is examined. The dynamic effect of rotation is the subject of the next section.

Figures 5.11a-c show the DSV cores for three different reduced frequencies and two different yaw angles (case 9 of Table 5.1). All motions are sinusoidal and the $AR = 10$ wing is based on a NACA 0012 aerofoil. On the left column, the freestream is vertical to the LE of the wing and on the right column the angle between the freestream and the LE is 75^o. The sinusoidal motion has 10^o of mean angle and 10^o of amplitude, at $Re = 10^6$ and $M = 0.3$. All figures correspond to the maximum angle during this motion of $\alpha = 20^o$. Figures 5.11a-c correspond to $k = 0.05$, $k = 0.1$ and $k = 0.15$ respectively. The effect of the sideslip (right column of Figure 5.11) is to blow the DSV away from the symmetric configuration it has in zero sideslip conditions (left column of Figure 5.11). However, the main part of the DSV remains in all cases parallel to the wing's TE. This indicates that it is primarily the planform shape rather than the orientation of the freestream the defining parameter of the shape of the DSV.

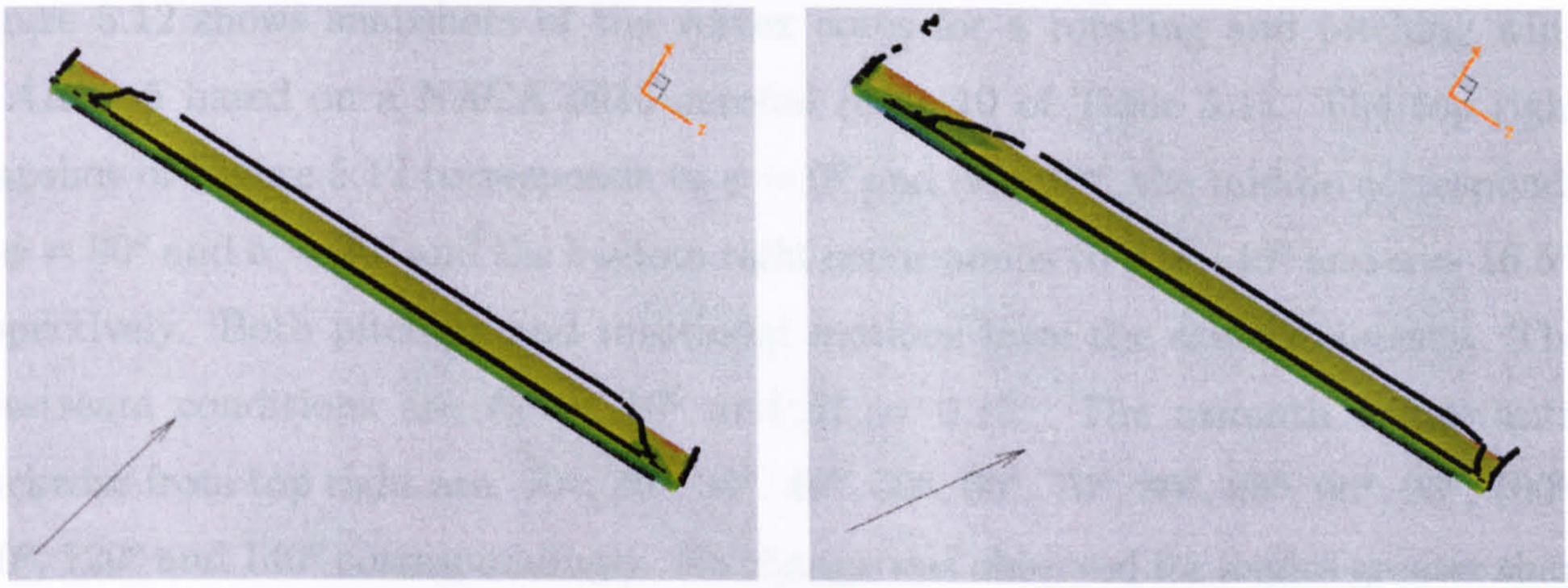

(a)

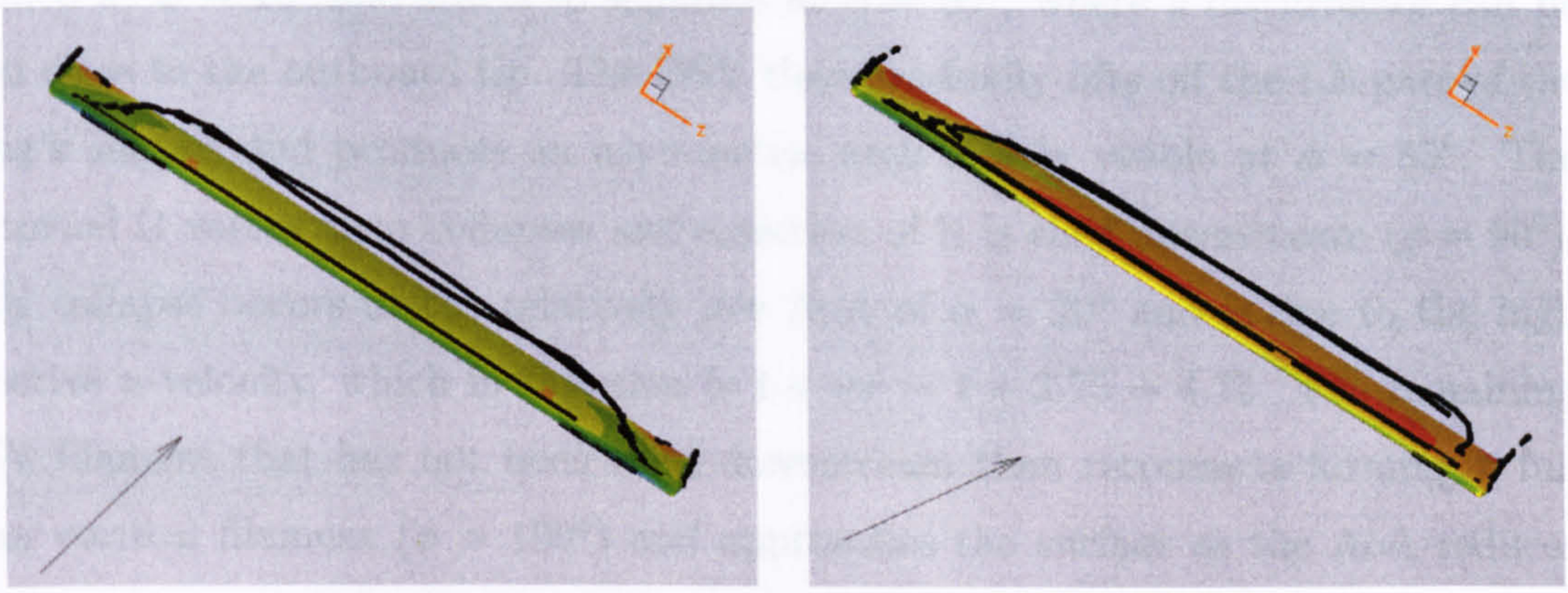

(b)

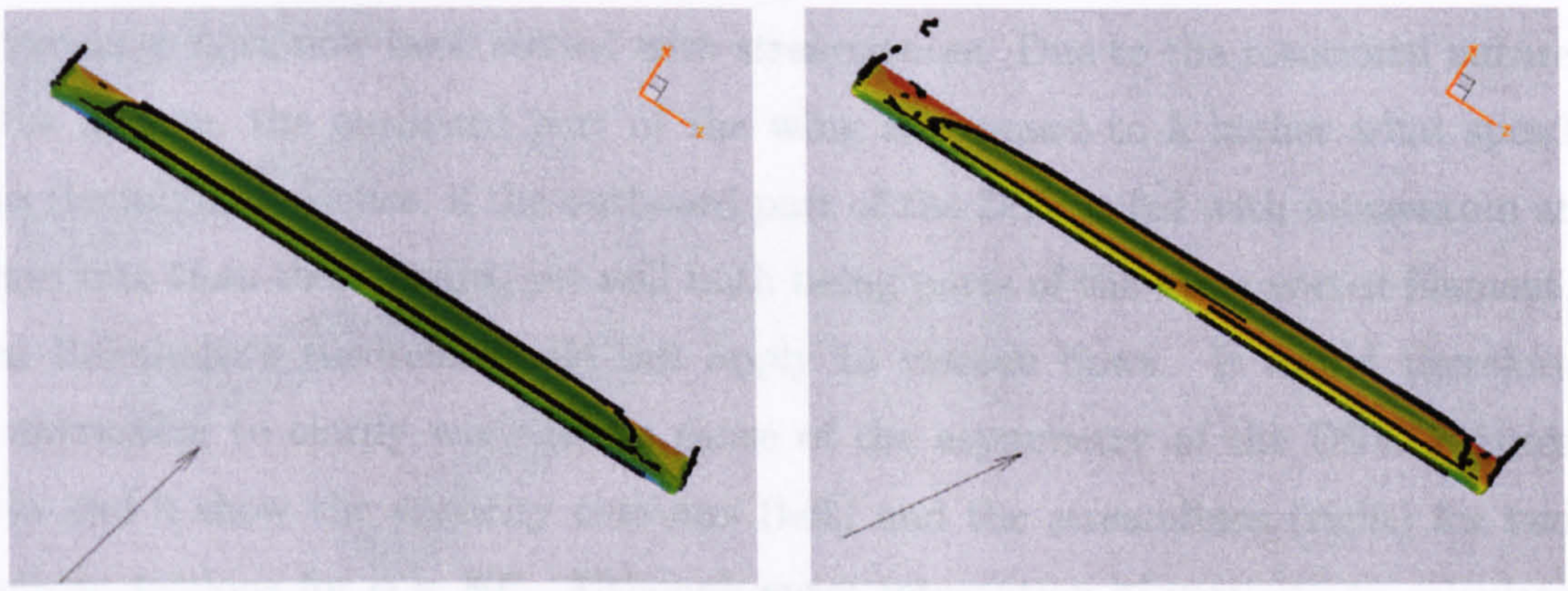

(c)

Figure 5.11: Vortex cores for three different reduced frequencies and two different yaw angles shown at $\alpha = 20^o$ (case 9 of Table 5.1). In the left column the freestream is parallel to the chord while in the right the yaw angle is $\beta = 15^o$. (a) $k = 0.05$, (b) $k = 0.1$ and (c) $k = 0.15$.

5.8 Effect of Rotation to the shape of DSV

Figure 5.12 shows snapshots of the vortex cores for a rotating and pitching wing of $AR = 5$ based on a NACA 0015 aerofoil (case 10 of Table 5.1). The top right snapshot of Figure 5.12 corresponds to $\phi = 0^o$ and $\alpha = 10^o$, the middle corresponds to $\phi = 90^o$ and $\alpha = 20^o$ and the bottom right corresponds to $\phi = 140^o$ and $\alpha = 16.5^o$, respectively. Both pitching and rotational motions have the same frequency. The freestream conditions are $Re = 10^6$ and $M = 0.15$. The azimuth angles anti-clockwise from top right are: 10^o, 20^o, 30^o, 40^o, 50^o, 60^o, 70^o, 80^o, 85^o, 90^o, 95^o, 100^o, 110^o, 120^o and 140^o correspondingly. No change was observed for angles greater than 140^o and therefore, they have been omitted from Figure 5.12. An LEV is already formed at $\phi = 10^o$ and starts to separate at $\phi = 50^o$, where a disturbance can be seen close to the outboard tip. The DSV then gradually lifts off the LE part of the wing's surface and produces an asymmetric arch clearly visible at $\phi = 85^o$. The distorted Ω vortex then collapses and a section of it is shed downstream ($\phi = 90^0$). This collapse occurs at the relatively low AoA of $\alpha = 20^o$ and is due to the high effective u-velocity, which in this case is $1 + wr = 1 + 3.75 = 4.75$. The remaining DSV filament that has not been shed downstream then reconnects forming a full span vortical filament ($\phi > 100^o$) and approaches the surface as the AoA reduces for azimuths $\phi > 90^0$. Figures 5.13a-c show three instances of the same rotating case for azimuth angles of (a) $\phi = 85^o$, (b) $\phi = 90^o$ and (c) $\phi = 110^o$ where the vortex cores have now been seeded with streamtraces. Due to the rotational nature of the motion, the outboard part of the wing is exposed to a higher wind speed than the inboard. Hence, if the outboard part of the DSV is fed with momentum at higher rate than the inboard, yet still both being parts of the same vortex filament, then Helmholtz's theorem would not apply to viscous flows. It would therefore be interesting to clarify what is the cause of the asymmetry of the DSV. Figures 5.14a and b show the vorticity contours (left) and the streamlines (right) for two spanwise sections for $\phi = 80^o$. Although exact integration of vorticity to calculate the circulation of the DSV for each of the two sections has not been performed (Figure 5.14 (left)), they appear similar despite the different locations and sizes of the vortex cores (Figure 5.14 (right)). Therefore, the assymetry of the DSV shown in Figure 5.12, could be due to the faster downstream shedding of the outboard part of the DSV, being subjected to higher wind velocities. Thus, in this case Helmholtz's theorem does not seem to be violated.

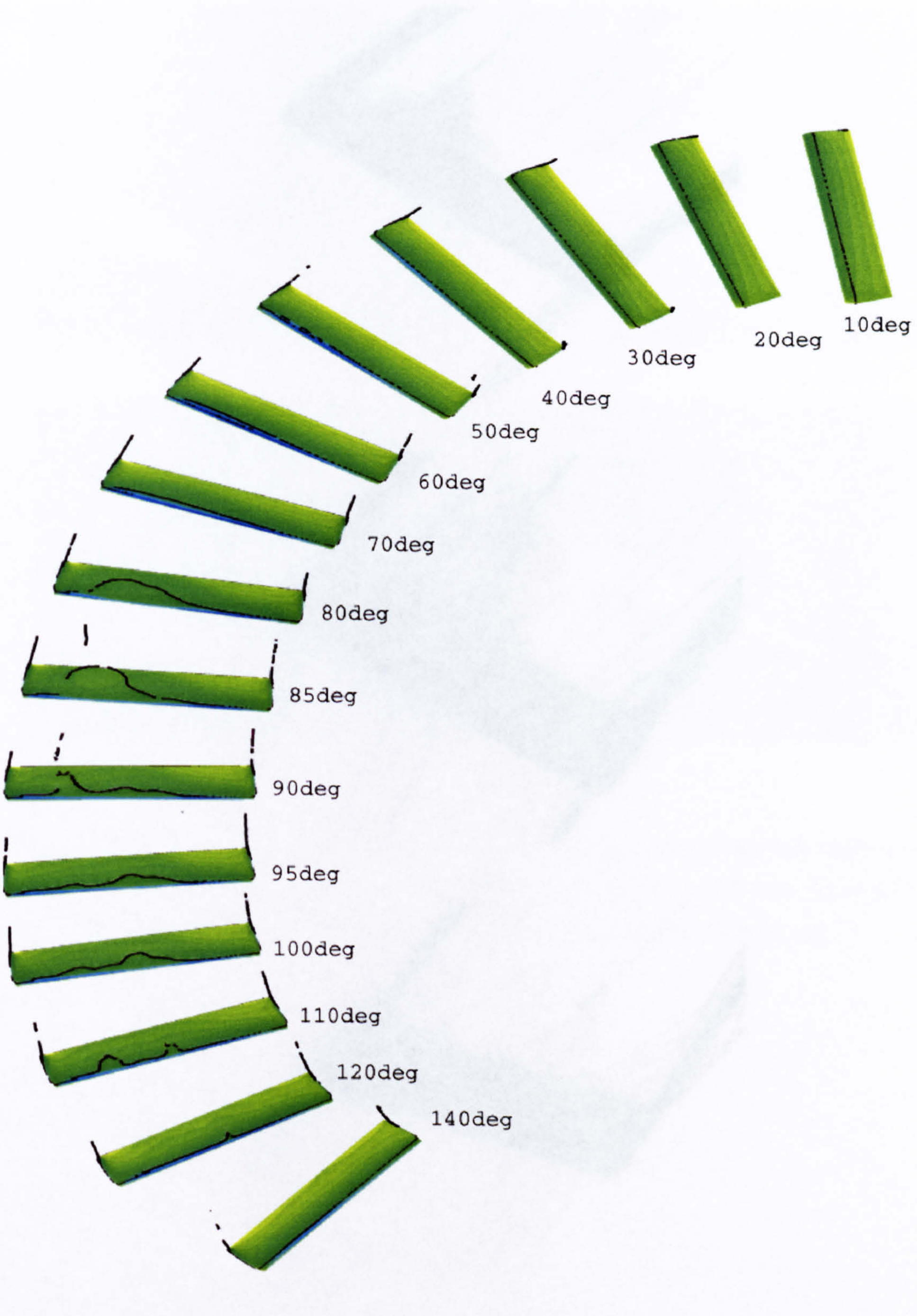

Figure 5.12: Vortex cores for a rotating wing (case 10 of Table 5.1). The AR of the wing is 5 and the tip radius is 12.5. The direction of the freestream is from the bottom of the page to the top. Azimuth angles anti-clockwise from top: 10^o, 20^o, 30^o, 40^o, 50^o, 60^o, 70^o, 80^o, 85^o, 90^o, 95^o, 100^o, 110^o, 120^o and 140^o.

5.8. EFFECT OF ROTATION TO THE SHAPE OF DSV

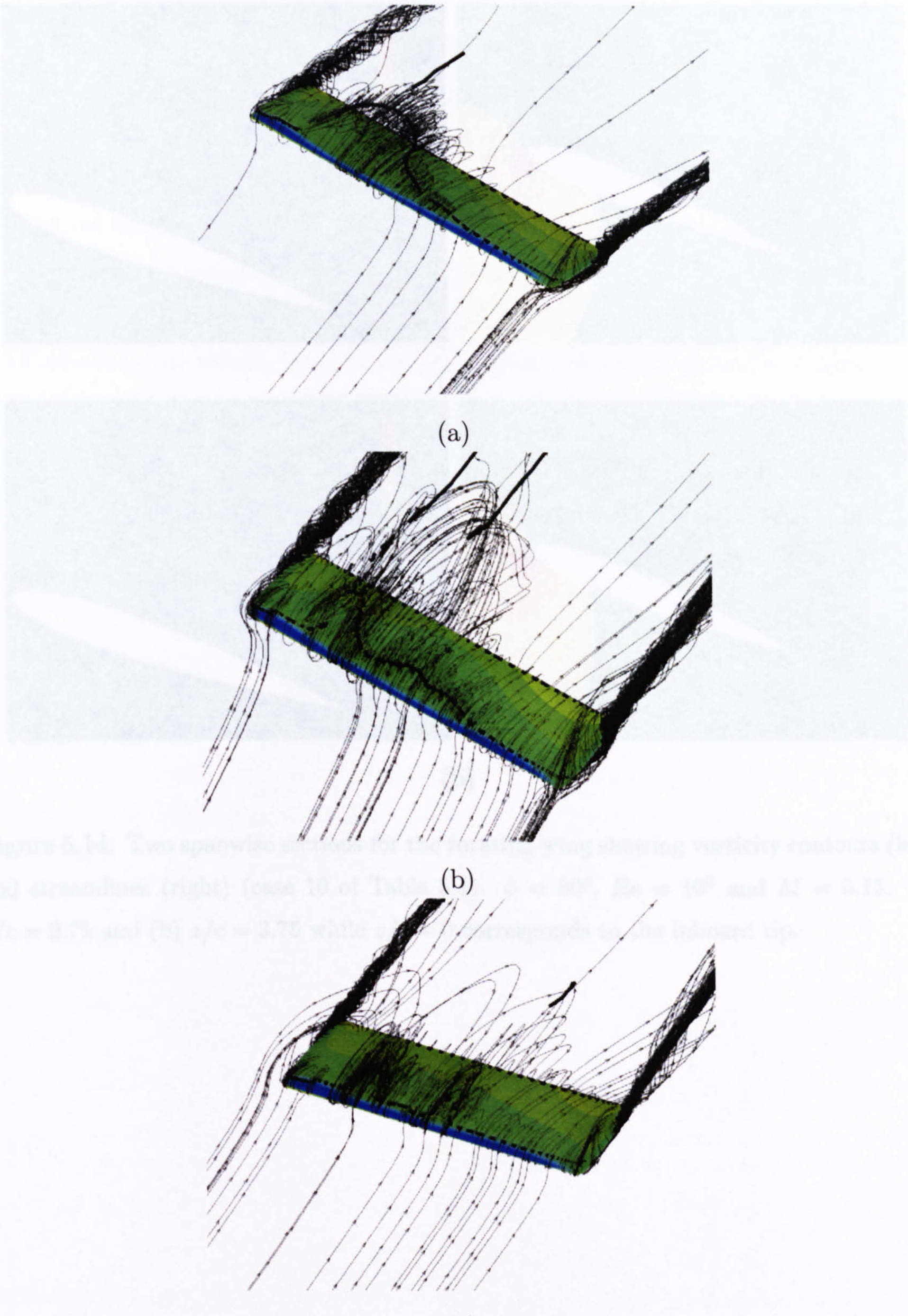

Figure 5.13: Vortex cores and streamtraces for a rotating wing (case 10 of Table 5.1). The AR of the wing is 5 and the tip radius is 12.5. Azimuth angles (a) 85^o, (b) 90^o and (c) 110^o.

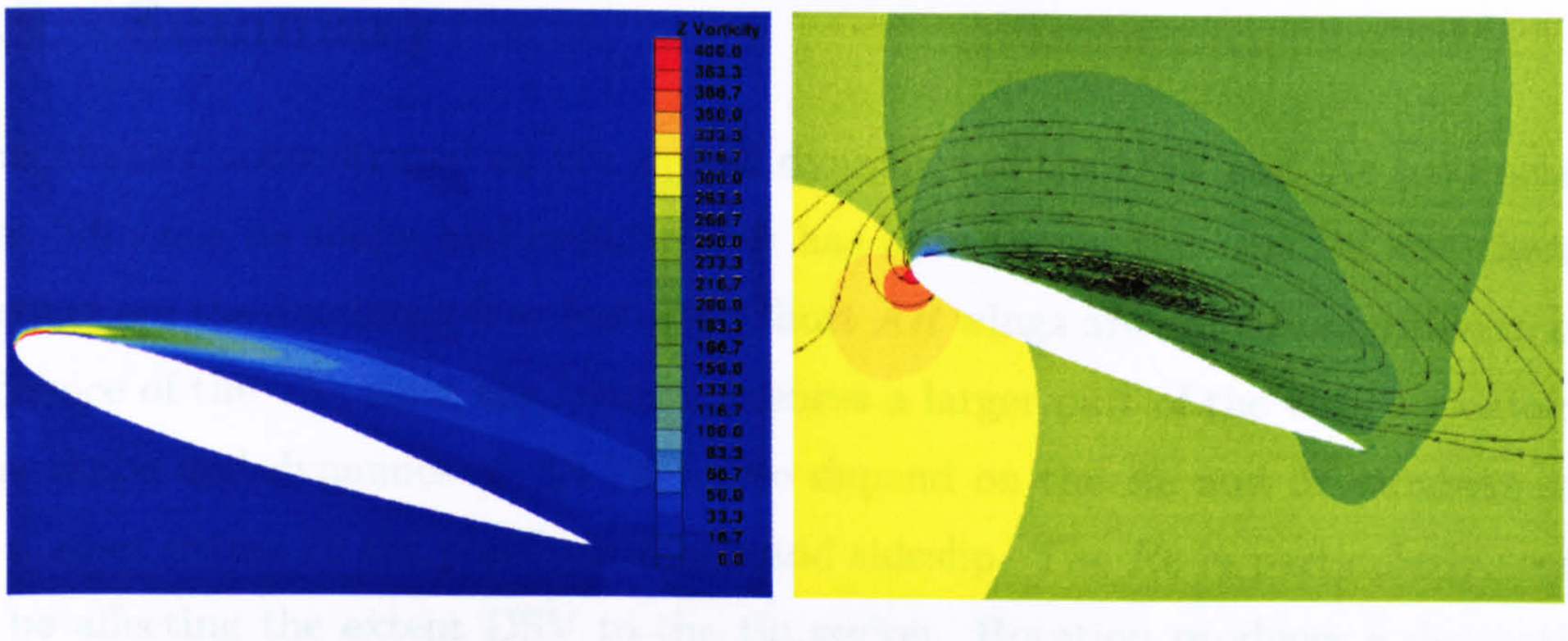

(a)

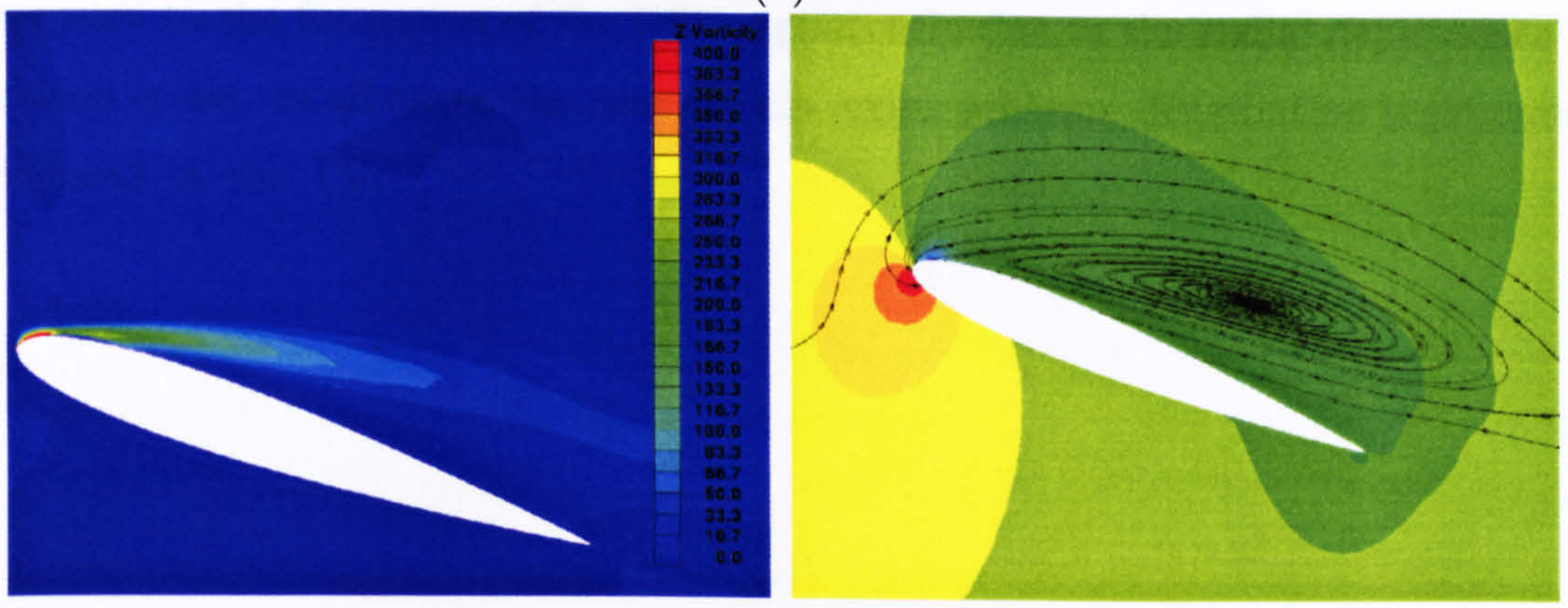

(b)

Figure 5.14: Two spanwise sections for the rotating wing showing vorticity contours (left) and streamlines (right) (case 10 of Table 5.1). $\phi = 80^o$, $Re = 10^6$ and $M = 0.15$. (a) $z/c = 2.75$ and (b) $z/c = 3.75$ while $z/c = 0$ corresponds to the inboard tip.

5.9 Summary

This chapter concentrated on the overall dynamics of the DSV and the parameters that influence its shape and evolution. It has been shown that the DS and the tip vortices are the dominant flow features. Short AR wings are more susceptible to the influence of the TV, since the latter influences a larger part of the wing's planform. The shape and dynamics of the DSV also depend on the Re and M numbers and to a lesser extent to the planform shape and sideslip. The Re in particularly seems to be affecting the extent DSV to the tip region. Rotation produces a distinctive assymetry to the formation of the DSV, apparently due to the radial dependence of the wind speed. In all cases, the near the tip region pressure distribution is primarily influenced by the TV.

Chapter 6

Validation of The Neural Network

6.1 Introduction

The sole published work on Neural Networks (NNs) as a model of DS has been performed by Faller *et al.*[65, 66]. In this chapter, firstly, the performance of the Feed Forward Back Propagation (FFBP) NN and Recursive NN (RNN) models described in chapter 3 is assessed. The data for eight ramping motions (Table 6.1) from the experiments of Coton and Galbraith [44] are used during this test. Then, the FFBP NN model was trained to predict more complex motions involving yaw and rotation. The training and validation data for these motions, were derived from CFD simulations.

6.2 Preliminary Results Based on Experimental Data

The first step in the present analysis, has been the use of the readily available experimental data provided by Coton & Galbraith [44], in order to check the suitability of both the NN and RNN approaches described in chapter 3. Data for a total of 8 ramping cases were used, the details of which are summarised in table 6.1.

Out of these eight data sets, five were used for training and the remaining three were used for prediction, two outside the training regime (cases 1 and 8 of table 6.1) and the third within (case 5 of table 6.1). The rationale behind this choice was to assess both the interpolating and extrapolating qualities of the NN model. After convergence was attained, the NNs were switched into the predictive mode and

Case	Reduced Ramp Rate	Ramp Rate (deg/s)	Used for Training/Prediction
1	0.0044	67.34	Prediction
2	0.0061	91.26	Training
3	0.0095	143.36	Training
4	0.0120	184.16	Training
5	0.0140	213.85	Prediction
6	0.0190	283.97	Training
7	0.0250	371.97	Training
8	0.0300	429.02	Prediction

Table 6.1: Details of the experimental data used [44] for the training and validation of the NN. $Re = 1.4710^6$, $M = 0.16$ and the range of angles was $-5^o - 39^o$.

simulated the evolutionary characteristics of a further three ramping cases (Table 6.1, cases 1,5,8) which were not included in the training dataset. The cpu times taken to both models to produce full motion predictions were of the order of few miliseconds on a 2.5 GHz linux pentium-4 machine.

6.2.1 NN vs RNN

The performance of the two models was assessed by predicting the experimentally measured time histories of 15 chordwise transducers located at 57% of span [44]. Each ramping case was discretised in time into 150 unsteady steps and for each unsteady step readings from 15 transducers covering the suction side of the wing were used. Therefore the total number of patterns was equal to $5 \times 150 \times 15 = 11,250$. The convergence criterion used required that the final error should be less than 5% of the total initial error. The variables used to train the NN where the reduced ramp rate (α^+), angle of attack (α), time (t) and the x coordinate of the Cp transducers on the wing's suction side. The NN was thereafter trained to approximate the functional: $C_p = f(\alpha^+, \alpha, t, x)$ and is shown on Figure 6.1a. The RNN model was trained by the true time sequence for each one of the 15 transducers, together with their corresponding α and α^+. Thus the total number of patterns was $5 \times 150 = 750$ and the schematic of the model can be seen in Figure 6.1b.

Several NNs were tested, mainly with two and three hidden layers. RNN models with three hidden layers did not converge. Figure 6.2 shows the convergence histories for three different NN models, an RNN model with 2×45 neurons on the hidden

layers and two NN models with 2×45 and 3×40 neurons on the hidden layers respectively.

Figure 6.2 shows that the convergence behaviour of the NN models is very similar. The initial convergence speed of the RNN model is lower than that of the NN models, however, it finally converged to a 2% lower residual value. The reason for the seemingly higher convergence speed of the RNN model, is that over the same length of time ($18hrs$) the RNN model will iterate over more epochs than the NN model. Each epoch for the RNN model consists of 5×150 patterns (5 datasets with 150 time steps each). However, each epoch in the case of the NN models consists of $5 \times 150 \times 15$ patterns (5 datasets with 150 time steps for each of the 15 pressure transducers).

Figures 6.3a-c show the comparisons of the C_p histories for the 15 transducers of the experimental readings *vs* the NN and RNN predictions. Both the NN and RNN models had 2 hidden layers with 45 neurons each. In particular, Figures 6.3a and 6.3c suggest that the RNN model performs slightly better in the extrapolation cases (cases 1 and 9 of Table 6.1 correspondingly) whereas the NN provides more accurate predictions in the interpolated case (case 5 of Table 6.1). Also, the NN model was found to be more stable numerically allowing for larger learning and momentum terms (0.1 as opposed to 0.001). These conclusions coupled with the fact that the NN model also benefits from incorporating the spatial information of the transducer locations, established the NN as the preferred choice for the rest of this investigation. Such detailed comparisons were never reported by Faller [65, 66] who just employed the RNN model.

6.2.2 C_p Surface Contour Predictions Using the NN Model

Next, the NN model was trained by all 90 transducer readings, for the same set of experimental data described in the previous paragraphs. Each ramping case was discretised in time into 150 unsteady steps and for each unsteady step readings from 90 transducers covering the suction side of the wing were used. Therefore the total number of patterns was equal to $5 \times 150 \times 90 = 67,500$ and a total of around 10^5 epochs were necessary to achieve convergence. The total computing time during training was around 24 hours on a single processor 2.5 GHz Pentium 4 computer. The convergence criterion used required that the total error should be less than 5% of the total initial error.

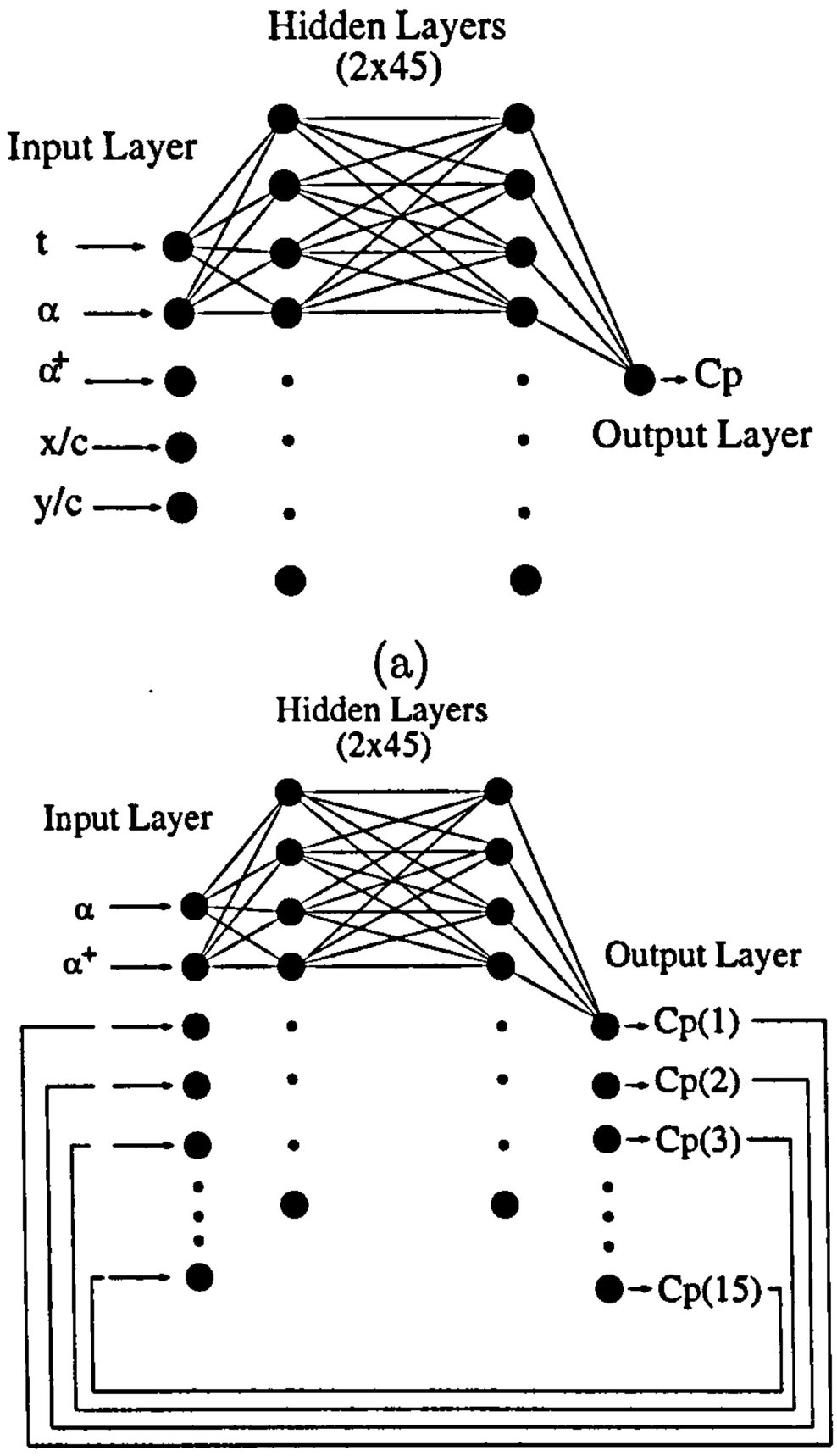

Figure 6.1: The neural network models used. (a) 2-layer, no feedback, (b) 2-layer with feedback, (c) 3-layer, no feedback.

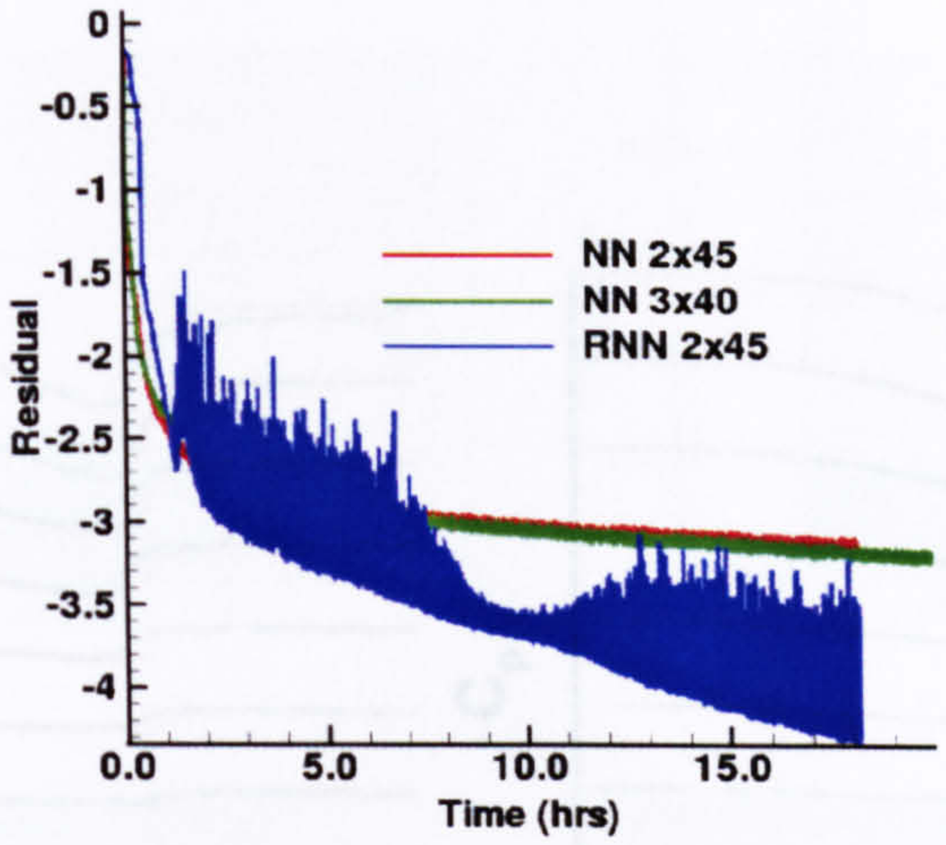

Figure 6.2: Convergence histories (logarithmic scale) of the RNN and NN models. The RNN model had 2×45 neurons on the hidden layers and the two NN models had 2×45 and 3×40 neurons respectively.

The variables used to train the NN where the reduced ramp rate (α^+), angle of attack (α), time (t) and the x and y coordinates of the Cp transducers on the suction side of the wing. The NN was thereafter trained to approximate the functional: $C_p = f(\alpha^+, \alpha, t, x, y)$ and is shown on Figure 6.1c.

Comparisons between the experimental (left) and predicted (right) surface C_p distributions can be seen in Figures 6.4, 6.5 and 6.6, for two different angles of attack for each case. The top row in Figures 6.4, 6.5 and 6.6 corresponds to angles of attack just before the formation of the DSV and the bottom row, corresponds to angles of attack were the DSV has been fully formed and is shed towards the trailing edge. The comparison is good as both the overall loading and the location of the DSV footprint have been accurately predicted. The only exception is Figure 6.4 were the NN computation predicts the DSV suction peak closer to the wing root as opposed to the experiment which shows the trajectory of the DSV to be slightly closer to the tip. It should also be noted that the interpolation case (case 5 of Table 6.1) shown in Figure 6.5 shows an exceptionally good agreement between the experiment and the NN prediction. This also is the prevailing conclusion throughout this work, *ie*, whenever adequate training is provided, the NN model provides very good predictions within the training envelope.

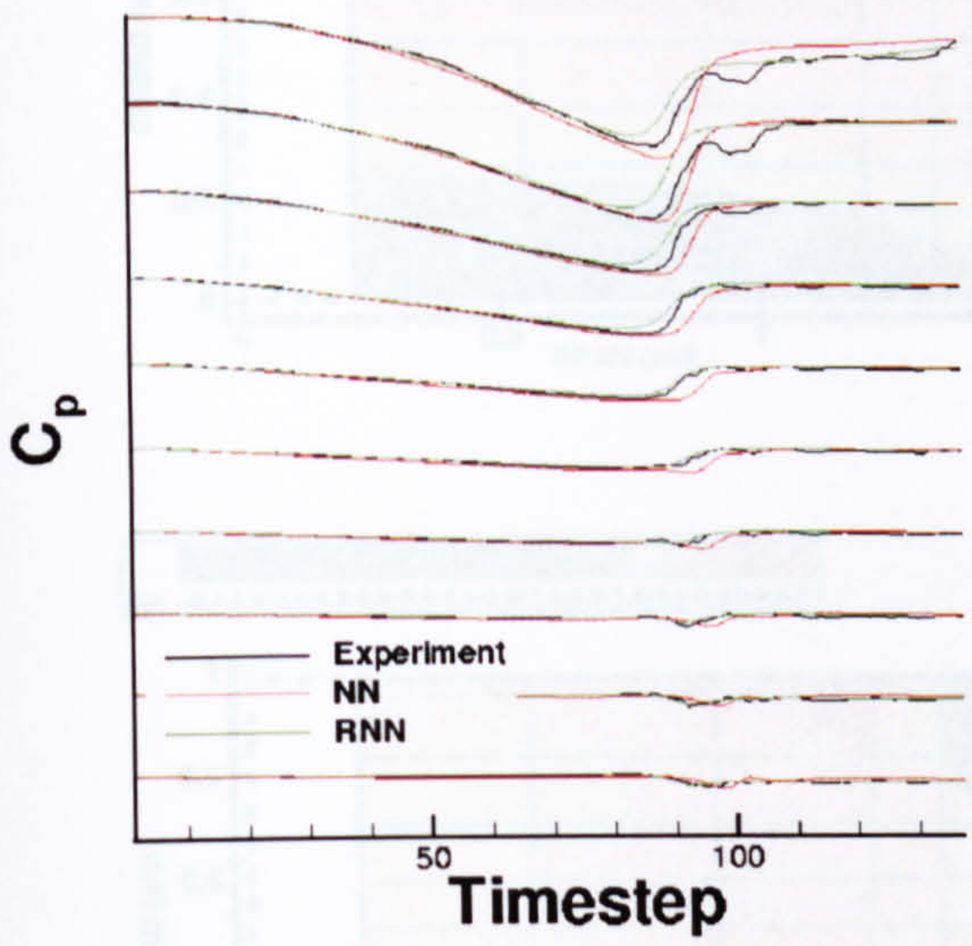

(a)

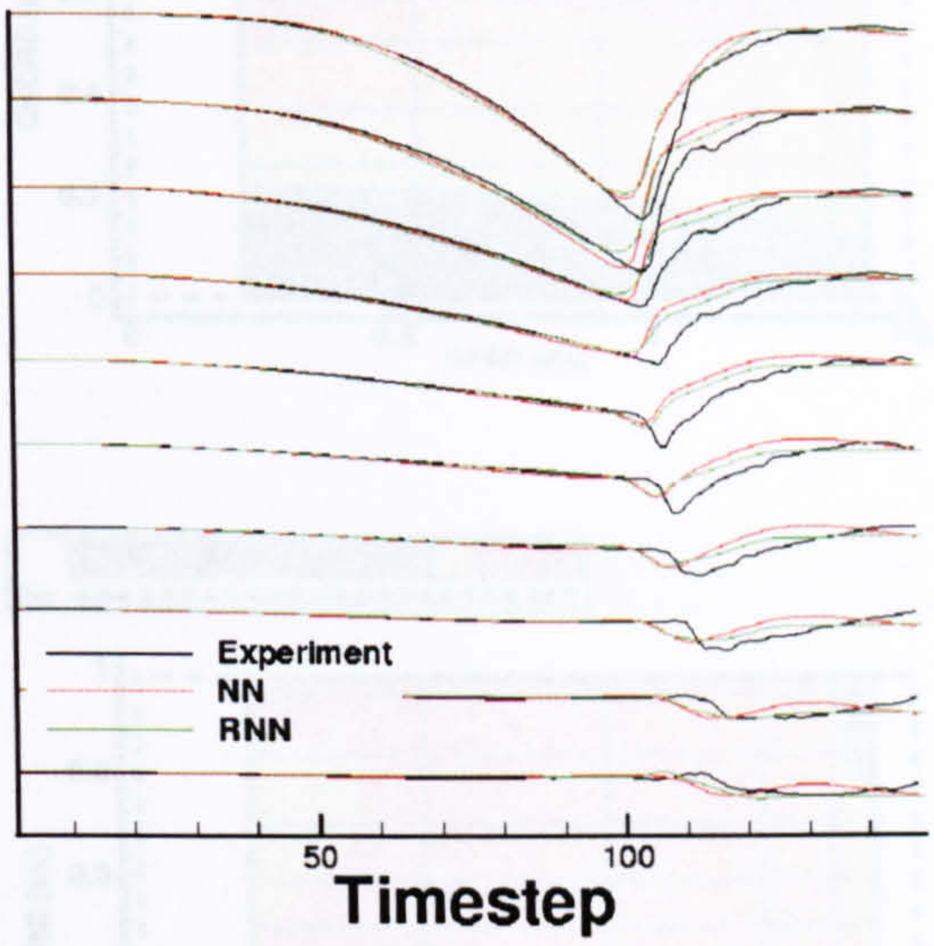

(c)

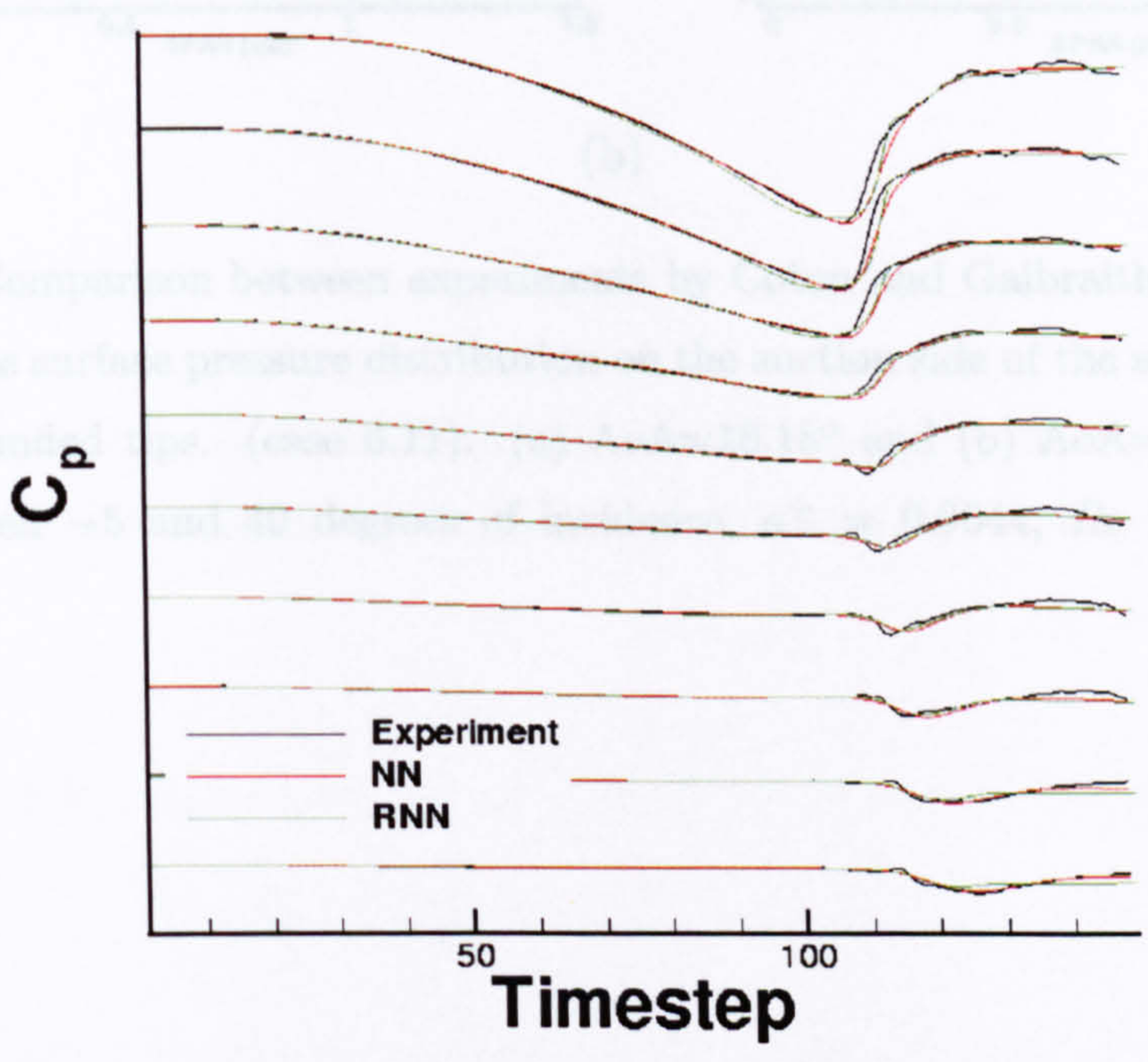

(b)

Figure 6.3: Comparison between the predictions of the NN (red) and RNN (green) models against experiments (black) [44] for cases (a) 1, (b) 5 and (c) 9 of Table 6.1 respectively.

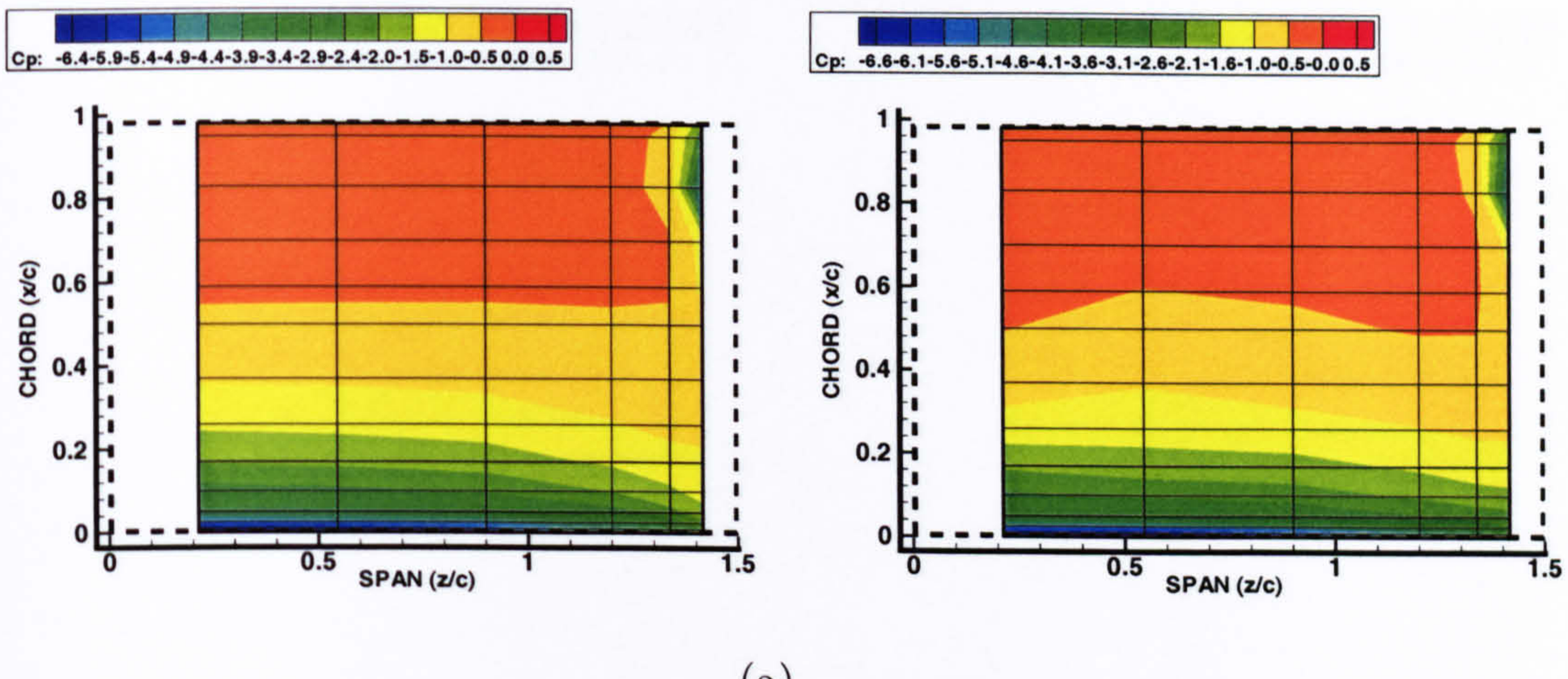

(a)

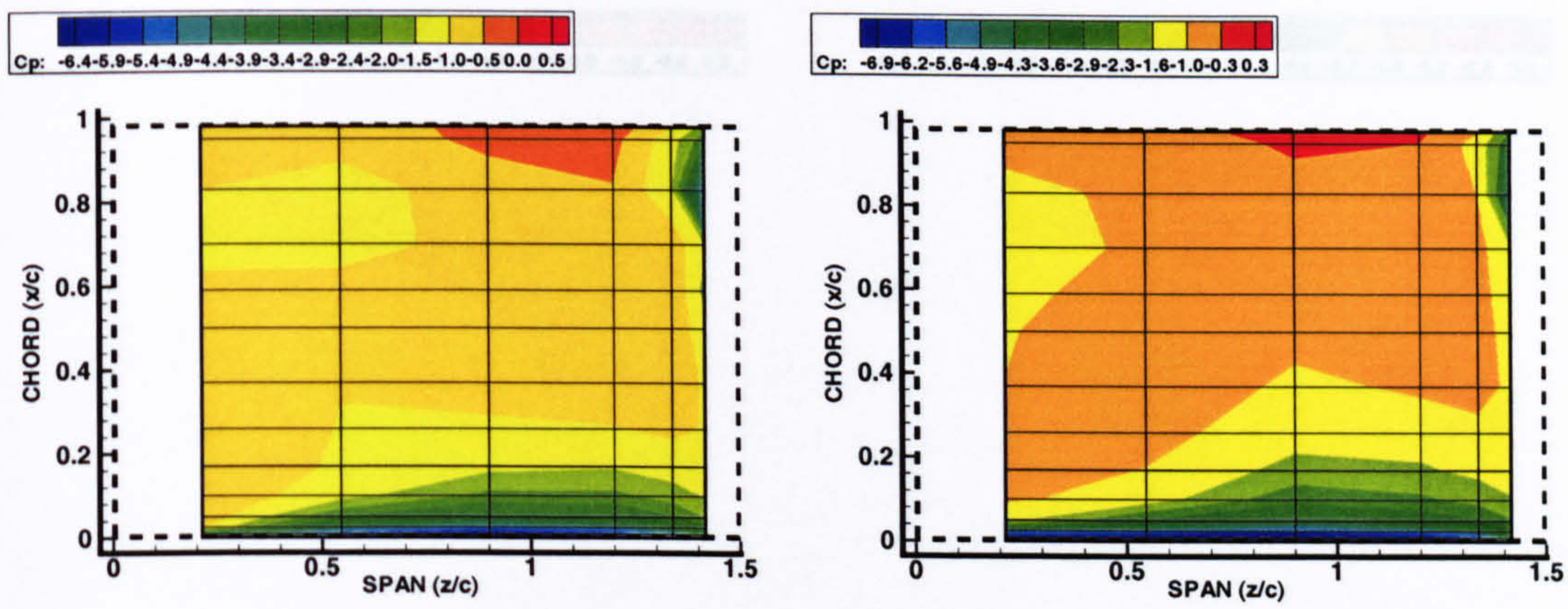

(b)

Figure 6.4: Comparison between experiments by Coton and Galbraith [44] and NN predictions for the surface pressure distribution on the suction side of the square NACA-0015 wing with rounded tips. (case 6.11). (a) AoA=18.18^o and (b) AoA=23.84^o. Ramping motion between -5 and 40 degrees of incidence, $a^+ = 0.0044$, $Re = 1.47 \times 10^6$ and $M = 0.16$.

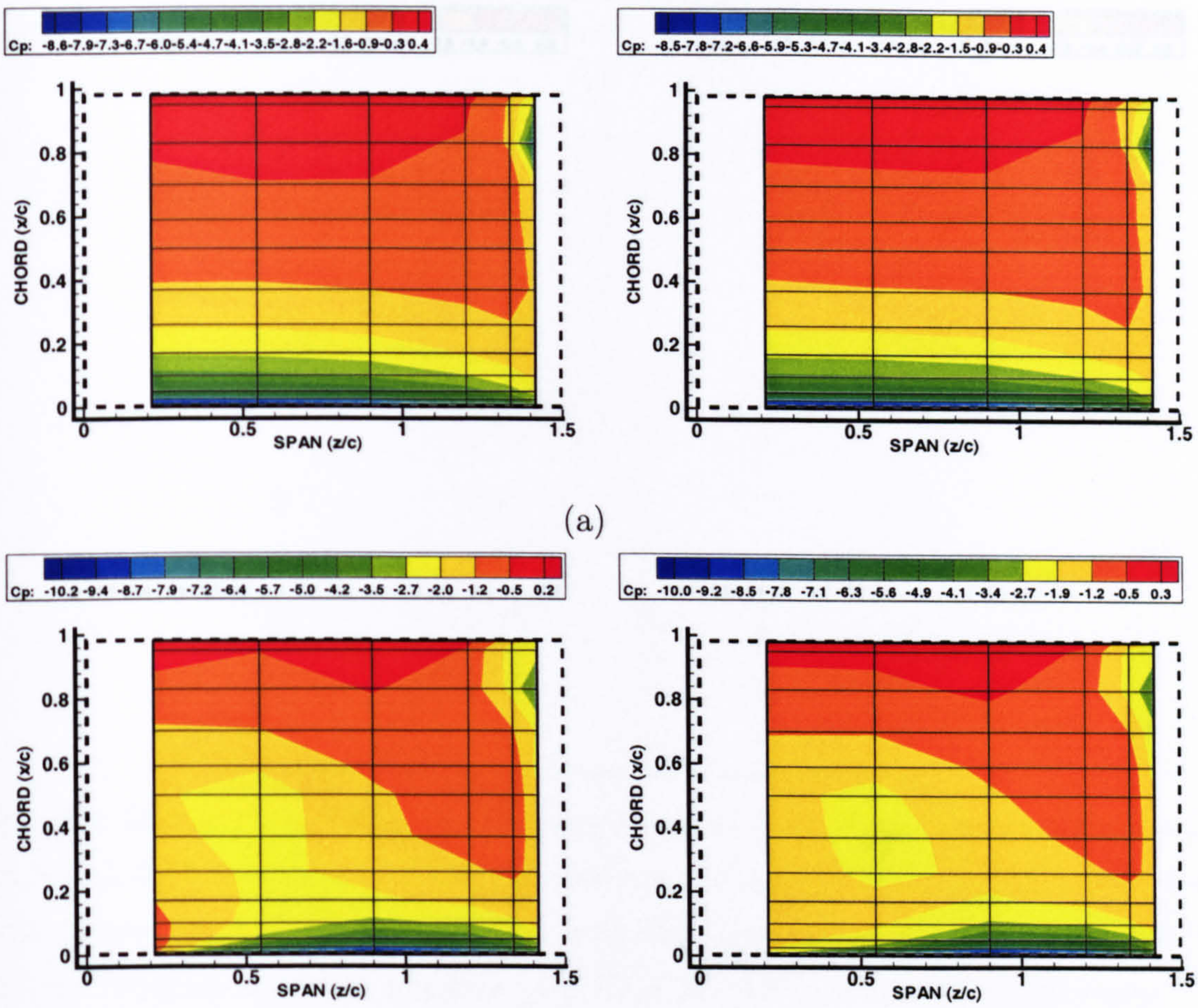

Figure 6.5: Comparison between experiments by Coton and Galbraith [44] and NN predictions for the surface pressure distribution on the suction side of the square NACA-0015 wing with rounded tips. (case 6.15). (a) AoA=24.44^o and (b) AoA=28.74^o. Ramping motion between -5 and 40 degrees of incidence, $a^+ = 0.014$, $Re = 1.47 \times 10^6$ and $M = 0.16$.

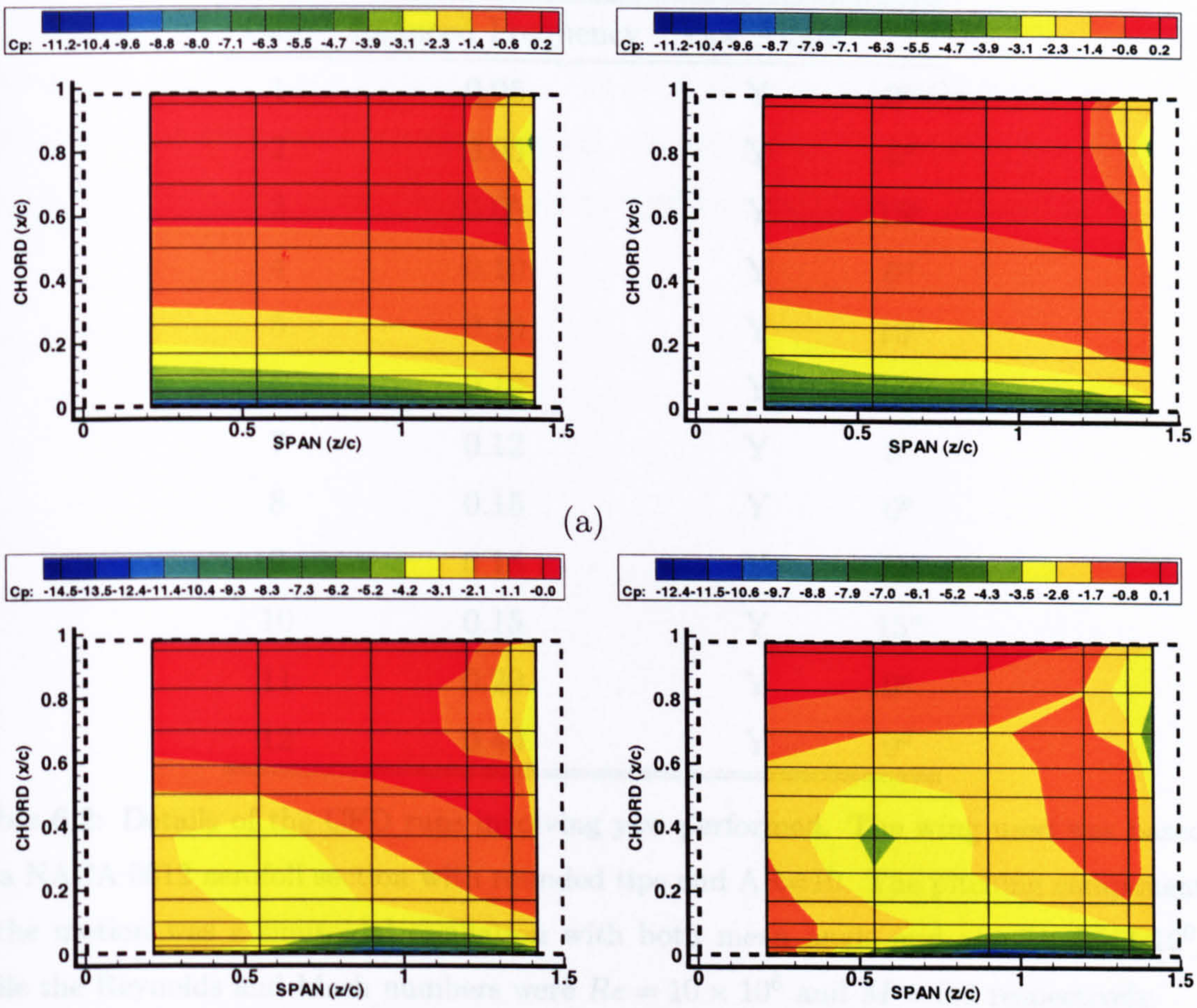

Figure 6.6: Comparison between experiments by Coton and Galbraith [44] and NN predictions for the surface pressure distribution on the suction side of the square NACA-0015 wing with rounded tips. (case 6.18). (a) AoA=27.27^o and (b) AoA=35.55^o. Ramping motion between -5 and 40 degrees of incidence, $a^+ = 0.03$, $Re = 1.47 \times 10^6$ and $M = 0.16$.

6.3 Exploitation of Neural Networks for Dynamic Stall Modelling

The next step was to exploit the ability of the NN to model DS (a) by increasing the complexity of the problem through the introduction of the yaw angle as an extra variable and (b) by testing the NN model in rotating geometries.

Case	Reduced Frequency	Yaw Angle	
1	0.05	Y	0^o
2	0.05	Y	5^o
3	0.05	Y	15^o
4	0.10	Y	0^o
5	0.10	Y	10^o
6	0.10	Y	15^o
7	0.12	Y	8^o
8	0.15	Y	0^o
9	0.15	Y	10^o
10	0.15	Y	15^o
11	0.20	Y	0^o
12	0.40	Y	0^o

Table 6.2: Details of the CFD runs involving yaw performed. The wing used was based on a NACA 0012 aerofoil section with rounded tips and AR=10. The pitching component of the motion was a sinusoidal oscillation with both mean angle and amplitude of 10^0, while the Reynolds and Mach numbers were $Re = 10 \times 10^6$ and $M = 0.3$ respectively.

6.3.1 Yaw

Cases 1-12 of Table 6.2, refer to sinusoidal pitching motions with an amplitude and mean angle of 10^o for different yaw angles. Various combinations of these cases were used to train and validate the NN, in order to assess its interpolating as well as extrapolating capabilities. Each sinusoidal motion was discretised in 150 unsteady steps and pressure values spread along 11 spanwise and 9 chordwise locations on the suction surface of the wing were recorded for each time step. Therefore, each training dataset was comprised by $99 \times 150 = 14850$ patterns. Consequently, the NN was trained to approximate the function $C_p = C_p(t, k, \alpha, \beta, x, y)$.

Interpolation in Reduced Frequency and Yaw

The training cases were 4,5,8 and 9 of Table 6.2, whereas the validation case was case 7 of Table 6.2. Figure 6.7 shows the comparison of the CFD simulation and NN prediction for case 7 of Table 6.2, for 10^o*upstroke*, 20^o, 10^o*downstroke* and 0^o angles of attack (Figures 6.7a,b,c and d correspondingly. The comparison is outstanding, as both the magnitude and the finer details of the C_p contour topology have been

captured by the NN. Figure 6.11a shows the comparison of the normalised normal force acting on the wing's suction side. The peak of the graph corresponding to the shedding of the DSV has been very slightly over estimated by the NN, however, the instance the shedding occurs, has been captured very accurately (Figure 6.7b).

6.3. EXPLOITATION OF NEURAL NETWORKS FOR DYNAMIC STALL MODELLING

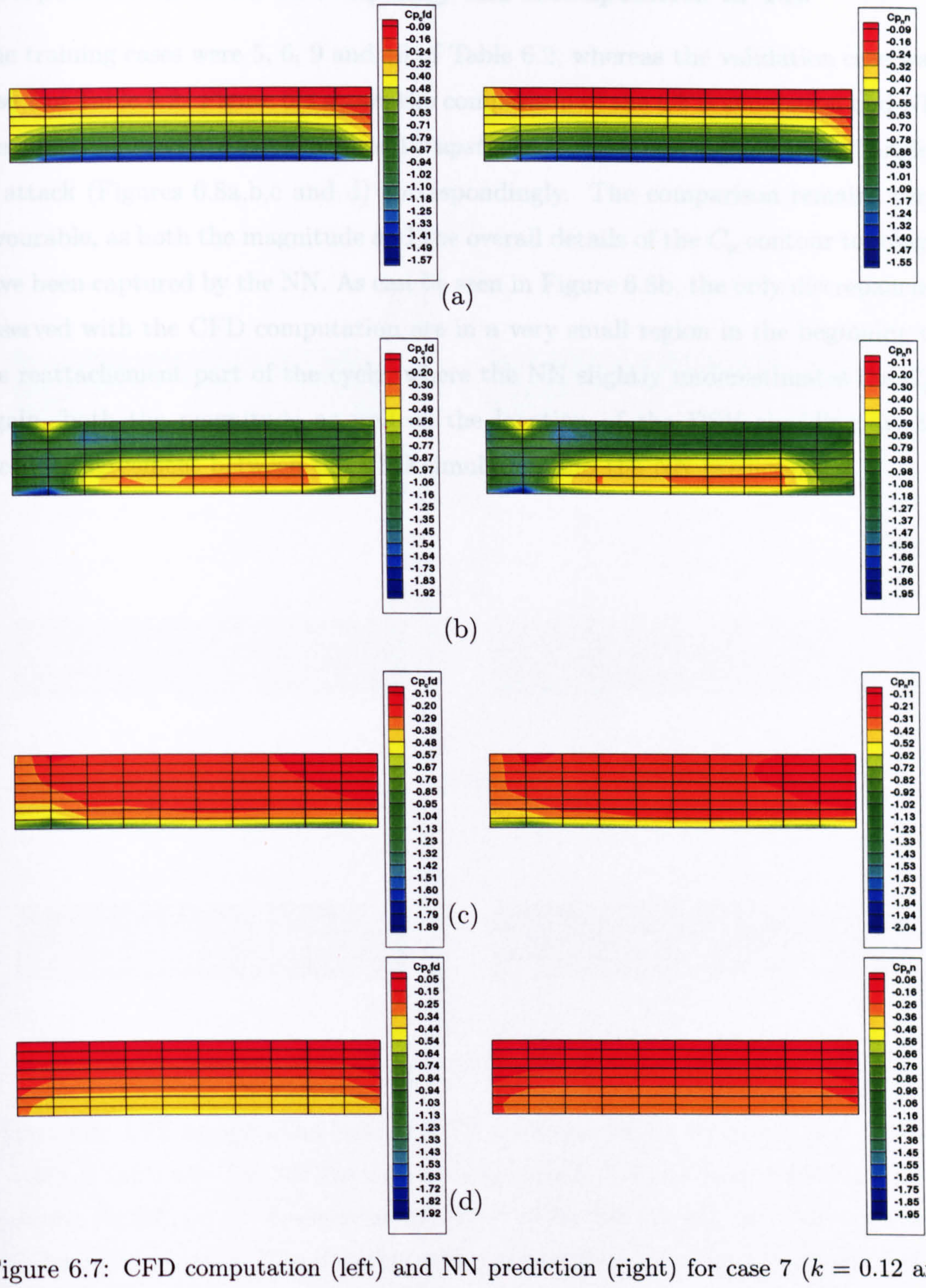

Figure 6.7: CFD computation (left) and NN prediction (right) for case 7 ($k = 0.12$ and $\beta = 8^o$) of Table 6.2. The NN was trained using cases 4, 5, 8 and 9 of Table 6.2. (a) 10^o upstroke, (b) 20^o, (c) 10^o downstroke and (d) 0^o. Note that the AR has been compressed for illustration purposes. The direction of the freestream is the same as in Figure 6.7.

6.3. EXPLOITATION OF NEURAL NETWORKS FOR DYNAMIC STALL MODELLING

Interpolation in Reduced Frequency and Extrapolation in Yaw

The training cases were 5, 6, 9 and 10 of Table 6.2, whereas the validation case was case 7 of Table 6.2. Figure 6.8 shows the comparison of the CFD simulation and NN prediction for case 7 of Table 6.2, for 10^o*upstroke*, 20^o, 10^o*downstroke* and 0^o angles of attack (Figures 6.8a,b,c and d) correspondingly. The comparison remains very favourable, as both the magnitude and the overall details of the C_p contour topology have been captured by the NN. As can be seen in Figure 6.8b, the only discrepancies observed with the CFD computation are in a very small region in the beginning of the reattachement part of the cycle, where the NN slightly underestimates the C_p. Again, both the magnitude as well as the location of the DSV shedding are in excellent agreement between the CFD simulation and the NN prediction.

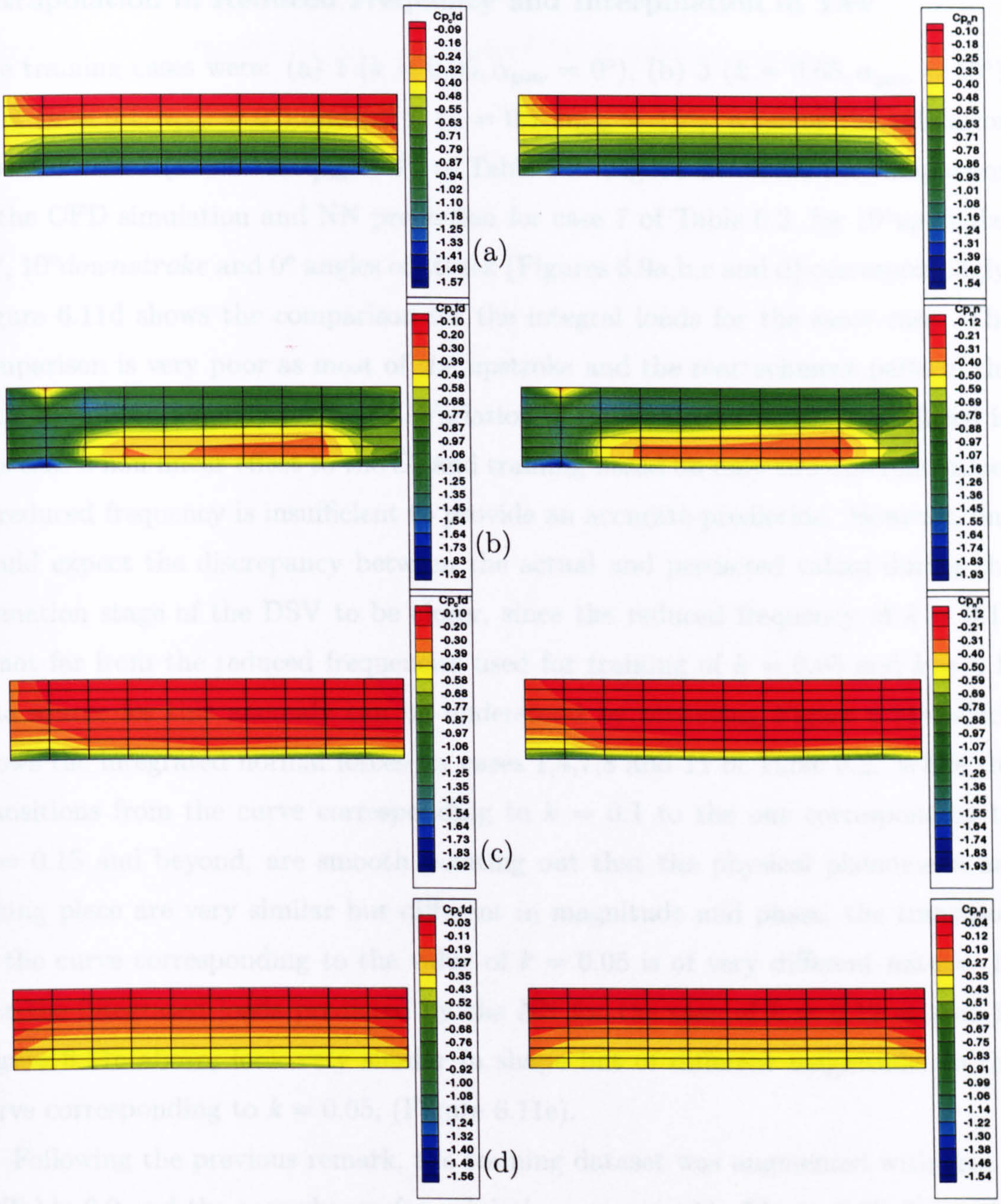

Figure 6.8: CFD computation (left) and NN prediction (right) for case 7 ($k = 0.12$ and $\beta = 8^o$) of Table 6.2. The NN was trained using cases 5, 6, 9 and 10 of Table 6.2. (a) 10^o upstroke, (b) 20^o, (c) 10^o downstroke and (d) 0^o. Note that the AR has been compressed for illustration purposes. The direction of the freestream is the same as in Figure 5.11.

6.3. EXPLOITATION OF NEURAL NETWORKS FOR DYNAMIC STALL MODELLING

Extrapolation in Reduced Frequency and Interpolation in Yaw

The training cases were: (a) 1 ($k = 0.05, \alpha_{yaw} = 0^o$), (b) 3 ($k = 0.05, \alpha_{yaw} = 15^o$), (c) 4 ($k = 0.1, \alpha_{yaw} = 0^o$) and (d) 6 ($k = 0.1, \alpha_{yaw} = 15^o$), whereas the validation case was case 7 ($k = 0.12, \alpha_{yaw} = 8^o$) of Table 6.2. Figure 6.9 shows the comparison of the CFD simulation and NN prediction for case 7 of Table 6.2, for 10^o*upstroke*, 20^o, 10^o*downstroke* and 0^o angles of attack (Figures 6.9a,b,c and d) correspondingly. Figure 6.11d shows the comparison for the integral loads for the same case. The comparison is very poor as most of the upstroke and the reattachment parts of the cycle have been wrongly predicted. Variation of the reduced frequency produced in this case a non linear effect to the C_p and training based on only two different values of reduced frequency is insufficient to provide an accurate prediction. However, one would expect the discrepancy between the actual and predicted values during the formation stage of the DSV to be closer, since the reduced frequency of $k = 0.12$ is not far from the reduced frequencies used for training of $k = 0.05$ and $k = 0.1$. The source for this anomaly can be understood by observing Figure 6.11e which shows the integrated normal forces for cases 1,4,7,8 and 11 of Table 6.2. While the transitions from the curve corresponding to $k = 0.1$ to the one corresponding to $k = 0.15$ and beyond, are smooth pointing out that the physical phenomena are taking place are very similar but different in magnitude and phase, the transition to the curve corresponding to the value of $k = 0.05$ is of very different nature. In fact the integrated loads predicted by the NN for the case of $k = 0.12$ as seen in Figure 6.11c above, look very similar in shape but of different magnitude, to the curve corresponding to $k = 0.05$, (Figure 6.11e).

Following the previous remark, the training dataset was augmented with case 8 of Table 6.2 and the case chosen for validation was case 11. Figure 6.10 shows the comparison of the CFD simulation and NN prediction for case 11 of Table 6.2, for 10^o*upstroke*, 20^o, 10^o*downstroke* and 0^o angles of attack. The comparison is now is very good, since the physics incorporated in the training datasets were adequate for an accurate extrapolating prediction.

The results shown in the previous paragraphs indicate that NNs can successfully model DS in ramping and pitching motions, following the appropriate training. The numerical experiments described so far, have yielded one important insight into the behaviour of the NNs: Predictions are exemplary provided the free parameters (k and β, in the examples involving yaw) are adequately enveloped by the training

examples. Extrapolations beyond the training envelope are also possible if their values do not correspond to cases with significantly different physics.

6.3. EXPLOITATION OF NEURAL NETWORKS FOR DYNAMIC STALL MODELLING

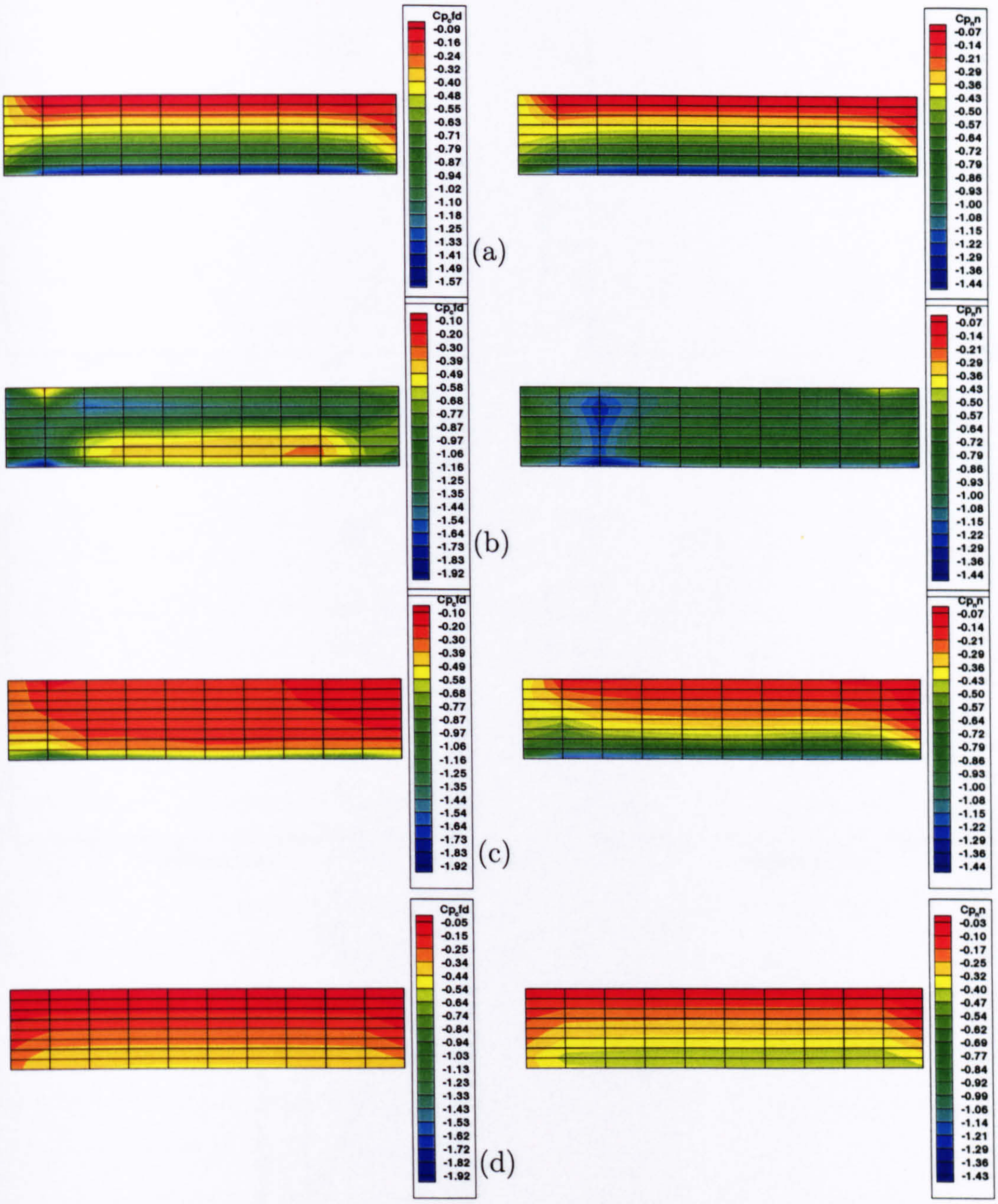

Figure 6.9: CFD computation (left) and NN prediction (right) for case 7 ($k = 0.12$ and $\beta = 8^o$) of Table 6.2. The NN was trained using cases 1, 3, 4 and 6 of Table 6.2. (a) 10^o upstroke, (b) 20^o, (c) 10^o downstroke and (d) 0^o. Note that the AR has been compressed for illustration purposes. The direction of the freestream is the same as in Figure 6.9.

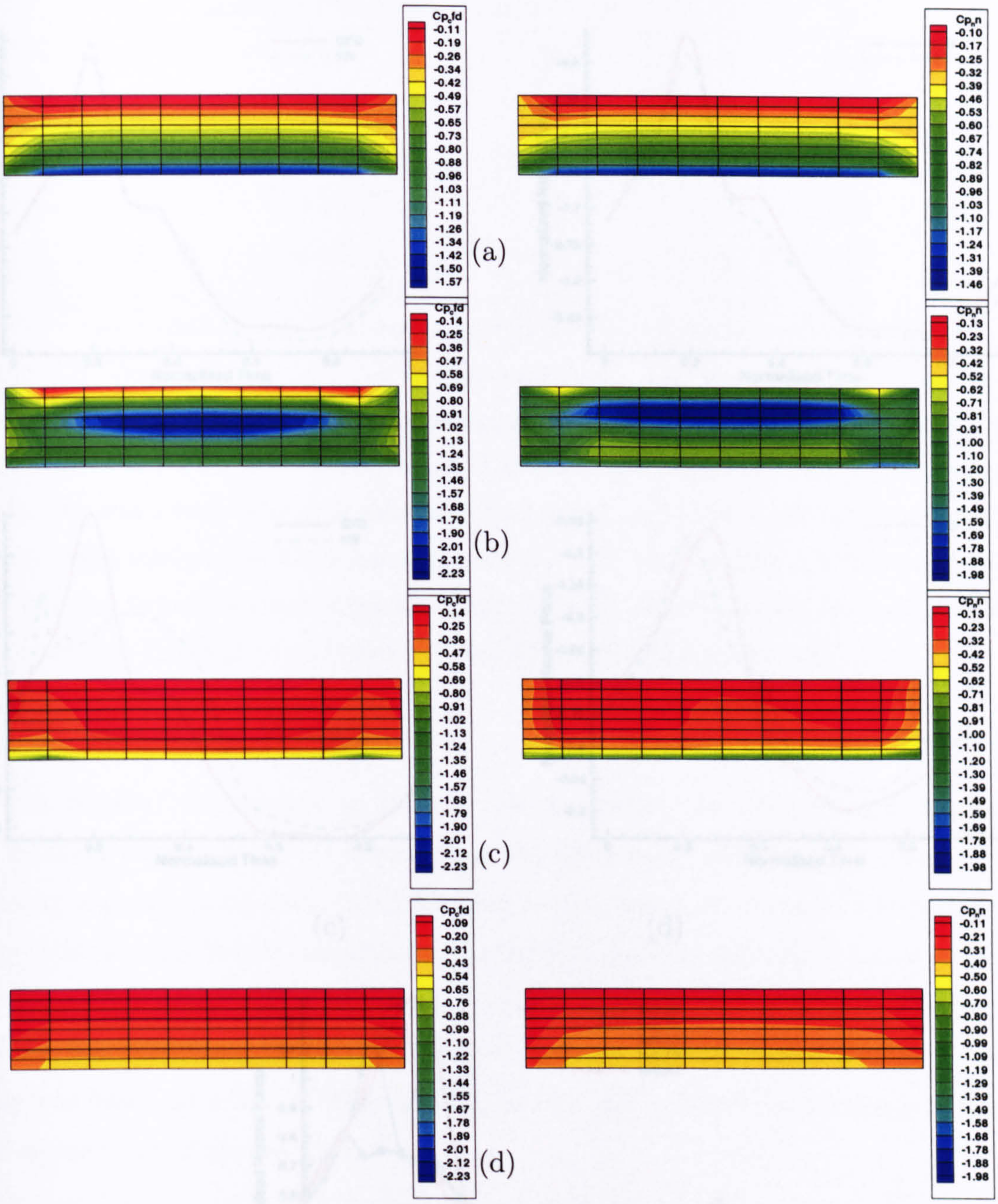

Figure 6.10: CFD computation (left) and NN prediction (right) for case 7 ($k = 0.12$ and $\beta = 8^o$) of Table 6.2. The NN was trained using cases 1, 3, 4 and 6 of Table 6.2. (a) 10^o upstroke, (b) 20^o, (c) 10^o downstroke and (d) 0^o. Note that the AR has been compressed for illustration purposes. The direction of the freestream is the same as in Figure 6.10.

6.3. EXPLOITATION OF NEURAL NETWORKS FOR DYNAMIC STALL MODELLING

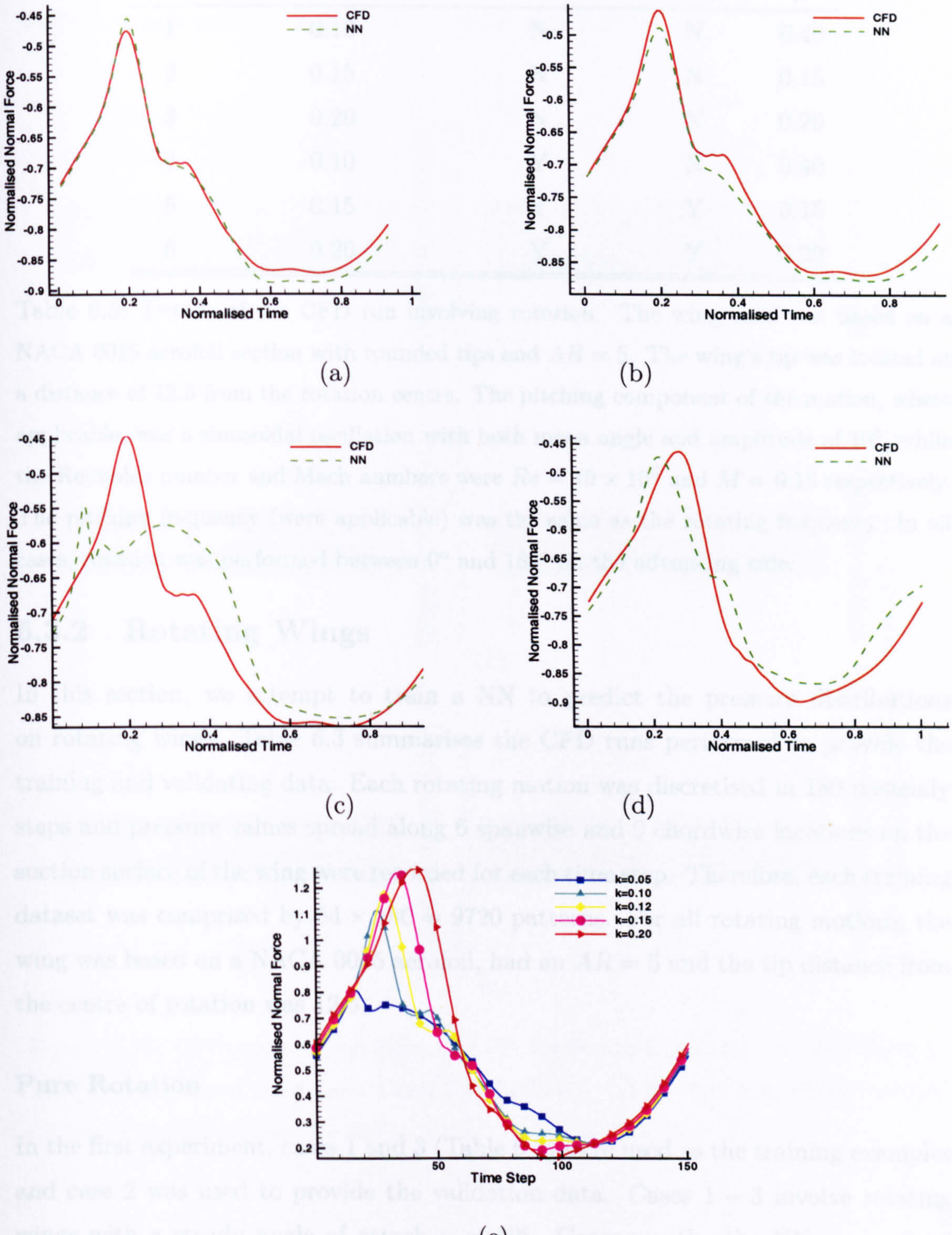

Figure 6.11: Normalised normal force *vs* normalised time corresponding to the cases described in paragraphs (a) 5.4.1, (b) 5.4.2, (c) 5.4.3 and (d) 5.4.4 correspondingly. (e) integrated normal forces for cases 1,4,7,8 and 11 of Table 6.2.

6.3. EXPLOITATION OF NEURAL NETWORKS FOR DYNAMIC STALL MODELLING

Case	Reduced Frequency	Pitch (Y/N)	DS (Y/N)	μ
1	0.10	N	N	0.40
2	0.15	N	N	0.15
3	0.20	N	N	0.20
4	0.10	Y	N	0.40
5	0.15	Y	Y	0.15
6	0.20	Y	Y	0.20

Table 6.3: Details of the CFD run involving rotation. The wing used was based on a NACA 0015 aerofoil section with rounded tips and $AR = 5$. The wing's tip was located at a distance of 12.5 from the rotation centre. The pitching component of the motion, where applicable, was a sinusoidal oscillation with both mean angle and amplitude of 10^0, while the Reynolds number and Mach numbers were $Re = 10 \times 10^6$ and $M = 0.15$ respectively. The pitching frequency (were applicable) was the same as the rotating frequency. In all cases, rotation was performed between 0^o and 180^o on the advancing side.

6.3.2 Rotating Wings

In this section, we attempt to train a NN to predict the pressure distributions on rotating wings. Table 6.3 summarises the CFD runs performed to provide the training and validating data. Each rotating motion was discretised in 180 unsteady steps and pressure values spread along 6 spanwise and 9 chordwise locations on the suction surface of the wing were recorded for each time step. Therefore, each training dataset was comprised by $54 \times 180 = 9720$ patterns. For all rotating motions, the wing was based on a NACA 0015 aerofoil, had an $AR = 5$ and the tip distance from the centre of rotation was 12.5.

Pure Rotation

In the first experiment, cases 1 and 3 (Table 6.3) were used as the training examples and case 2 was used to provide the validation data. Cases $1 - 3$ involve rotating wings with a steady angle of attack $\alpha = 10^o$. Consequently, the NN was trained to approximate the function $C_p = C_p(t, k, \psi, x, y)$. The NN employed had 3×15 neurons in the hidden layers. Figures 6.13(a-f) show the pressure loading on the wing for the CFD computations (left) and the NN predictions (right) for case 2 of Table 6.3. The runs were performed for a half azimuthal cycle and Figures 6.13a-f correspond to 30, 60, 90, 120, 150 and 180 degrees of azimuth respectively. Due to

the non pitching motion, no DS takes place and the NN was able to predict very well the wing's pressure loading, throughout the motion.

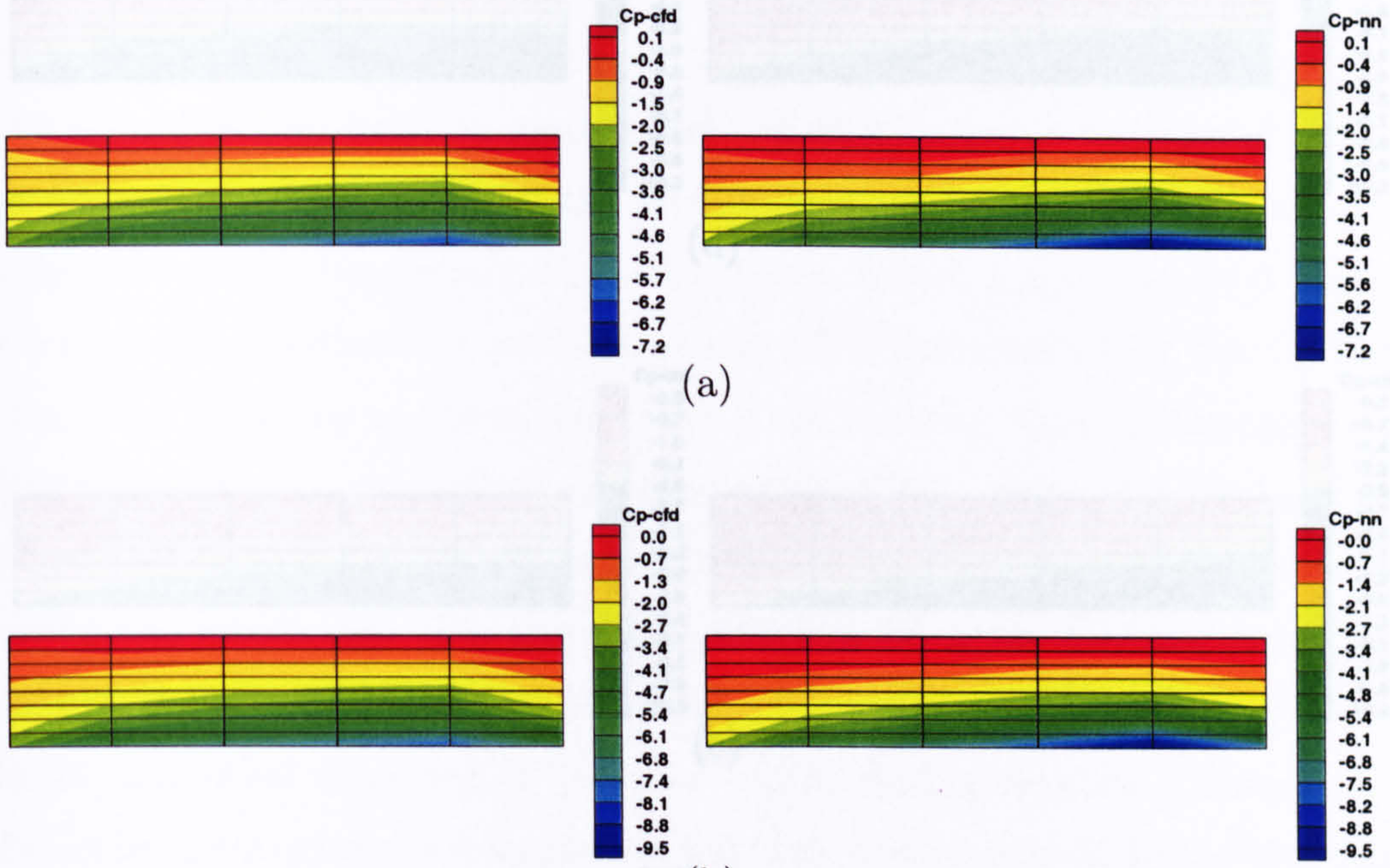

Figure 6.12: CFD computation (left) and NN prediction (right) for case 2 of Table 6.3. The NN was trained using cases 1 and 3 of Table 6.3. (a) 30^o azimuth, (b) 60^o azimuth, (c) 90^o azimuth, (continued over...).

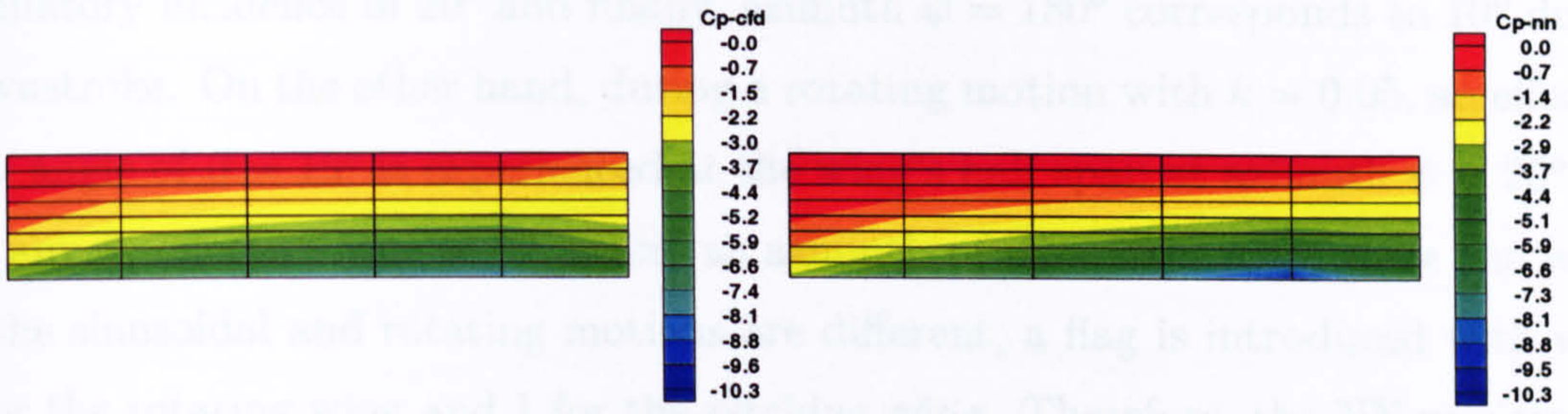

(d)

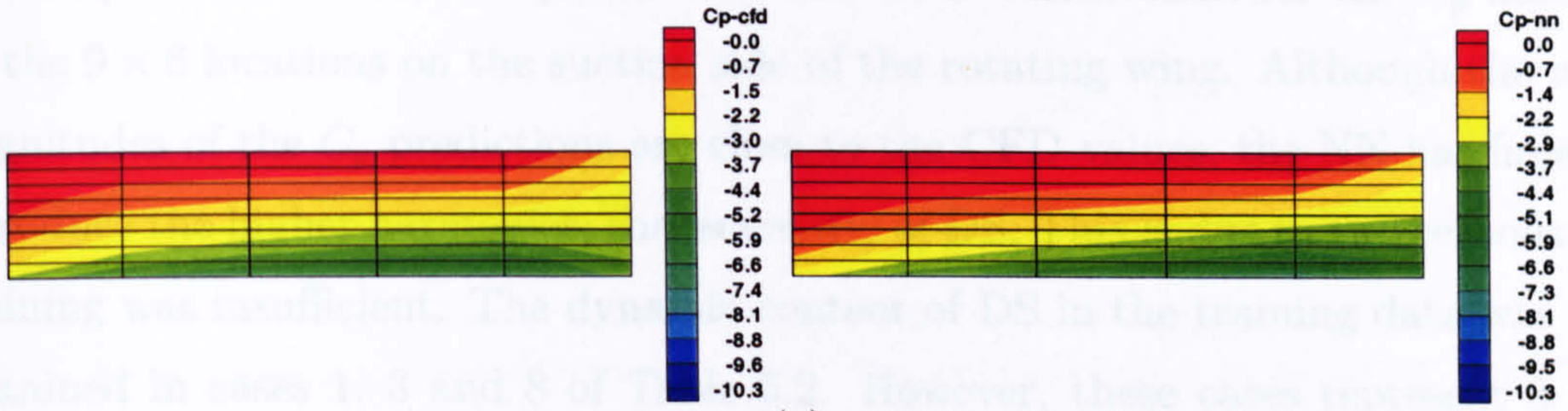

(e)

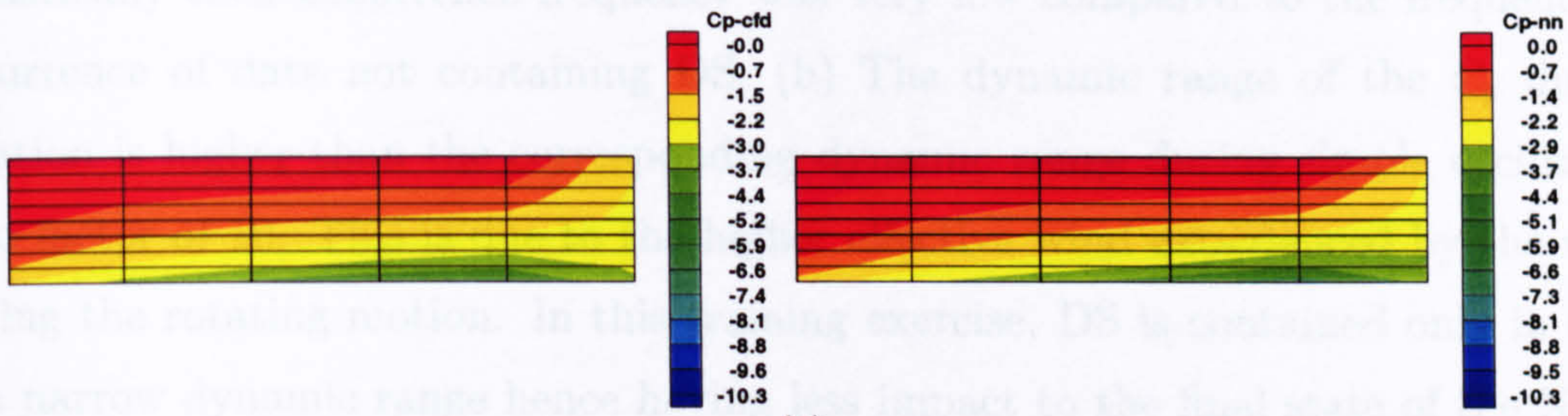

(f)

Figure 6.13: (d) 120^o azimuth, (e) 150^o azimuth and (f) 180^o azimuth (...concluded).

Rotation with Pitch

So far, the NN has yielded very good results for pitching/ramping motions (DS present) as well as motions involving pure rotation (DS absent). In this section a wild extrapolation is attempted. The NN will be trained by the pure sinusoidal motions of cases 1, 3 and 8, shown on Table 6.2 as well as the pure rotational motion of case 2 of Table 6.3 in an attempt to predict the dynamics of the pitching-rotational motion of case 5 of Table 6.3. The data from all these cases need to be presented to the NN in a unified way. Since the pitching and the rotating components are in phase and of equal frequency, a half azimuthal cycle of the rotation corresponds to a half period of the oscillation. Azimuth $\psi = 0^o$ corresponds to the mean angle of

the oscillation (10°) during upstroke, azimuth $\psi = 90^o$ corresponds to the maximum oscillatory incidence of 20^o and finally, azimuth $\psi = 180^o$ corresponds to 10^0 during downstroke. On the other hand, during a rotating motion with $k = 0.05$, an effective yaw angle of $\beta = 15^o$ is experienced at the wing's half span at azimuth $\psi = 25^o$ and for any k, effective yaw of 0^o occurs at azimuth of $\psi = 90^o$. Also, since the wings of the sinusoidal and rotating motions are different, a flag is introduced with value 0 for the rotating wing and 1 for the pitching wing. Therefore, the NN was trained to approximate the functional: $C_p = C_p(flag, \alpha, \psi, k, t, x, y)$. Figures 6.14a-f show the comparison between NN predictions and CFD calculations for the C_p histories for the 9×6 locations on the suction side of the rotating wing. Although the mean magnitudes of the C_p predictions are close to the CFD values, the NN has failed to reproduce the higher harmonics, characteristic of DS. This is due to two reasons: (a) Training was insufficient. The dynamic content of DS in the training data was only contained in cases 1, 3 and 8 of Table 6.2. However, these cases represent 3 only different azimuthal steps out of the total of 180 during rotation. Therefore, their statistically their occurrence frequency was very low compared to the frequency of occurrence of data not containing DS. (b) The dynamic range of the C_p during rotation is higher than the corresponding dynamic range during simple oscillation by a factor of 10. This is due to the higher effective wind experienced by the wing during the rotating motion. In this training exercise, DS is contained only in data of a narrow dynamic range hence having less impact to the final state of the NN.

6.3. EXPLOITATION OF NEURAL NETWORKS FOR DYNAMIC STALL MODELLING

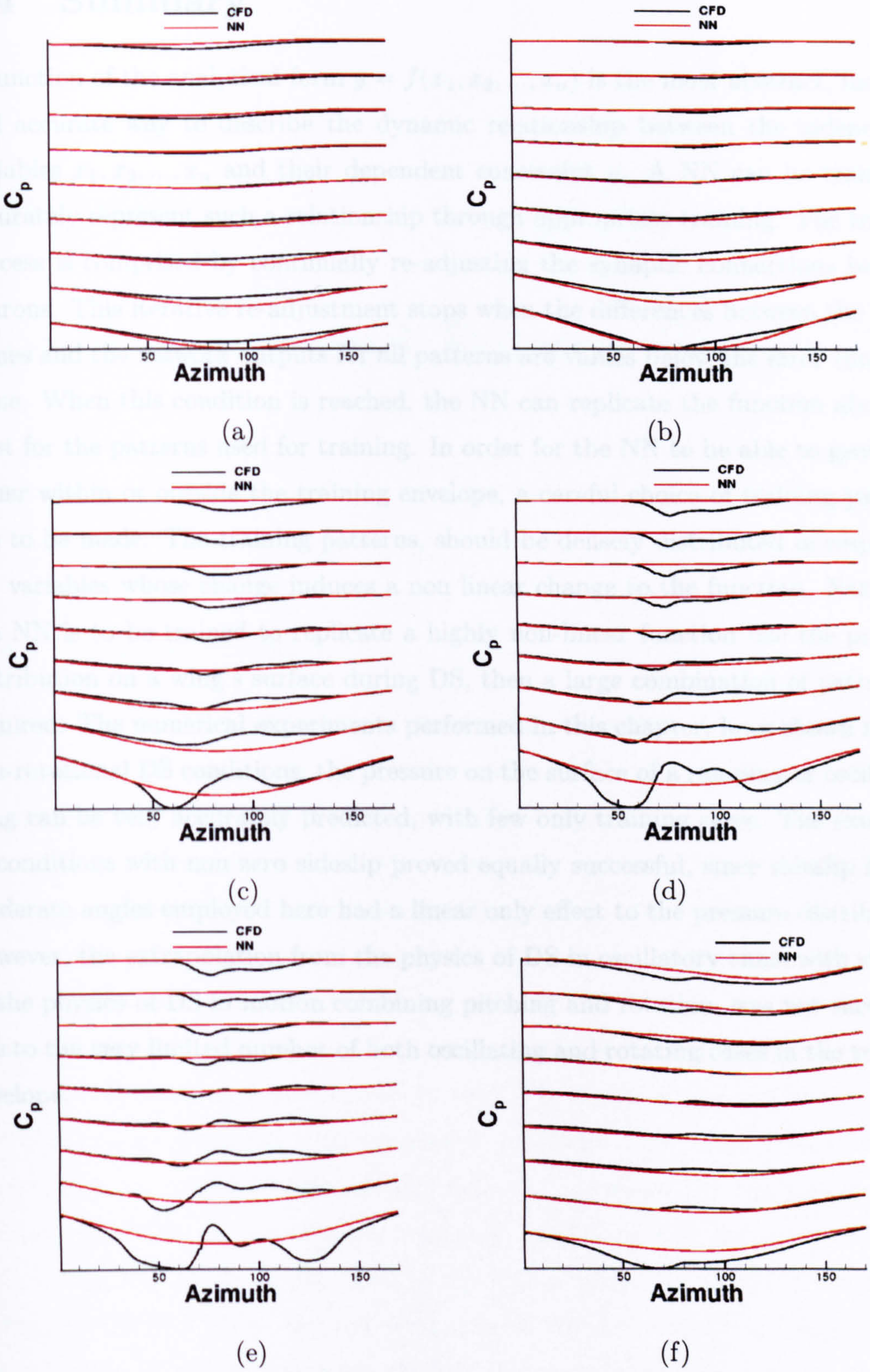

Figure 6.14: CFD computations vs NN predictions of the C_p histories for case 5 of Table 6.3. The NN was trained using cases 1, 3 and 8 of Table 6.2 and case 2 of Table 6.3. Spanwise rakes at (a) 0%, (b) 20%, (c) 40%, (d) 60%, (e) 80% and (f) 100% are shown.

6.3. EXPLOITATION OF NEURAL NETWORKS FOR DYNAMIC STALL MODELLING

6.4 Summary

A function of the analytical form $y = f(x_1, x_2, ..., x_n)$ is the most abstract, inclusive and accurate way to describe the dynamic relationship between the independent variables $x_1, x_2, ..., x_n$ and their dependent constraint y. A NN can be trained to accurately represent such a relationship through appropriate training. The training process is comprised by continually re-adjusting the synaptic connections between neurons. This iterative re-adjustment stops when the differences between the target values and the network outputs for all patterns are values below the error threshold value. When this condition is reached, the NN can replicate the function above, at least for the patterns used for training. In order for the NN to be able to generalise either within or outside the training envelope, a careful choice of training patterns has to be made. The training patterns, should be densely distributed in respect to the variables whose change induces a non linear change to the function. Naturally, if a NN is to be trained to replicate a highly non-linear function like the pressure distribution on a wing's surface during DS, then a large combination of patterns is required. The numerical experiments performed in this chapter, have shown that in non-rotational DS conditions, the pressure on the surface of a ramping or oscillating wing can be very accurately predicted, with few only training cases. The extension to conditions with non zero sideslip proved equally successful, since sideslip for the moderate angles employed here had a linear only effect to the pressure distribution. However, the extrapolation from the physics of DS in oscillatory cases with sideslip to the physics of DS in motion combining pitching and rotation, was not successful due to the very limited number of both oscillating and rotating cases in the training envelope.

Chapter 7

Conclusions and Future Work

In this chapter the conclusions drawn from this work are summarised and suggestions for future work are put forward.

7.1 Conclusions

The first part of this work has been the detailed validation of a CFD method for 3D dynamic stall cases. The 3D structure of the DSV and the time evolution of the dynamic stall phenomenon were revealed and found to agree well with the only flow visualisation study available [44]. This is the first time in the literature that extensive computations have been undertaken for this very complex unsteady flow phenomenon. The first encouraging result has been to establish that CFD was able to match the available experimental data with good accuracy, and moderate computational cost. For the low-Re cases, all flow structures identified with the smoke visualisation were present [42] in the CFD solutions and the flow topology was found to be predicted with remarkable precision. The comparisons with the experiments performed by Schreck and Helin [41], revealed the importance of the accurate modelling of the inboard boundary conditions and provided confidence in the modelling of the highly vortical tip region where the DSV-TV interaction dominates the flow. The tapered wing case of the Laboratory of Marseilles [45] was predicted extremely well given the fact that velocity profiles were compared at various ϕ angles during the oscillation of the wing and at various spanwise locations. This highlights that accurate field data from experiments can be predicted well. In addition, this is the first time field data for DS are compared against CFD. The ramping cases by Coton and Galbraith [44] were predicted reasonably well with

some discrepancies in the stall angle attributed to differences between the conditions of the experimental investigation (for example, the CFD computations have been performed with free-stream conditions at the far field of the computational domain while the real wing model was confined by both tunnel walls and supports) and the present simulation results.

The comparisons between CFD and the PIV experiments of Wernert *et al.*showed that both the flowfield and the evolution of DS can be predicted well by CFD.

Following the necessary comparisons between CFD and experiments to build confidence on the numerical results, the overall dynamics of the DSV and the parameters that influence its shape and evolution were assessed. It has been shown that the DS and the tip vortices are the dominant flow features. Short AR wings are more susceptible to the influence of the TV, since the latter influences a larger part of the wing's planform. The shape and dynamics of the DSV also depend on the Re and M numbers and to a lesser extent to the planform shape and sideslip. The Re in particularly seems to be affecting the distance of the DSV's extremum to the tip region. Rotation produces a distinctive asymmetry to the formation of the DSV, possibly due to the radial dependence of the inflow velocity. In all cases, the near the tip region pressure distribution is primarily influenced by the TV.

Finally, the capability of a NN to predict the pressure distribution on the suction side of a wing during DS was assessed. It has been shown that the pressure on the surface of a ramping or oscillating wing can be very accurately be predicted, both within and outside the training envelope, with few only training cases. The extension to conditions with non zero sideslip proved equally successful, since sideslip for the moderate angles employed here had a linear only effect to the pressure distribution. However, the extrapolation from the physics of DS in oscillatory cases with sideslip to the physics of DS in motion combining pitching and rotation, was not successful due to the very limited number of both oscillating and rotating cases considered.

7.2 Future Work

Three-dimensional DS is primarily encountered on rotating surfaces like helicopter rotors and wind turbine blades. However, there is a lack in literature of detailed measurements on rotating wings. Therefore experiments conducted on realistic rotating conditions are necessary to assess the potential of CFD to simulate accurately such flows. Such measurements should include both on and off-surface data.

Also, this work has not addressed the performance of different turbulence models, along the lines of which, the following three points need to be adressed:

1. Investigation of the effect of turbulence model for flows with significant rotation such as the core of dynamic stall vortex. In some comparisons, the growth and diffusion of the DS vortex in the computation appears to be greater that the one measured. This may be due to turbulence model or due to the diffusion of the scheme especially when TVD limiters are on.

2. The flow conditions of some computations are probably in the transitional flow regime. For 3D there is no too much hope that the transition location can be predicted (and if the transition location is not right then the transitional flow prediction is difficult and not very accurate). I am not therefore suggesting that somebody has to look at transitional flow effects especially for the very complex problem 3D, DS that you looked in your thesis. You may just want to add some commends on the effect of transition.

3. Large eddy simulations (LES) or Detached Eddy Simulations (DES) could reveal more on the fundamental mechanisms of vortex formation and convection over the wing surface given that the DS vortex away from the surface would move in an almost uniform mesh (needed for LES) where the accuracy of the numerical scheme will not be affected by grid stretching which can degrade the accuracy of the scheme to less than the design order of accuracy. There are several papers in the literature where the effect of grid stretching on the accuracy of the computations has been investigated and it was shown that even 2nd order schemes are not truly second order accurate with large grid stretching.

The NN approach although has already provided promising results, is still far from being established as the weapon of choice in modelling of 3D DS as encountered in rotorcraft. The high computational times involved in rotating geometries are the only limiting factors towards building a detailed training database. This database will provide the ultimate test on the suitability of the NN approach. Thereafter, research in the direction of designing and testing a controller able to provide on-the-fly adjustments, should be the next step.

Thorough analysis of the 3D DS phenomenon in rotating conditions is of primary importance in the efficient rotorcraft and wind turbine design. Advances on this direction will have multi-faceted benefits, as they will lead to not only faster but also safer rotorcraft and more efficient power generation.

7.2. FUTURE WORK

Bibliography

[1] Carr L.W. McCroskey W.J. and McAlister K.W. Dynamic stall experiments on oscillating airfoils. *AIAA J.*, 14(1):57–63, 1976.

[2] Prouty R.W. *Helicopter Aerodynamics.* PJS Publications, 1985.

[3] Spentzos A. et al. Investigation of three-dimensional dynamic stall using computational fluid dynamics. *AIAA J.*, 43(5):1023–1033, May 2005.

[4] Web of Knowledge. *http://wok.mimas.ac.uk/.*

[5] NASA Technical Report Server. *http://ntrs.nasa.gov/.*

[6] AIAA Database. *http://www.aiaa.org/content.cfm?pageid=413.*

[7] Telionis D.P. Unsteady boundary layers, separated and attached. In *Unsteady Aerodynamics*, AGARD Conference Proceedings, CP-227, Ottawa Canada, 1977. AGARD.

[8] McCroskey W.J. *et al.*. Dynamic stall of advanced airfoil sections. *J. American Helicopter Society*, pages 40–50, July 1981.

[9] Mehta U.B. and Lavan Z. Starting vortex, separation bubbles and stall: A numerical study of laminar unsteady flow around an airfoil. *J. Fluid Mech.*, 67(2):227–256, 1975.

[10] Gulcat U. *Separate Numerical Treatment of Attached and Detached Flow Regions in General Viscous Flows.* PhD thesis, Georgia Institute of Technology, Atlanda, Georgia, 1981.

[11] Davis S.S. Chyu W.J. and Chang K.S. Calculation of unsteady transonic flow over an airfoil. *AIAA J.*, 19(6):684–690, 1981.

[12] Baldwin B.S. and Lomax H. Thin layer approximation and algebraic model for separated turbulent flows. *AIAA Paper 78-257*, January 1978.

[13] Shamroth S.J. and Gibeling H.J. Analysis of turbulent flow about an isolated airfoil using a time-dependent navier-stokes procedure. In *AGARD Conf Proc 296, Boundary Layer Effects on Unsteady Airloads, Paper Presented at 51st Meet of AGARD Structures & Materials Panel*, pages 8.1–8.14, Aix-en-Provence, France, September 14-19 1980. AGARD.

[14] Wu J.C. Zonal solution of unsteady viscous flow problems. *AIAA Paper 84-1637*, 1984.

[15] Wu J.C. Wang C.M. and Tuncer I.H. Unsteady aerodynamics of rapidly pitched airfoil. *AIAA Paper 86-1105*, 1986.

[16] Tuncer I.H. *Unsteady Aerodynamics of Oscillating and Rapidly Pitched Airfoils.* PhD thesis, Georgia Institute of Technology, Atlanta, Georgia, USA, 1988.

[17] Various authors. Compendium of unsteady aerodynamic measurements. In *AGARD Advisory Report AR-702.* AGARD, August 1982.

[18] L.W. Carr. Progress in analysis and prediction of dynamic stall. *J. Aircraft*, 25(1):6–17, January 1988.

[19] Visbal M.R. Effect of compressibility on dynamic stall. *AIAA Paper 88-0132*, 1988.

[20] Srinivasan G.R. Ekaterinaris J.A. and McCroskey W.J. Present capabilities of predicting two-dimensional dynamic stall. In *Aerodynamics and Aeroacoustics of Rotorcraft*, AGARD Conference Papers, CP-552, August 1995.

[21] Graham J.M.R. The lift on an aerofoil in starting flow. *J. Fluid Mechanics*, pages 413–425, August 1983.

[22] Piziali R.A. An experimental investigation of 2d and 3d oscillating wing aerodynamics for a range of angle of attack including stall. *NASA-TM-4632*, 1993.

[23] Chandrasekhara M.S. *et al.*. A phase-locked high-speed real-time interferometry system for large amplitude unsteady flows. *Experiments in Fluids*, 20:61–67, 1995.

[24] Cricelli A.S. Ekaterinaris J.A. and Platzer M.F. A zonal method for unsteady viscous compressible airfoil flows. *Journal of Fluids and Structures*, 8:107–123, 1994.

[25] Ekaterinaris J.A. Compressible studies on dynamic stall. *AIAA Paper 89-0024*, 1989.

[26] Lorber P.F. and Carta F.O. Unsteady stall penetration experiments at high Reynolds number. *AFSOR TR-87-1202*, 1987.

[27] Fu D.X. Guo W.H. and Wa Y.W. Numerical investigation of dynamic stall of an oscillating aerofoil. *Int. J. Num. Meth. Fluids*, 19(8):723–734, August 1994.

[28] McCroskey W.J. The phenomenon of dynamic stall. *NASA-TM-81264*, March 1981.

[29] Launder B.E. and Spalding D.B. The numerical computation of turbulent flows. *Comp. Methods Appl. Mech. Engng.*, 3:269–289, 1974.

[30] Jones W.P. and Launder B.E. The prediction of laminarization with a two-equation model of turbulence. *Int. J. Heat and Mass Transfer*, 15:301–314, February 1972.

[31] Yap C.R. *Turbulent heat and Momentum Transfer in Recirculating and Impinging Flows.* PhD thesis, Faculty of Technology, University of Manchester, 1987.

[32] Launder B.E. and Sharma B.I. Application of the energy-dissipation model of turbulence to the calculation of flow near a spinning disk. *Letters in Heat and Mass Transfer*, 1:131–138, 1974.

[33] Chien K.-Y. Predictions of channel and boundary-layer flows with a low-Reynolds-number turbulence model. *AIAA J.*, 20(1):33–38, January 1982.

[34] Wilcox D.C. and Traci R.M. A complete model of turbulence. *AIAA Paper 76-351*, July 1976.

[35] Wilcox D.C. *Turbulence Modeling for CFD.* DCW Industries, 1993.

[36] F.R. Menter. Influence of freestream values on $k-\omega$ turbulence model predictions. *AIAA J.*, 30(6):1657–1659, July 1992.

[37] Liu F. Multigrid solution of the navier-stokes equations with a two-equation turbulence model. In D.A. Caughey and M.M. Hafez, editors, *Frontiers of Computational Fluid Dynamics*, pages 339–359. John Wiley and Sons, 1994.

[38] Wernert P. *et al.*. Experimental and numerical investigation of dynamic stall on a pitching airfoil. *AIAA J.*, 34(5):982–989, 1996.

[39] Freymuth P. Three dimensional vortex systems of finite wings. *Journal of Aircraft*, 10:971–972, 1988.

[40] Horner M. B. Controlled three-dimensionality in unsteady separated flows about a sinusoidally oscillating flat plate. In *AIAA Paper 90-0689*. AIAA, January 8-11 1990. 28th Aerospace Sciences Meeting, Reno, Nevada, USA.

[41] Schreck S.J. and Helin H.E. Unsteady vortex dynamics and surface pressure topologies on a finite wing. *J. Aircraft*, 31(4):899–907, 1994.

[42] Moir S. Moir and Coton F. N. An examination of the dynamic stalling of two wing planforms. *Glasgow University Aero. Rept. 9526*, 1995.

[43] Tang D.M. and Dowell E. H. Experimental investigation of three-dimensional dynamic stall model oscillating in pitch. *J. of Aircraft*, 32(5):163–186, Sept-Oct 1995.

[44] Coton F. Coton and Galbraith R. An experimental study of dynamic stall on a finite wing. *The Aeronautical Journal*, 103(1023):229–236, 1999.

[45] Favier D. Berton E., Allain C. and Maresca C. *Experimental Methods for Subsonic Flow Measurements, in Progress in Computational Flow-Structure Interaction, Haase W., Selmin V. and Winzell B., Eds.*, volume 81. Springer Verlag, 2003.

[46] Favier D. Berton E., Allain C. and Maresca C. *Database for Steady and Unsteady 2-D and 3-D Flow, in Progress in Computational Flow-Structure Interaction, Haase W., Selmin V. and Winzell B., Eds.*, volume 81. Springer Verlag, 2003.

[47] McCroskey W.J. Vortex wakes of rotorcraft. *AIAA Paper 95-0530*, 1995.

[48] Piquet J. Guilmineau E. and Quentey P. Unsteady two-dimensional turbulent viscous flow past airfoils. *Int. J. Num. Meth. Fluids*, 25(3):315–366, 1997.

[49] Cebeci T. and Smith A.M. *Analysis of Turbulent Boundary Layers.* Academic Press, New York, 1974.

[50] Johnson D.A. and King L.S. A mathematically simple turbulence closure model for attached and separated turbulent boundary layers. *AIAA J.*, 23(11):1684–1692, November 1985.

[51] Spalart P.R. A one-equation turbulence model for aerodynamic flows. *La Recherche A'erospatiale*, 1:5–21, 1994.

[52] Spalart P.R. and Allmaras S.R. A one-equation turbulence model for aerodynamic flows. *AIAA Paper 92-0439*, 1992.

[53] Baldwin B.S. and Barth T.J. A one equation turbulence model for high Reynolds number wall-bounded flows. *NASA TM-102847*, NASA Ames, August 1990.

[54] Ekaterinaris J.A. Numerical investigation of dynamic stall of an oscillating wing. *AIAA J.*, 33(10):1803–1808, October 1995.

[55] Ekaterinaris J.A. and Platzer M.F. Computational prediction of airfoil dynamic stall. *Progress in Aerospace Sciences*, 33(11-12):759–846, 1997.

[56] Barakos G. and Drikakis D. Unsteady separated flows over maneuvering lifting surfaces. *Phil. Trans R. Soc. Lond. A*, 358:3279–3291, 2000.

[57] Barakos G. and Drikakis D. Computational study of unsteady turbulent flows around oscillating and ramping aerofoils. *Int. J. Num. Meth. Fluids*, 42:163–186, 2003.

[58] Newsome R. W. Navier-stokes simulation of wing-tip and wing-juncture interactions for a pitching wing. In *AIAA Paper 94-2259.* AIAA, June 20-23 1994. 24th AIAA Fluid Dynamics Conference, Colorado Springs, Colorado, USA.

[59] Morgan P.E. and Visbal M.R. Simulation of unsteady three-dimensional separation on a pitching wing. *31st AIAA Fluid Dynamics Conference and Exhibit, Anaheim, CA, June 11-14, 2001*, 31(4):784–786, 2001.

[60] Tran C.T. and Petot D. Semi-empirical model for the dynamic stall of airfoils in view of application to the calculation of responcses of a helicopter forward flight. *Vertica*, 5(1):35–53, January 1981.

[61] Beedy J. *et al.*. Non-linear analysis of stall flutter based on the onera aerodynamic model. *AERONAUTICAL JOURNAL*, 107(1074):405–509, 2003.

[62] Beddoes T.S. and Leishman J.G. A generalised model for airfoil unsteady aerodynamoc behaviour and dynamic stall using the indicial method. 42nd Annual Forum of the American Helicopter Society, 1986.

[63] Beddoes T.S. and Leishman J.G. Using cfd to improve simple aerodynamic models for rotor codes. 4th Decennial Conference by the Americal Helicopter Society, 2004.

[64] R. Vepa. Non-linear aerodynamics modelling for modal analysis of aircraft dynamics. Number 94 in CEAS Aerospace Aerodynamics Conferences, June 2002.

[65] Faller W.E. Schreck S.J. and Helin H.E. Real-time model of three dimensional dynamic reattachment using neural networks. *Journal of Aircraft*, 32(6):1177–1182, 1995.

[66] Faller W.E. and Schreck S.J. Unsteady fluid mechanics applications of neural networks. *AIAA Journal*, 34(1):48–55, 2005.

[67] Badcock K.J. *et al.*. Elements of computational fluid dynamics on block structure grids using implicit solvers. *Prog. in Aerospace Sc.*, 36(6):351–392, 2000.

[68] Jameson A. Time Dependent Calculations Using Multigrid with Applications to Unsteady Flows Past Airfoils and Wings. In *Proceedings of the AIAA*, Honolulu, HI, June 1991. Paper 91-1596.

[69] Osher S.and Chakravarthy S. Upwind Schemes and Boundary Conditions with Applications to Euler Equations in General Geometries. *Journal of Computational Physics*, 50:447–481, 1983.

[70] Roe P.L. Approximate Rieman Solver, Parameters Vectors and Difference Schemes. *Journal of Computational Physics*, 43:357–372, 1981.

[71] Woodgate M. *et al.*. A Parallel 3D Fully Implicit Unsteady Multiblock CFD Code Implemented on a Beowulf Cluster. In *Parallel CFD Conference*, Williamsburg, USA, 1999.

[72] Wilcox D.C. Reassessment of the scale-determining equation for advanced turbulence models. *AIAA J.*, 26(11):1299–1310, November 1988.

[73] Morkovin M.V. Effects of Compressibility on Turbulent Flows. In A. Favre, editor, *Méchanique de la Turbulence*, pages 367–380. CNRS, 1962.

[74] Menter F.R. Two-equation eddy-viscosity turbulence models for engineering applications. *AIAA J.*, 32(8):1598–1605, August 1994.

[75] Moir S. and Gould A. VoTMATA - British Aerospace Default Model. Technical report, BAE SYSTEMS, 1998.

[76] Kolmogorov A.N. Equations of turbulent motion of an incompressible fluid. *Izvestiya Akademii Nauk. Seriya Fizicheskaya*, 6:55–58, 1942.

[77] Harlow F.H. and Nakayama P.I. Transport of Turbulence Energy Decay Rate. Technical Report LA-3854, Los Alamos Sci. Lab., 1968.

[78] Spalding D.B. The Prediction of Two-Dimensional Steady Turbulent Flows. Heat Transfer Section Report EF/TN/A/16, Imperial College, 1969.

[79] Abid R. Speziale C.G. and Anderson E.C. Critical Evaluation of Two-Equation Models for Near-Wall Turbulence. *AIAA*, 30:324–331, 1992.

[80] Nayyar P. and Barakos G. A Summary of Turbulence Modelling Approaches in CFD. Aero Report 0206, University of Glasgow, Aerospace Engineering Dept., September 2002.

[81] Wilcox D.C. Simulation of transition with a two-equation turbulence model. *AIAA*, 32:247–255, 1994.

[82] McCulloch W.S and Pitts W. A logical calculus of the ideas immanent in nervous activity. *Bulletin of Mathematical Biophysics*, 5:115–133, 1943.

[83] Von Neumann J. The computer and the brain. *New Haven: Yale University Press*, 1958.

[84] Lapedes A. and Farber R. How neural networks work. *Neural Information Processing Systems*, pages 442–456, 1988.

[85] Kolmogorov A.T. On the representaton of continuous functions of many variables by superposition of continuous functions of one variable and addition. *Translated in American Mathematical Society Translations*, 28(2):55–59, 1963.

[86] Kavzoglu T. Mather P.M. The use of backpropagating artificial neural networks in land cover classification. *INT. J. of Remote Sensing*, 24(23):4907–4938, 2003.

[87] Picton P. *Introduction to Neural Networks.* MACMILLAN PRESS LTD, 1994.

[88] Schreck S.J. Addington G.A. and Luttges. Flow field structure and development near the root of a straight wing pitching at constant rate. *AIAA-1991-3264*, 1991.

Appendix A

FFBP NN Source Code

```
1           program neural_net
2           parameter(imax1=100000,imax2=64,ilay=3)
3           integer epoch,istart
4           integer i,j,k,p,np,list(imax1)
5           integer numpattern,numinput,numhidden
6           integer numoutput,nml
7           real*8 input(0:imax1,0:imax2)
8           real*8 target(0:imax1,0:imax2)
9           real*8 output(0:imax1,0:imax2)
10          real*8 hidden(ilay,imax1,imax2)
11          real*8 sum(0:imax1,0:imax2),summ(0:imax1)
12          real*8 weightIH(0:imax2,0:imax2)
13          real*8 weightHH(ilay,0:imax2,0:imax2)
14          real*8 weightHO(0:imax2,0:imax2)
15          real*8 deltaO(0:imax1),deltaH(ilay,0:imax1)
16          real*8 deltaweightIH(0:imax1,0:imax2)
17          real*8 deltaweightHO(0:imax1,0:imax2)
18          real*8 deltaweightHH(ilay,0:imax1,0:imax2)
19          real*8 inp(imax1,imax2)
20          real*8 error,eta,alpha,smallwt,error1
21          real*8 errormax,r
22          character*50 patfile
23          character*13 wfile
24
25  11      format(60(f12.6,2X))
26  12      format(A50)
27  13      format(A1)
28
29          smallwt=0.1
30          iepoch=1
31          error0=0.0
32
33          open(1,file='input')
34          read(1,*)patfile
35          read(1,*)numinput
36          read(1,*)nml
```

```
37          read(1,*)numhidden
38          read(1,*)numoutput
39          read(1,*)ifresh
40          read(1,*)cerror
41          read(1,*)eta
42          read(1,*)alpha
43          close(1)
44    C
45    C     intitialise input_to_hidden weights
46          do j=1,numhidden
47             do i=1,numinput
48                deltaweightIH(i,j)=0.0
49                weightIH(i,j)=2.0*(rand(0))*smallwt
50             enddo
51          enddo
52    C
53    C     intitialise hidden_to_output weights
54          do k=1,numoutput
55             do j=1,numhidden
56                deltaweightHO(j,k)=0.0
57                weightHO(j,k)=2.0*(rand(0))*smallwt
58             enddo
59          enddo
60    C
61    C     initialise hidden to hidden weights
62          do il=1,nml
63             do i=1,numhidden
64                do j=1,numhidden
65                   deltaweightHH(il,j,i)=0.0
66                   weightHH(il,j,i)=2.0*(rand(0))*smallwt
67                enddo
68             enddo
69          enddo
70    C
71          open(1,file=patfile)
72          i=1
73    10    list(i)=i
74          read(1,*,END=777)(inp(i,j), j=1,numinput+numoutput)
75          do j=1,numinput
76             input(i,j)=inp(i,j)
77          enddo
78          do j=1,numoutput
79             target(i,j)=inp(i,j+numinput)
80          enddo
81          i=i+1
82          goto 10
83    777   continue
84          numpattern=i-1
85          write(*,*) '# ',numpattern,' patterns'
86          close(1)
87    C
```

```
88  c  Training begins here
89           do epoch=iepoch,50000000
90              error=0.0
91              errormax=-10.0e+6
92              do np=1,numpattern
93                 np=1+int(rand(0)*float(numpattern))
94  c
95  c           propagate forward from input to hidden1
96                 do j=1,numhidden
97                    sum(p,j)=weightIH(0,j)
98                    do i=1,numinput
99                       sum(p,j)=sum(p,j)+
100       &              input(p,i)*weightIH(i,j)
101                   enddo
102                   hidden(1,p,j)=1.0/(1.0+exp(-sum(p,j)))
103                enddo
104 c
105 c  propagate forward from hidden-1 to hidden-n
106                do il=1,nml-1
107                   do j=1,numhidden
108                      sum(p,j)=weightHH(il,0,j)
109                      do i=1,numhidden
110                         sum(p,j)=sum(p,j)+
111      &                  hidden(il,p,i)*weightHH(il,i,j)
112                      enddo
113                      hidden(il+1,p,j)=1.0/(1.0+exp(-sum(p,j)))
114                   enddo
115                enddo
116
117 c  propagate forward from hidden-n to output, calculate error &
118 c  remedy per output node
119                do k=1,numoutput
120                   sum(p,k)=weightHO(0,k)
121                   do j=1,numhidden
122                      sum(p,k)=sum(p,k)+
123                      hidden(nml,p,j)*weightHO(j,k)
124                   enddo
125                   output(p,k)=1.0/(1.0+exp(-sum(p,k)))
126                   if (epoch.eq.1) error0=error
127                      r=target(p,k)-output(p,k)
128                      r=abs(r)
129                      r=0.5*r*r
130                      error=error+r
131                      errormax=dmax1(errormax,r)
132                      if (errormax.eq.r) i1=p
133                      delta0(k)=(target(p,k)-output(p,k))*
134      &               (output(p,k)*(1.0-output(p,k)))
135             enddo
136             if (epoch.eq.1) error0=error
137             error1=error/error0
138
```

```
139
140   c  backpropagate from output to hidden-n, use output remedy
141   c  to calculate remedy per hidden-n node
142                 do j=1,numhidden
143                    summ(j)=0.0
144                    do k=1,numoutput
145                       summ(j)=summ(j)+
146         &             weightHO(j,k)*deltaO(k)
147                    enddo
148                    deltaH(nml,j)=summ(j)*hidden(nml,p,j)*
149         &          (1.0-hidden(nml,p,j))
150                 enddo
151
152   c  backpropagate from hidden-n to hidden1, use hidden-n remedy
153   c  to calculate remedy per hidden-n-1 node
154                 do il=nml-1,1,-1
155                    do j=1,numhidden
156                       summ(j)=0.0
157                       do jk=1,numhidden
158                          summ(j)=summ(j)+
159         &                weightHH(il,j,jk)*deltaH(il+1,jk)
160                       enddo
161                       deltaH(il,j)=summ(j)*
162         &             hidden(il,p,j)*(1.0-hidden(il,p,j))
163                    enddo
164                 enddo
165
166   c  backpropagate from hidden1 to input & use hidden1 remedy
167   c  to re-calculate i-h1 weights
168                 do j=1,numhidden
169                    deltaweightIH(0,j)=eta*deltaH(1,j)+
170         &          alpha*deltaweightIH(0,j)
171                    weightIH(0,j)=weightIH(0,j)+
172         &          deltaweightIH(0,j)
173                    do i=1,numinput
174                       deltaweightIH(i,j)=
175         &             eta*input(p,i)*deltaH(1,j)+alpha*
176         &             deltaweightIH(i,j)
177                       weightIH(i,j)=weightIH(i,j)+
178         &             deltaweightIH(i,j)
179                    enddo
180                 enddo
181
182   c  propagate from hidden1 to hidden_n & use hidden2 remedy
183   c  to recalculate h_n-h_n+1 weights
184                 do il=1,nml-1
185                    do j=1,numhidden
186                       deltaweightHH(il,0,j)=eta*deltaH(il+1,j)
187         &             +alpha*deltaweightHH(il,0,j)
188                       weightHH(il,0,j)=weightHH(il,0,j)+
189         &             deltaweightHH(il,0,j)
```

```
190                     do i=1,numhidden
191                        deltaweightHH(il,i,j)=
192       &                eta*hidden(il,p,i)*deltaH(il+1,j)
193       &                +alpha*deltaweightHH(il,i,j)
194                        weightHH(il,i,j)=weightHH(il,i,j)+
195       &                deltaweightHH(il,i,j)
196                     enddo
197                  enddo
198               enddo
199
200   c  propagate from hidden3 to output & use output remedy
201   c  to re-calculate h3-o weights
202               do k=1,numoutput
203                  deltaweightHO(0,k)=
204         &        eta*delta0(k)+alpha*deltaweightHO(0,k)
205                  weightHO(0,k)=weightHO(0,k)+
206         &        deltaweightHO(0,k)
207                  do j=1,numhidden
208                     deltaweightHO(j,k)=eta*hidden(nml,p,j)*
209         &           delta0(k)+alpha*deltaweightHO(j,k)
210                     weightHO(j,k)=weightHO(j,k)+
211         &           deltaweightHO(j,k)
212                  enddo
213               enddo
214            enddo
215            if (error1.lt.cerror) goto 1000
216            enddo
217   1000     continue
218            write(*,*) 'The End'
219            stop
220            end
221
222
223   c sample input file for a 5-input 1-output NN:
224   c
225   c in1(1) in2(1) in3(1) in4(1) in5(1) target(1)
226   c in1(2) in2(2) in3(2) in4(2) in5(2) target(2)
227   c ..........................................
228   c in1(n) in2(n) in3(n) in4(n) in5(n) target(n)
229
230
```

Appendix B

FFBP RNN Source Code

```
231           program neural_net
232           parameter(imax1=750,imax2=256,ilay=2)
233           integer epoch,istart,ps(imax2),pe(imax2)
234           integer i,j,k,p,np,list(imax1)
235           integer numpattern,numinput
236           integer numhidden,numoutput,numlay
237           real*8 input(imax1,imax2)
238           real*8 target(imax1,imax2)
239           real*8 output(imax1,imax2)
240           real*8 hidden(ilay,imax1,imax2)
241           real*8 sum(0:imax1,0:imax2),summ(0:imax2)
242           real*8 weightIH(0:imax2,0:imax2)
243           real*8 weightHH(ilay,0:imax2,0:imax2)
244           real*8 weightHO(0:imax2,0:imax2)
245           real*8 deltaO(0:imax2),deltaH(ilay,0:imax2)
246           real*8 deltaweightIH(0:imax2,0:imax2)
247           real*8 deltaweightHO(0:imax2,0:imax2)
248           real*8 deltaweightHH(ilay,0:imax2,0:imax2)
249           real*8 error,eta,alpha,smallwt,error1,r
250
251           character*50 patfile
252           character*13 wfile
253
254     11    format(222(f12.6,2X))
255     12    format(A50)
256     13    format(A1)
257
258           smallwt=0.05
259           iepoch=1
260           error0=0.0
261
262           open(1,file='rinput')
263           read(1,*)patfile
264           read(1,*)numinput
265           read(1,*)numlay
266           read(1,*)numhidden
```

```
267           read(1,*)numoutput
268           read(1,*)ifresh
269           read(1,*)cerror
270           read(1,*)eta
271           read(1,*)alpha
272           read(1,*)wfile
273           close(1)
274
275   c       intitialise input_to_hidden weights
276           do j=1,numhidden
277              do i=1,numinput
278                 deltaweightIH(i,j)=0.0
279                 weightIH(i,j)=2.0*(rand(0))*smallwt
280              enddo
281           enddo
282   c        intitialise hidden_to_output weights
283           do k=1,numoutput
284              do j=1,numhidden
285                 deltaweightHO(j,k)=0.0
286                 weightHO(j,k)=2.0*(rand(0))*smallwt
287              enddo
288           enddo
289   c        initialise hidden to hidden weights
290           do il=1,numlay
291              do i=1,numhidden
292                 do j=1,numhidden
293                    deltaweightHH(il,j,i)=0.0
294                    weightHH(il,j,i)=2.0*(rand(0))*smallwt
295                 enddo
296              enddo
297           enddo
298   C
299   C
300           open(1,file=patfile)
301           do i=1,9999999
302           read(1,*,END=666)(input(i,j), j=1,numinput)
303           enddo
304   666     continue
305           numpattern=i-1
306           write(*,*) '# ',numpattern,' pattern lines'
307           close(1)
308
309           print*,'enter number of sets'
310           read*,numsets
311           print*,'enter p-start for each
312        &          (starting from the 2nd)'
313           do i=2,numsets
314              read*,ps(i)
315              pe(i-1)=ps(i)-1
316           enddo
317           ps(1)=1
```

```
318         pe(numsets)=numpattern
319         write(*,*) '# ',numsets,' sets'
320         index=0
321         numdif=numinput-numoutput
322
323         do i=1,numsets
324            list(i)=i
325            print*,'set ',i,ps(i),pe(i)
326            do ii=ps(i),pe(i)-1
327               do j=1,numoutput
328                  target(ii,j)=input(ii+1,j+numdif)
329               enddo
330            enddo
331         enddo
332         open(1,file='target.pat')
333         do i=1,numsets
334            do j=ps(i),pe(i)-1
335               write(1,11)(target(j,k),k=1,numoutput)
336            enddo
337         enddo
338
339         if (istart.eq.0) then
340            call system('rm ./history.dat')
341         endif
342
343   c     START TRAINING
344         do epoch=iepoch,50000000
345   c
346   c     shuffle training sets
347            do i=1,numsets-1
348               number=int(rand(0)*float(2))
349               if (number.eq.1) then
350                  iii=list(i)
351                  list(i)=list(i+1)
352                  list(i+1)=iii
353               endif
354            enddo
355            error=0.0
356   c
357            do ins=1,numsets
358               index=1
359               do p=ps(list(ins)),pe(list(ins))-1
360
361   c RECCURENT FEEDBACK
362                  if (index.gt.1) then
363                     do j=1,numoutput
364                        input(p,j+numdif)=output(p-1,j)
365                     enddo
366                  endif
367   c
368   c propagate forward from input to hidden1
```

```
                    do j=1,numhidden
                      sum(p,j)=weightIH(0,j)
                       do i=1,numinput
                          sum(p,j)=sum(p,j)+
     &                    input(p,i)*weightIH(i,j)
                       enddo
                       hidden(1,p,j)=
     &                 1.0/(1.0+exp(-sum(p,j)))
                     enddo

c propagate forward from hidden-1 to hidden-n
                    do il=1,numlay-1
                       do j=1,numhidden
                          sum(p,j)=weightHH(il,0,j)
                          do i=1,numhidden
                             sum(p,j)=sum(p,j)+
     &                       hidden(il,p,i)*
     &                       weightHH(il,i,j)
                          enddo
                          hidden(il+1,p,j)=
     &                    1.0/(1.0+exp(-sum(p,j)))
                       enddo
                    enddo

c propagate forward from hidden-n to output,
c calculate error & remedy per output node
                    do k=1,numoutput
                       sum(p,k)=weightHO(0,k)
                       do j=1,numhidden
                          sum(p,k)=sum(p,k)+
     &                    hidden(numlay,p,j)*weightHO(j,k)
                       enddo
                       output(p,k)=1.0/(1.0+
     &                 exp(-sum(p,k)))
                       r=0.5*(target(p,k)-
     &                 output(p,k))**2
c                       r=abs(r)
                       error=error+r
                       deltaO(k)=(target(p,k)
     &                 -output(p,k))*
     &                 (output(p,k)*
     &                    (1.0-output(p,k)))
                    enddo
                    if (epoch.eq.1) error0=error
                    error1=error/error0
                    index=index+1

c backpropagate from output to hidden-n,
c use output remedy to calculate
c remedy per hidden-n node
                    do j=1,numhidden
```

```
420                     summ(j)=0.0
421                     do k=1,numoutput
422                        summ(j)=summ(j)+
423      &                 weightHO(j,k)*deltaO(k)
424                     enddo
425                     deltaH(numlay,j)=
426      &              summ(j)*hidden(numlay,p,j)*
427      &              (1.0-hidden(numlay,p,j))
428                  enddo
429
430  c backpropagate from hidden-n to hidden1, use hidden-n
431  c remedy to calculate remedy per hidden-n-1 node
432                  do il=numlay-1,1,-1
433                     do j=1,numhidden
434                        summ(j)=0.0
435                        do jk=1,numhidden
436                           summ(j)=summ(j)+
437      &                    weightHH(il,j,jk)*
438      &                    deltaH(il+1,jk)
439                        enddo
440                        deltaH(il,j)=summ(j)*
441      &                 hidden(il,p,j)*
442      &                 (1.0-hidden(il,p,j))
443                     enddo
444                  enddo
445
446  c backpropagate from hidden1 to input
447  c & use hidden1 remedy to re-calculate i-h1 weights
448                  do j=1,numhidden
449                     deltaweightIH(0,j)=eta*deltaH(1,j)+
450      &              alpha*deltaweightIH(0,j)
451                     weightIH(0,j)=weightIH(0,j)+
452      &              deltaweightIH(0,j)
453                     do i=1,numinput
454                        deltaweightIH(i,j)=
455      &                 eta*input(p,i)*deltaH(1,j)+
456      &                 alpha*deltaweightIH(i,j)
457                        weightIH(i,j)=weightIH(i,j)+
458      &                 deltaweightIH(i,j)
459                     enddo
460                  enddo
461
462  c propagate from hidden1 to hidden_n &
463  c use hidden2 remedy to recalculate h_n-h_n+1 weights
464                  do il=1,numlay-1
465                     do j=1,numhidden
466                        deltaweightHH(il,0,j)=
467      &                 eta*deltaH(il+1,j)
468      &                 +alpha*deltaweightHH(il,0,j)
469                        weightHH(il,0,j)=
470      &                 weightHH(il,0,j)+
```

```
471         &                   deltaweightHH(il,0,j)
472                             do i=1,numhidden
473                                deltaweightHH(il,i,j)=
474         &                      eta*hidden(il,p,i)*
475         &                      deltaH(il+1,j)
476         &                      +alpha*deltaweightHH(il,i,j)
477                                weightHH(il,i,j)=
478         &                      weightHH(il,i,j)+
479         &                      deltaweightHH(il,i,j)
480                             enddo
481                          enddo
482                          enddo
483
484   c propagate from hidden3 to output
485   c & use output remedy to re-calculate h3-o weights
486                          do k=1,numoutput
487                             deltaweightHO(0,k)=
488           &                 eta*delta0(k)+alpha*deltaweightHO(0,k)
489                             weightHO(0,k)=weightHO(0,k)+
490           &                 deltaweightHO(0,k)
491                             do j=1,numhidden
492                                deltaweightHO(j,k)=
493           &                    eta*hidden(numlay,p,j)*
494           &                    delta0(k)+alpha*deltaweightHO(j,k)
495                                weightHO(j,k)=weightHO(j,k)+
496           &                    deltaweightHO(j,k)
497                             enddo
498                          enddo
499
500                       enddo
501                    enddo
502   C
503   C
504                    if ((epoch/ifresh)*ifresh.eq.epoch) then
505
506                       call weights(epoch,error0,numinput,numlay,
507           &                 numhidden,numoutput,
508           &                 weightIH,weightHH,weightHO,wfile)
509                       write(*,*) epoch,error1
510                       open(3,file='output.pat')
511                       do i3=1,numsets
512                          do j3=ps(i3),pe(i3)-1
513                             write(3,11)(input(j3,k3),k3=1,numinput)
514   C       &                            (output(j3,k3),k3=1,numoutput)
515                          enddo
516                       enddo
517                       close(3)
518                       open(11,file='history.dat',access='append')
519                       write(11,*)epoch,error1
520                       close(11)
521                       call system('./predictr')
```

```
522               endif
523               if (error1.lt.cerror) goto 1000
524            enddo
525
526   1000     continue
527            call weights(epoch,error0,numinput,numlay,numhidden,
528         & numoutput,weightIH,weightHH,weightHO,wfile)
529            write(*,*) epoch,error1
530            write(*,*) 'The End'
531            end
532
533   cccccccccccccccccccccccccccccccccccccccccccccccccccccccccccccccccccc
534            subroutine weights(epoch,error0,ninput,nl,nhidden,noutput,
535         &                     wweightIH,wweightHH,wweightHO,wwfile)
536   cccccccccccccccccccccccccccccccccccccccccccccccccccccccccccccccccccc
537            parameter (imax2=256,ilay=2)
538            integer epoch
539            real*8 wweightHH(ilay,0:imax2,0:imax2)
540            real*8 wweightHO(0:imax2,0:imax2)
541            real*8 wweightIH(0:imax2,0:imax2)
542            character*13 wwfile
543
544            open(1,file=wwfile)
545            write(1,*)epoch,error0
546            write(1,*)ninput,nl,nhidden,noutput
547            do i=0,ninput
548               do j=0,nhidden
549                  write(1,*)wweightIH(i,j)
550               enddo
551            enddo
552            do il=1,nl
553            do i=0,nhidden
554               do j=0,nhidden
555                  write(1,*)wweightHH(il,i,j)
556               enddo
557            enddo
558            enddo
559            do i=0,nhidden
560               do k=0,noutput
561                  write(1,*)wweightHO(i,k)
562               enddo
563            enddo
564            close(1)
565            return
566            end
567
568
569
570   c sample input file for a 5-input 4-output RNN:
571   c t1 in1(t1) in2(t1) in3(t1) in4(t1)
572   c t2 in1(t2) in2(t2) in3(t2) in4(t2)
```

```
573  C ..............................
574  c tn in1(tn) in2(tn) in3(tn) in4(tn)
575
```